Magnetic Suspension Techniques

for

Precision Motion Control

by

David Lippincott Trumper

B.S. Massachusetts Institute of Technology
(1980)
S.M. Massachusetts Institute of Technology
(1984)

Submitted to the Department of
Electrical Engineering and Computer Science
in Partial Fulfillment of the Requirements for the
Degree of

Doctor of Philosophy

at the

Massachusetts Institute of Technology

September 1990

Signature of Author _____
Department of Electrical Engineering and Computer Science
September 7, 1990

Certified by _____
Professor James K. Roberge
Thesis Supervisor

Accepted by _____
Professor Arthur C. Smith
Chairman, Departmental Committee on Graduate Students

Magnetic Suspension Techniques

for

Precision Motion Control

by

David Lippincott Trumper

Submitted to the Department of Electrical Engineering and Computer Science
at the Massachusetts Institute of Technology on September 7, 1990, in partial
fulfillment of the requirements for the Degree of
Doctor of Philosophy in Electrical Engineering

Abstract

Magnetic suspension techniques applicable to precision motion control systems are investigated. Linear and nonlinear control techniques, electromagnetic actuator designs, and mechanical system designs appropriate for magnetic suspensions are presented. A class-room demonstration of nonlinear magnetic suspension control, and a linear magnetic bearing system are developed in the laboratory. A magnetic bearing X-Y stage system is developed in theory.

In the classroom demonstration, a 2.54 cm diameter, 67 gm steel sphere is suspended below an electromagnet consisting of 3100 turns of #22 wire wound on a 2.5 cm diameter, 10 cm length core. Position of the sphere is sensed optically. The sphere position is controlled with an 8088/8087 based single board computer with a sampling rate of 400 Hz. The control laws implement nonlinear terms which compensate for the electromagnet and sensor nonlinearities, which were measured experimentally. Implementing such nonlinear compensation allows the system stability and dynamic response to be essentially independent of operating point.

In the linear bearing system, a 10.7 kg platen measuring about 12.5 cm by 12.5 cm by 35 cm is suspended and controlled in five degrees of freedom by seven electromagnets. Position of the platen is measured by five capacitance probes which have nanometer resolution. The suspension acts as a linear bearing, allowing linear travel of 50 mm in the sixth degree of freedom. In the laboratory this bearing system has demonstrated position stability of 5 nm peak-to-peak. This is believed to be the highest position stability ever demonstrated in a magnetic suspension system. Performance at this level confirms that magnetic suspensions can address motion control requirements at the nanometer level.

The experimental effort associated with this linear bearing system is described in detail. Major topics are the development of models for the suspension, imple-

mentation of control algorithms, and measurement of the actual bearing performance.Suggestions for future improvement of the bearing system are given.

The X-Y stage is designed for precision control of planar motion and is capable of providing travel in X and Y on the order of 300 mm with nanometer resolution while simultaneously providing Z-axis travel on the order of 1 mm. This capability makes such a stage ideal for applications such as the X-Y positioning of semiconductor wafers for photolithography.

A key subsystem of this X-Y stage is a linear motor capable of simultaneously controlling forces along the motor axis and normal to the motor axis. The electromechanics of this motor are developed to demonstrate that such control is possible. The design of the X-Y stage and the linear motor subsystem embody a novel approach to the control of planar motion.

Thesis Supervisor: Dr. James K. Roberge
Professor of Electrical Engineering

Acknowledgements

First and foremost, I want to thank my thesis advisor Professor James K. Roberge for his assistance and guidance. He has consistently lead me in the direction of work which has both practical and theoretical relevance and instilled in me as well as his other students an appreciation for the art of design. It has been an honor and a privilege to have the opportunity to work with him.

I also want to thank Professors Jefferey H. Lang and Alex H. Slocum for serving on my thesis committee. Jeff has taught me a tremendous amount about the control of electromechanical systems and has served as a sounding board for many of the design ideas embodied in this thesis. He also served as my Master's thesis advisor, and through our long association has helped me to focus my interests on the inter-relationship between control system and actuator design.

Alex supplied the catalyst which lead to the major results of this thesis and to the focus on magnetic suspension precision motion control. Alex was always available to discuss ideas and was particularly of assistance in helping with the mechanical and precision aspects of the designs.

In his Continuum Electromechanics class, Professor James R. Melcher taught me the largest amount of material which I have ever absorbed in a single semester. The ideas presented in this class were instrumental in formulating the linear motor and X-Y stage designs. Professor Melcher was very helpful in discussing the design of the linear motor and the ideas presented in his class were the source of much inspiration.

Group Leader Carl Much and Assistant Group Leader Ed Corbett of Group 76 at Lincoln Laboratory were instrumental to the success of this thesis. They provided laboratory and office space, and put up with me absorbing a significant amount of square footage on a crowded optical table for a time much longer than predicted at the outset of this project. It has been a pleasure to work with them over the last three years, and this thesis would not have been possible without their support.

In addition, I would like to thank everyone in Group 76 for friendly discussions, the loan of critical pieces of equipment, and for being impressed at the proper moments when I would collar them for an impromptu demonstration of the latest results of my thesis. In particular, Hardy Prince was of tremendous assistance in the construction of various pieces of the design. Pete Rossini taught me how to use the Intel development system and put up with me as an office-mate for three years. Mike Johnson was always willing to lend an ear for discussing the latest design problems, despite his own over-committed schedule. Paul Mitiguy, as a summer student in Group 76 gave me invaluable assistance in formulating the mechanical dynamics. Group secretary Ardeth Grant was also very helpful with all my questions. I also want to thank all the group technicians for lending

me uncountable numbers of hand-tools, soldering irons, etc.

At MIT in Professor Slocum's group, Van Pham developed some of the control ideas in his Bachelor's thesis and assembled many of the mechanical parts. Specifically, he helped with gluing-up the bearing assemblies and with moving the experiment to Lincoln Laboratory. Tim Hawkey designed the electromagnetic actuators and oversaw their construction. Eric Heatsig was involved with the early parts of the linear bearing project. Dave Gessel built many of the parts, especially those that were difficult to machine. Art Rudolf of the civil engineering machine shop provided precision grinding of the bearing faces.

I want also to thank my parents David Keim Trumper and Virginia Lippincott Rose without whom, as they say, this work would not have been possible. I thank my father for instilling in me an interest in science from an early age and my mother for always supporting my efforts. My wife's parents Rev. Donald William Romlein and Eunice Marie Romlein have been a tremendous help, especially since the boys were born, and made it possible for me to devote many additional hours to this thesis. They also are tremendous personal examples of how to live ones life with energy, enthusiasm, and integrity.

Finally, I want to thank my wife Beth, and sons William and Paul for putting up with the unreasonable number of hours which I was forced to spend away from them in order to work on the 'thesis'. At two years old, my twin sons' vocabulary includes this word. I kept telling them that I would be done soon, now I finally am. To Beth, William, and Paul this work is respectfully dedicated.

This work was sponsored by the Department of the Air Force, and performed at the MIT Lincoln Laboratory.

To

Beth, William, and Paul

Contents

List of Figures

List of Tables

Chapter 1

Introduction

Precision motion control at the nanometer level is required in many contemporary applications. Requirements for even higher precision in future applications are pointed to by the sub-Ångstrom resolution demanded of scanning tunneling microscope stages. This thesis presents techniques for high-resolution motion control through the use of magnetic bearings. These techniques are applicable to any fine-motion control system, such as the stages which position semiconductor wafers for photolithography. Additional applications of the technology developed in this thesis are envisioned in areas such as scanned-probe microscopy of large structures, the production of masks for integrated circuits, surface profilometry, and in other areas where precision control of large planar motion is required.

Extremely high resolution magnetic bearing positioning stages have been proposed on paper [Slocum and Eisenhaure 1988], but this thesis represents the first time that magnetic bearing positioning resolution at the nanometer level has been demonstrated in a laboratory implementation. Specifically, a linear bearing system has been constructed in which five degrees of freedom are controlled, and which has demonstrated 5 nanometer position stability. This experimental result verifies that it is possible for magnetic bearing systems to address positioning tasks with nanometer resolution requirements.

Additionally, this thesis proposes a magnetic suspension technique which is capable of controlling planar motion with travel on the order of 100-300 mm in each of the two axes lying in the plane, as well as small motions out of the plane. This suspension uses only a single moving platen to realize planar motion control, and thus is far simpler than earlier systems which use crossed-axis linear slides. This approach is thus a viable solution for many precision positioning tasks which require planar motion control. In conjunction with the systems described above, the thesis also contributes to an understanding of the application of nonlinear control laws appropriate to magnetic suspensions.

1.1 Statement of the Problem

This section gives a brief review of the approaches which have been used for precision positioning, in order to provide a context for the work of this thesis.

For small ranges of motion, flexure systems can satisfy many positioning requirements. Current scanning tunneling microscope stages are based on flexures, and realize 10^{-2}nm resolution but with only about 1000 nm travel. Their dynamic range is therefore on the order of 10^5. Flexure systems become more difficult to employ as the travel is increased to above 1 mm. Further, flexures inherently allow control of only a single degree of freedom, and must be compounded to allow control of multiple degrees of freedom. In such compound flexures, it is difficult to control error motions and cross-coupling between axes. Another disadvantage is that it is difficult to make flexures stiff in all but the desired degrees of freeedom. Hence the use of flexures tends to introduce resonances which make such positioning systems difficult to control.

Large-travel motion control requires much higher dynamic range than can be provided with flexures. A system with 1 nm resolution and 100 mm travel requires a dynamic range of 10^8. Currently, large-travel precision motion control systems such as the diamond turning machine described by [Donaldson and Patterson 1983] are based on bearings coupled with separate actuators. The bearings constrain motions to the desired degrees of freedom, and the actuators provide the forces which control motion within these degrees of freedom. Several problems limit the precision attainable via current techniques.

Firstly, mechanical bearings introduce disturbances due to roughness of the bearing elements. Roughness can be reduced, but not eliminated, by expensive hand-finishing operations. Carefully constructed machines such as the Nanosurf 2 described by [Lindsey and Steuart 1987] can achieve sub-nanometer smoothness of motion, but it is doubtful that the polymeric bearings used in this design can provide a long life, or that such a design can readily be reproduced for production applications. Gas and liquid fluid bearings as used in [Donaldson and Patterson 1983] eliminate surface contact and extreme finishing operations, but it can be difficult to control the dynamics of such bearings. They require a source of gas or fluid at pressure, are sensitive to contamination, and are unsuitable in a high vacuum environment.

Secondly, it is impossible to perfectly align the actuator/bearing pair, and difficult to design a coupling between the actuator and bearings which does not transmit undesired actuator motions. Thus, the application of control forces via the actuator results not only in forces in the desired directions but in forces in undesired directions as well. These forces are constrained by the bearings, but necessarily result in error motions. Although the resulting errors can be made small by careful design, for high precision systems the above problem presents a

severe challenge.

The actuator alignment issue can be resolved by using a flexural coupling which is designed to be compliant in all but the direction of actuation. However, it is difficult to design a coupling which is stiff in the direction of actuation, yet sufficiently compliant in all other degrees of freedom. The compliance between the actuator and the load introduces resonances which greatly increase the difficulty of the control system design.

Fine motion control with large travel is sometimes addressed by designing systems with cascaded coarse/fine positioners. For instance, a fine motion controller realized with piezoelectric actuators can be mounted on a coarse motion controller realized with conventional electromagnetic actuators and mechanical bearings. The combination is driven to control motion of a sample carried on the fine motion stage. This approach has the disadvantage of requiring a more complex mechanical system and associated controller.

Suspension with magnetic bearings can potentially solve these problems. Because there is no surface contact, the problems of mechanical roughness and expensive hand-finishing are eliminated. Also, this thesis demonstrates that it is possible to use magnetic suspensions to simultaneously provide the functions of bearings and actuators with very high precision. This is achieved through the design of a linear motor which can be used to control linear motion over large travel and simultaneously control linear motion normal to the plane of the motor's magnetic air-gap. This linear motor thus performs as a combined actuator and bearing. By this means, the alignment and coupling problems described above can be eliminated. As well, it is then possible to design a single-stage sytem wherein fine motion control and large dynamic range are realized with a single set of magnetic bearings. This eliminates the difficulties of the conventional two-stage, coarse-fine systems described above.

Magnetic bearings seem to be the only support system in which the suspension properties can easily be controlled on-line. The stiffness of a magnetic suspension can be made essentially infinite at low frequencies, and can be tailored as a function of frequency and time by choice of the control algorthm. Also, in the suspension of a six-degree-of-freedom system, the cross-coupling between modes can be controlled and minimized by utilizing fully-multivariable control laws. This theory is well developed in the literature at the current time. Additionally, nonlinear bearing behavior and the variation of the plant inertia matrix as seen by the suspension can be addressed throught the use of nonlinear control laws. It is difficult to envision achieving such control of cross-coupling and nonlinear terms in the other types of bearing systems discussed above.

For linear and planar motion, mechanical and fluid-type bearings tightly constrain motion to lie in the bearing plane. Thus, for these conventional bearings, to achieve motion out of the plane (such as Z-axis focusing in a wafer stepper)

requires the use of additional stages of motion control carried on top of the X-Y stage. However, the planar magnetic bearing motion control system developed in this thesis can readily provide motion of several millimeters in the Z-axis while simultaneously controlling motion in the plane. Only one moving part is required to realize this control, resulting in a much simpler mechanical system, the structure of which can more readily be made stiff to allow high-bandwidth motion control.

For the reasons stated above, magnetic bearing systems are an attractive solution for many motion control problems. Further, the control theory and the electronics used to implement suspension control algorithms have progressed to the point that the difficult control problems posed by magnetic bearings can be readily solved. Magnetic bearings impose critical demands on the control implementation, but in return offer many performance advantages.

The remainder of this thesis is described in the following section.

1.2 Thesis overview

This thesis develops an understanding of the use of magnetic suspensions for precision motion control, from the perspectives of applied control theory and electromechanics. As a foundation, Chapter 2 surveys the problem background in the literature, and issues which are relevant to all tractive-type magnetic suspensions are presented in Chapter 3.

As the main contribution of this thesis, a number of magnetic suspension designs are investigated in theory, and two of these designs have been constructed and tested in the laboratory.

The first design demonstrates the utility of nonlinear control laws for large travel magnetic suspensions. It served as the initial impetus for this thesis, and was used as a classroom demonstration. In this system a 1 inch diameter steel ball bearing is suspended below an electromagnet at an 0.4 inch air gap. Nonlinear control techniques are used to achieve stability essentially independent of position for motions of ± 0.3 inches about the nominal air gap. The nonlinear control laws are implemented at a 400 Hz sampling rate on an 8088/8087 based single-board computer. This control laws associated with this system are described in more detail in Chapter 3. In this context we also investigate issues relating to the implementation of the nonlinear control laws in discrete time.

The second design studies a precision magnetically-suspended linear bearing which grew out of the Ångstrom Resolution Measuring Machine (ARMM) proposal by [Slocum and Eisenhaure 1988]. In the author's implementation, a 10.7 kg platen is suspended and controlled in five degrees of freedom by seven electromagnets. Position of the platen is measured by five capacitance probes

which have nanometer resolution. The suspension acts as a linear bearing, allowing linear travel of 50 mm in the uncontrolled degree of freedom. The control design associated with this linear bearing suspension addresses the challenges of controlling five coupled degrees of freedom. In the laboratory this bearing system has demonstrated position stability of 5 nm peak-to-peak. This is believed to be the highest position stability ever demonstrated in a magnetic suspension system. Performance at this level confirms that magnetic suspensions can address motion control requirements at the nanometer level. Control of Ångstrom-level motions via magnetic suspension will be possible as adequate measurement technologies become available. It is expected that laser interferometric techniques will be able to address this level of resolution with adequate bandwidth in the near future. Thus one can readily envision the use of a magnetic suspension stage for performing scanning tunneling microscopy of large objects such as molecules or integrated circuit structures.

The mechanical and electromechanical details of the linear bearing design and photographs of its laboratory implementation are presented in Chapter 4, and the nonlinear and linear mechanical dynamics of the suspended platen are developed in Chapter 5. The development of linear models, control theory, instrumentation and power amplifiers for this system are presented in Chapter 6, and the experimental performance of the linear bearing system is given in both Chapters 6 and 7. Suggestions for ways in which the linear bearing design could be improved are presented in Chapter 8.

The third design studies the precision control of planar motion on magnetic bearings. This design has been developed on paper to provide travels of 300 mm in X and Y with nanometer resolution. A key subsystem of this X-Y stage is a linear motor capable of simultaneously controlling forces along the motor axis and normal to the motor axis. The electromechanics of this motor are developed to demonstrate that such control is possible. The design of the X-Y stage and the linear motor subsystem embody a novel approach to the control of planar motion, and a patent covering this design has been applied for. The linear motor and X-Y stage designs are given in Chapter 9.

Chapter 2

Literature Review

This chapter reviews literature relevant to magnetic suspension systems.

2.1 Prior Art in Precision Machines

The work of this thesis draws on previous research in precision machine design and control. Areas where useful references may be found are in scanning tunneling microscopy (STM), precision mechanically suspended linear slides and x-y stages, and diamond turning machines. These areas are discussed below.

The field of STM is well developed at this point. Current STMs differ significantly from the magnetic suspension systems developed in this thesis in that their dynamic range is much more limited, on the order of 10^4, with scans covering about 1000 Å range. This dynamic range can be addressed with the use of piezoelectric actuators which offer the advantage of high stiffness and fine resolution (< 0.1 Å). A good overview of the STM field is given in [IBM 1986a] and [IBM 1986b] which are complete issues of the IBM Journal of Research and Development devoted to STM. Many new types of scanned-probe microscopes have evolved from the technology developed to realize the STM, as described in [Wickramasinghe 1989]. Among these are the atomic force microscope, the laser force microscope, magnetic and electrostatic force microscopes, scanned thermal microscope, scanning ion conductance microscope, and scanned near-field optical microscopes. [Hansma et al 1988] gives a good overview of applications of the scanning tunneling microscope and the atomic force microscope. All these systems rely on piezoelectric actuators to provide the scanning motion.

Piezoelectric actuators are not suitable for the current purposes because of the long travel required in the main axes (50–300 mm). Another reason that magnetic bearings have been used is that they allow multiple actuators to apply forces to a platen in independent directions with little cross-coupling among actuators. It is very difficult to design a piezoelectric actuator to be stiff in one direction

of actuation, yet uncoupled to orthogonal motions. Thus we have been lead to develop a linear magnetic bearing with variable reluctance actuators, and an electromagnetic motor structure, both of which are capable of the long travel required. At least three of these motors are used to suspend and stabilize the X-Y stage which is described in more detail in a later section.

Mechanically supported stages have been widely used to provide precision x-y positioning. Examples of this use are as wafer steppers in the semiconductor industry, coordinate measuring machines, and precision profilometers as described by [Lindsey and Steuart 1987]. In wafer steppers, planar motion control is achieved through the use of crossed-axis designs in which the Y-stage is carried on top of the X-stage. Further, the mechanical bearings used in these designs require expensive hand-finishing operations. Additionally, the Z-axis focus control is implemented via a separate mechanical subsystem. In the magnetic suspension system which we propose in this thesis, control of all three axes of travel is achieved with only one stage with a single moving part, greatly simplifying the stage mechanical design. Coordinate measuring machines typically use air bearings. It is difficult to control the stiffness of air bearings as a function of frequency, and resonant modes can result in the measuring machine. The precision finishing operations and polymeric bearings used in the linear slide of [Lindsey and Steuart 1987] preclude its use in more than specialized applications.

Precision mechanical design and control has been well developed in the area of diamond turning machines used for producing optical lenses and mirrors [Donaldson and Patterson 1983]. This machine uses laser interferometers for the high resolution position measurement required, over the 32-inch radius by 20-inch length working volume of the machine. Machine accuracy is predicted to be approximately one microinch rms (25 nm). The system uses fluid bearings in order to carry large loads with low friction. The mechanical design uses a vertical Z-axis carriage carried on an X-axis carriage. There is much to learn from this design in terms of the implementation of precision machines. However the specific machine geometry is specialized to single-point diamond turning of optics up to 64 inches in diameter and 3000 pounds weight, and thus is not directly suitable for the control of planar motion which is desired in the current application.

2.2 Prior Art in Magnetic Suspensions

Previous work in magnetic suspensions spans many fields, and a large volume of literature is extant. We choose to classify the magnetic suspension literature into the following broad areas:

- General overview and bibliographic compilations.

- Early efforts.
- Single degree of freedom suspensions.
- Multiple degree of freedom suspensions.
- Transportation applications.
- Wind tunnel suspensions.
- Replacement/augmentation of mechanical bearings.
- Electrodynamic suspensions.

These classes are discussed in detail below.

2.2.1 General overview and bibliographic compilations.

Several studies provide overviews of the general area of magnetic suspensions and a large number of bibliographic references. [Geary 1964] gives an overview and a large bibliography, which well summarizes the work to that time. [Jayawant 1981a] gives a good review of the various uses of magnetic suspension and levitation and an extensive bibliography. His largest emphasis is on transportation applications, but many other areas are covered as well. The studies by [Covert et al 1973] and [Bloom et al 1982] survey the use of suspensions in wind tunnel applications, and a comprehensive bibliography of this area is given by [Tuttle et al 1983].

The literature above is primarily survey in nature. More detailed technical studies of suspension systems are given in the books by [Laithewaite 1977], [Jayawant 1981b], and [Sinha 1987], with major emphasis on transportation applications, and the book by [Frazier et al 1974] with major emphasis on suspension of gyroscopes for inertial guidance.

2.2.2 Early efforts.

The results of [Earnshaw 1842] and [Braunbek 1939] are of fundamental importance in understanding magnetic suspension techniques. As stated by [Basore 1982]:

> Samuel Earnshaw proved in 1842 that any fixed arrangement of freely suspended point particles whose forces vary as the inverse square of distance cannot exist in a state of stable equilibrium. Later, in 1939, Braunbek used an energy argument to extend Earnshaw's result to conclude that the stable suspension of a finite body in a static

magnetic (or electric) field is impossible unless diamagnetic material is present. Superconductors are often included in this category, as their ability to shield out magnetic fields can be interpreted as an effective permeability of zero. Braunbek's result, known as Earnshaw's theorem, applies only if all conductors in the system carry a constant current. If the current is allowed to change upon displacement of the body, then the theorem no longer applies and stability is possible. This is the more natural explanation for the stabilizing influence of superconductors, and this reasoning extends to conventional conductors also.

Early suspension systems predate the emergence of electronics for automatic control, and typically rely on fixed magnets for support. Since, as discussed above, not all degrees of freedom can be simultaneously stabilized by a passive system, they typically use mechanical bearing elements to constrain some motions of the suspended member. An example is the watt-hour meter spindle support bearings developed by [de Ferranti 1890], and [Pratt 1902].

Here, magnets were used to reduce loading and hence friction on the mechanical spindle bearings, resulting in higher meter accuracy. These bearings were limited by the available magnetic materials, and did not see practical use until better materials were developed [Geary 1964].

2.2.3 Single degree of freedom suspensions.

These systems are such that only one degree of freedom of the suspended body is actively stabilized. Typically the other degrees of freedom are either stabilized passively by the shape of the suspending field, or are unimportant due to symmetry of the suspended object. This represents one of the earliest classes of actively controlled suspensions.

The early work in this area is described by [Sinha 1987]:

> The explicit feedback mode using d.c. excitation was first proposed by Graeminger in his conceptual letter-carrying system where the current in the magnet winding was controlled through a mechanical lever ..... Although a slightly modified version of this scheme was later proposed, ... owing to the absence of subsequence [sic] reference in the literature, it is not clear whether any experimental model or full-scale prototype was built to assess the performance of Graeminger's design. An alternative configuration was proposed about a decade later by Anschutz-Kaempfe in the context of floating gyroscopic motors .... However, the first prototype system using active feedback of position resembling the configuration of modern suspension systems was

> built a decade later by Kemper. The heaviest model which Kemper successfully suspended by using thermionic valves weighed 210 kg requiring 270 watts when operating at an airgap of 15 mm .... Kemper's work was aimed at demonstrating the feasibility of a radical wheel-less train.

See [Graeminger 1912], [Anschutz-Kaempfe 1923, 1926], and [Kemper 1937, 1938].

Kemper's results were closely followed by those of [Holmes 1937]. He built an axial magnetic suspension using a controlled electromagnet to stabilize a vertical 6 gm ferromagnetic needle. Position was measured optically. His interest was in developing a low torque suspension for instrumentation purposes, and torsion constants down to 7×10^{-6} dyne-cm/radian were reported. This was the first in a long line of magnetic suspension research at the University of Virginia.

[Beams et al 1946] used a magnetic suspension to spin small steel spheres in vacuum up to their bursting speeds. The balls were driven as the rotor of an induction machine by two pairs of external drive coils, and were spun about the vertical axis of the suspension. The bursting speeds of various sized ball bearings were in good agreement with theoretical predictions based on the strength of the bearing steel. Speeds in excess of 20 million rpm were achieved for balls on the order of 1 mm diameter. In the evacuated chamber the decay rate of speed was remarkably small; for a ball of 1.59 mm diameter spinning at 7.2 million rpm, at a pressure of about 10^{-5} mm Hg, it required roughly two hours to lose one percent of the ball's speed.

Position of the ball was sensed inductively, and schematics for the vacuum-tube based control circuits are given. This appears to be the first use of the idea of immersing part of the magnetic circuit in oil in order to effect viscous damping of the radial motions of the rotor. See also [Beams 1954].

Magnetic suspensions can provide a near-ideal support in terms of freedom from friction and other disturbances. This capability is dramatically illustrated in [Beams 1947]. Here, rotors suspended in a vacuum were shown to be sensitive to the pressure of a light beam falling on them. In experiments, including one using light from a 100 W arc lamp focused on a 1.59 mm diameter rotor in air at a pressure of 10^{-6} mm Hg, rotors were observed to accelerate when driving light was applied.

[Beams et al 1955] describe the use of a magnetic suspension as an analytical balance. The material to be weighed is attached to a ferromagnetic body suspended beneath an electromagnet. Changes in the nonferromagnetic masses of the suspended bodies are determined by the resulting changes in the current through the solenoid necessary to keep the bodies freely suspended at a fixed position. Masses from 10^5 gms to 2×10^{-6} gms were suspended. Weight changes down to 5×10^{-11} gms in a suspended weight of 2.3×10^{-6} gms were measured. See also [Clark 1947].

[Beams 1954] presents the use of a magnetic suspension as an ultra-centrifuge. The core of the suspension solenoid is hung by a wire in an oil-filled cup in order to create damping of the suspended rotor in the radial degrees of freedom. Schematics for the suspension circuits are given, as well as a review of over fifteen years of magnetic suspension work at the University of Virginia. [Beams 1963] presents a double magnetic suspension system in which two concentric rotors are suspended. This of course requires two solenoids and two position sensors to control the two degrees of freedom.

The idea here is to spin both rotors at the same speed in order to reduce frictional drag on the inner rotor to a minimum. The vertical position stability of the inner rotor was shown to be better than a wavelength of the 5460.7 Å line of mercury. This was accomplished by arranging the rotor as the end mirror of a Michelson interferometer, and observing the clearly defined fringing pattern which resulted.

More recently, suspensions similar to the ones discussed above have been implemented using digital control techniques. Typically, this simply involves the replacement of an analog scheme with its digital approximation, and thus offers little new insight. Many of the control schemes are somewhat ad hoc and not grounded in the solid theory which exists for digital control systems. See [Carmichael et al 1986], [Histani et al 1986], and [Scudiere et al 1986]. [Williams et al 1989] use the backward difference approximation to transform standard continuous-time proportional-derivative controllers into discrete-time controllers for active bearings suspending a flexible rotor. They then study theoretical and experimental results for the resulting bearing stiffness and damping at various sampling rates and with several controllers.

[Sinha and Hulme 1983] describe the application of adaptive control techniques to a one degree of freedom magnetic suspension problem. The design is studied via simulation only, with no experimental verification.

Single degreee of freedom magnetic suspension systems have also been widely used as examples in control system textbooks, primarily in the context of the linearized analysis of nonlinear systems (see [Roberge 1975], [Woodson and Melcher 1968], [Franklin and Powell 1980], [Franklin et al 1986], and [Kuo 1987]). As well, the single degree of freedom magnetic suspension problem is used as a lab excercise and classroom demonstration in several courses at M.I.T and at other universities.

A single degree of freedom system has been developed by the author for use as a classroom demonstration. A one inch steel ball bearing is suspended below an electromagnet consisting of 3100 turns of #22 magnet wire wound on an one inch core. The system is digitally controlled by an 8088/8087-based single-board computer and data acquisition system. The control law uses a nonlinear compensation scheme to linearize the magnetic force relationship. This allows the

stability of the closed-loop system to be essentially independent of the operating point. The control law for the linearized system is then developed via classical techniques applied in the discrete-time domain.

Position is sensed optically, and nonlinearities in the relation between position and sensor output are corrected in software. The magnet force-relationship was verified experimentally via construction of a balance for measuring the magnetic force on the ball. The effects of saturation at high currents were apparent. This system is further described in the context of nonlinear control in section 3.4.2 in the next chapter.

2.2.4 Multi-degree of freedom suspensions

The systems described above actively stabilize only one degree of freedom. It appears that the first system to successfully stabilize more than one degree of freedom was developed by [Jenkins and Parker 1959], and [Fosque and Miller 1959]. Theoretical results pertaining to suspension of a steel sphere in three actively controlled dimensions are presented by [Jenkins and Parker 1959]. This paper derives conditions for electro-magnet arrangements in which the three magnetic forces are mutually perpendicular and uncoupled. The paper points out that many arrangements are possible, but gives two examples which seem readily apparent.

The first of the two arrangements was constructed, and the experimental results are described in [Fosque and Miller 1959]. Although this is a short article, many useful insights are provided as to the practical issues invloved in implementing this suspension. Details of the mechanical, magnetic, optical, and electronic aspects are presented.

Many recent applications involve control of multiple degrees of freedom. For instance magnetic suspensions for trains and in wind tunnels are of necessity multi-axis. The same is true for suspensions used for magnetic bearings for machine tools, and in vibration control. These applications are discussed below in their respective sections.

2.2.5 Wind tunnel suspensions

Suspension of models in wind tunnels is another area where the unique properties of magnetic suspensions may be exploited. There are two chief advantages. First, the model may be suspended without any mechanical contact, which can interfere with the airflow. This allows more accurate measurement of the forces and moments acting on the model. Secondly, if properly calibrated, the suspension may be used to *measure* the aerodynamic forces and moments acting on the model, thus replacing the balances used in conventional wind tunnels where the model

is mounted on a stinger. Systems of this type are referred to as magnetic suspension and balance systems. Typical working cross-sections are on the order of five inches to one foot. The studies by [Covert et al 1973] and [Bloom et al 1982] survey the use of suspensions in wind tunnel applications, and a comprehensive bibliography of this area is given by [Tuttle et al 1983].

[Covert et al 1982] investigates roll control techniques, i.e., torque generation and position measurement in the model roll component. They found that the roll information could be derived from the electromagnetic position sensor (EPS) already in use at MIT for over a decade. Use of microprocessor control was recommended but not implemented.

[Britcher et al 1979] gives an overview concerned with issues of system reliability and the problems associated with various model position sensing systems. [Britcher 1983] focuses on the issues of generation of roll torque and of suspension reliability. It also provides a useful discussion of the current state of the art and directions for future research. [Britcher 1984] discusses recent developments and current research efforts leading toward realization of large-scale (i.e. four foot cross-section) wind tunnel magnetic suspension and balance facilities. [Britcher et al 1984] describes the design and testing of a superconducting core for aircraft model wind tunnel suspensions. The core is in a dewar of helium contained within the model, which can keep the core superconducting for about one half hour before the helium boils away. While superconducting, the core maintains a constant current to generate a magnetic field on which the wind tunnel suspension acts.

[Fortescue and Bouchalis 1981] investigate digital controllers which are used to replace and directly mimic (i.e. same transfer function) analog controllers from two channels of a model suspension and balance system. The control was implemented in fixed-point arithmetic.

[Britcher et al 1987] presents digital controllers for magnetic suspension and balance systems. A general overview of the hardware and controllers at NASA Langley and University of Southampton is given. A double lead compensator is described both theoretically and in terms of its performance in actual model suspension tests. Some interesting aspects of the position sensor systems are also presented. Specifically, long photodiode arrays are used to detect shadow lines from the illuminated model.

This article also discusses methods for on-line identifcation of the suspension parameters (i.e. force vs. current, etc.) by applying sinusoids of varying frequency. This technique is refered to as 'dynamic calibration'. Currently, it is accurate to about 2%, which is enough for control purposes (i.e. achieving robustly stable suspension), but not accurate enough for aerodynamic measurement purposes. Further research is required in this direction.

2.2.6 Transportation applications

Magnetic suspensions for transportation applications have seen a tremendous amount of development, dominating other applications in the volume of literature which has been published. It is also likely that this is where magnetic suspensions will initially see their largest commercial application.

As noted recently in Time magazine [Benjamin 1988], maglev train systems for commercial use are being developed in both West Germany and Japan. The Japanese system is being built by Japan Railways Group, and is a repulsive system utilizing superconducting magnets for suspension. The German system, known as the Transrapid, uses conventional electro-magnets in an attractive mode. Both systems use linear induction motors for propulsion. The German system is farther along in development, with a route planned in Germany, and the possibilty of a high-speed Los Angeles-Las Vegas line is being explored.

A 25 m.p.h. maglev people mover is already operational in Birmingham airport in England, and ground has been broken on 50 m.p.h., 1.3 mi. transit system in downtown Las Vegas. U.S. maglev transportation efforts were terminated in 1975, however there has been a recent resurgence of interest in maglev transportation within the U.S.

The review article by [Jayawant 1981a], and the books [Laithewaite 1977] and [Jayawant 1981b], provide a good overview of transportation applications for magnetic suspensions. The book by [Sinha 1987] also gives an overview as well as greater technical details. Of particular interest is the flux feedback technique which allows linearization of the suspension position dependence.

This technique is also discussed in [Jayawant et al 1974], and [Jayawant et al 1976a]. [Jayawant et al 1974] describes the control system design for suspension of a 1-ton, 4-passenger vehicle. A flux sensor is located on the pole-face of the suspension magnet. A minor feedback loop is closed on flux which linearizes the dependence of magnetic force on position. The force still goes as the square of flux, so an additional square root linearization is still required. They mention the idea of using an analog multiplier to compute the ratio i/x, which would allow elimination of the flux sensor. However, this technique was prone to drift and noise, and was abandonded. The problem of coordinating the four actuator/sensor pairs corresponding to the four corners of the vehicle is also considered. The flux feedback scheme is described in more detail in [Jayawant et al 1976a].

[Jayawant et al 1976b] reviews the vehicle, guideway and electromagnetic dynamics relevant to control systems for magnetically suspended vehicles. [Jayawant and Sinha 1977] study the control of a one degree of freedom suspension which simulates the behavior of a transportation vehicle suspended below a guideway. They built a rig which used a hydraulic cylinder to vibrate a guideway which the suspension was attempting to follow. The layout of this rig is shown. They also

discuss the allowable vibration power spectral density for passenger ride comfort.

[Gottzein et al 1977] presents the control aspects of a high-speed test vehicle running at speeds up to 400 km/hr. The vehicle was accelerated with a rocket sled, and contained no independent traction generation. Power for on-board electronics and the magnet drives was supplied by on-board batteries. The controller is based on using observers to estimate the state of a linearized version of the system. Vehicle and guideway bending modes were considered, and a reduced order model developed. They discuss the issues of controlling the five vehicle degrees of freedom with a greater number of actuators.

This is apparently an overview of the results of an extended program of investigation. It is a well written and solid paper and thus the other work given in their references would bear reading if further information was needed on the application of magnetic suspension to transportation systems.

A unique transportation system utilizing magnetic suspensions is the semiconductor wafer transporter presented by [Morishita et al 1986], [Azukizawa et al 1986], and [Takagi et al 1987]. This system is used to carry semiconductor wafers between processing stations in ultra clean rooms in semiconductor manufacturing plants. The system is arranged as a track which is attached to the ceiling of the clean room. The wafer carrier contains the wafers in an enclosed cassette which is electromagnetically suspended below the track. The suspension magnets are powered by on-board batteries, thus allowing suspension with no electrical or mechanical contact required. The batteries are recharged when the carrier is stopped at a processing station. In order to conserve power, the suspension magnets incorporate a permanent magnet which supplies the static suspension force, and thus control current is required only to stabilize the carrier about this equilibrium. That is, the magnet gap setpoint is varied in a closed-loop fashion so as to drive the average current in each magnet to zero. Thus, even when the load weight is varied, the power required to suspend the carrier is minimized. This idea has frequently been used in flywheel suspensions for energy storage where low power operation is also essential.

Electromagnets are located at each of the four top corners of the carrier. The electromagnets act on a pair of guide rails which hang from the ceiling. Each electromagnet has an integral sensor which measures the gap between the magnet and guide rail. The current in each of the four electromagnets appears to depend only on the measured gap associated with that electromagnet. Standard state feedback techniques are used to stabilize each of the four localized loops. The magnets are arranged in pairs on pivoting bogies to prevent overconstraint on the four gap lengths and allow each magnet to reach a gap at which its average current is zero. Auxilliary wheels are used to catch the carrier in the event of a failure.

The suspension magnets actively control the gap length. Lateral positioning

of the carrier on the guide rails is achieved passively by making the guide rail about the same width as the electromagnet. Thus lateral offsets result in a restoring force which recenters the electromagnet on the guide rail.

Propulsion of the carrier is accomplished by locating a linear induction motor structure in the center of the guideway between the two rails. This linear induction motor acts on a copper reaction plate carried on the top of the carrier. No iron backing is used behind the reaction plate in order to minimize attractive forces resulting from the linear induction drive, as these forces would appear as disturbances to the suspension control loops. Linear induction motors are located at the beginning and end of straight sections of track and at switching points and on curved sections. The induction motors are used to control the speed and position of the carrier in a closed-loop fashion while it is under a particular motor section. In between motors, the carrier moves freely under its own inertia at near constant velocity. This motion is possible due to the low friction realized via magnetic suspension.

The system is advantageous in that it generates little noise or vibration which would disturb the wafers or processing equipment in the clean room. Further, since there is no mechanical contact, no dust is generated by movement of the carrier. Thus the carrier system can be used even in clean rooms where no human operators are permitted. The system is reported to be operational in a semiconductor manufacturing plant in Japan.

2.2.7 Replacement/augmentation of mechanical bearings

Magnetic suspension techniques have wide applicability for replacing or augmenting conventional mechanical bearings. Areas in which magnetic suspensions have been applied include: centrifuges, turbines, machine tools, gyroscopes for inertial navigation, momentum wheels, linear bearings, and for vibration control.

Linear slides

The linear slide proposed by [Slocum and Eisenhaure 1988] provided the initial impetus for this thesis. Here, they propose a linear slide with Ångstrom resolution, suspended by magnetic bearings in five of its degrees of freedom, which they refer to as the Ångstrom Resolution Measuring Machine. These five degrees of freedom are to be regulated to near zero displacement. The sixth degree of freedom is linear translation along the long axis of the suspended member. This axis is to be actuated with a piezoelectric inchworm driver to allow positioning over a 50 mm travel with Ångstrom resolution. Position is to be measured with laser interferometry on all six axes. Capacitive or inductive sensors are to be used to give a zero reference to initialize the laser interferometer.

A version of this slide has constructed by the author as part of this thesis. The slide is described in detail in following chapters. It differs from [Slocum and Eisenhaure 1988] in that the inchworm driver was not be used. Rather, a linear motor has been studied on paper which has the capability to provide control over the sixth axis translation as well as one of the other five degrees of freedom. This version is described in more detail in a subsequent section. In the laboratory implementation, due to time constraints, no control was implemented for the long axis of travel; only five degrees of freedom were actively controlled via the seven electromagnets. Position stability of 5 nm has been demonstrated in the laboratory using this slide system.

Another interesting application of magnetic bearings to a linear slide is presented by [Matsuda et al 1984]. A contactless linear guide for manufacturing is described. Six electromagnets and five sensors are used to control five degees of freedom of the guide which remains free to move in the sixth degree (z axis) of freedom. The guide rides upon two parallel steel rods on which the magnets act. Position is sensed relative to these guides, and thus accuracy of position is dependent upon their accuracy and stiffness.

Linearized equations of motion for the electromechanical system are presented, and a controller is developed based on these linear equations. The controller is multivariable and designed with standard LQ theory, where the weighting matrix Q has been chosen by trial and error. Experimental and theoretical results show that the slide control loop has a 100 Hz bandwidth.

Vibration control

[Ellis and Mote 1979] describe an intriguing application of magnetic techniques to vibration control of a saw blade. The idea here is to allow the use of thinner saw blades which achieve lateral stiffness via active control of a magnetic bearing. Such a thinner blade will waste less material in the cut allowing greater production yield. A pair of electromagnets and a saw blade lateral position sensor are arranged to act on the blade of a circular saw in the region which is exiting from the material being cut. The electromagnets are driven in a closed-loop fashion so as to regulate out lateral displacements of the saw blade. Good results are reported on increasing the stiffness and damping of test disks in the laboratory. Tests in a production environment showed at least no deterioration of the saw performance. The control is implemented with a proportional-derivative controller.

In [Gondhalekar and Holmes 1984] a shaft spinning on conventional bearings is stabilized in vibration by an electromagnetic bearing. Thus the electromagnetic bearing does not support the weight of the shaft, but just controls its dynamic behavior. Pole-face flux measurements are used to linearize the position

dependence of the electromechanical system, and a piecewise linear square root approximation is used to eliminate the variation of force as the square of flux. This linearization is shown to result in improvements in the polar force diagram as seen by the shaft.

In order to effect control in the x and y directions, the magnet uses six poles at 60 degree angles - three with coils at 120 degrees spacing, and three flux return poles. The control law is simply a time varying proportioning of the x and y errors among the three actuators, which runs synchronously with the shaft rotation. An analysis is given of how the shaft modes shift with changes in the control law stiffness.

[Nikolajsen et al 1979] study the area of transmission shaft vibration control. A controlled electromagnet is used to regulate the radial vibrations of a transmission shaft, a technique which they refer to as electromagnetic damping. The control electromagnet has four poles arranged at a 90 degree spacing. The electromagnetic damper allows operation through the critical speeds of the shaft.

Rotating machinery

In some environments such as vacuum systems or corrosive atmospheres, magnetic bearings allow applications which would be difficult using conventional bearings. Also, magnetic bearings are attractive for very high speed machinery such as the ultracentrifuges described by Beams and his collaborators.

[Schweitzer and Ulbrich 1980] give a general review and brief specific description of the design of a suspension for the rotor of a centrifuge in a vacuum. Other application examples are cited in machine tools and turbomachinery. The controller design is based on a linearized model of the plant (5 degree of freedom). The controller is designed by optimal control techniques with no essential details given. Velocity is estimated by an observer and by differentiation of measured position. The observer is shown to give smoother response.

In [Traxler et al 1984] a magnetic bearing support for a rotating shaft is described. The shaft mass is 13.5 kg, and its length is 1.2 meters. The bearings run at 10 mm air gaps, and control radial motions of both ends of the shaft. Axial motion of the shaft is dealt with separately and not described here. A motor attached to the center of the shaft is used to spin it.

The system was built for an exhibition to demonstrate magnetic bearing technology. The design of the microprocessor-based controller, electromagnetic actuators, optical position sensors, and switched power amplifier is described. The nonlinearity of the bearing force relationship is linearized within the microprocessor. The bearings are controlled in a decentralized fashion, and the individual control laws are based on state feedback techniques.

Flywheel energy storage

The theses by [Johnson 1985, 1986], and [Downer 1980, 1986], describe the use of magnetic bearings for a Combined Attitude, Reference, and Energy Storage system for spacecraft use. The purpose is to use a single magnetically suspended flwheel which can be gimballed through a large angle to provide energy storage, inertial reference, and attitude control for a space craft.

The theses by [Basore 1980, 1982] investigate techniques for stabilizing permanent-magnet, radially-active magnetic bearings using a control concept which requires only coils of wire for transducers. These systems sense the radial velocity in two orthogonal directions as control inputs. A 7.4 kg magnetically suspended flywheel was built using velocity- feedback control, and required only 100 mW of power in the steady state. This low power dissipation is important for energy storage applications for which this flywheel is designed. A notation for combining two symmetric orthogonal axes into a single complex-valued function of the Laplace transform variable s is introduced. This notation allows classical control theory to be applied to the design of radial magnetic bearings. Flywheel energy storage systems are also investigated by [Milner 1979].

[Groom and Waldeck 1979] study the control of an annular momentum wheel which is supported by magnetic bearings, to be applied for energy storage. The annular momentum wheel is difficult to stabilize, because it exhibits vibration modes, while they have modeled it as a rigid body, and the controller does not consider its distributed nature.

They also use a nonlinear correction law to address the inverse square law magnet behavior. The nonlinear compensation was implemented with analog multiplier and square root circuits. They also suggest that, due to the negative magnet spring constant, there is a minimum control-loop bandwidth required to stabilize the magnetic suspension, but offer no proof of this result. In the following chapter, we explain in detail why this minumum-bandwidth result holds for any practical magnetic-suspension control loop.

2.2.8 Gyroscope suspensions

Magnetic suspensions have played a critical role in achieving near ideal supports for gyroscopes for inertial navigation. Work in this area has been ongoing at the Draper Laboratory since the mid-1950's. The book by [Frazier et al 1974] describes this development, providing many useful technical details which have applicability to a wide range of magnetic suspensions.

2.2.9 Electrodynamic suspensions

Electrodynamic suspensions operate quite differently from the suspensions described above. They function by using an alternating field to induce currents in the object to be suspended. This creates a repulsion which levitates the object. Further, a *stable* equilibrium is possible here without closed-loop control, whereas attractive-type suspensions are always unstable in at least one degree of freedom, except in the presence of diamagnetic material.

Electrodynamic suspensions have been used to simultaneously levitate and melt an electrically conductive material, as in [Arnold and Folan 1987]. See also [Geary 1964], [Jayawant 1981a], and [Jayawant 1981b]. Electrodynamic suspensions will not be considered further in this work.

Chapter 3

Fundamental Issues

This chapter considers issues which are fundamental to all tractive-type magnetic suspensions, i.e., all suspensions which act as variable-reluctance devices. First, a model is developed from first principles for a one-degree-of-freedom suspension. Then this model is linearized and normalized. The normalized model is used as a vehicle to study linear control issues such as the minimum bandwidth limit for magnetic suspensions, stability robustness, and disturbance rejection. Then the nonlinear model is used to study nonlinear controllers, and their implementation in discrete time. In this context we describe the implementation of a single degree of freedom suspension which was constructed as a classroom demonstration.

3.1 Nonlinear Suspension Model

In this section, the open-loop dynamics for a simple one-degree-of-freedom suspension are presented. This system exhibits the essential issues faced in the design of tractive type suspensions, that is, suspensions which operate as variable reluctance devices. I have drawn my example system from [Woodson and Melcher 1968] pgs. 22-23, 84-86, and 193-200. The only change is that the system is inverted such that gravity acts to open the air-gap. This system is shown in Figure 3.1.

The details of the electromagnetics are worked out in [Woodson and Melcher 1968]; for our purposes, the important details are the coil voltage

$$v_c = \frac{2wd\mu_0 N^2}{g_0 + x}\frac{di}{dt} - \frac{2wd\mu_0 N^2 i}{(g_0 + x)^2}\frac{dx}{dt} + iR \tag{3.1}$$

and the force on the plunger

$$f_x = -wd\mu_0 N^2 \left(\frac{i}{g_0 + x}\right)^2 + Mg - f_d, \qquad (x > 0) \tag{3.2}$$

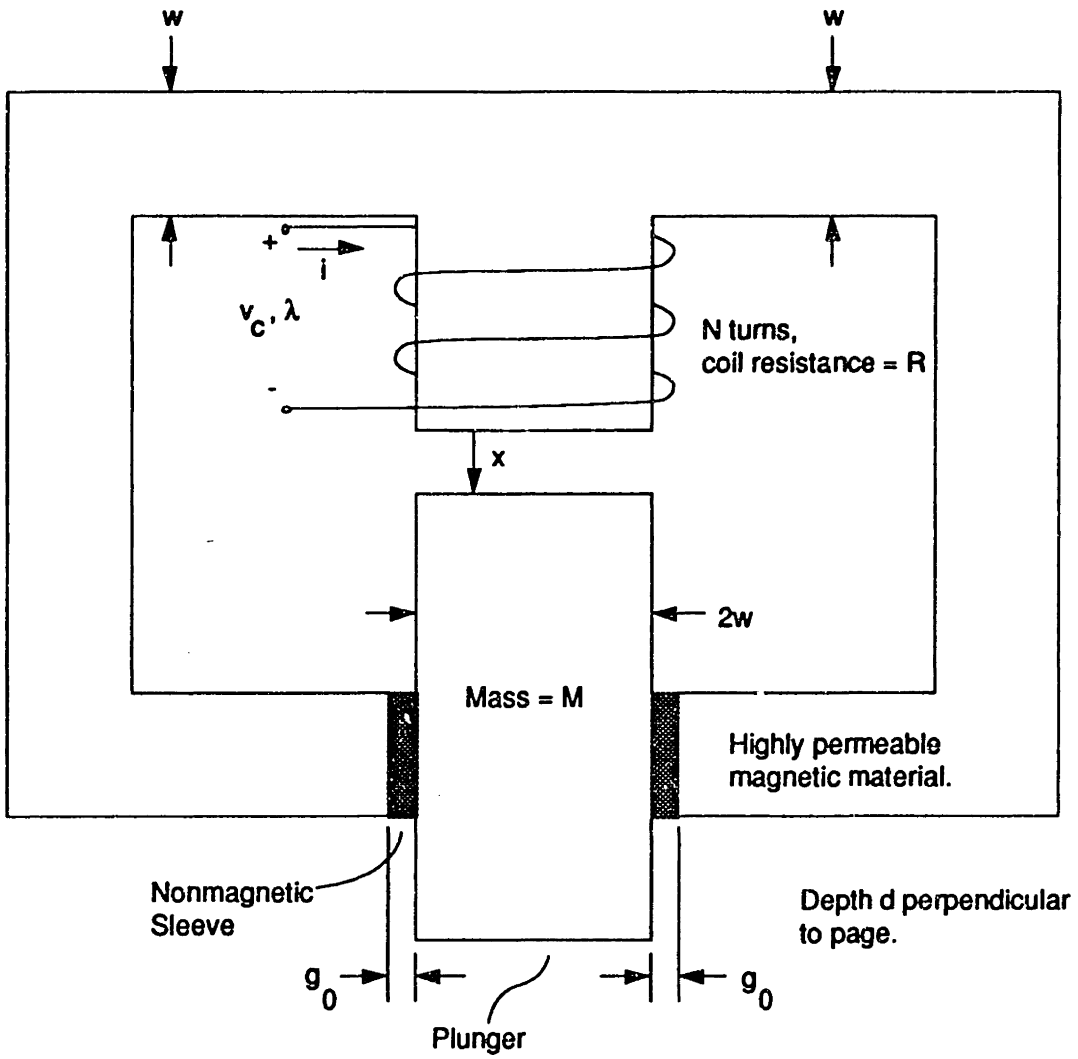

Figure 3.1: Single degree of freedom suspension.

where the first term is the electromagnet force, the second term is the gravitational force on the plunger, and the third term is a disturbance force acting on the plunger in the direction the electromagnet force. The nonmagnetic sleeve is assumed to exert no frictional forces on the plunger.

If we define

$$\begin{aligned} u &= v_c \\ C &= wd\mu_0 N^2 \\ x_1 &= x + g_0, \qquad (x_1 > g_0) \\ \dot{x}_1 &= x_2 \end{aligned}$$

then the state equations for the open-loop suspension are

$$\begin{aligned} \dot{x}_1 &= x_2 \\ \dot{x}_2 &= -\frac{C}{M}\left(\frac{i}{x_1}\right)^2 + g - \frac{f_d}{M} \\ \dot{i} &= \frac{ix_2}{x_1} - \frac{Rx_1 i}{2C} + \frac{x_1 u}{2C}. \end{aligned} \tag{3.3}$$

3.1.1 Second order system

If the coil current is assumed to be the control input, then the suspension state equations are reduced to second order.

$$\begin{aligned} \dot{x}_1 &= x_2 \\ \dot{x}_2 &= -\frac{C}{M}\left(\frac{i}{x_1}\right)^2 + g - \frac{f_d}{M} \end{aligned} \tag{3.4}$$

These equations will adequately model the system if the coil current is controlled by a high-bandwidth current loop with sufficiently high voltage-drive capabilities. In applications, it is most typical to drive the coil with such a current loop, as this essentially eliminates the dependence of position-loop performance upon the electromagnet coil resistance and inductance. Thus, this second-order model will be used for most of the analysis which follows.

3.2 Linearized Suspension Model

In this section, we develop a linearized model for the second-order suspension (3.4). To begin, write the suspension state and inputs in terms of operating point plus incremental quantities. That is let $x_1 = \bar{x}_1 - \tilde{x}_1$, $x_2 = \bar{x}_2 - \tilde{x}_2$, $i = \bar{i} + \tilde{i}$, and $f_d = \bar{f}_d + \tilde{f}_d$. The overbar indicates the operating point value, and the tilde

indicates the incremental value of the variable. The minus sign is used in the definition of the incremental state quantities so that the linearized plant transfer function from $\tilde{i}$ to $\tilde{x}_1$ will have a positive sign in the numerator. In physical terms, this corresponds to using a sensor which provides an *increasing* voltage as the air-gap closes.

The operating point values of the state variables are

$$\begin{aligned} \bar{x}_2 &= 0 \\ \frac{\bar{i}}{\bar{x}_1} &= \sqrt{\frac{Mg + \bar{f}_d}{C}}. \end{aligned} \tag{3.5}$$

Taking the appropriate Jacobians and evaluating them at the operating point yields the linearized system equations as

$$\begin{aligned} \dot{\tilde{x}}_1 &= \tilde{x}_2 \\ \dot{\tilde{x}}_2 &= \frac{2(Mg + \bar{f}_d)}{M\bar{x}_1}\,\tilde{x}_1 + \frac{2\sqrt{C(Mg + \bar{f}_d)}}{M\bar{x}_1}\,\tilde{i} + \frac{1}{M}\,\tilde{f}_d. \end{aligned} \tag{3.6}$$

Thus the transfer function from current to position is given by

$$\frac{X_1(s)}{I(s)} = \frac{a_0}{s^2 - \omega_k^2} \tag{3.7}$$

and the transfer function from disturbance force to position is given by

$$\frac{X_1(s)}{F_d(s)} = \frac{1/M}{s^2 - \omega_k^2} \tag{3.8}$$

where

$$a_0 = \frac{2\sqrt{C(Mg + \bar{f}_d)}}{M\bar{x}_1} \tag{3.9}$$

and

$$\omega_k^2 = \frac{2(Mg + \bar{f}_d)}{M\bar{x}_1}. \tag{3.10}$$

Both transfer functions have real axis poles at $s = \pm\omega_k$. The pole at $+\omega_k$ is of course unstable.

It is interesting to note that the disturbance force $\bar{f}_d$ affects both the gain and the pole locations. Thus any linear controller designed for this plant must be robust with respect to variations in the incremental plant dynamics, as well as stiff with respect to disturbance forces. If this variation of dynamics with disturbance force is not considered, it is possible that the closed-loop system will be destabilized by a disturbance force of sufficient magnitude.

Another point to note is that if the operating point disturbance force is set to zero then the open-loop pole locations depend only upon the operating point air gap and the acceleration of gravity. Specifically, in this case, $\omega_k = \sqrt{2g/\bar{x}_1}$. This points out a fundamental trade-off in magnetic suspension design between air-gap and loop bandwidth. As we shall investigate in a later section, the higher the unstable open-loop natural frequency, the harder it is to control the system. Thus extremely small air gaps are undesirable. On the other hand large air gaps reduce the electromagnet power/force efficiency. Thus extremely large air gaps are undesirable. For this reason, suspension air gaps are typically chosen to be on the order of 0.5–1 mm. This results in open-loop natural frequencies ω_k on the order of 100–200 rad/sec, and loop crossover frequencies on the order of 600–1000 rad/sec. It is difficult to obtain loop crossovers higher than this due to high-frequency effects in the magnets and the mechanical structure. This simple formula allows one to estimate the time constants of a suspension from just the knowledge of the operating point air gap.

The critical assumption in the analysis of the previous paragraph is that the suspension electromagnet is supporting all of the gravity load on the suspended member. In space applications or where permanent magnets are used to carry the gravity load, and where the electromagnets are arranged in push/pull pairs, it is possible to circumvent this air-gap/bandwidth tradeoff by operating the permanent magnets at large air-gaps, and the electromagnets at small air-gaps with low bias currents. This approach is discussed in more detail in the suggestions given in Chapter 8.

3.2.1 Normalized plant

In this section, we present a normalized model for the suspension linear dynamics. This model is used as a vechicle to investigate the open-loop eigenstructure, and to develop the design of linear controllers in the following section. Use of such a normalized model greatly reduces the analytical overhead, while retaining generality. We also obtain a simple overview of the important issues without cluttering the analysis with specific numerical values.

With proper scaling, the plant given in (3.4) can be normalized without loss of generality to the form

$$\begin{aligned} \dot{\hat{x}}_1 &= \hat{x}_2 \\ \dot{\hat{x}}_2 &= \hat{x}_1 + \hat{i} + \hat{f}_d \end{aligned} \tag{3.11}$$

where the hats indicate normalized incremental quantities. For this system the

transfer function from normalized current to normalized position is given by

$$\frac{\hat{X}_1(s)}{\hat{I}(s)} = \frac{1}{s^2 - 1} \tag{3.12}$$

and the transfer function from normalized disturbance force to normalized position is given by

$$\frac{\hat{X}_1(s)}{\hat{F}_d(s)} = \frac{1}{s^2 - 1} \tag{3.13}$$

Eigen-analysis for this system yields eigenvalues $\lambda_1 = 1$ and $\lambda_2 = -1$. The eigenvector associated with λ_1 is $v_1 = [\ 1 \quad 1\ ]'$, and the eigenvector associated with λ_2 is $v_2 = [\ 1 \quad -1\ ]'$. Interpreting these modes develops a physical feel for the suspension open-loop behavior. The mode associated with λ_1 grows exponentially with time and corresponds to an initial condition where velocity and position are of equal magnitude and sign. That is, the suspended member is moving away from the equilibrium point. As it moves away from equilibrium, the force driving it away from equilibrium increases linearly with position. Thus the divergence is exponentially increasing with time.

Conversely, the mode associated with λ_2 decays exponentially with time and corresponds to an initial condition where velocity and position are of equal magnitude and opposite sign. That is, the suspended member is moving toward the equilibrium point with the proper velocity such that the velocity will decay to zero just as the equilibrium point is reached. As it moves toward equilibrium, the force driving it away from equilibrium decreases linearly with position. Thus the convergence to the equilibrium position is exponential with time. This is perhaps the harder mode to understand physically, since it is stable. We know that this trajectory will never occur in the laboratory, since it predicts settling at the unstable equilibrium point. The influence of even a small disturbance or noise will eventually force the system off of the pure λ_2 mode and drive the system onto the unstable mode associated with λ_1. The unstable mode will then dominate over times long compared with one second. However, note that both modes are required to satisfy initial conditions with arbitrary position and velocity.

3.3 Linear Control Issues

In this section the normalized model developed above is used to study various options for controlling the suspension with a linear compensator. The open-loop unstable plant dynamics impose a number of constraints on acceptable compensators. We start by designing a compensator by pole-placement. The loop-transmission shapes which result from this design technique show that the issues

of robustness and disturbance rejection are vitally important. In this context we argue that all reasonable compensators must have crossover frequencies significantly higher than the open-loop unstable frequency ω_k. We also describe why this is a physically reasonable constraint. Finally, we present the design of a lag/lead compensator, and investigate its robustness, disturbance rejection, and settling-time characteristics.

3.3.1 Pole-placement design

In pole placement design it is considered conservative to place the poles at locations nearer to the origin than the plant open-loop poles. In many contexts this axiom holds true, however in the current situation this approach does not lead to an acceptable design. The reasons for this are best shown by example. In the following, we assume that both states are available for measurement.

The poles of (3.11) can be placed by the following state-feedback law

$$\hat{i} = k_1(\hat{u}_r - \hat{x}_1) - k_2\hat{x}_2 \tag{3.14}$$

where $\hat{u}_r$ is the normalized reference input and k_1 and k_2 are the state-feedback gains. The error $\hat{u}_r - \hat{x}_1$ is formed prior to multiplying by k_1 in order to increase the rejection of disturbance forces $\hat{f}_d$.

Under this feedback law, the closed-loop state equations are

$$\begin{aligned} \dot{\hat{x}}_1 &= \hat{x}_2 \\ \dot{\hat{x}}_2 &= (1-k_1)\hat{x}_1 - k_2\hat{x}_2 + k_1\hat{u}_r + \hat{f}_d. \end{aligned} \tag{3.15}$$

For this closed-loop system the transfer function from normalized reference to normalized position is given by

$$\frac{\hat{X}_1(s)}{\hat{U}_r(s)} = \frac{k_1}{s^2 + k_2 s + k_1 - 1} \tag{3.16}$$

and the transfer function from normalized disturbance force to normalized position is given by

$$\frac{\hat{X}_1(s)}{\hat{F}_d(s)} = \frac{1}{s^2 + k_2 s + k_1 - 1} \tag{3.17}$$

Note that the disturbance is attenuated by a factor of k_1 relative to the reference input.

The system will be closed-loop stable if $k_1 > 1$ and $k_2 > 0$. This corresponds to paralleling the suspension open-loop effective negative spring rate with a stiffer positive spring rate, and with a dashpot with positive damping coefficient. Thus

the requirements for stability appear to be quite simple and allow the closed-loop poles to be located anywhere in the the left-half of the s-plane.

However simply achieving stability is by no means sufficient in a realistic design setting, even if the closed-loop pole locations appear to be quite 'stable'. This is so because the closed-loop pole locations give no indication as to the stability robustness or control performance of the resulting design. This point is best illustrated by example.

Consider the system of (3.15) where we take what appears to be a conservative approach and place the closed-loop poles at $s = -0.1$. Thus the desired characteristic equation is $s^2 + 0.2s + 0.01$. This can be realized by $k_1 = 1.01$ and $k_2 = 0.2$. Thus the design is a success in this limited context. However, when the issues of stability robustness and disturbance rejection are considered, the design is seen to be wholly inadequate. These issues are best studied from a loop transmission viewpoint.

The negative of the loop transmission for (3.15) is given by

$$-\text{L.T.} = k_1 \frac{(k_2/k_1)s + 1}{(s+1)(s-1)} \tag{3.18}$$

Evaluating this expression we find a crossover frequency of 0.101 rad/sec with a gain reduction margin of 1.01 and phase margin of 1.1 degrees. By gain reduction margin we mean that the system will be on the verge of instability if the gain is reduced by this amount.

Thus a 1% reduction in loop transmission gain or a decrease in phase of 1.1 degrees would be sufficient to bring the loop to the brink of instability. The lack of adequate gain margin can also be seen by looking at the characteristic polynomial $s^2 + k_2 s + k_1 - 1$. Reducing k_1 below 1 will invert the sign of the last term, thereby pushing a closed-loop pole into the right-half plane. Finally, disturbances are only attenuated by a factor of 1.01 relative to the reference input. Thus, this design is wholly unacceptable.

We can learn several points from this design exercise. First, for good disturbance rejection and acceptable gain and phase margins, the constant k_1 must be made large. Once a sufficiently large value of k_1 is chosen, then k_2 is set to realize an acceptable damping ratio. If k_1 is chosen large, then the loop must cross over at a frequency large compared to the open-loop unstable frequency ω_k; in this normalized case $\omega_k = 1$ rad/sec. If crossover is at a frequency well above ω_k then a good model of the loop dynamics is required to frequencies above ω_k. Put another way this requirement means that the model must be accurate to time scales shorter than the open-loop unstable time constant, and that the control loop must be capable of responding in times shorter than the unstable time constant. This requirement supports the intuition that if the system is capable of exponentially diverging from equilibrium in τ seconds then the controller

must respond in times faster than τ. The bottom line is that there is a definite lower frequency limit for crossover. This is in marked contrast to the controller design for a stable plant where crossover can be made arbitrarily low with proper compensation.

As an example which does achieve good performance and robustness, consider a design in which the poles are placed at $s = -10$, ten times further from the origin than the open-loop poles. This can be realized by $k_1 = 101$ and $k_2 = 20$. For this design, the performance and stability robustness are quite good as indicated by the plot of the negative of the loop transmission magnitude and phase versus frequency shown in Figure 3.2. Crossover is at about 20 rad/sec, the phase margin is approximately 76 degrees, and the gain reduction margin is approximately 101.

Note that this design with $k_1 = 101$ and $k_2 = 20$, and the earlier design with $k_1 = 1.01$ and $k_2 = 0.2$ have identical loop transmission zero locations, i.e. at $s = -(k_1/k_2) = -5.05$. Thus the two closed-loop systems can be found on the root locus shown in Figure 3.3. The closed-loop poles for the first design lie at the break-away point $s = -0.1$ on the right side of the circle, and the closed loop poles for the second design lie at the re-entry point $s = -10$ on the left side of the circle. The circle diameter is 9.9, and it is centered on the zero at $s = -5.05$.

Also note that the loop-transmission zero at $s = -(k_1/k_2) = -5.05$ does not appear in any of the closed-loop transfer functions. This is so because the use of state-feedback effectively locates the zero in the feedback path, whereby it does not appear in the closed-loop transfer function. State feedback places no poles in the feedback path; thus there are no closed-loop zeros associated with this design. The zero in the feedback path does however attract a pole in the root-locus sense, and thus for sufficiently high loop transmission magnitude a pole will be located in the vicinity of the loop transmission zero at $s = -5.05$.

3.3.2 Series compensation

In the previous section we designed the compensator by pole placement under the assumption that all states were available for measurement. In practical applications this is not often the case. In this section we study designs which use series compensation to stabilize the suspension. This is the approach which is generally used in practice as it only assumes measurement of position. First, in the next section a design using only lead compensation is explored. It is seen that the lead compensator should be located in the feedback path in order to reduce control effort and to give an acceptable step-response. However the lead compensator alone does not provide good disturbance rejection. Thus, in the subsequent section we develop the design of a lag/lead compensator which gives better disturbance rejection.

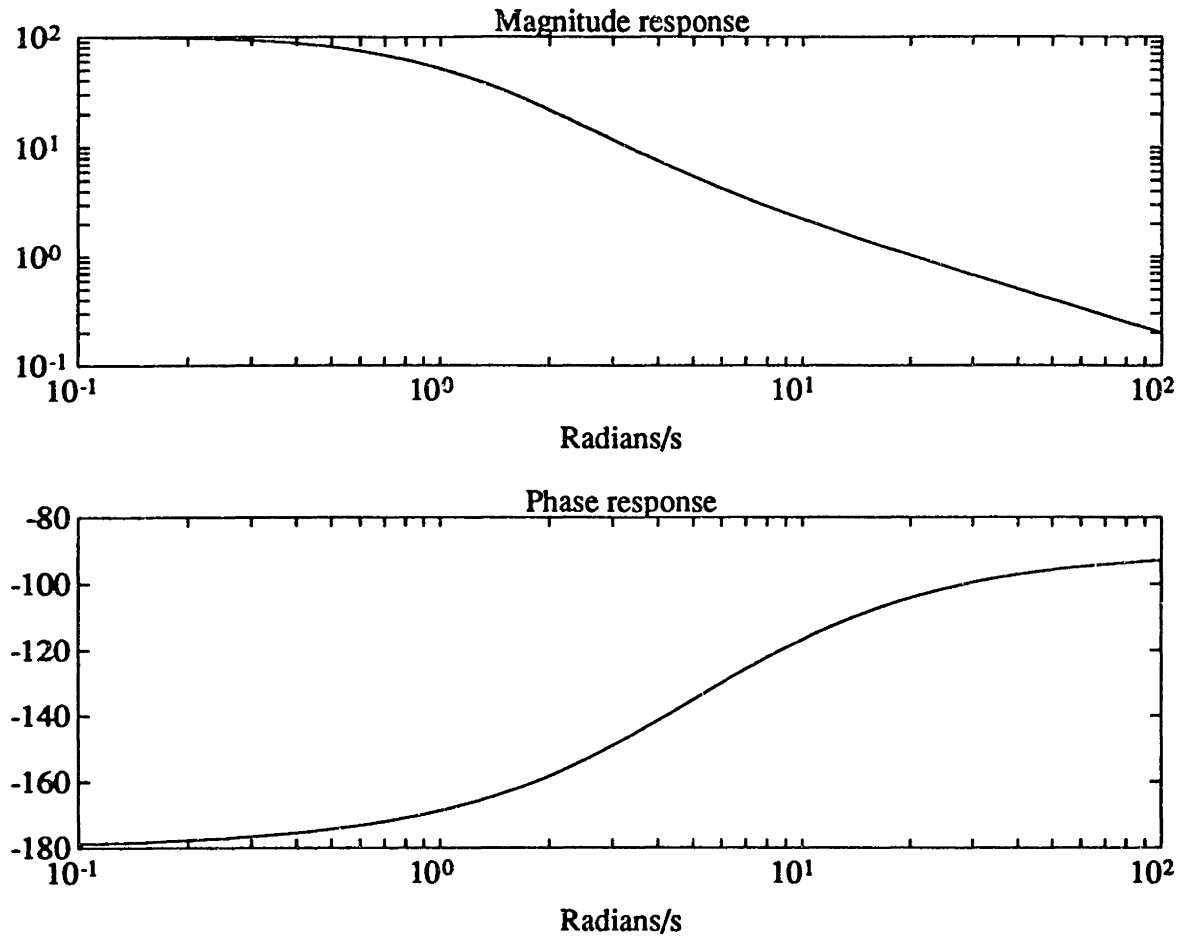

Figure 3.2: Plot of negative of loop transmission magnitude and phase versus frequency for the system (3.15) with $k_1 = 101$ and $k_2 = 20$.

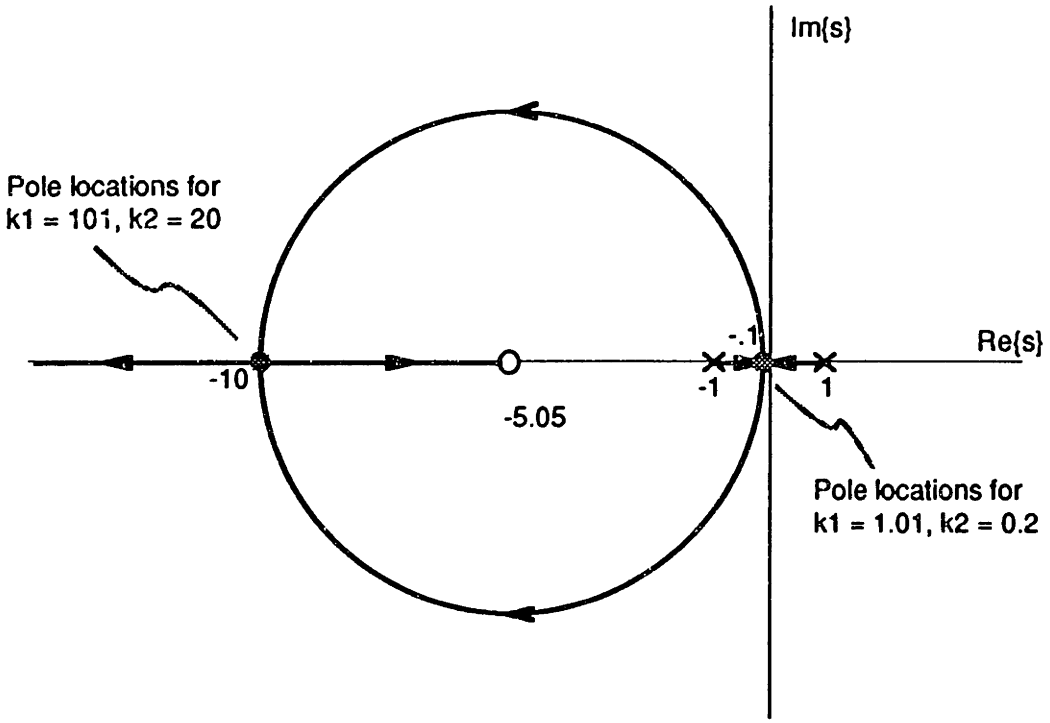

Figure 3.3: Root locus for both of the pole-placement design examples.

Lead compensator

The lead network is arbitrarily chosen to have a pole-zero separation factor $\alpha = 10$. The loop is designed to cross over at 10 rad/sec, and the lead time constant $\tau = 3.16 \times 10^{-1}$ sec is chosen to place the phase maximum at this frequency. The plant is again the normalized suspension (3.11). For this plant and the chosen lead network the loop gain must be multiplied by $a_1 = 32$ in order to set crossover at 10 rad/sec. Block diagrams for the two loops studied in this section are shown in Figure 3.4.

The loop transmission for the lead compensated systems is shown in Figure 3.5. Obviously this loop transmission represents both the loop with lead in the forward path and the loop with lead in the feedback path. The phase margin is approximately 55 degrees. The DC loop gain is about 30. This is too low for many applications; the lag compensator given in the next section addresses this issue.

For the forward-path lead compensated system the step response in position and the corresponding transient in current are shown in Figure 3.6. The final value of position is about 3% higher than the setpoint. This is due to the finite DC loop gain of 30. The settled value is higher than the setpoint because the loop is noninverting at low frequencies (positive feedback). This is due to the suspension open-loop unstable dynamics.

The final value of current is approximately -1. Thus, the initial current is 300 times larger than the final value. This extremely large transient current demand will likely saturate the current-drive amplifier and generates large transient forces which can excite high-frequency structural modes. As well, the overshoot in position is undesirable.

For the feedback-path lead compensated system the step response in position and the corresponding transient in current are shown in Figure 3.7. Placing the lead network in the feedback path reduces the peak current by a factor of 10 (the alpha of the lead network) relative to the peak current when the lead network is in the forward path. Additionally, the step response is overdamped, and there is much less high-frequency energy dumped into the mechanical system. Note again that the final position is about 3% higher than the setpoint. Since it has unity DC gain, the location of the lead network will not affect the DC position.

Another way to achieve a smoother step response with lower peak currents is to precede the loop with a command pre-filter. The pre-filter takes the form of a low-pass filter with its time constant chosen so that if a step is input to the pre-filter, the loop position setpoint rises slowly enough that the step response is smooth. Prefilters of this type are frequently used in the control of mechanical systems such as in the case of pointing an antenna for tracking spacecraft. Here it is undesirable to subject the structure to high-frequency transients, thus by

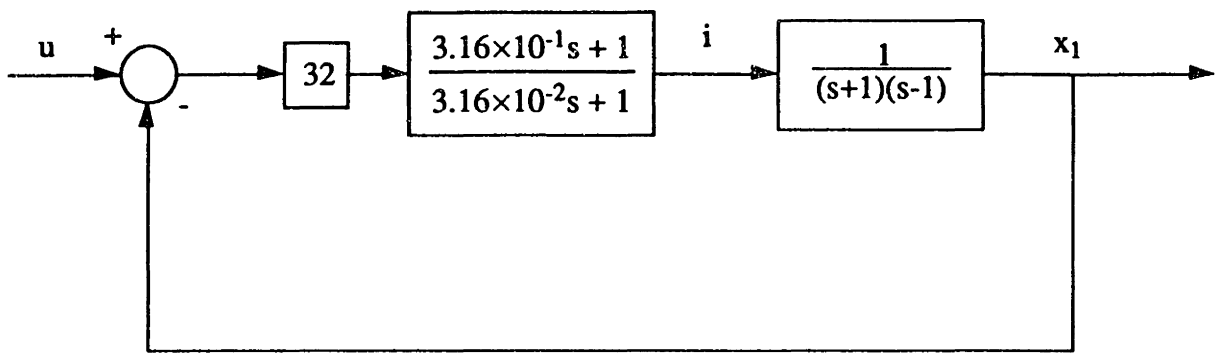

Lead network in forward path

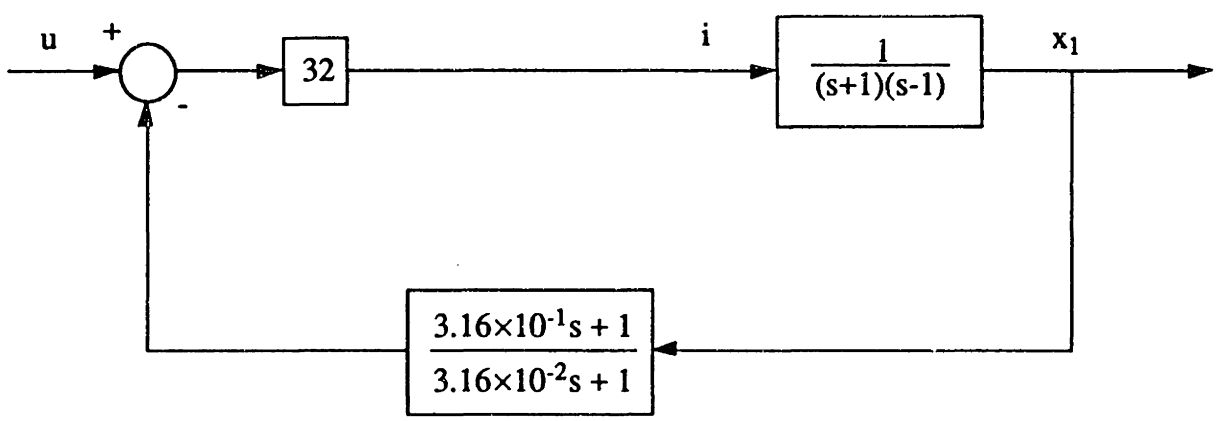

Lead network in feedback path

Figure 3.4: Block diagrams for lead compensated systems with the lead network in the forward path and in the feedback path.

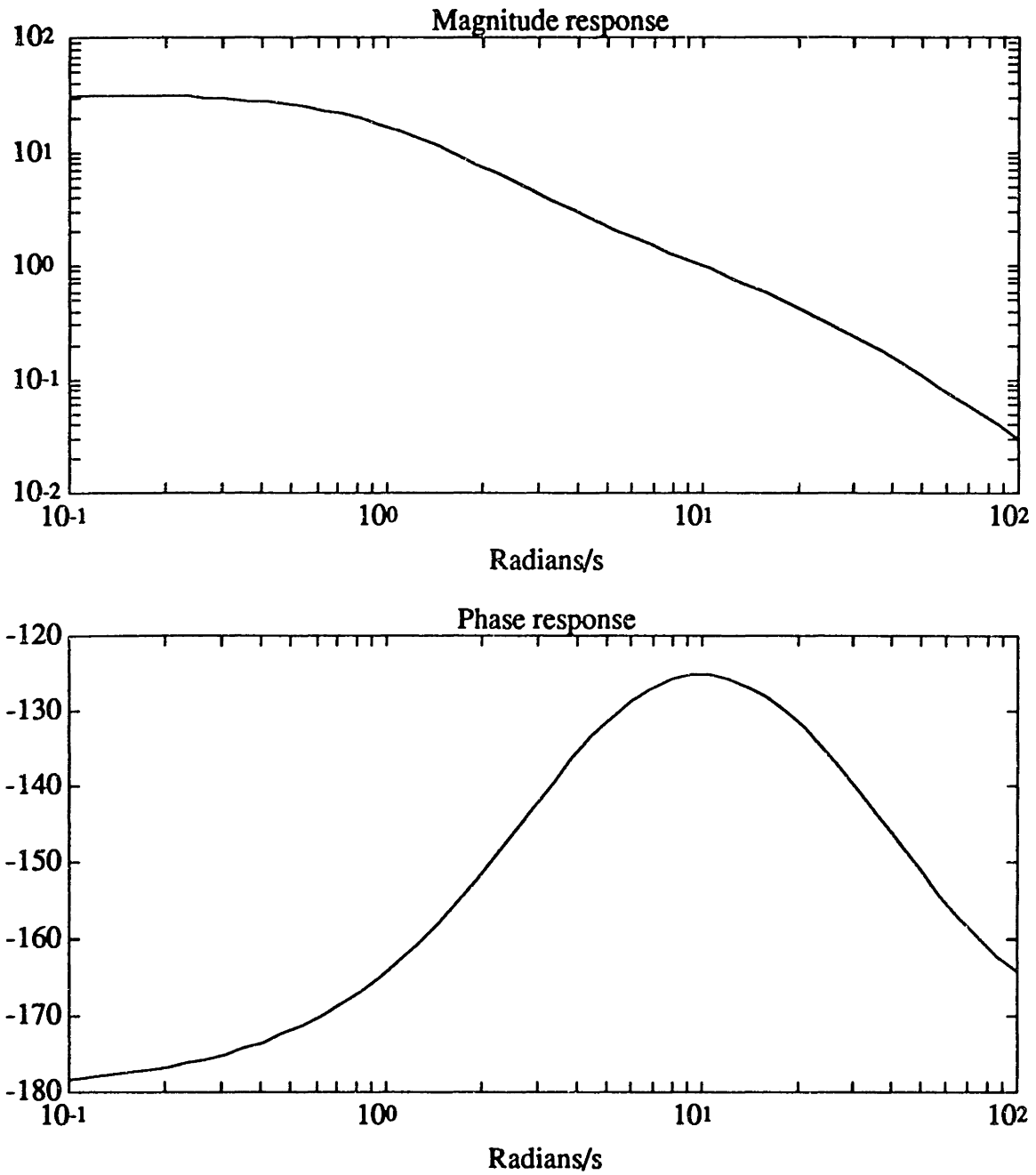

Figure 3.5: Bode plot of the negative of the loop transmission for the lead-compensated system.

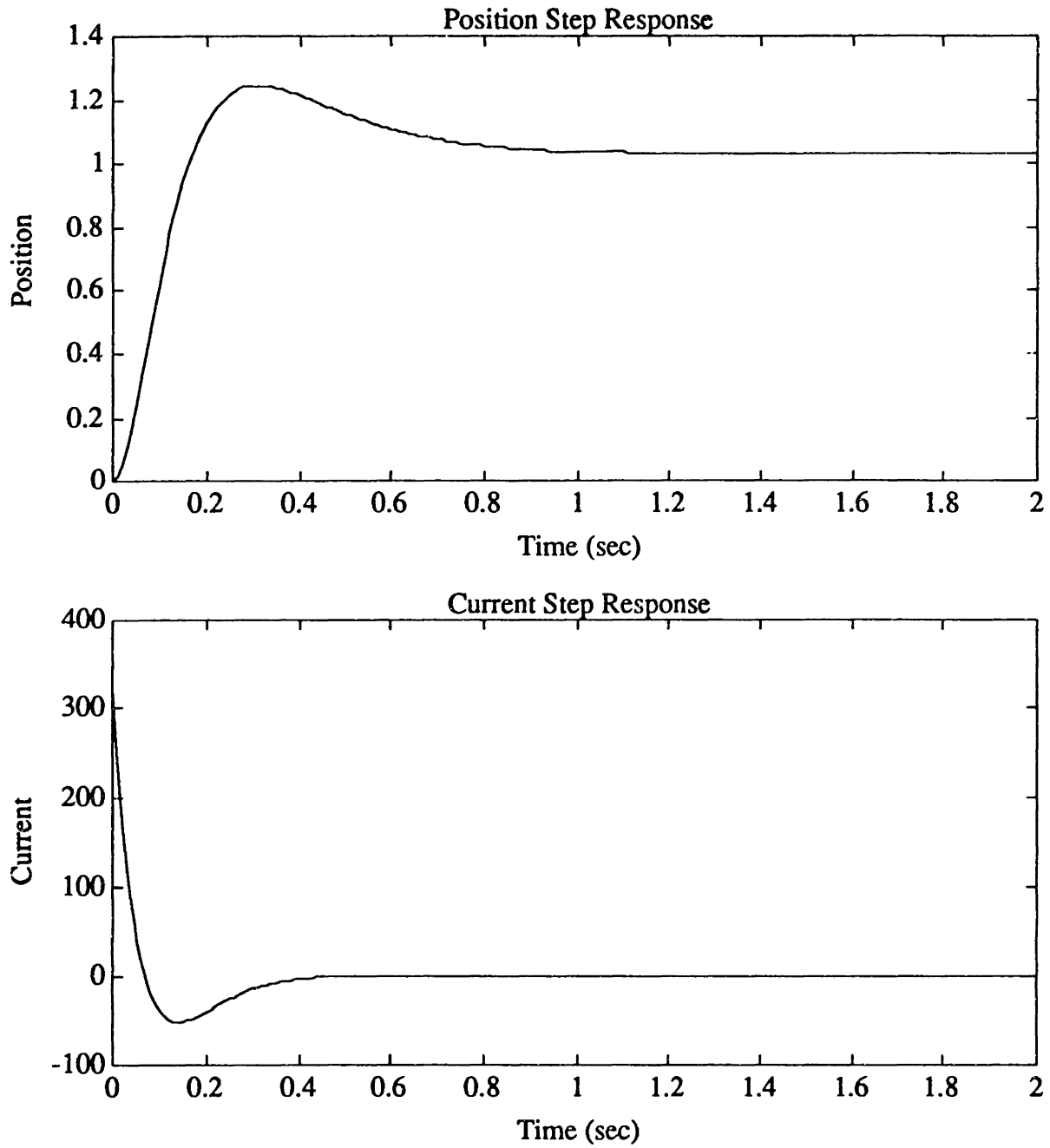

Figure 3.6: Position step response and associated current response for the lead compensated system with compensator in the forward path.

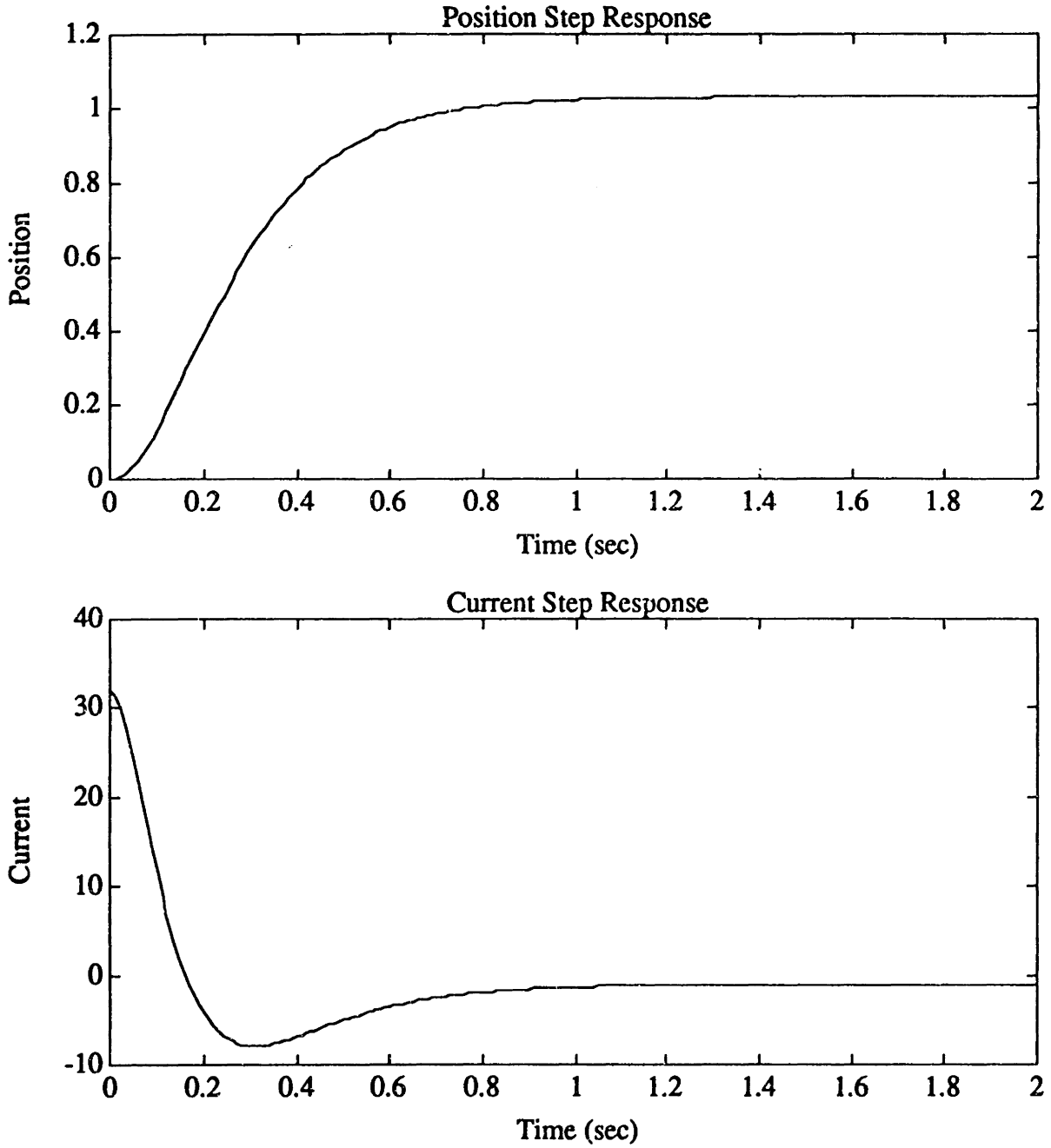

Figure 3.7: Position step response and associated current response for the lead compensated system with compensator in the feedback path.

using a low-pass prefilter the setpoint is not allowed to take the form of a sharp step. However, placing the lead network in the feedback path achieves this goal without requiring the additional command prefilter, and thus without introducing another pole into the closed-loop response.

To achieve higher positioning accuracy requires some form of lag compensation. This is taken up in the next section.

Lag/lead compensator

A block diagram for the lag/lead compensated system is shown in Figure 3.8. The loop crosses over at 10 rad/sec, with a phase margin of about 37 degrees. The loss in phase margin relative to the lead compensated system is due to the residual phase of the lag network. This phase margin could be raised to 45 degrees by using a lead factor of 15. The disturbance rejection is very high at low frequencies.

The closed-loop transfer function for this system is

$$\frac{X_1(s)}{U(s)} = \frac{9.986 \times 10^{-3}s^2 + 3.476 \times 10^{-1}s + 1}{3.277 \times 10^{-4}s^4 + 1.037 \times 10^{-2}s^3 + 9.953 \times 10^{-2}s^2 + 6.216 \times 10^{-1} + 1} \tag{3.19}$$

This transfer function has two zeros which are located at $s = -3.164$ and $s = -31.64$, and four poles which are located at $s = -2.236$, $s = -21.23$, and $s = -4.090 \pm j6.896$.

The step-responses in position and current are shown in Figure 3.9. This step response settles in about the same time as the lead compensated system, although it is somewhat more complex. The damped ringing is due to the complex pair at $s = -4.090 \pm j6.896$. The damping of this closed-loop pair could be increased by increasing the loop phase margin. One way to accomplish this is to redesign the lead network with a larger lead factor. The long-tail response is due to the doublet formed by the pole at s=-2.236 and the zero at $s = -3.164$. Because the zero is located further from the origin than the pole, the doublet response takes the form of an undershoot which slowly rises to the final value. This slow rise is what limits the settling time. However, the settling time is comparable to the lead compensated system discussed in the previous section.

The response settles to a final value of exactly unity. The use of the lag term allows good disturbance rejection and position accuracy with little degradation in the step response compared with lead alone.

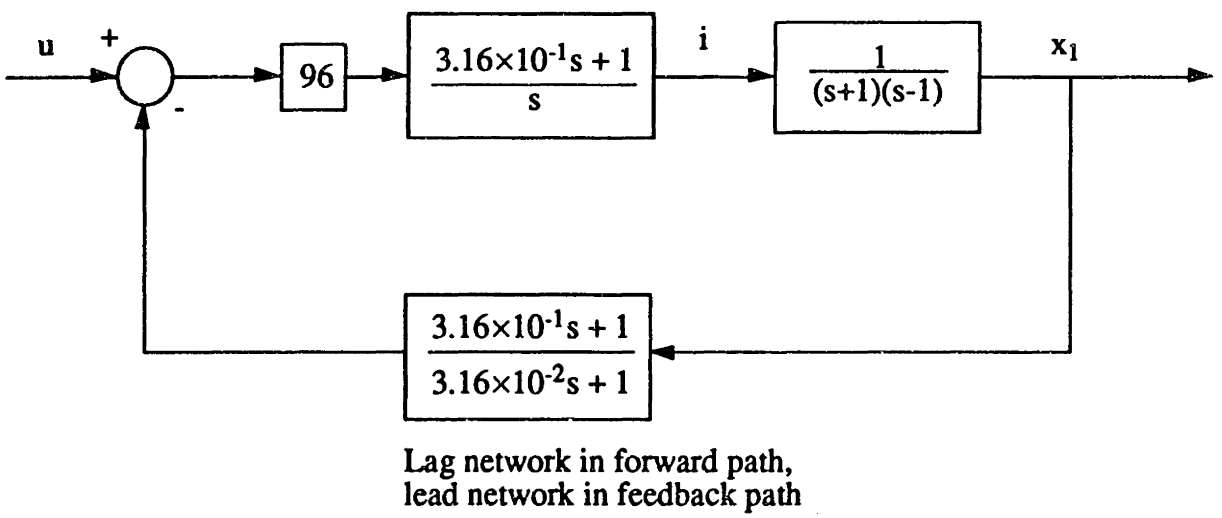

Figure 3.8: Block diagram for lag/lead compensated system with the lead network in the feedback path.

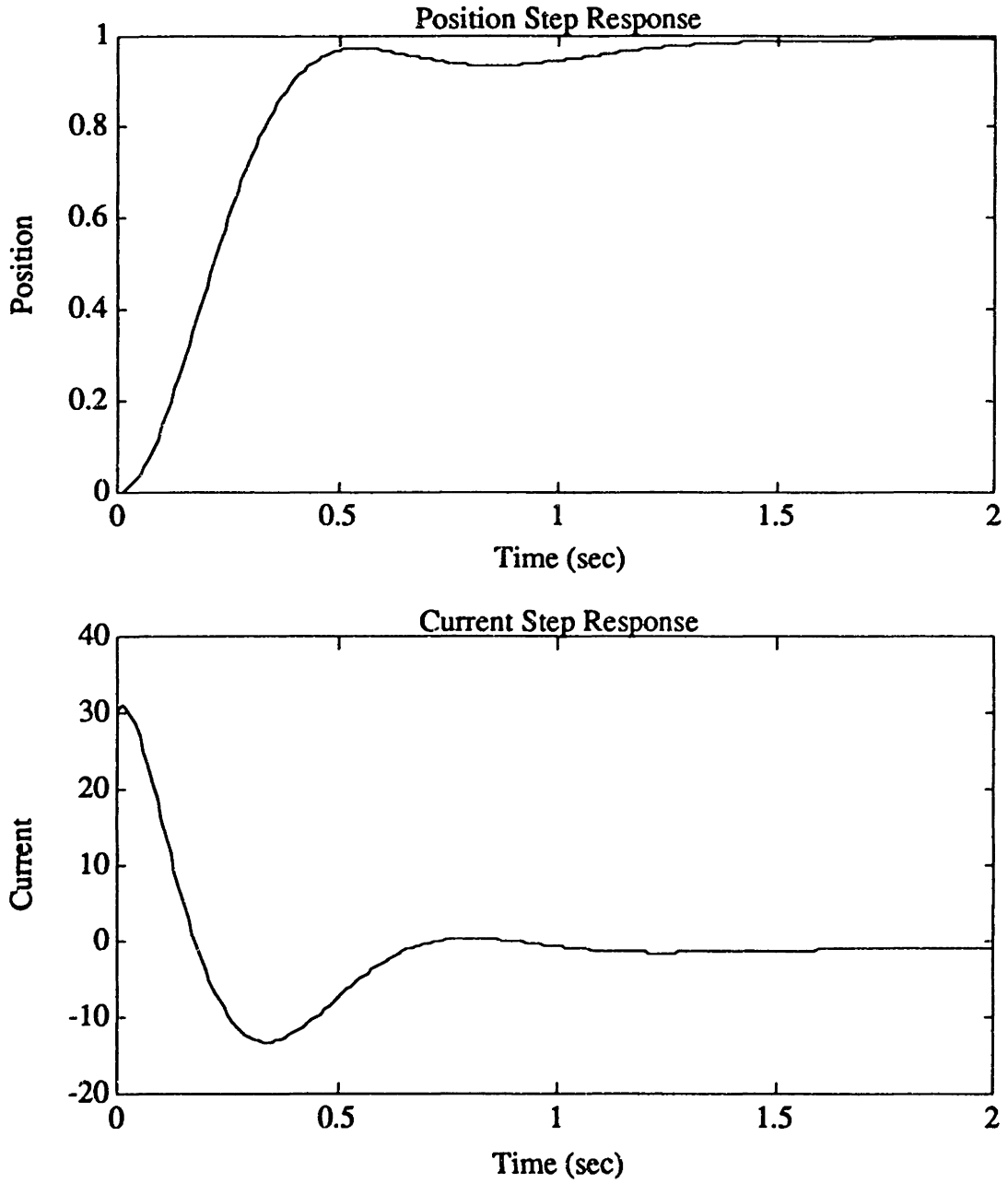

Figure 3.9: Position step response and associated current response for the lag/lead compensated system with lead compensator in the feedback path.

3.4 Some Nonlinear Control Issues

The linear suspension model investigated in the previous sections is only valid for small motions about the operating point. Also it has been pointed out that disturbance forces move the system poles and can destabilize the suspension. If operation over large travel or with significant disturbance forces is required, then nonlinear compensation techniques become attractive.

Nonlinear compensators have received only limited attention in the magnetic suspension literature. [Jayawant et al 1974] describes the control system design for suspension of a 1-ton, 4-passenger vehicle. A flux sensor is located on the pole-face of the suspension magnet. A minor feedback loop is closed on flux which linearizes the dependence of magnetic force on position. The force still goes as the square of flux, so an additional square root linearization is required. They mention the idea of using an analog multiplier to compute the ratio i/x, which would allow elimination of the flux sensor. However, this technique was prone to drift and noise, and was abandonded. This flux-feedback scheme is described in more detail in [Jayawant et al 1976a]. [Groom and Waldeck 1979] study the control of an annular momentum wheel which is supported by magnetic bearings, to be applied for energy storage. They also use a nonlinear correction law to correct the inverse square law magnet behavior. The nonlinear compensation was implemented with analog multiplier and square root circuits. [Traxler et al 1984] implement microprocessor-based linearizing transformations used in a demonstration system.

In recent years, progress has been made in the theory of nonlinear control systems, and in the sub-area of feedback linearization. Here, the work of [Su 1982] is of fundamental importance in that it presents the conditions under which a system may be globally linearized. In a subsequent section Su's results are applied to the third order suspension (3.3). However, for a simple system, it is often possible to construct the linearizing transformations by inspection. We start then by demonstrating the idea of feedback linearization using the second order system (3.4).

3.4.1 Linearization of second-order suspension

The basic idea of feedback linearization is to define transformations on the states and input(s) such that the nonlinear system appears linear and operating-point invariant in terms of the transformed representation. Then a controller can be designed for the transformed variables. This allows the closed-loop system stability to be made independent of operating point.

For the second-order equations (3.4), a transformation on the input is all that is required to linearize the system. This transformation may be derived by

inspection without using any formal mathematical machinery. That is, if the coil current i is made to vary as

$$i = x_1\sqrt{\frac{-vM}{C}} \tag{3.20}$$

then the suspension is globally linearized in terms of the new input v. The notation for the auxiliary input v has been chosen to match the notation in [Su 1982].

Specifically, substituting from (3.20) into (3.4), the system state equations become

$$\begin{aligned} \dot{x}_1 &= x_2 \\ \dot{x}_2 &= v + g - \frac{f_d}{M} \end{aligned} \tag{3.21}$$

These equations are linear, with an input v, and disturbance terms g and f_d.

Here, v is a signal internal to the compensator which may be thought of as a setpoint for acceleration in the direction of increasing airgap. In operation, the signal v will be computed within the compensator, and constrained to be less than or equal to zero. Since the magnet can only supply accelerations in the direction of decreasing air gap it would not be physically meaningful to ask for acceleration in the direction of *increasing* air gap by setting v greater than zero. Thus the term $-v$ in (3.20) will always be greater than or equal to zero, and the square root will yield a real number.

The plant appears linear in terms of the new input v. This compensation of the nonlinear term does not however stabilize the plant. To stabilize the system, the nonlinear compensator is preceded by a linear compensator. The resulting closed-loop system is shown in Figure 3.10. The compensator may be thought of as having two parts, a nonlinear compensation section and a linear compensation section. It is the function of the nonlinear section to implement (3.20) in order to adjust i as a function of x_1 and v such that the acceleration of the ball is equal to v. It is the function of the linear section to specify the value of v as a function of the error between the position setpoint and the measured position such that the linearized plant is robustly stabilized and has good disturbance rejection and settling time properties. The signal v forms the connection between the linear and nonlinear sections of the compensator.

This combination of linear and nonlinear compensation sections stabilizes the plant such that the loop dynamics are independent of operating point. Such operating point independence is the main advantage of using a nonlinear compensator. Note that as viewed from the input to the nonlinear section, the incremental relationship between v and x_1 is equal to $1/s^2$, independent of operating point. Thus, the linear compensator can be designed to control a double integrator via

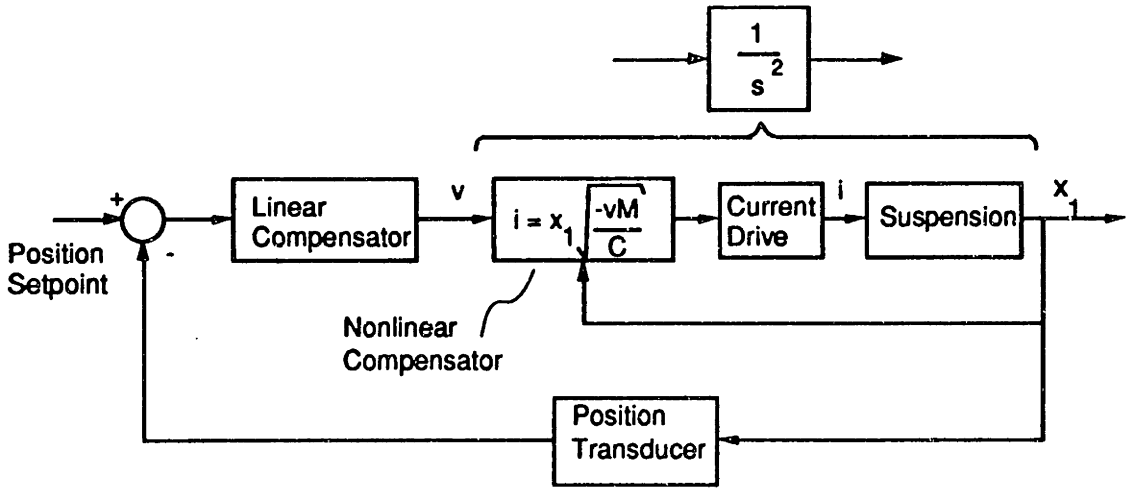

Figure 3.10: Nonlinear compensation of second-order magnetic suspension system.

standard linear techniques. If it is desirable to reject static disturbance forces with no position error, then the linear compensator can be designed to include an integral term. This integral term will adjust the value of v to balance gravity and any low-frequency components of the disturbance f_d.

In applications where large excursions or disturbance forces are anticipated, the additional complexity of the nonlinear compensation approach is justified. The major caveat is that we are assuming that the suspension model is accurate. For the electromagnetics an accurate model can readily be developed, and thus nonlinear compensation techniques are applicable. The nonlinear compensation technique was used in the construction of a class demonstration system which is described below.

3.4.2 Classroom demonstration implementing linearization

In the Spring of 1988, I constructed a single degree of freedom levitation system for use as a classroom demonstration which implemented the nonlinear compensation technique described in the previous section. As developed there, if the plant state equations are given by (3.4), then applying the nonlinear compensation law (3.20) results in a system which appears to be linear in terms of the intermediate signal v. The demonstration system uses a high-bandwidth current-drive to regulate the electromagnet current, and thus (3.4) is applicable.

In the demonstration system, a one inch steel ball bearing is suspended below an electromagnet consisting of 3100 turns of #22 magnet wire wound on an 1 inch diameter by 4 inch length steel core. The coil current is controlled by a Bose-type switching regulator, with a half-scale current switching frequency of 10 kHz, and a full scale current of 2 Amperes. The operating point current is about 0.4 Amperes at a typical operating point air gap of 1 cm. The system is digitally controlled by an 8088/8087-based single-board computer and data acquisition system at a 400 Hz sampling rate. The control law for the nonlinear compensation section uses (3.20) to linearize the magnetic force relationship. This allows the stability of the closed-loop system to be essentially independent of the operating point. The control law for the linear compensation section is then developed via classical techniques applied in the discrete-time domain. The position of the ball is sensed optically, and nonlinearities in the sensor output versus position are compensated for in software.

In order to apply the nonlinear compensation technique, an accurate model of the plant is required. For the classroom demonstration, this model is developed by measuring the force on the ball as a function of current and position. This measurement is accomplished by using a balance beam for measuring the magnetic force on the ball. A 1 inch ball bearing is glued into one end of an

aluminum balance beam of rectangular tubular cross-section measuring 1 inch wide by 0.75 inches deep by 12 inches long. The beam pivots at the center on a thin wire which is held by fixed side supports. Balance pans were hung from the beam on both sides of the pivot midway between the pivot and the ends of the beam. These pans are used to add or subtract weight carried by the suspension. At the end of the beam opposite the ball, a micrometer was positioned to push against the beam and thus provide a postion reference.

The idea here is that the ball glued into the end of the beam can be placed into suspension. The beam thus provides a handle on the ball by which the force applied to the ball can be varied. This is accomplished by putting weights into the balance pans on either side of the pivot. The beam is made of aluminum, and thus does not interact with the electromagnet. At the ball end, the beam is made thin so as not to interfere with the optical measurement. The ball is attached to the bottom of the thinned end beam in such a fashion that it interacts with the optical sensor in the same fashion as a freely suspended ball.

The force relationship (3.2) was well fit by the experimental data with the parameters $C = 4.43 \times 10^{-4}$ Nm^2/A^2 and $g_0 = 0.25$cm. The mass of the ball is 67 grams. These parameters are used in the nonlinear compensation law (3.20). The only deviation from the relationship (3.2) was at high currents (> 1A), where the effects of magnetic saturation are apparent.

The optical position sensor is constructed as follows. A 24 volt, 5 watt incandescent lamp is used as the source, and a piece of cadmium sulfide photo-cell is used as the sensor, in what is a standard position sensor for magnetic suspensions. Using the balance beam described above, the sensor output is measured for a number of ball positions. When the shadow-line cast on the sensor is in the central region of the sensor, the sensor output is essentially linear with ball position. However, as the shadow-line approaches the upper or lower edge of the photo-cell, the sensor sensitivity begins to decrease. This nonlinearity in the relation between ball position and sensor output is corrected in software in the section of code which inputs the sensor voltage. The corrected position measurement is then linear with actual ball position. It is this corrected position measurement which is passed to the rest of the control loop.

The position sensor was found to have several defects which limit the system performance. First, the incandescent bulb output decreases significantly as a function of time. This is believed to be due to the evaporation of the filament. Material driven off of the filament is deposited on the inside of the glass envelope, thereby decreasing the bulb brightness. The second problem is that the cadmium sulfide sensor is sensitive to any light falling on its surface, independent of the source. Thus ambient lighting is indistinguishable from the light emitted by the bulb.

Both of these effects cause problems in the nonlinear compensation law (3.20)

and in the correction of the sensor nonlinearities. First, the decrease in bulb intensity and any changes in average ambient light act as offset terms which drive the system to incorrect points on the sensor correction curve and in the magnet nonlinearity correction law (3.20). This offset deteriorates the system stability. Secondly, the ambient light has a large component at twice the power line frequency, especially in rooms with flourescent lighting. This signal at 120 Hz acts as a large noise source which causes error motions in the ball position.

The above problems can be solved as follows. First, the light source needs to be made more constant with time. This can be achieved by using a more specialized incandescent bulb, or by switching to a semiconductor light source such as an infra-red light emitting diode. The ambient lighting offset and noise problems can be solved by either or both of two approaches which are classical in their application to many problems. The first is to make the system narrow-band. Commonly available IR diodes emit a relatively narrow-band optical signal; laser diodes are narrower. In this case, an optical band-pass filter can be placed in front of the sensor, so that only the emitted frequencies are sensed, and the ambient lighting is greatly attenuated. The second approach is to switch the light-source on and off at a high frequency and use synchronous detection to reject signals which are not at the same frequency and phase as the source. The frequency of switching must be made much higher than the cross-over frequency of the position control loop, perhaps on the order of 10 kHz switching frequency. This rate is easily within the capabilities of available electronics.

The results derived in the previous section for the nonlinear compensation laws assume that these are implemented in continuous time. For discrete-time implementation, the issue of sampling rate becomes important. This issue is investigated in the next section.

3.4.3 Sampling rate issues

Due to the complexity of the transformations it is most likely that a linearizing compensator will be implemented in discrete time. As an introduction to one issue involved in discrete-time implementation, the effect of sampling rate on the second-order suspension system (3.4) is investigated by simulation. For this example, the suspension parameters have been been given the values developed for the class demonstration system described above. These values are $M =$ 67 grams, and $C = 4.43 \times 10^{-4}$ Nm^2/Amp^2.

The system was simulated assuming a nonlinear compensation law of the form (3.20). The four graphs shown in Figure 3.11 indicate the system behavior when a net 0.05g acceleration ($v = -0.05$ in (3.20)) is specified. The lines labelled 'ideal' show that if the nonlinear compensation was perfectly implemented, the force on the ball would be constant, and the graph of velocity vs. time would be

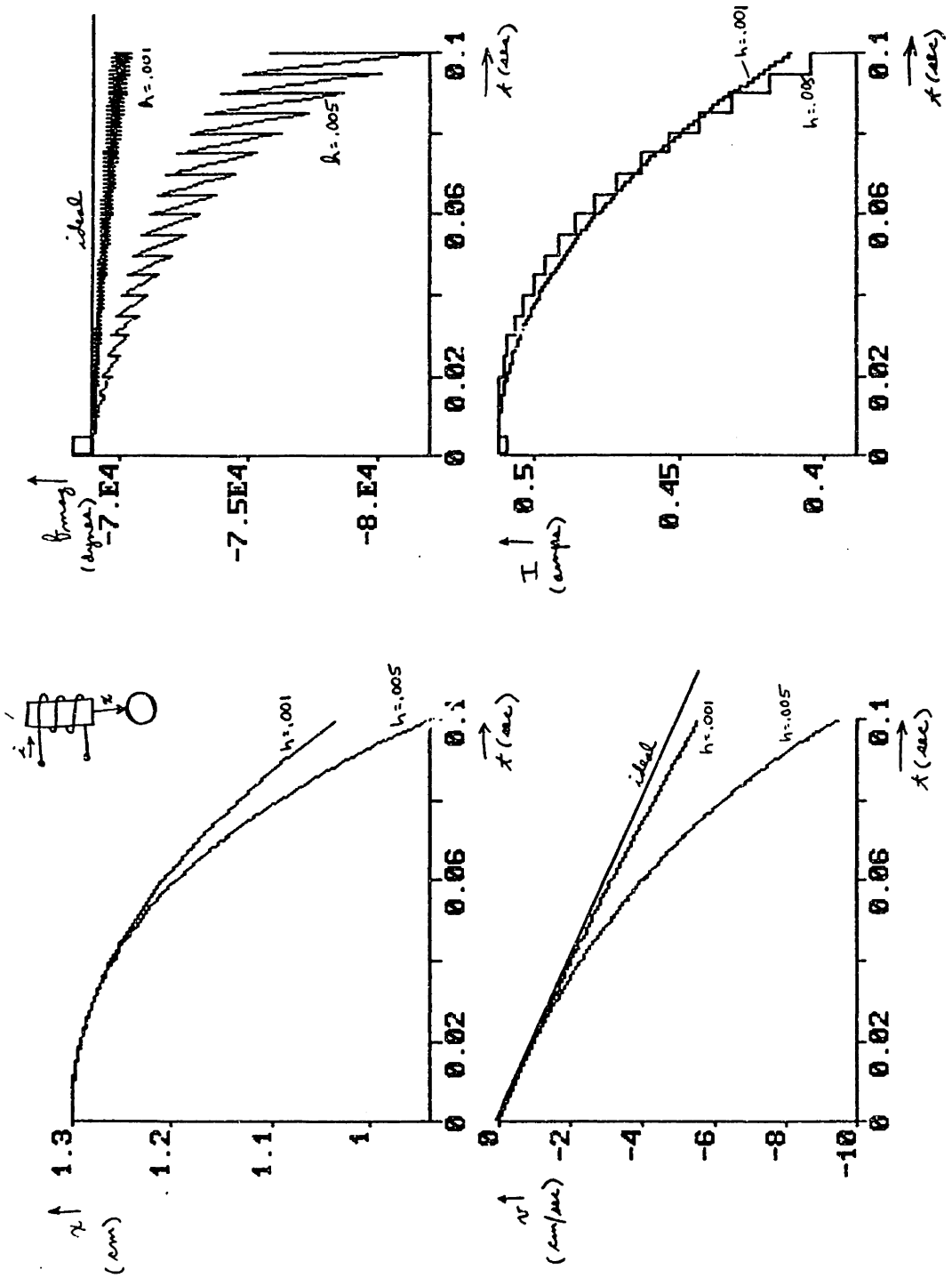

Figure 3.11: The open-loop system with nonlinear compensation showing its performance with sampling periods h of 1 and 5 milliseconds. Position x is in cm separation from the pole face, velocity v is in cm/sec, force on the ball is in dynes, and current I is in amps.

a straight line. However, with any finite sampling rate this is not the case. The system is open-loop unstable and uncontrolled between sampling instants. Thus it 'runs away' during the interval in which the control current is held constant. The graphs show the result of this process for sampling rates of 1 kHz and 200 Hz. To get reasonable behavior, it can be seen that a sampling rate on the order of 1 kHz is required. In the class demo, due to computational speed limitations a 400 Hz sampling rate was used. This was found to be adequate as long as the ball was not allowed to approach too close to the pole face.

Another way to look at the effect of sampling rate is to examine the system behavior under closed-loop position control. To this end, a linear proportional plus lead compensator is designed in discrete-time to stabilize the nominal plant which would result if the nonlinear compensation were perfect. That is, in the ideal case, the nonlinear compensated system appears as a double integrator independent of operating point. In the finite sampling time implementation, the quality of this approximation deteriorates as the air gap closes. This can be seen in Figure 3.12 which displays simulated step responses for the closed-loop system at four nominal operting points and for the two sampling rates. Note that the system with 200 Hz sampling goes unstable at the 0.5 cm and smaller air gaps, whereas the behavior of the 1000 Hz sampled system only begins to deteriorate when the air gap approachs 0.3 cm. The unstable response for 200 Hz sampling is not shown for the 0.3 cm air gap.

The bottom line for this example is that the practical implementation of these linearizing transformations may require very high sampling rates. Also, what may be considered a satisfactory sampling rate depends on the range of operating points which are encountered in system operation. Certainly, the issue of discrete-time implementation merits further study.

Experience with this simple nonlinear compensation system provided the impetus toward an understanding of feedback linearization techniques in more generality. A description of the application of feedback linearization to the third order suspension system is given in the next section.

3.4.4 Linearization of third-order suspension

For more complex plants it may be difficult to develop linearizing transformations by inspection. The results of [Su 1982] provide a general approach to this problem. A good introduction to these ideas is presented in [Spong and Vidyasagar 1989]. Their presentation assumes no more than an undergraduate background in control theory and is thus a good place to start for someone new to this area.

Without reviewing the results from the above references, suffice it to say the if the plant satisfies a controllability condition and a condition on the existence of solutions to a set of partial differential equations, then transformations

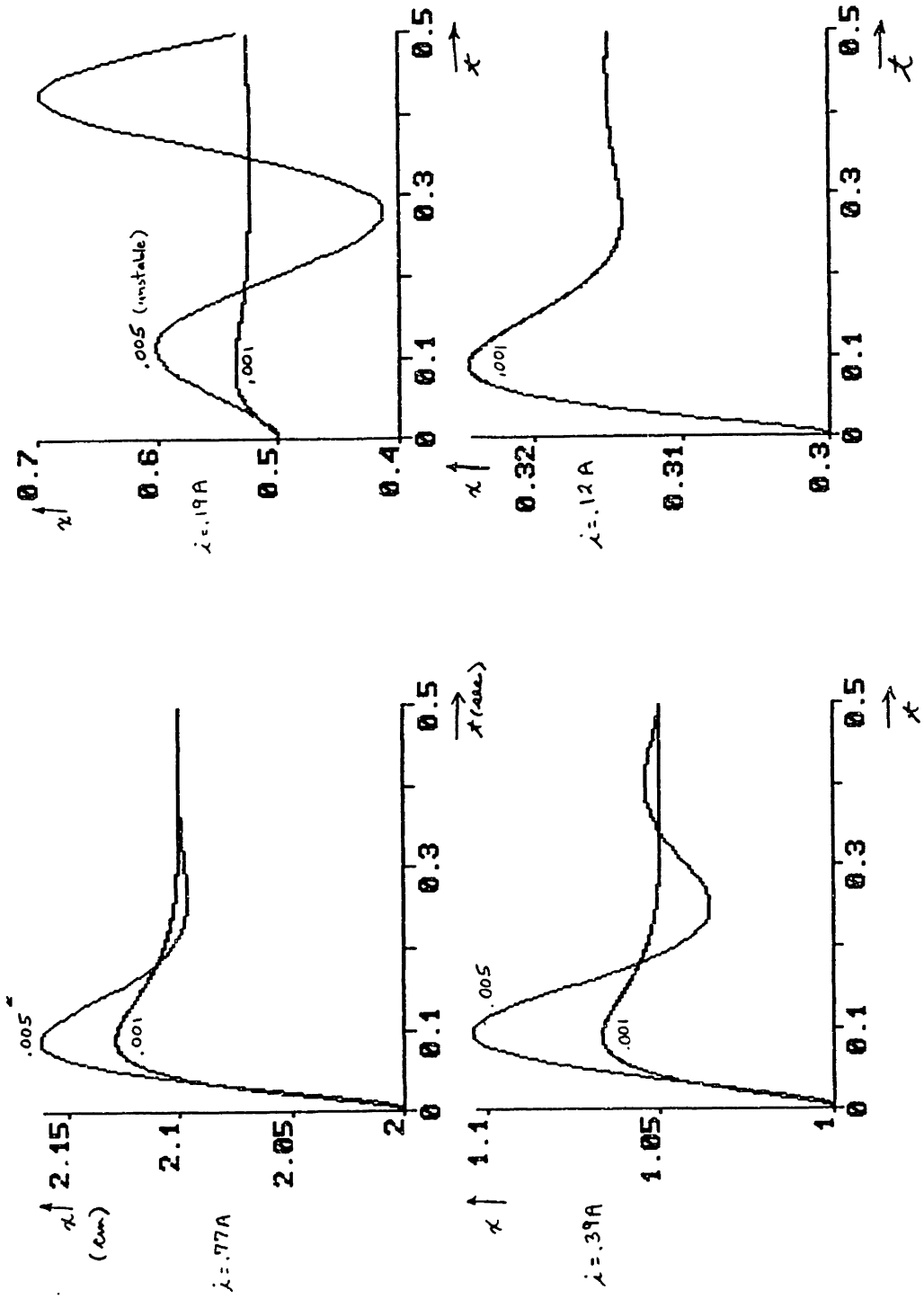

Figure 3.12: The closed-loop system with nonlinear compensation showing its performance with sampling periods h of 1 and 5 milliseconds as the operating point position is moved towards the pole face. Position x is in cm separation from the pole face. The nominal operating points are 2, 1, 0.5, and 0.3 cm respectively.

$z_1 = T_1(x), \ldots, z_n = T_n(x), v = T_{n+1}(x, u)$ can be constructed such that in the z-v space the system appears linear. Here, x is the state-vector of the nonlinear system, z is the state-vector of the linearized system, and n is the system order. Under these transformations, the nonlinear system is mapped to the controllability canonical form

$$\frac{d}{dt}\begin{pmatrix} z_1 \\ \vdots \\ z_{n-1} \\ z_n \end{pmatrix} = \begin{pmatrix} z_2 \\ \vdots \\ z_n \\ 0 \end{pmatrix} + \begin{pmatrix} 0 \\ \vdots \\ 0 \\ 1 \end{pmatrix} v. \tag{3.22}$$

For the system (3.3), Su's results yield the linearizing transformations $z_1 = x_1$, $z_2 = x_2$, $z_3 = -(C/M)(i/x_1)^2$, and $z_4 = \frac{i}{Mx_1}(Ri - u)$. Thus the system appears linear in terms of state varibles z_1, z_2, and z_3, and with a properly redefined input v. The states z_1 and z_2 are simply the original position and velocity. State z_3 is the acceleration applied to the suspended member. Thus it makes physical sense that the suspension will appear linear in z_3. The suspension force happens to vary nonlinearly with the untransformed state and input, but Newton's law guarantees linearity in terms of a transformed state varible which is proportional to acceleration. In an implementation, the voltage drive u must be computed in terms of v

$$u = -\frac{Mx_1 v}{i} + iR \tag{3.23}$$

Since v drives the derivative of z_3, we can think of v as being a setpoint for the *slope* of the acceleration. Note that the coil resistance voltage drop iR is directly added to the input u.

Thus we have found a set of linearizing transformations. However the transformations are not unique. Direct substitution will verify that the transformations $T_1 = x_1^2$, $T_2 = 2x_1x_2$,

$$T_3 = 2x_2^2 - \frac{2Ci^2}{Mx_1} \tag{3.24}$$

and

$$T_4 = -\frac{6Cx_2i^2}{Mx_1^2} + \frac{2i}{M}(Ri - u) \tag{3.25}$$

though more complex than the first set, do indeed globally linearize the system. Actually, there are an infinity of such transformations which linearize this system. This is a consequence of the nature of nonlinear systems. It is clear however that the first set has the greatest physical meaning, and thus would be chosen in any practical context. Note also that in this case the transformed state z_3 need never be computed. This is so because the system is linear between the transformed input v and the original position state variable x_1. Further, note that the input

transformation (3.23) depends only upon position x_1 and current i. Both of these quantities may be readily measured.

3.4.5 Areas for further study

As we have seen in the magnetic suspension examples, the technique of feedback linearization is of great utility in designing control loops for nonlinear systems such that the closed-loop systems are well-behaved despite large variations in operating point or disturbance forces. Sampling rates for discrete-time implementations have been shown to be critical, especially at small air gaps. For practical applications, the most important area which we have overlooked is that of robustness with respect to plant modeling errors. This is an area which has also been a topic of current research. [Spong and Vidyasagar 1989] discuss it in their presentation. Another approach is to verify robustness through simulations under varying parameter conditions. I would certainly like to understand more about this area, but one only has so much time.

Another area which reading these papers has motivated me to study further is nonlinear system theory. If one is attempting to modify the system properties of a nonlinear plant, it is a good idea to have a strong background in the behavior of nonlinear systems. The fact that a first order discrete-time system can exhibit chaotic behavior should make one very humble about understanding nonlinear systems based upon intuition developed primarily in the linear context.

Chapter 4

Linear Bearing Mechanical System Description

This chapter describes the linear bearing operating principles, mechanical architecture, how the parts were assembled to the necessary tolerances, and modifications which were made as problems with the original architecture became apparent. Suggestions for further improvements in the design are presented.

4.1 Design Concepts

The linear bearing system grew out of the Ångstrom Resolution Measuring Machine (ARMM) proposed by [Slocum and Eisenhaure 1988]. The operating principle of the ARMM is to suspend a platen using seven electromagnets such that the platen is capable of significant travel in the direction of the long axis of the platen. Two such suspended platens are then arranged so that their long axes of travel are perpendicular and lie in a horizontal plane. In this manner a sample attached to one platen can be scanned by a probe attached to the second platen. Thus the sample can be scanned over a square area of length and width equal to the travel of the two platens.

In the current work, a single platen suspension was built in order to demonstrate proof of concept for this system. Pictures of the completed suspension are shown at the end of Section 4.2.7. The basic operating principles of the linear bearing suspension are described in the remainder of this section.

Three electromagnets act on the top surface of the platen and four electromagnets act on the sides of the platen. The three top electromagnets serve to control the platen's roll, pitch and vertical translation. Gravity is used to bias the suspension so as to supply force in the downward direction as the three top electromagnet currents are reduced. The four side electromagnets are arranged

in pairwise opposition, two on each side of the platen, so as to act in a push-pull fashion. These electromagnets control the platen's yaw and lateral translation. The sixth degree of freedom which is translation in the direction of the long axis of the platen is uncontrolled in our implementation, as described later in this chapter.

Since five platen degrees of freedom are controlled, five independent position measurements are required. This is achieved by locating capacitance probes in the center of each of the three top electromagnets and in the center of two side magnets. This arrangement allows the measurement of the five controlled platen degrees of freedom. Travel in the long axis of the platen is not measured in our implementation.

The platen consists of a hollow, rectangular-section steel tube, with dimensions of about 5 inches by 5 inches by 14 inches. This tubular form was chosen to be compatible with the taut-wire inchworm driver proposed in [Slocum and Eisenhaure 1988] to drive travel in the long axis of the platen. This inchworm drive was not implemented in the current effort.

The manner in which the electromagnet forces act on the platen is shown in Figure 4.1. Here, each arrow represents the force applied by the corresponding electromagnet. This force is normal to the platen, and acts through the center of the electromagnet. The black dots in the figure indicate the locations at which the capacitance probes measure position.

The mechanical details of the ARMM suspension system are presented in the next section.

4.2 Original ARMM Implementation

The ARMM operating principles have been discussed in Section 4.1, based on the initial concept presented in [Slocum and Eisenhaure 1988]. In order to implement the design proposed in that paper, electromagnets, magnet fixtures, the mechanical frame, the platen, probes, and probe electronics were developed or purchased under the direction of Prof. Alex Slocum at MIT, prior to my involvement with the project. Major credit is due to Prof. Slocum for originating the idea, and for continuing to push the design along. Several of his students were responsible for construction of important parts of the ARMM. Debra Thurston and Eric Heatzig were involved with the initial design. Tim Hawkey designed and oversaw the construction of the magnetic actuators. Dave Gessel designed the mechanical components and executed some of the more difficult machining. Van Pham worked on the project for a year and a half. He assisted with machining and other assembly tasks, and wrote his Bachelor's thesis [Pham 1989] on the dynamics and control issues of the suspension.

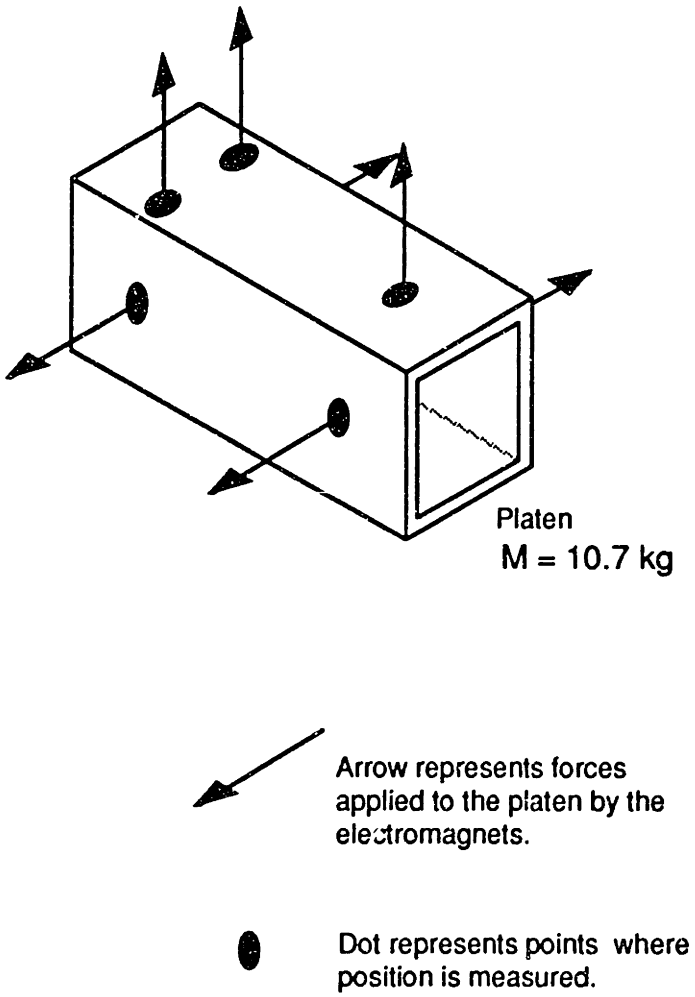

Figure 4.1: Platen.

I became involved with the project at the time when parts were beginning to come back from the machine shop, but these parts had not yet been assembled into the suspension system. I took overall responsibility for the project at that time. No control strategy had yet been developed, neither had ideas been worked out for the proper assembly and alignment of all the pieces. In this section I describe the intended mechanical arrangement as it existed when I first became involved with the project. Many significant changes were made from this initial conception; these changes are documented in Section4.3. Pictures of the completed system are shown at the end of Section 4.2.7. In the sections which follow, the suspension components are individually described, and mechanical drawings of their dimensions are given. After the individual parts are described, the assembly of these parts into the complete system is presented.

4.2.1 Platen

The suspended member is referred to as the platen, or sometimes as the log, due to its shape, and is shown in Figure 4.2. It consists of a piece of 5 inch square steel tube which was surface ground on all four faces for mechanical accuracy, nickel plated to prevent corrosion, and then annealed for better magnetic properties and dimensional stability. The platen weighs 10.7 kilograms.

4.2.2 Electromagnets

The design uses one large electromagnet and six small electromagnets. Both types contain a permanent magnet as well as the electromagnet coil. The magnetic circuits for the permanent magnet and the electromagnet are essentially independent. The large electromagnet is shown in cross section in Figure 4.3, which includes the materials used and detailed dimensions. Pole face and top views of the large electromagnet are given in Figure 4.4. The small electromagnet is shown in cross section in Figure 4.5, which includes the materials used and detailed dimensions. Pole face and top views of the small electromagnet are given in Figure 4.6. The coils were wound to the required dimensions by a local company[1]. Then the component parts of the magnets were assembled by gluing them together with epoxy.

4.2.3 Bearing Assemblies

Once the magnets were assembled, they were glued with epoxy into bearing fixtures, which are 6061 T651 aluminum blocks milled out to receive the electromagnet assembly such that the pole face protrudes from the fixture by several

[1] Ladesco, Inc., Manchester, New Hampshire

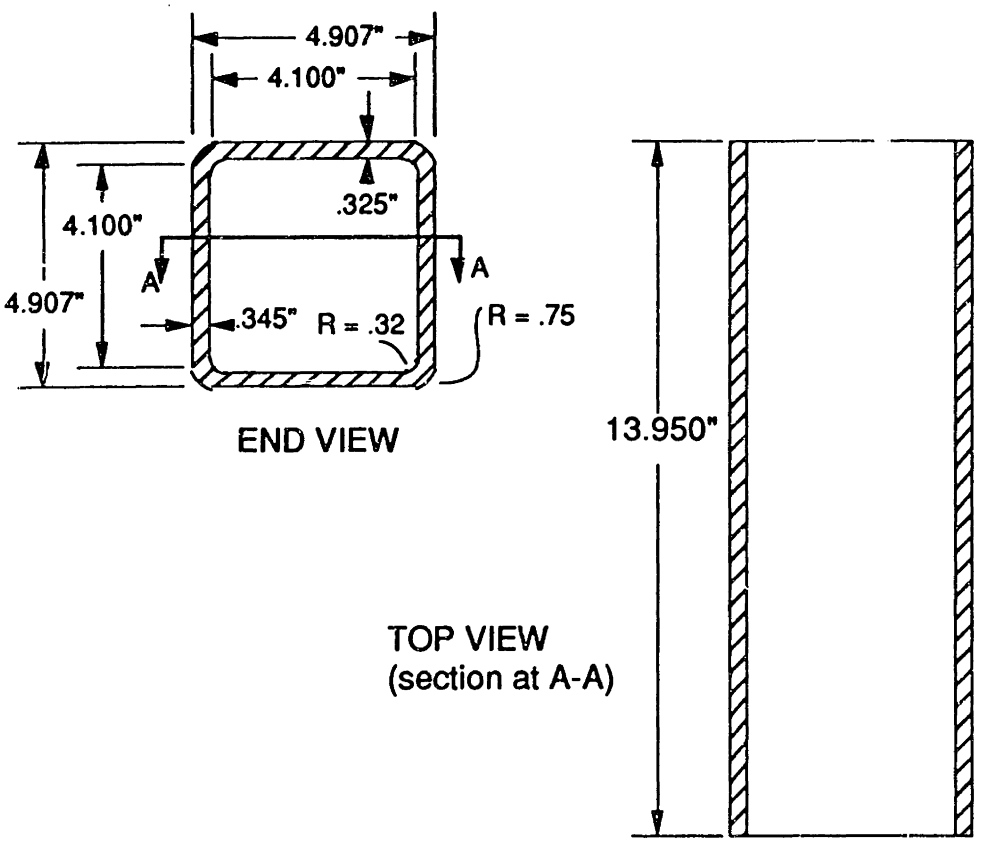

Figure 4.2: Platen.

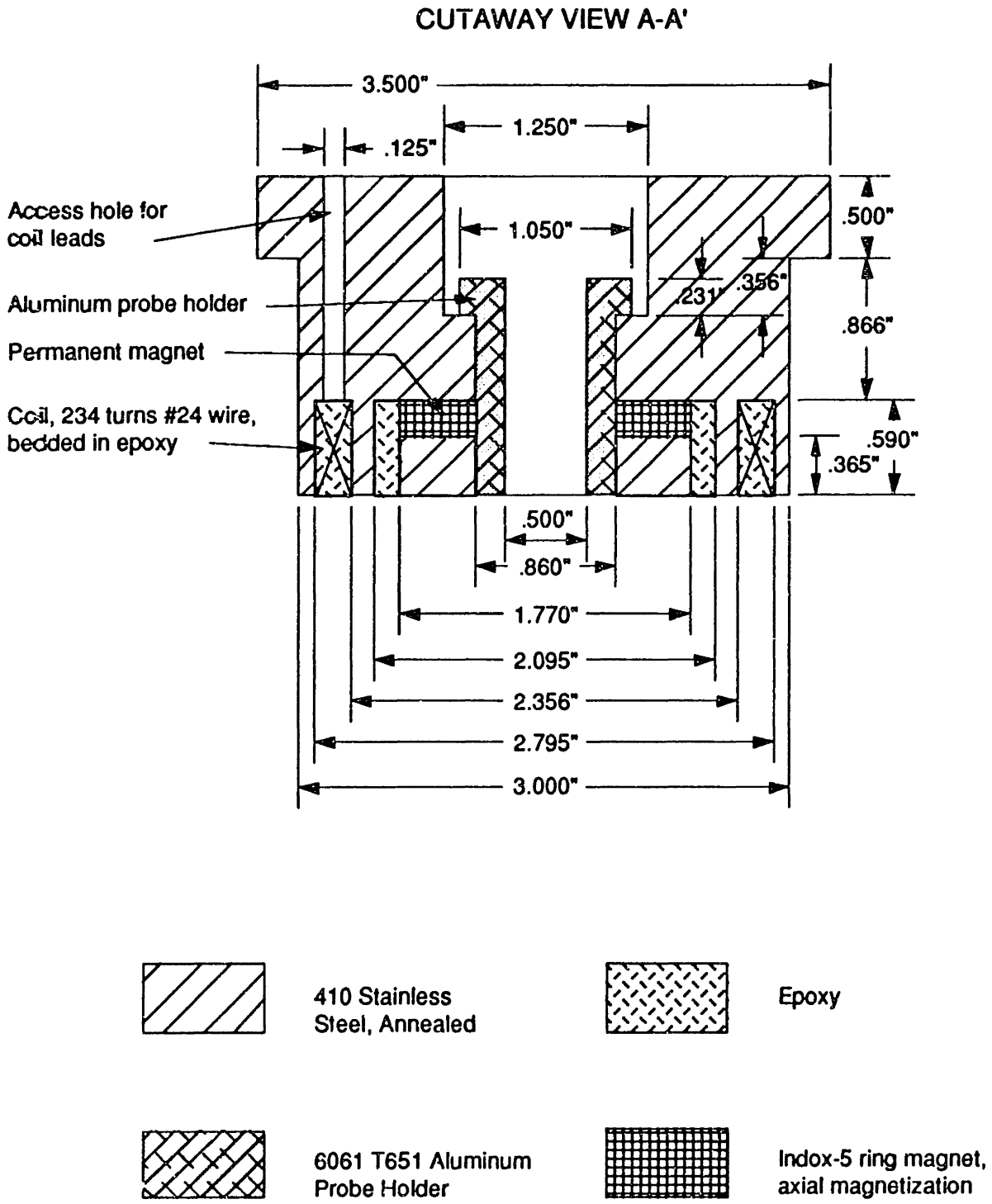

Figure 4.3: Large bearing in cross section.

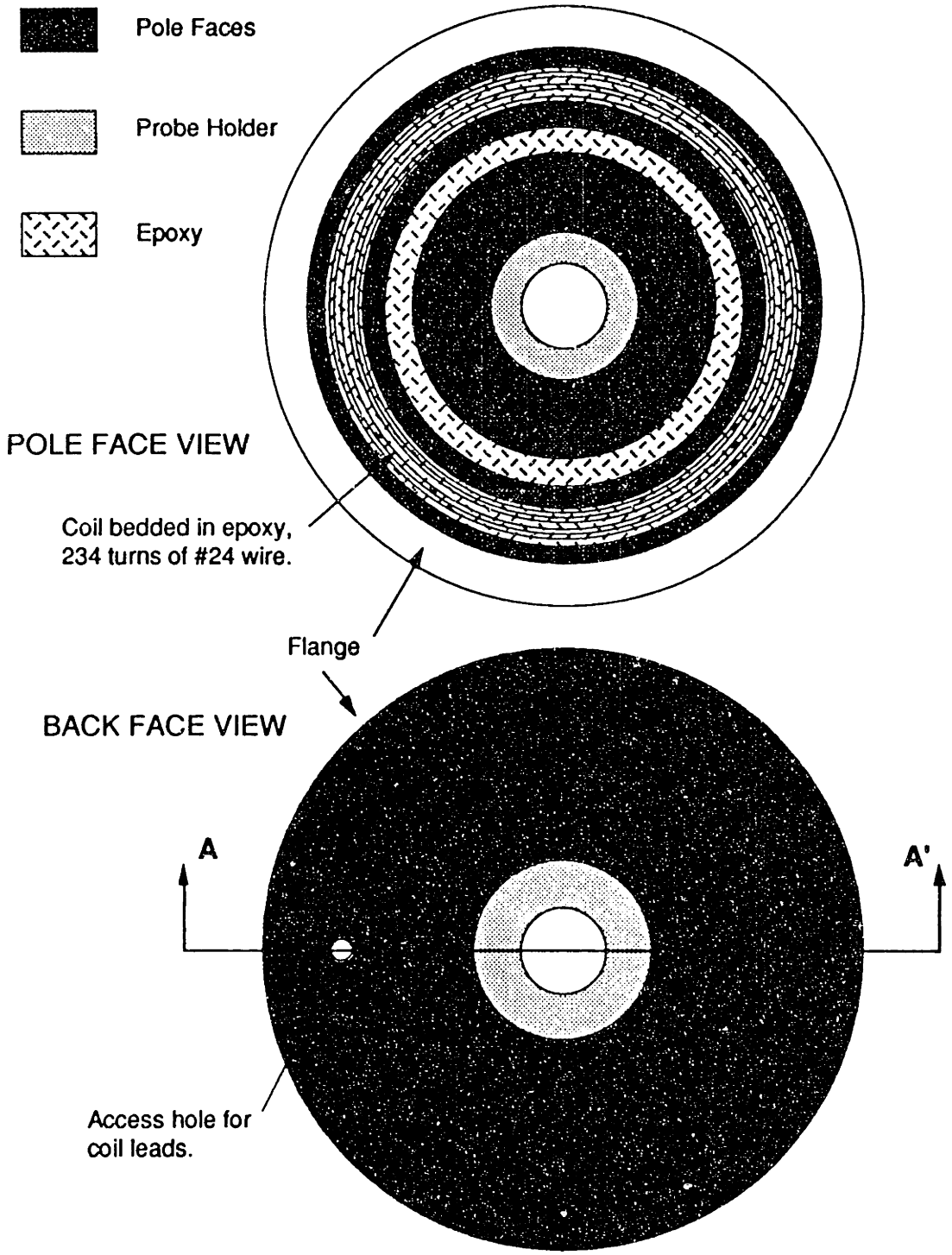

Figure 4.4: Large bearing pole-face and top views.

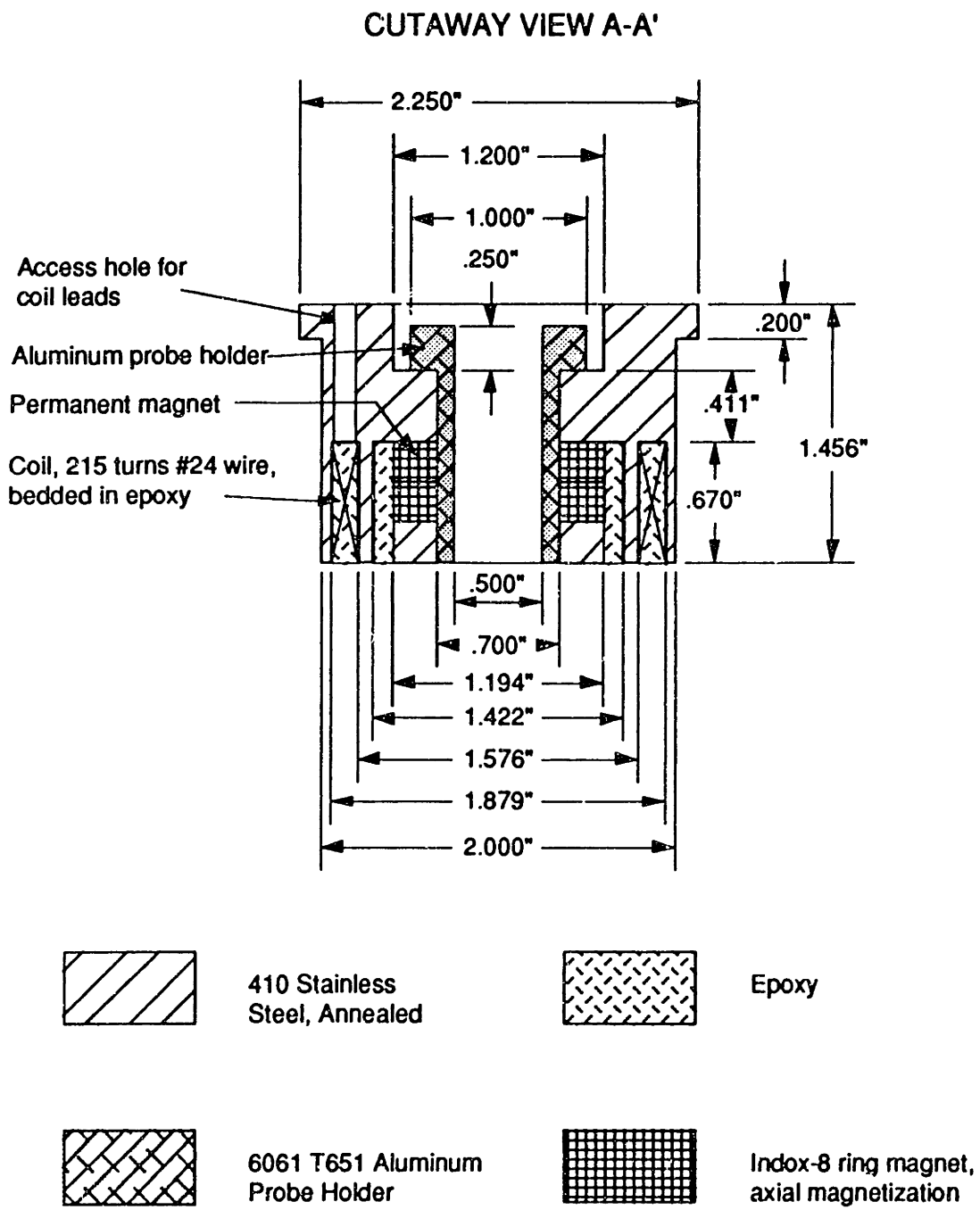

Figure 4.5: Small bearing in cross section.

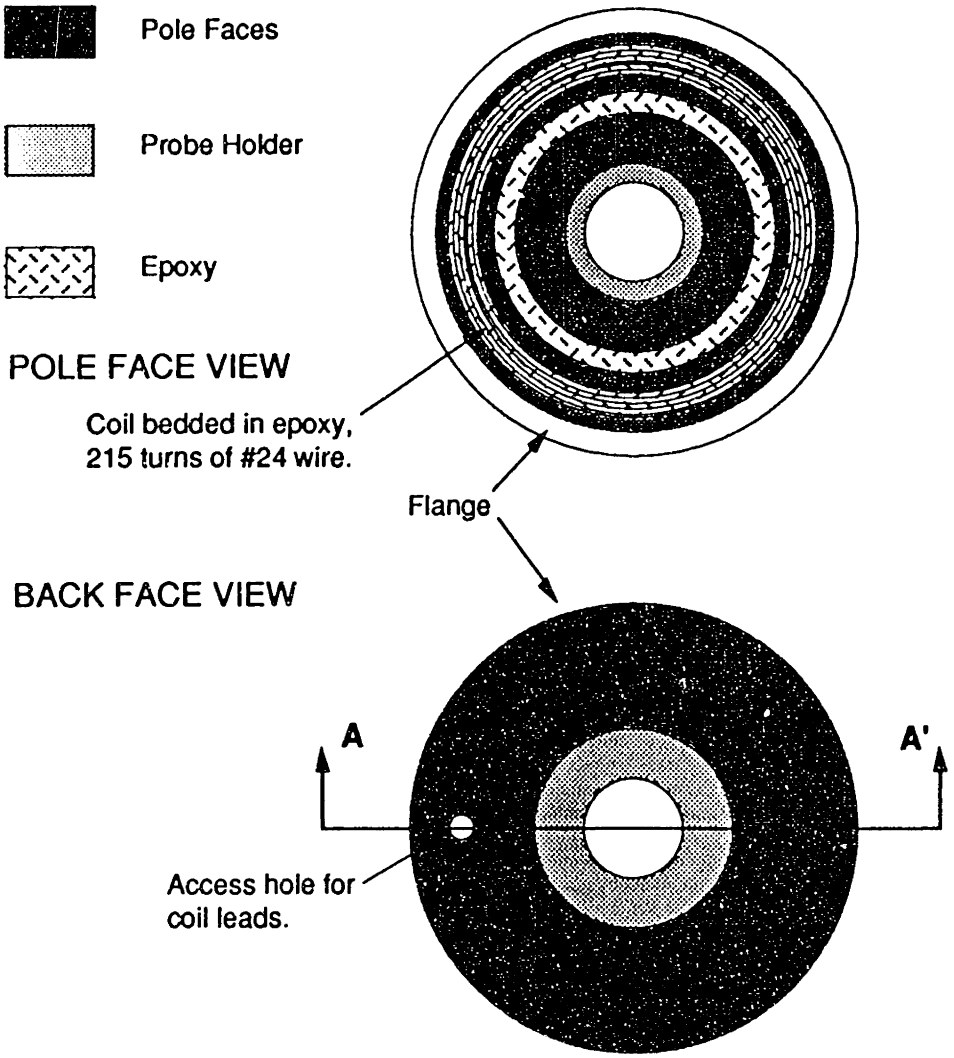

Figure 4.6: Small bearing pole-face and top views.

tenths of an inch. There are two top bearing fixtures. One supports the two small electromagnets which act on the top face of the platen; the completed assembly of the small magnets and fixture will be referred to as the small bearing assembly. This assembly is shown in detail in Figure 4.7. The other top bearing fixture supports the single large bearing; the completed assembly of the large magnet and fixture will be referred to as the large bearing assembly. It is shown in detail in Figure 4.8. The third type of bearing fixture supports a single small bearing and is used in four places acting in pairwise opposition on the sides of the platen. This assembly will be referred to as the side bearing assembly and is shown in detail in Figure 4.9.

Once the assemblies were completed and the epoxy had cured, the faces of the bearings were surface ground to the dimensions shown in the figures. This allowed a very good surface finish and tight matching of the resulting dimensions, which was especially important in order to guarantee that the bearing faces were coplanar to within a fraction of a thousandth of an inch after the system assembly was complete. After grinding, the bearing dimensions matched within .0002", as determined by using a height gauge on a surface plate. The grinding operation was done *after* the bearings were assembled into the bearing fixtures so that the bearing faces were coplanar with the opposite surfaces of the bearing fixtures. It is these surfaces, or surfaces which were accurately machined at right angles to them, which mate with the surfaces of the primary and secondary support brackets.

4.2.4 Support Brackets

The magnet assemblies bolt onto two support brackets, referred to as the primary and secondary support brackets. Each support bracket is a precision right-angle made of cast iron and surface ground to 0.0001" accuracy. These brackets were purchased commercially, and are the types which would be used in machine shop metrology departments. The primary support bracket holds the two top magnet assemblies, and two of the side magnet assemblies. The secondary support bracket holds the remaining two side bearing assemblies. In operation, the brackets are bolted down to the optical table. A sketch of the support brackets is given in Figure 4.10.

4.2.5 Position Probes

Position is measured by five position probes which operate by sensing a capacitance which varies with the spacing between the probe and platen. The five probes are inserted and glued into the central hole in the three top electromagnets and in the two primary side electromagnets. By this arrangement, motion can be

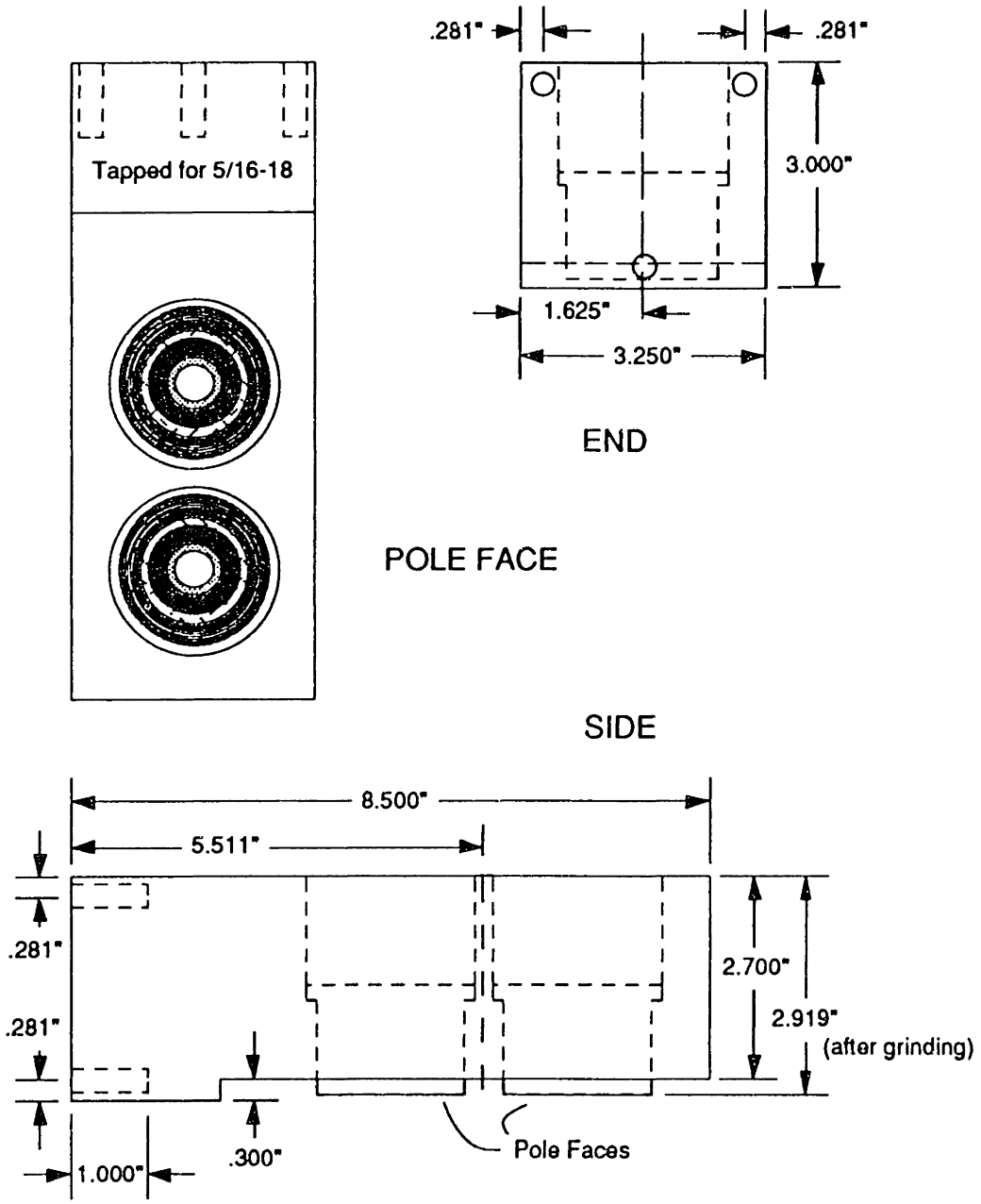

Figure 4.7: Small bearing assembly.

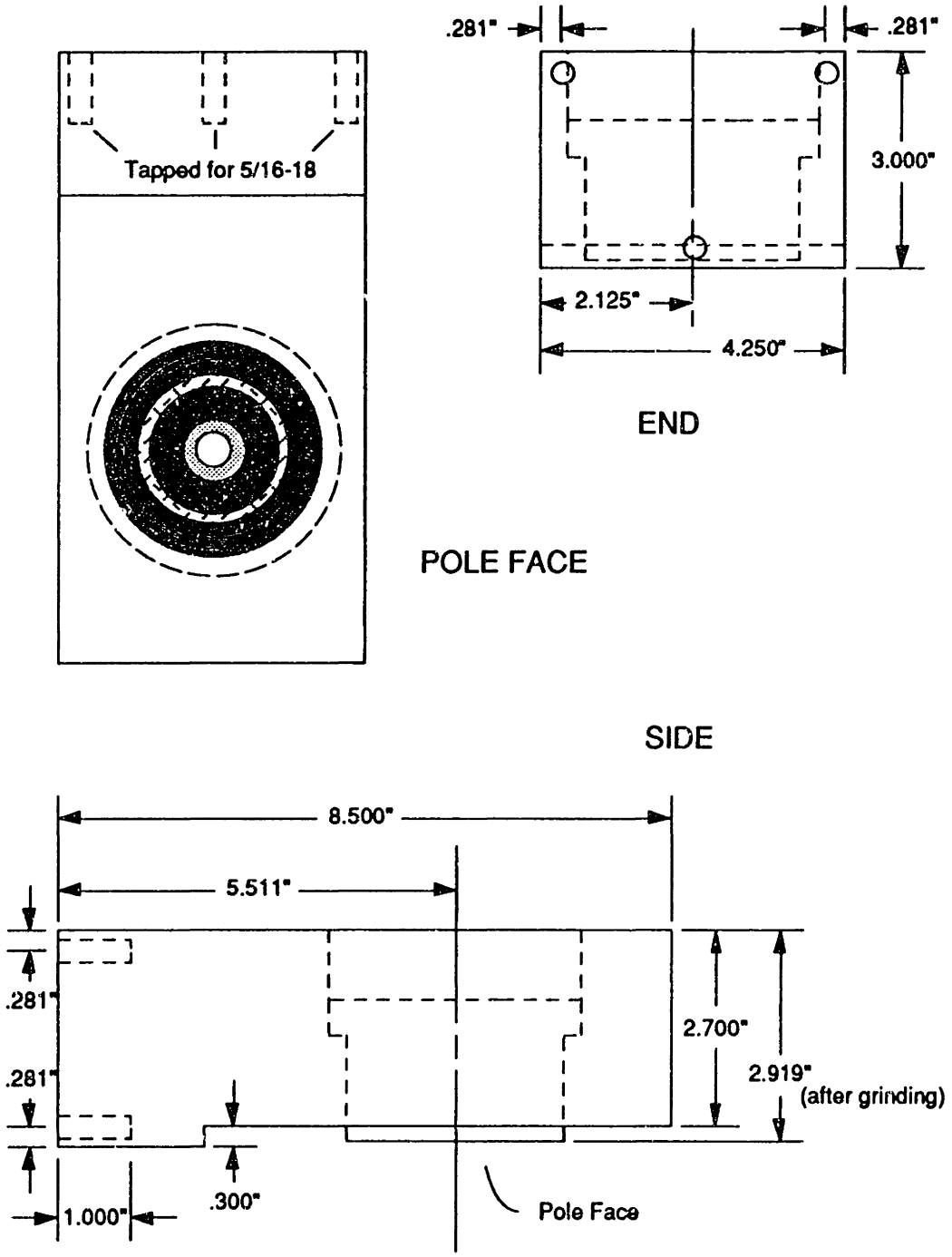

Figure 4.8: Large bearing assembly.

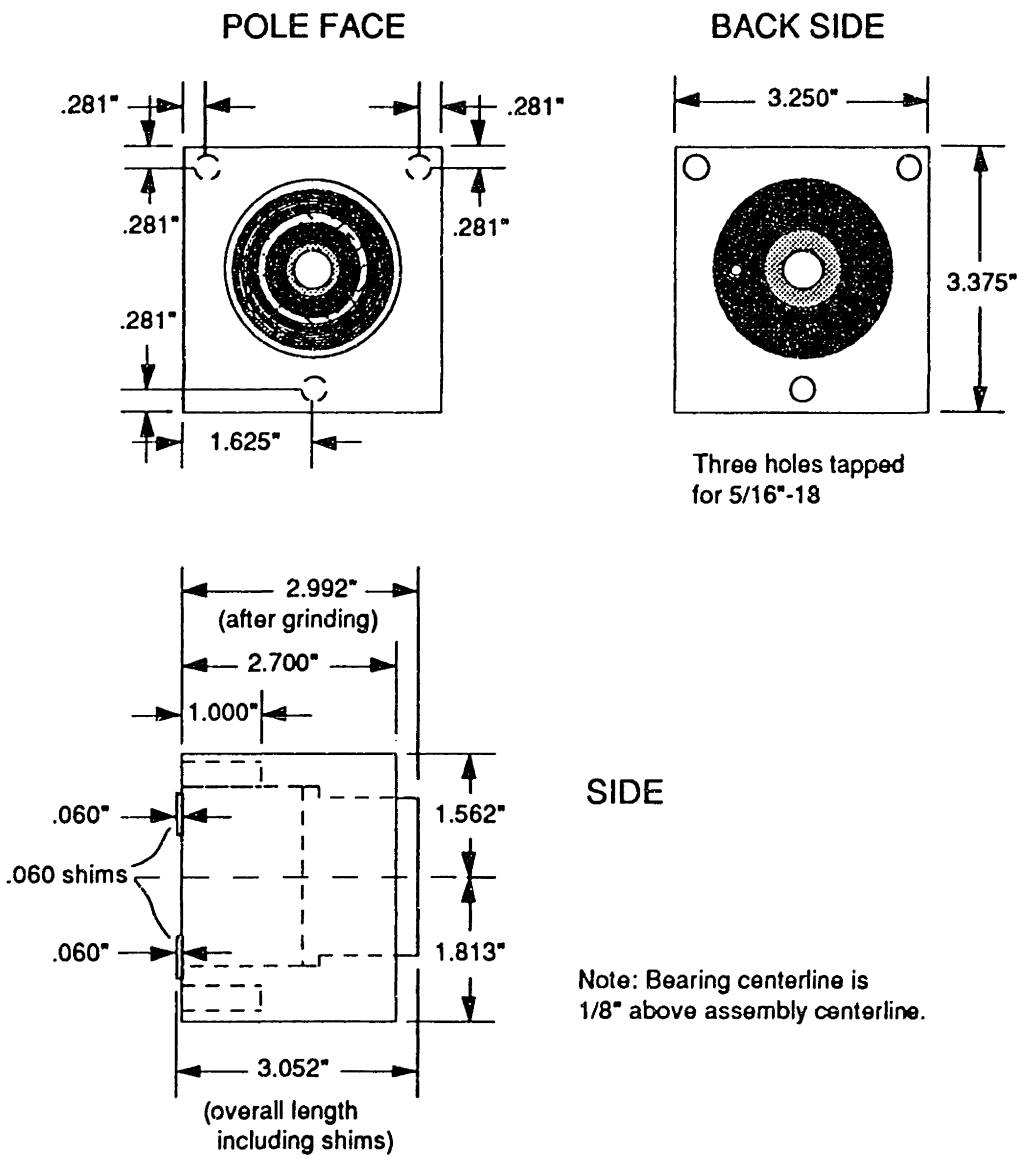

Figure 4.9: side bearing assembly.

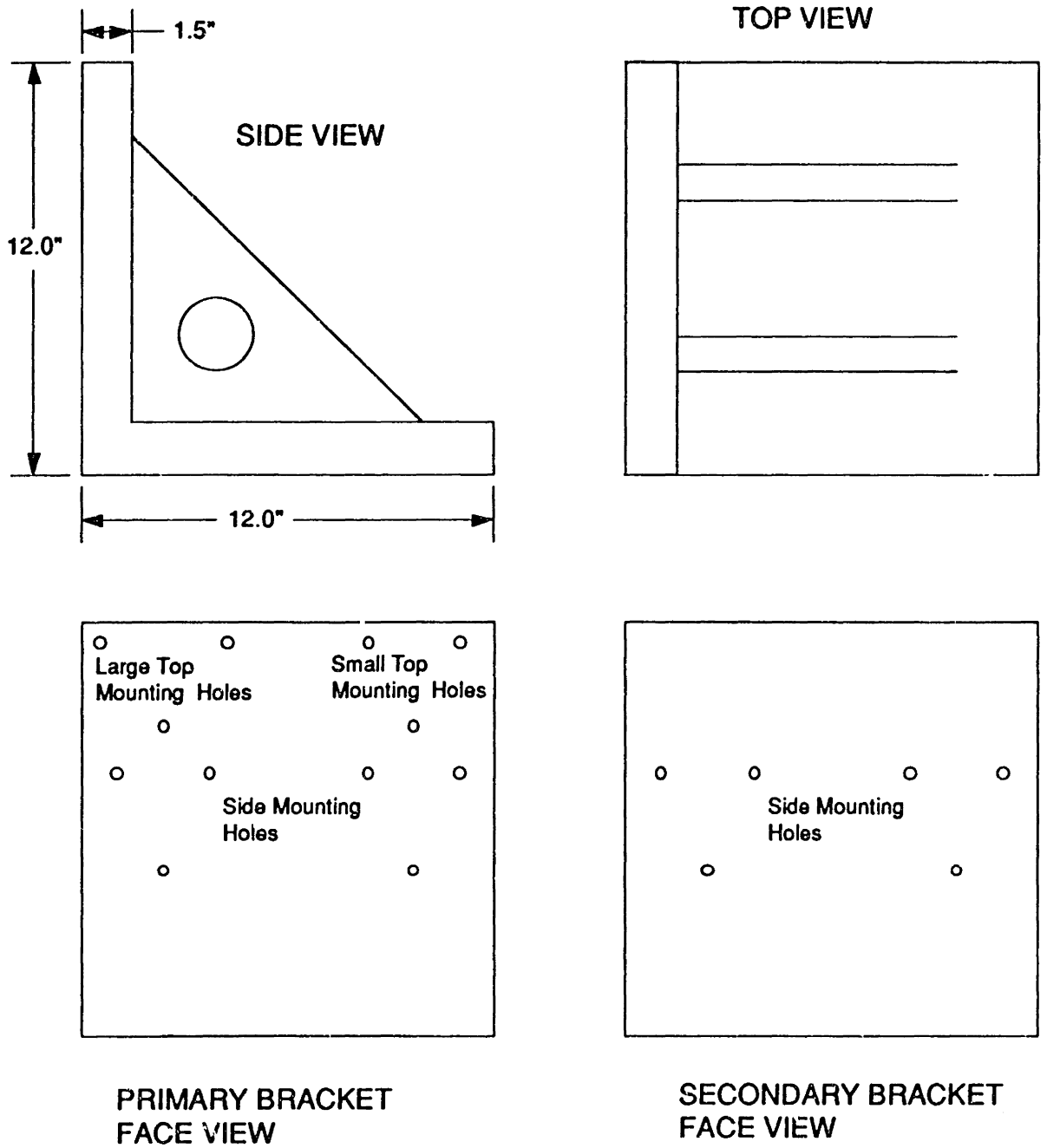

Figure 4.10: Primary and secondary support brackets.

Probe #	Crystal Freq. (MHz)	Excitation Freq. (MHz)
1	4.00	1.00
2	5.00	1.25
3	6.00	1.50
4	4.00	1.00
5	5.00	1.25

Table 4.1: Probe oscillator and excitation frequencies.

measured in the five degrees of freedom which are controlled by the electromagnets. The probes are manufactured by Pioneer Technology, Inc., of Sunnyvale, CA. They operate with an air gap of 0.005". The probes are driven by electronics which produce an output voltage of 5 volts per 0.001" of motion over a travel of ±0.0025". Their specified accuracy is ±0.2% of full scale with a linearity of 0.1% of full scale, and a bandwidth of 10 kHz. A drawing of one of the probes is given in Figure 4.11. Details of how the probes are glued into the electromagnets are given in Section 6.2.2.

The electronics for all five probes is contained in a single chassis, and consists of a card cage containing individual circuit boards connected to each probe. Each circuit board uses a local quartz crystal oscillator to set the frequency of probe excitation. Unfortunately, only three separate frequencies are used for the five probe boards. This leads to significant beat frequency noise between the probes which are operated at the same nominal frequency. This problem is described in more detail below.

The crystal oscillator is divided down by a factor of 4 to give the probe excitation frequency. The crystal frequencies and excitation frequencies for the five probes are summarized in Table 4.1.

Probes pairs #1 — #4 and #2 — #5 interact with a low frequency beat signal because they are operating on independent but nearly identical frequencies. The beat signal is at about 10 Hz with an amplitude on the order of tenths of a volt. The existence of this beat signal means that the true position stability capabilities of the suspension can not be demonstrated when all five of the probes are in use. They can be demonstrated if some of the probes are disabled; for instance if #4 and #5 are turned off, then the three top electromagnets can be used to stabilize the system in the vertical degrees of freedom, and with low noise contribution from the probes.

This is the approach which has been taken in this thesis. The system positioning noise baseline is demonstrated using only the vertical system operating on the first three probes alone. When all five degrees of freedom are controlled,

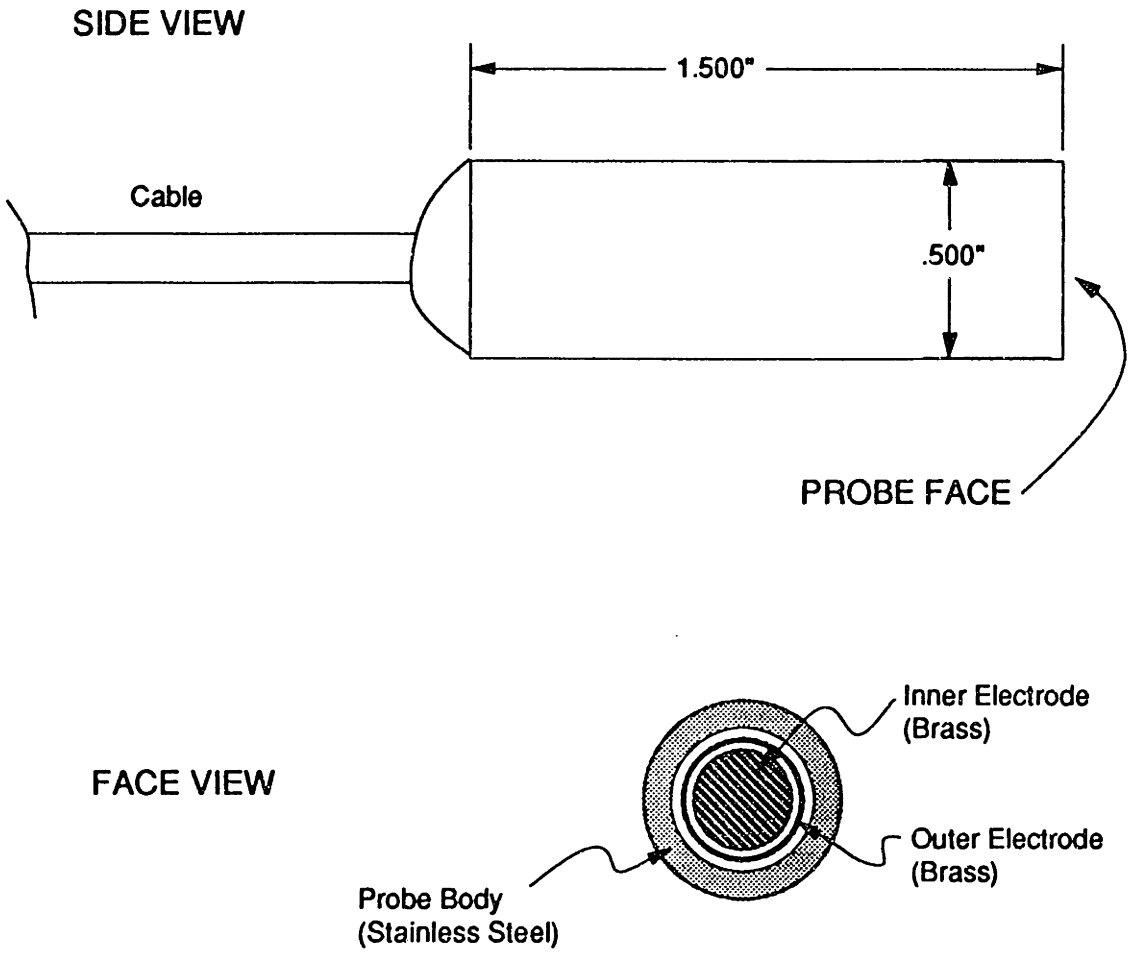

Figure 4.11: Position probe.

there is significant noise; however, the system step responses can be characterized through averaging on a digital oscilloscope, and the system frequency resonses can be measured using a dynamic analyzer since this instrument is inherently narrow-band.

An alternate approach which is clearly more desirable in the long-term is to change the probe operating frequencies so that they run on five independent frequencies. For instance, using crystals at 4.5 and 5.5 MHz to drive probes #4 and #5 will eliminate any low-frequency beat tones.

The option described above was considered. However, such crystals are non-standard items, and all manufacturers which were contacted required a minimum order of about 100 units at each non-standard frequency. Additionally, changing frequencies requires retuning and recalibration of the probe electronics. This requires fixtures capable of accurately adjusting the probe air-gap over the probe operating range with better than 0.1 μm resolution. Such a fixture is available at the manufacturer, however at the time when this problem was discovered, the probes were already permanently installed into the electromagnets. For this reason, this option was not pursued, and the choice was made to live with the noise problem, as all essential operational performance levels can still be characterized, in the manner described above.

The beat-tone noise problem is documented in Figures 4.12, 4.13 and 4.14. With all probes except #4 connected, the output voltage of probe #1 is shown in Figure 4.12 to be on the order of 1 mV peak to peak. (This and all other probe voltage traces have been filtered to a 1 kHz bandwidth with a first order filter.) Applying the probe gain factor, 1mV of noise is approximately equivalent to 5 nm of position noise, so with no beat-interference the probes may be considered accurate to the 5 nm level. This is comparable to the resolution levels attainable via off-the-shelf interferometric position transducers, such as are available from Hewlett-Packard Co.

Reconnecting probe #4 results in the 130 mV p-p sinusoid at about 8 Hz shown in Figure 4.13. The behavior of the other interfering pair of probes is similar. With all five probes connected, and facing a stationary platen, the probe voltages are as shown in Table 4.2.

This noise can be reduced somewhat by connecting a ground lead to the platen. With ground lead attached, the noises are reduced to the level shown in Table 4.3. In all cases, the noise voltage of probe #3 is less than 0.5 mV. This is because there are no other probes operating near its frequency.

If only the top three probes are used, then all three have output noise voltages on the order of 1 mV p-p as shown in Figure 4.14. This establishes a noise baseline for the three top electromagets used alone. This noise baseline will be referred to in later experiments.

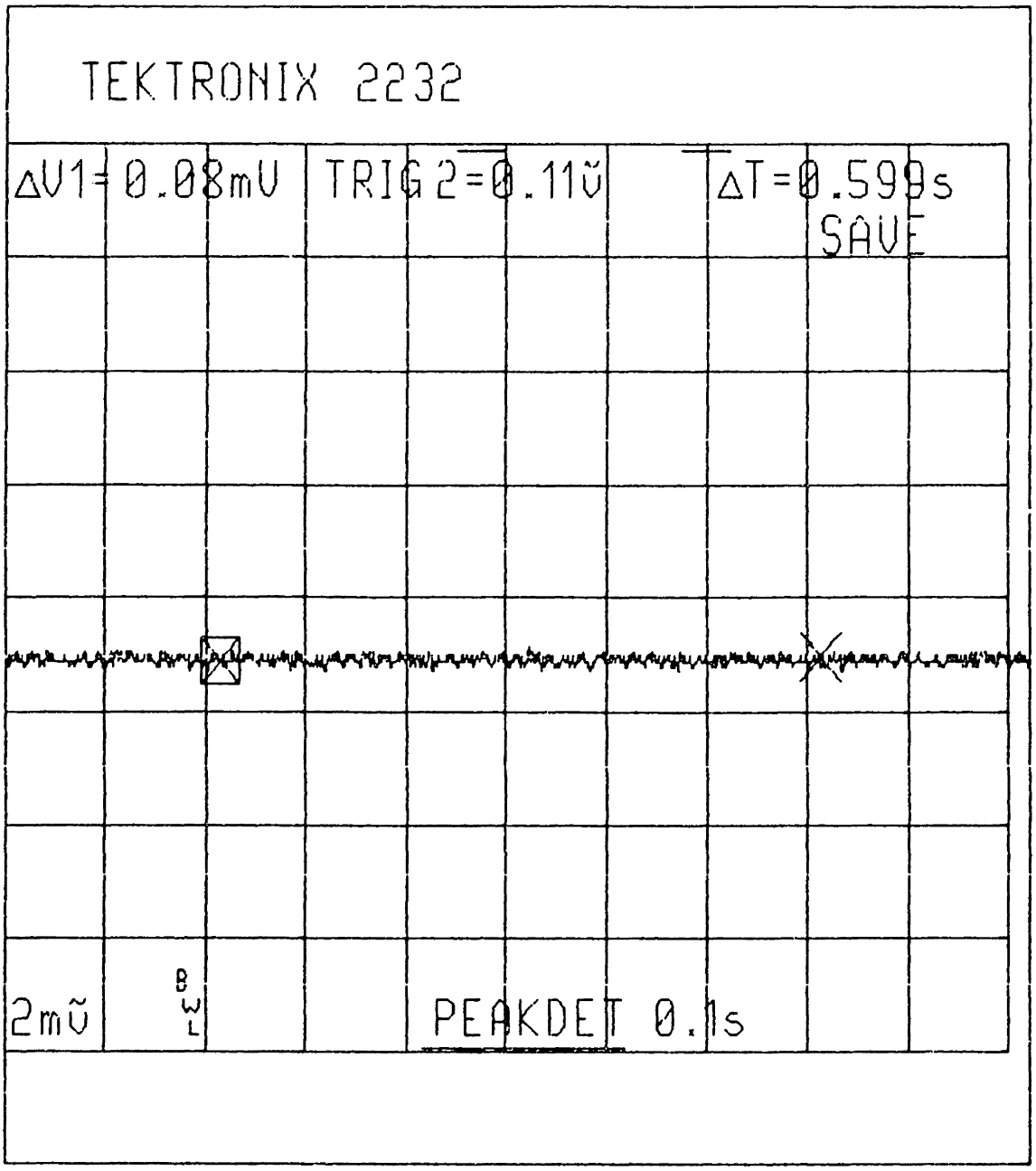

Figure 4.12: Probe #1 baseline noise with all probes *except* #4 connected.

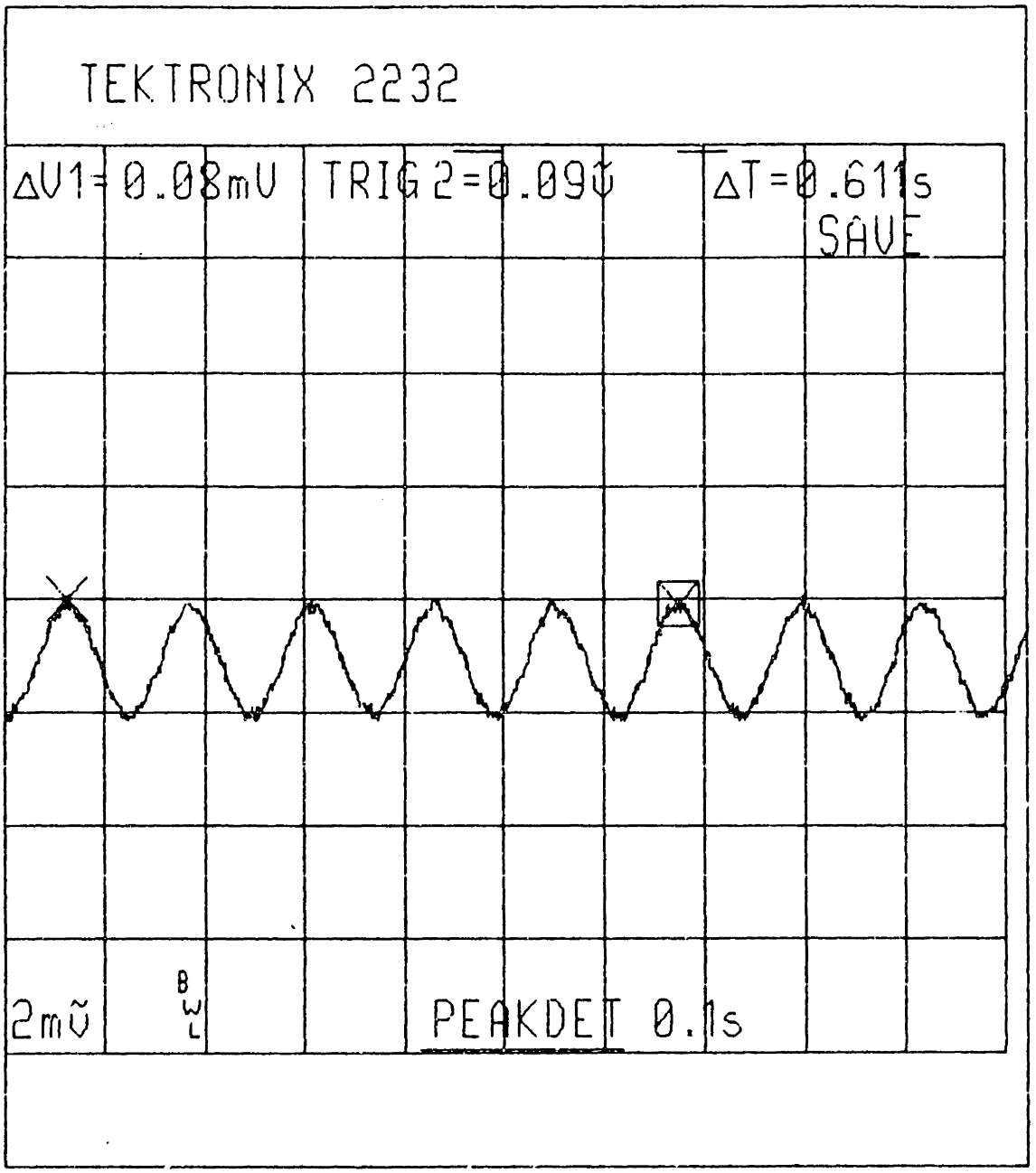

Figure 4.13: Probe #1 baseline noise with all probes *including* #4 connected.

Probe #	Beat-tone noise (millivolts p-p)
1	130
2	300
3	0.4
4	400
5	150

Table 4.2: Probe peak-to-peak beat-tone noise with all five probes connected.

Probe #	Beat-tone noise (millivolts p-p)
1	4
2	30
3	0.4
4	120
5	15

Table 4.3: Probe peak-to-peak beat-tone noise with all five probes connected and a ground lead attached to the platen.

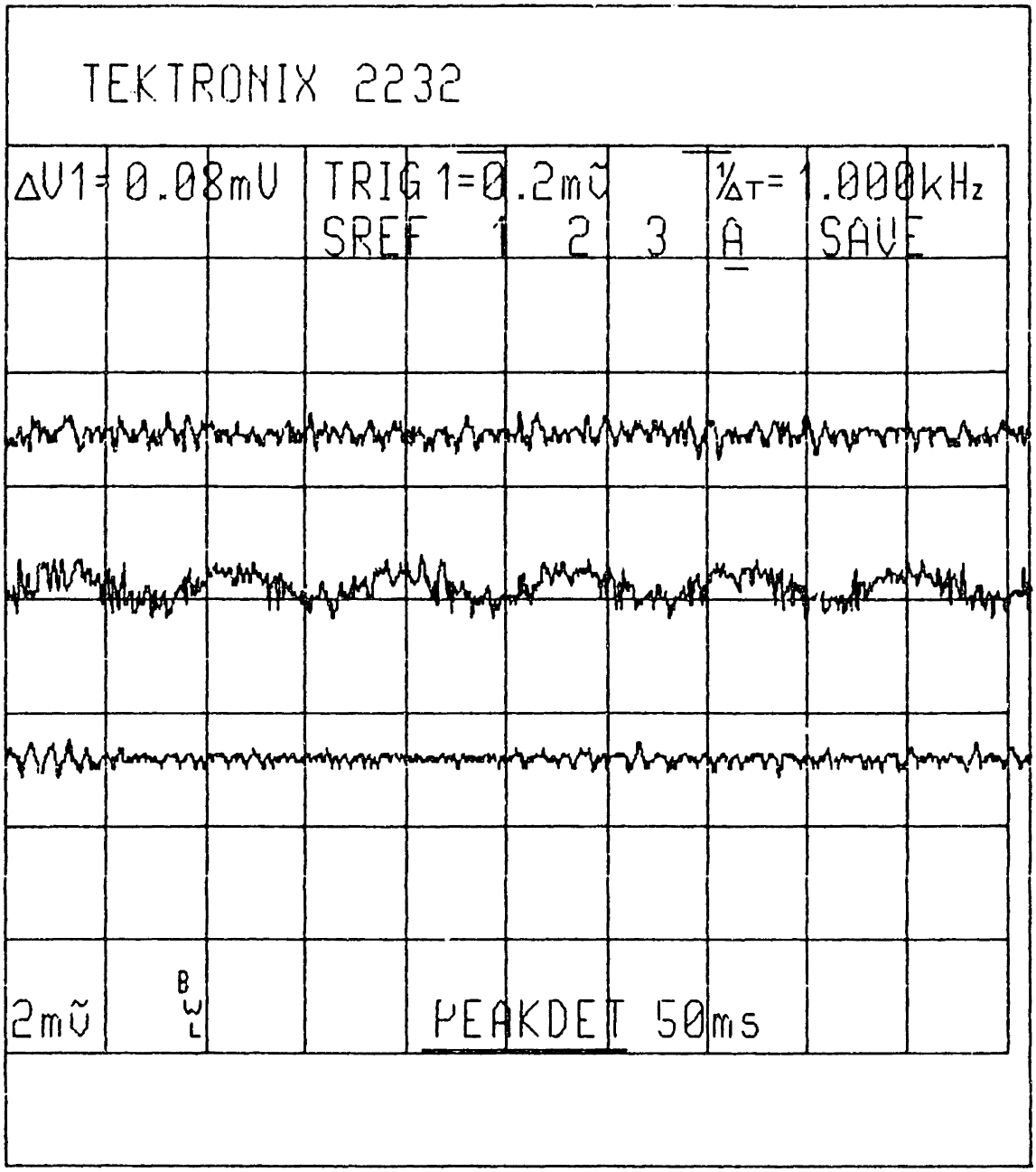

Figure 4.14: Baseline noise of probes #1, #2, and #3 with probes #4 and #5 disconnected.

4.2.6 Landing Pad

A three-legged aluminum table referred to as the landing pad is used to support the log from below when it is released from the suspension magnets. The table is surfaced with .25" thick bakelite in order to reduce sliding friction when manually positioning the platen when it is out of suspension, and to prevent scratching of the platen. When in suspension, the lower surface of the platen clears the landing pad by a distance of about 0.04", and drops this distance onto the landing pad when the suspension is turned off. In practice, I have placed two plastic sheets of about 0.015" thickness on the surface of the table so that the log sets down more softly than in the case where the bare bakelite is used. A sketch of the landing pad is given in Figure 4.15.

4.2.7 Assembled System

The above discussion describes the suspension system design as it existed at the time I joined the project. Several of the constructed pieces had been designed with improper dimensions, which resulted in pole faces misaligned by several millimeters. These defects were corrected by remachining or through the design of spacers and shims under my direction. The system was also designed under the assumption that the log measured 5.000" in width and height. This was its unmachined nominal dimension, however after surface grinding and nickel plating, it measured the 4.907" shown in Figure 4.2. This resulted in the center line of the platen not lining up with the center line of the electromagnets. Such a misalignment is not acceptable since it results in undesired coupling terms in the magnet to platen force relationships. Also, the system was designed under the assumption that the magnets would operate with an 0.015" air gap. However, the probes which were bought required operation at an 0.005" standoff.

In order to resolve these problems, I decided to run the magnets at an air gap of 0.005", so that the probes could be mounted with their face flush with the pole face of the electromagnet in which they were imbedded. Flush mounting in this manner protects the probes from impact when the platen crashes into the electromagnet, which is certain to happen in the event of control loop instabilities or a large disturbance. In order to correct the centerline problems, the top three magnets were shimmed back within their fixtures by an appropriate amount before gluing them into the fixtures, and the primary side magnet assemblies were shimmed away from the primary holding bracket by an 0.060" brass shim. The air-gap spacing of the secondary side magnets can be varied by simply sliding the secondary support bracket along the optical table surface, thus no spacers were required on the secondary side magnets.

Following these design alterations the assembled system appears as shown in

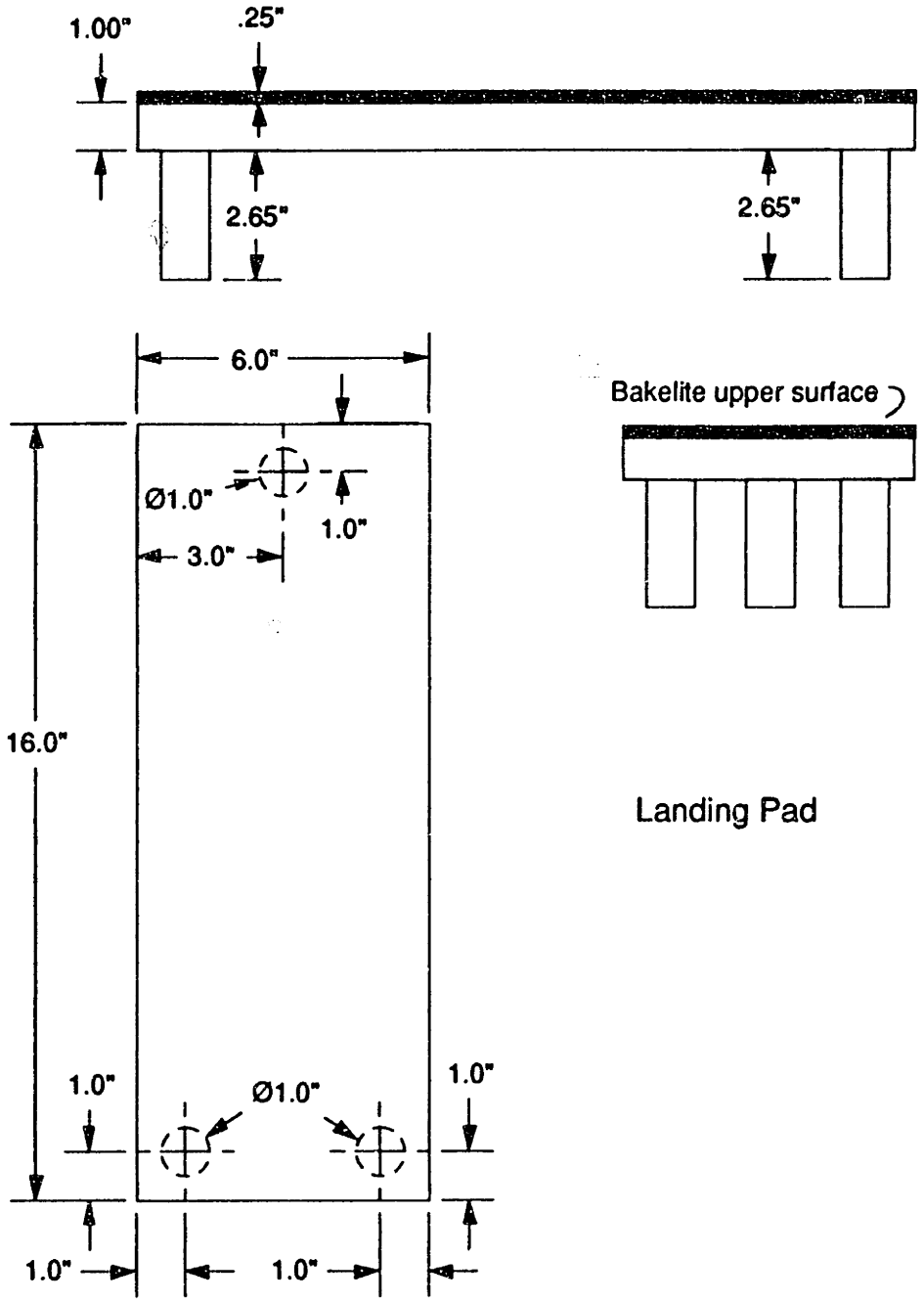

Figure 4.15: Landing pad.

the mechanical drawings of Figures 4.16, 4.17, and 4.18. The details of the actual assembly are described in Section 6. The 0.005" air gap is too small to be seen in these views. The 0.060" shims on the primary side bearings are visible at this scale. The electromagnet centerlines intersect with the log centerline as shown in the end views.

Photographs of the assembled system are shown in Figures 4.19, 4.20, 4.21, and 4.22. Figure 4.19 shows the linear bearing system (ARMM) as viewed from the large bearing end. The control electronics are in the foreground. The capacitance probe electronics, magnet current drives, and power supplies are located in a rack to the left of the field of view. Figure 4.20 shows the linear bearing system as viewed from the small bearing end. The massive support brackets are clearly visible on both sides of the system. Figure 4.21 shows the linear bearing system as viewed from the top. In Figure 4.22 the platen has been removed to show a wide-angle view looking through the space occupied by the platen. The three top electromagnets and the four side electromagnets are visible. The faces of the capacitance probes can be seen in the center of the three top electromagnets and in the center of two of the side electromagnets. The centers of the remaining two side electromagnets are empty. The clamps which hold the side balancing magnets described in section 6.10.3 can be seen on the near left electromagnet and the far right electromagnet.

Photographs which show the platen in suspension are given in Figures 4.23 and 4.24. In Figure 4.23, the platen is shown in suspension. The air gap (0.005") on the left side between the side magnets and the platen is visible as is the much larger air gap underneath the platen. Figure 4.24 is a time exposure which shows the platen motion in its long axis of travel.

4.3 Modifications to ARMM Design

I made a number of additional modifications to the original hardware design, in order to improve system performance. These are described in detail in this section.

4.3.1 Permanent Magnets

After considering the control issues and physics involved in the suspension, it became apparent that the inclusion of permanent magnets into the bearing assemblies is disadvantageous. The original reasoning was that a significant fraction of the platen weight would be supported by the permanent magnets in the three top electromagnets, in order to reduce the power requirements of the suspension. Permanent magnets were included in the side electromagnets as well under

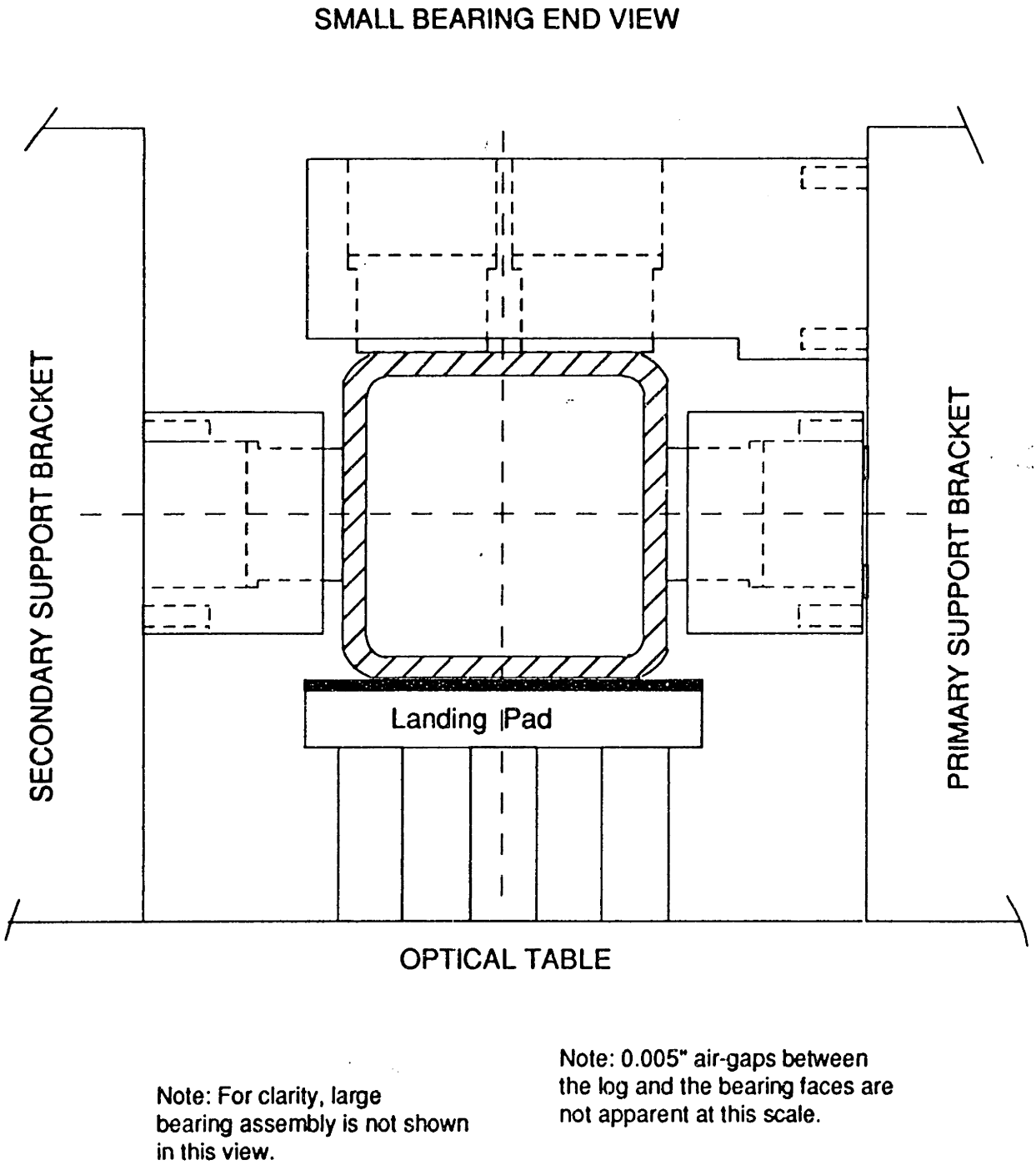

Figure 4.16: Small bearing end view.

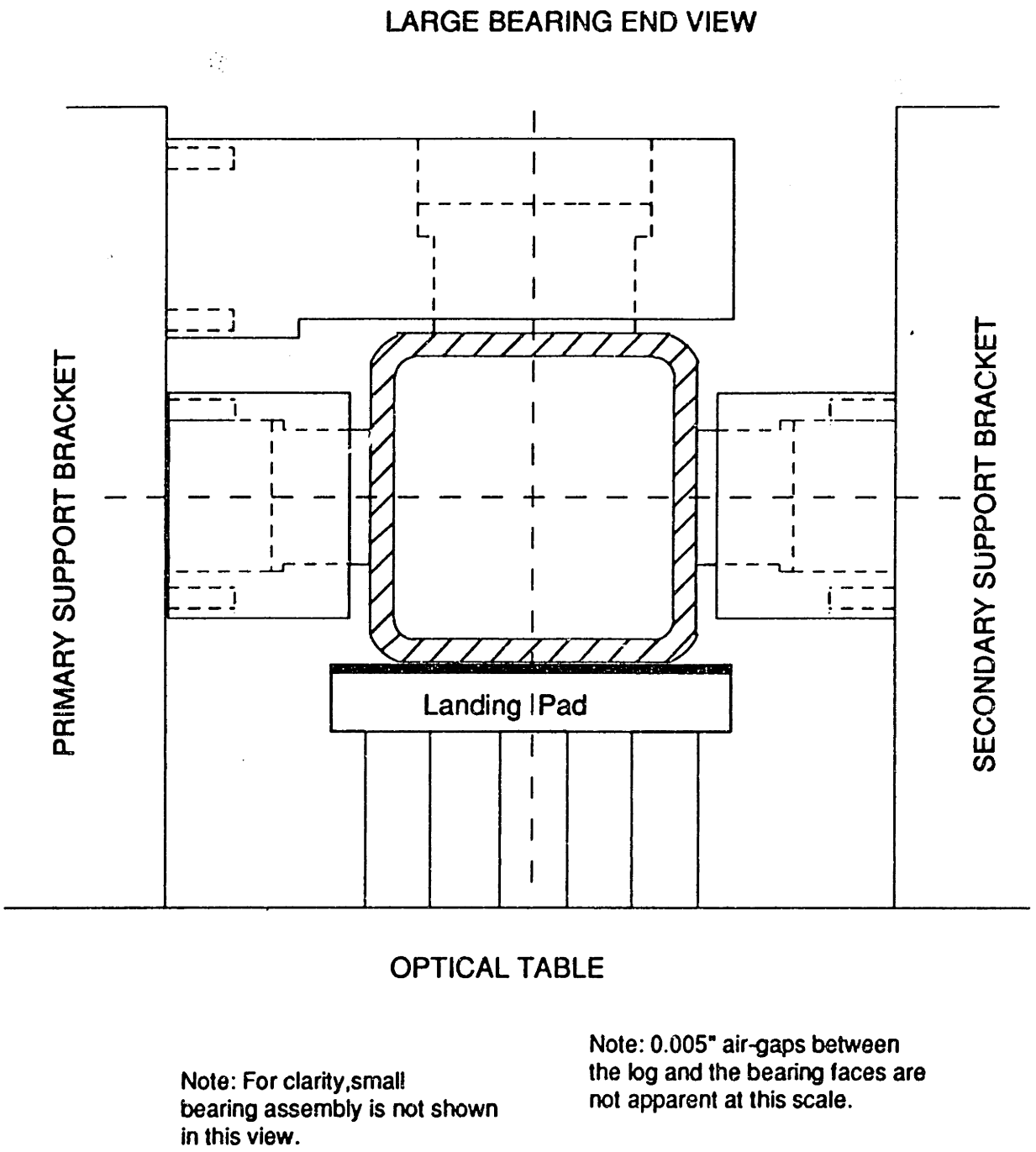

Figure 4.17: Large bearing end view.

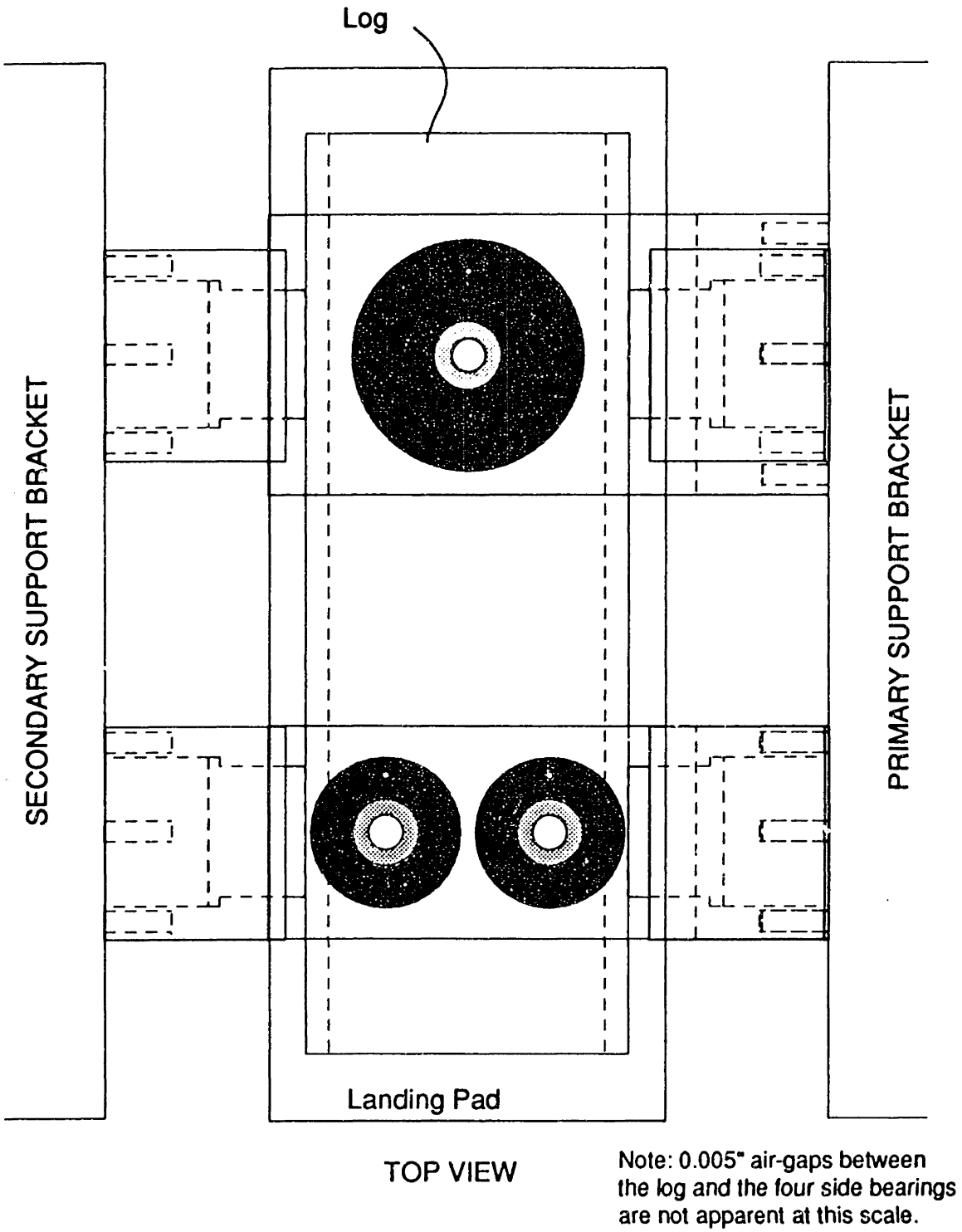

Figure 4.18: System top view.

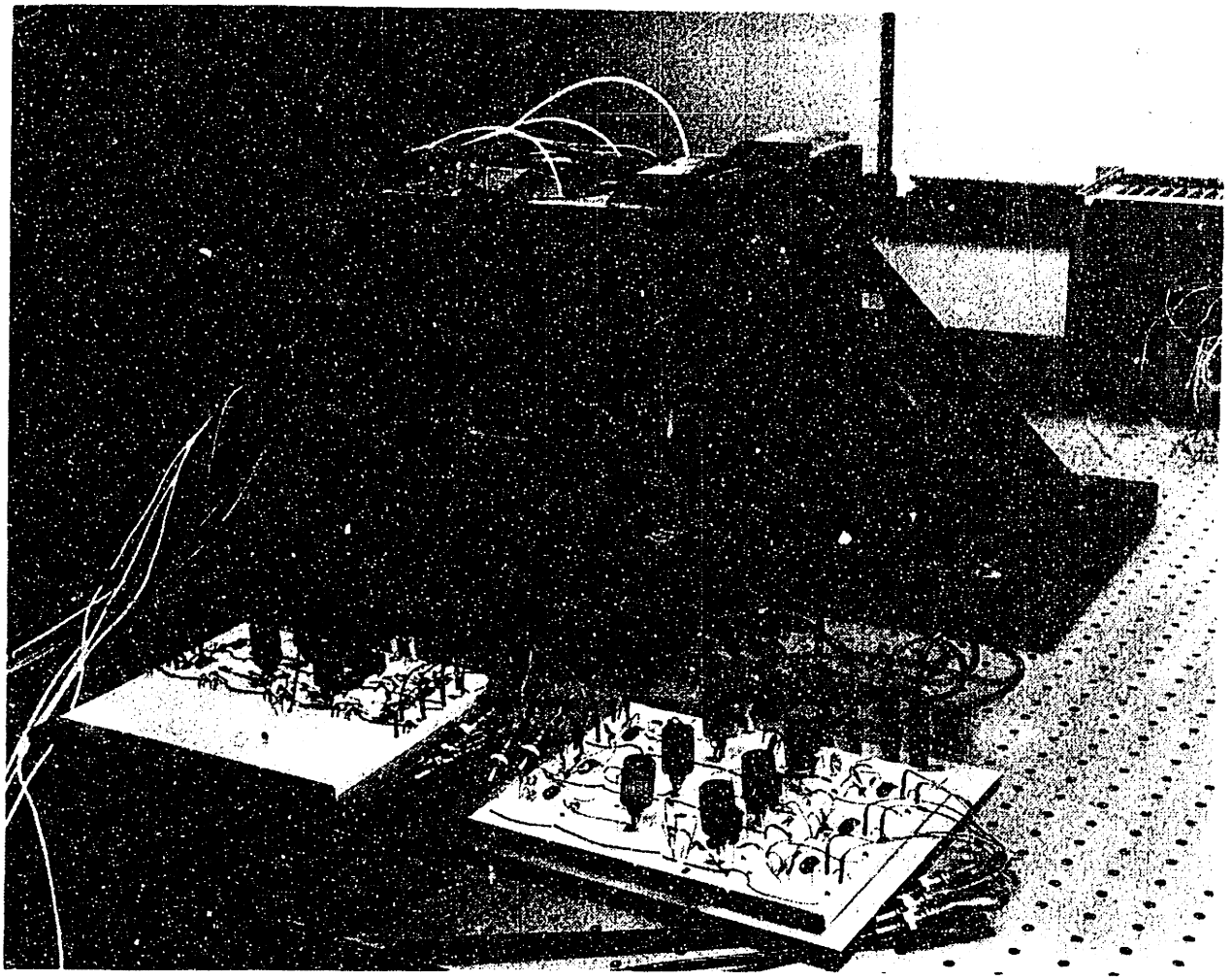

Figure 4.19: Photograph of the linear bearing system (ARMM) as viewed from the large bearing end. The control electronics are in the foreground.

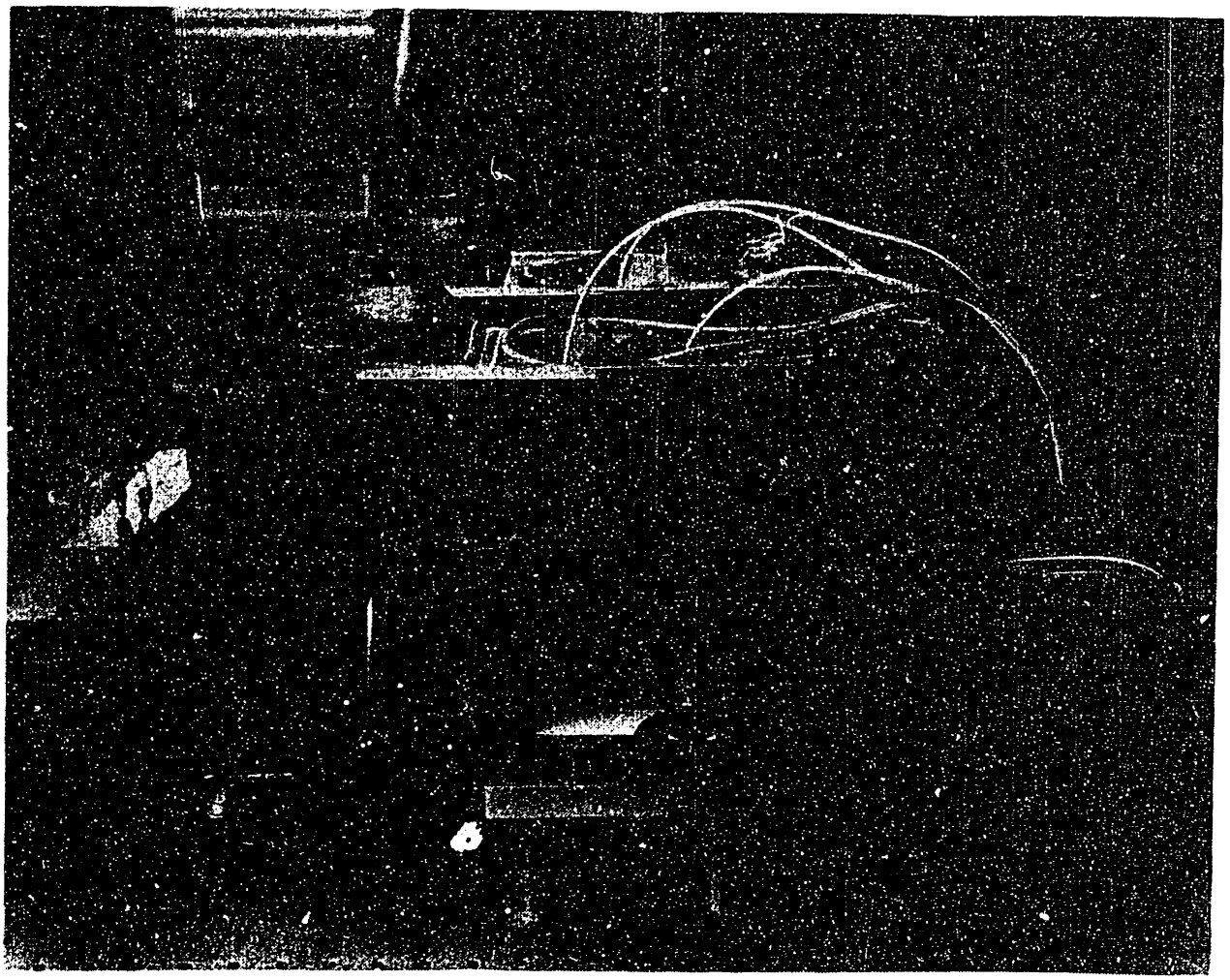

Figure 4.20: Photograph of the linear bearing system (ARMM) as viewed from the small bearing end. The white wires at the top of the assembly are connected to the capacitance probes installed in the center of the top electromagnets. The damping weight described in section 6.7.2 is visible in the lower right-hand corner of the platen interior.

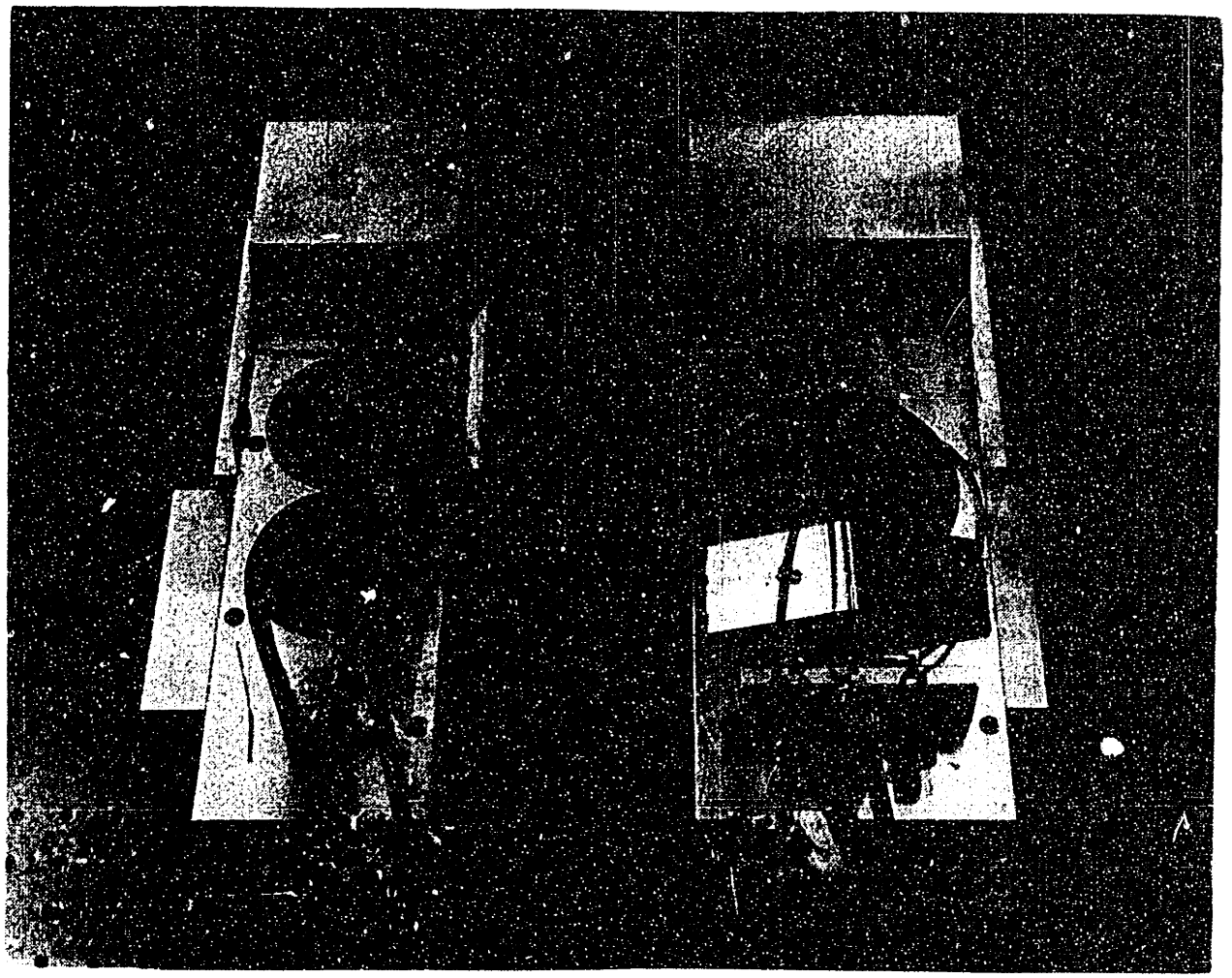

Figure 4.21: Photograph of the linear bearing system (ARMM) as viewed from the top. The back sides of the top three capacitance probes and electromagnets installed in the light-colored magnet assemblies are visible. The platen can be seen underneath and perpendicular to the top magnet assemblies. The blocks used to eliminate resonances in the top magnet assemblies are visible at the top of this view. These blocks are described in section 6.11.

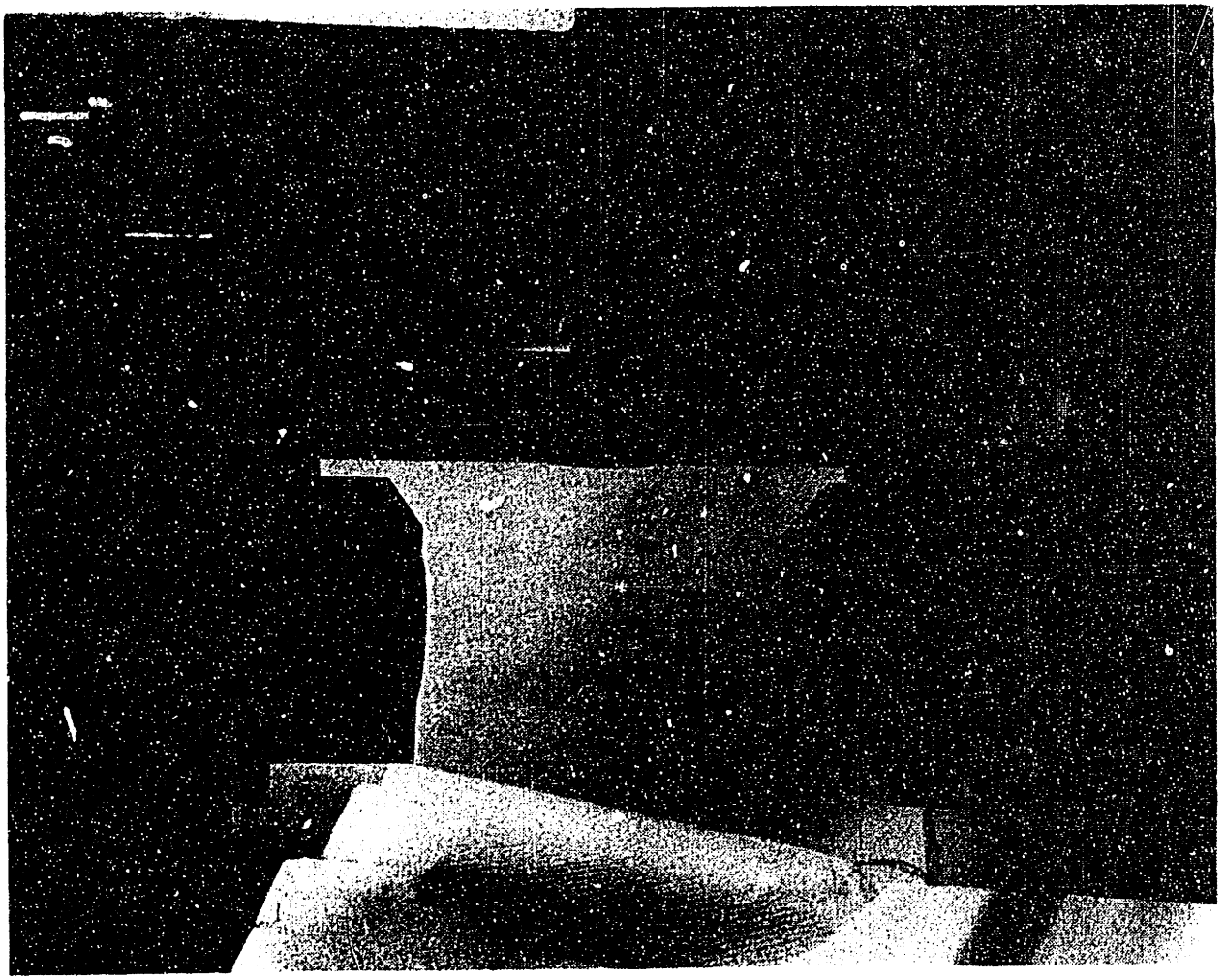

Figure 4.22: Photograph of the linear bearing system (ARMM) as viewed through the space occupied by the platen.

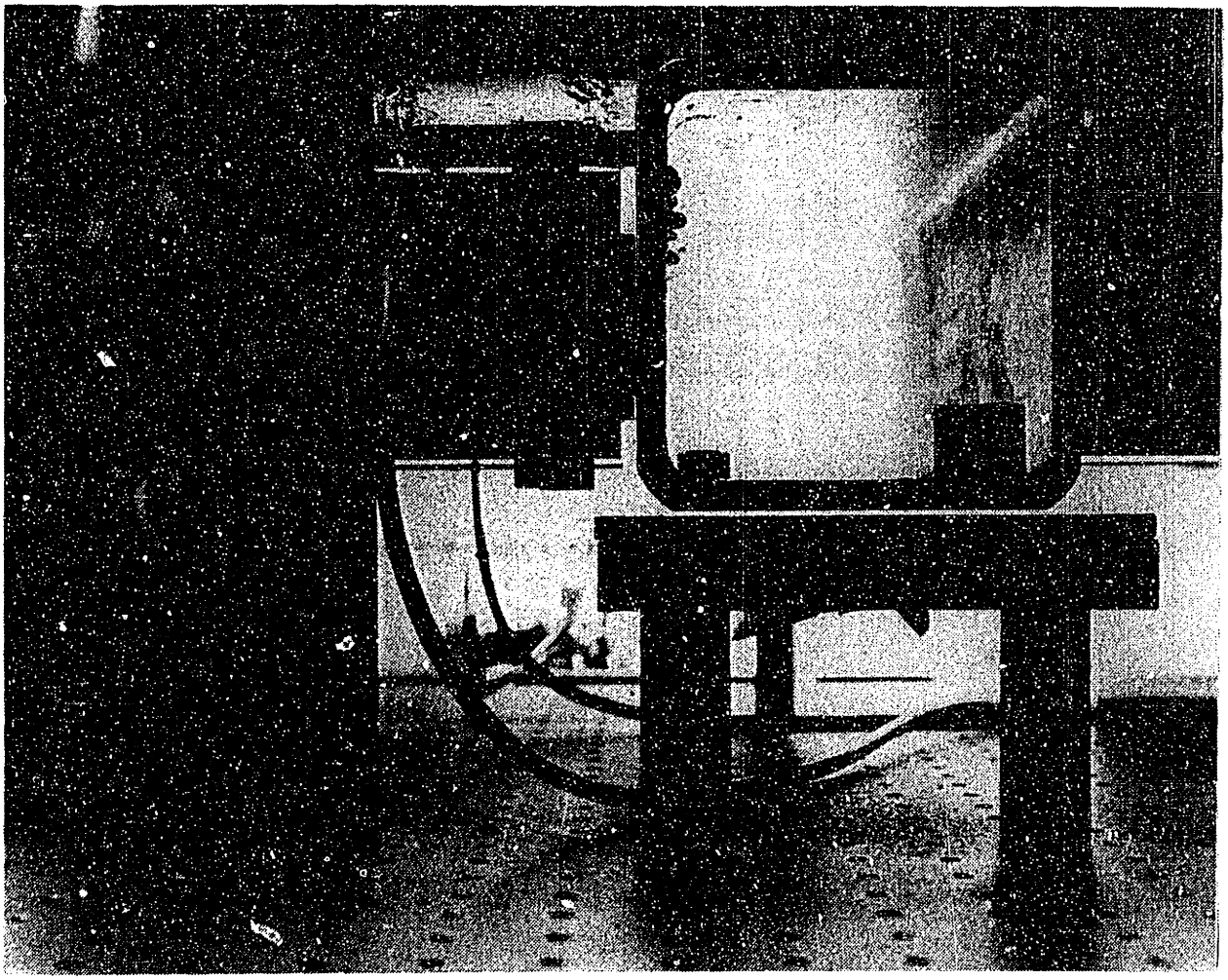

Figure 4.23: Photograph of the linear bearing system with the platen suspended. Large air gap (0.05") below platen and thin (0.005") air gap on left side bearings are visible.

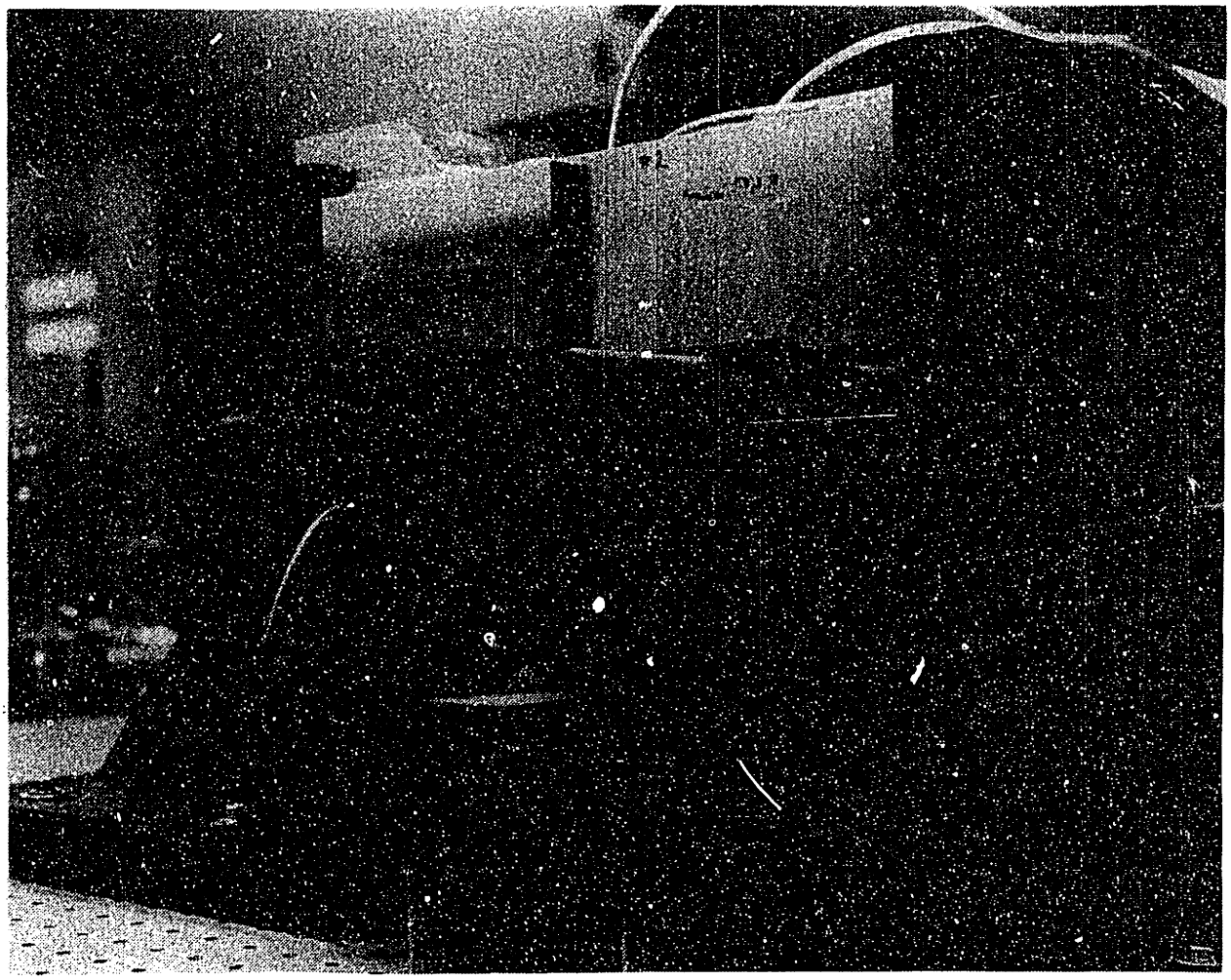

Figure 4.24: Time exposure showing platen linear motion.

the assumption that since they were arranged in pairwise opposition, the effects of the permanent magnets would cancel, and it was more convenient to make all six of the small electromagnets identical. Both of these original ideas are in error. The only electromagnets capable of controlling vertical motions of the platen are located on top of the platen. These electromagnets act on the platen as variable-reluctance devices and thus are only capable of applying attractive forces to the platen. Gravity acting on the platen is the only source of force in the downward direction. Thus, adding permanent magnets to the support electromagnets reduces the magnitude of the net force which can be applied to the platen in the downward direction to the portion of the gravity force acting on the platen which is *not* supported by the permanent magnets. In the extreme case where the permanent magnets carry all of the gravity load, it is not possible to apply any downward force, and the platen can not be controlled. Using any permanent magnets in this manner thus limits the magnitude of the disturbances which can be tolerated without saturating the actuators at the zero current limit. In an open-loop unstable system such as this one, any such saturation typically results in loss of the suspension stability, and consequent crashing into whatever mechanical limit stops are present. Whether the system can recover into active suspension again depends on details of the mechanics, sensors and controller. In the current case, the loss of control is permanent and following such a disturbance the suspension must be reinitialized.

The inclusion of permanent magnets into the side magnet assemblies is also a problem. The pairwise magnet forces do indeed cancel at the intended operating point, and thus an equilibrium exists there. However, this equilibrium point is unstable, and the strength of the instability is directly related to the strength of the permanent magnets. If one adopts a linearized viewpoint of this situation, there are the classic magnetic suspension pair of poles at $\pm k$ where the magnitude of k increases with increasing magnet strength. Thus as the permanent magnet strength is made larger, the speed at which the platen diverges from the equilibrium point increases. The bottom line is that as the permanent magnets are made stronger, the system becomes harder to control, and thus their pairwise effects do not cancel in this important sense.

Additionally, tests indicated that the pair of permanet magnets in the small top assembly were strong enough to clamp their end of the platen to their pole faces if the platen were brought into contact. Thus, as they were capable of carrying more than the gravity load on the platen, these permanent magnets were too strong to be used in operation, independent of the issues discussed above.

For these reasons, I decided to eliminate as much as possible the effect of the permanent magnets. The assemblies had already been glued up and surface ground, and thus it was not possible to remove the permanent magnets with any

reasonable effort. Limited in this respect, I chose to reduce the forces contributed by the permanet magnets by grinding away the central pole face which is part of the permanent magnet magnetic circuit, but not part of the electromagnet magnetic circuit. The permanent magnet in the large electromagnet was found to be weaker than those in the small electromagnets, and as its pole face is much larger, I decided not to grind away its pole face; only the six small electromagnets were modified.

The grinding operation was quite declicate in the sense that only the desired pole face area was to be removed, leaving adjacent surface ground areas untouched. Also any large forces applied by machine tools might result in breaking of the glue joints holding the assembly together. As no spare electromagnets or parts existed, any such damage to a single assembly would represent a significant setback. Thus I decided to take a slower, more delicate approach, and used a high speed half-inch aluminum oxide grinding wheel[2] operating at 10,000 rpm to remove the desired area from the pole face. As the stainless steel had been annealed, it was removed efficiently by this tool with minimal forces applied to the assembly. Heat loading into the magnet assembly was minimized by taking light cuts and stopping occasionally to allow cooling. The pole face on each of the six small electromagnets was removed to a depth of about 0.1". This depth was found empirically to reduce the permanent magnet force by about a factor of five, which was a sufficient reduction for my purposes. The price paid for this delicate approach was in time; each bearing face required three to four hours to grind. Thus I spent a significant part of one week in this endeavor. A drawing of the appearance of one of the small electromagnets after the grinding operation is shown in Figure 4.25, and a photograph of this assembly is shown in Figure 4.26.

The idea of using permanent magnets to carry the gravity load is a good one, and has been used many times in suspensions reported in the literature. In this context, the main advantage is the ability to reduce power requirements and resulting heating of the platen, which can deteriorate position accuracy through thermal expansion. However, if permanent magnets are to be used in this manner, the design must include electromagnets placed below the platen and thus able to exert control forces in the downward direction. That is, all of the electromagnets should be arranged in pairwise opposition. If this strategy is used, then it is possible for the permanet magnets to carry all of the gravity load on the platen with no reduction in the ability of the suspension to resist disturbance forces in the direction of, or opposed to gravity. The permanent magnets should be operated with relatively large air-gaps such that their force is not a strong function of position. This will result in a slow open-loop time constant, allowing easier

[2]Dremel tool and grinding wheel, available at Sears.

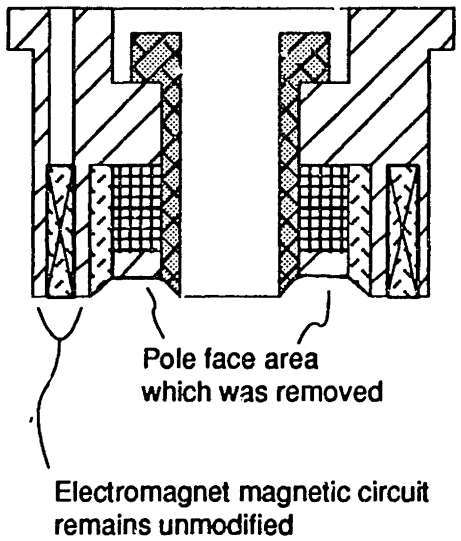

Figure 4.25: Mechanical drawing of the small bearing assembly after grinding the permanent magnet pole face.

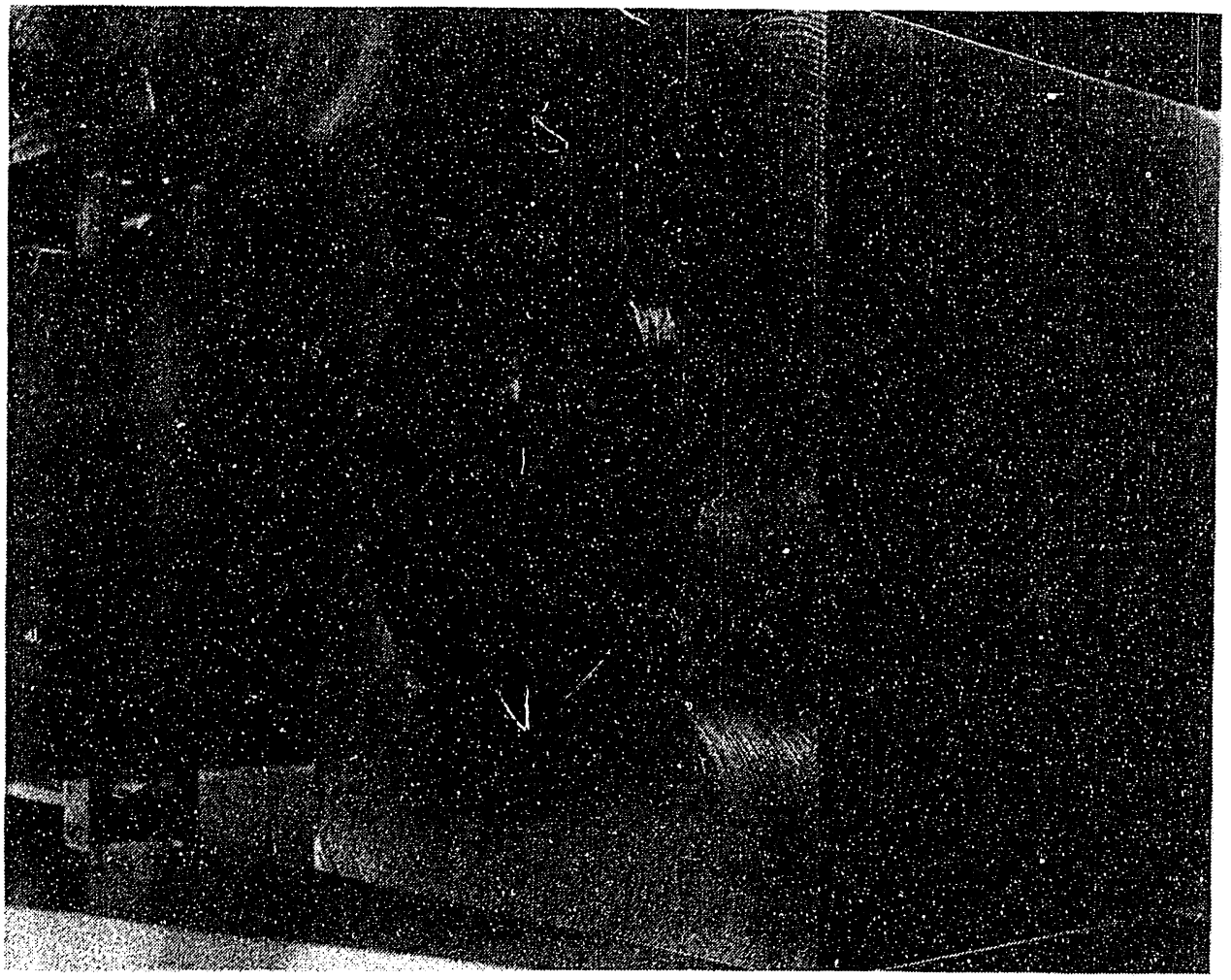

Figure 4.26: Photograph of the small bearing assembly after grinding the permanent magnet pole face. The capacitance probe is visible in the center of the electromagnet. Ground pole-face area surrounds the capacitance probe.

stabilization than if the magnets are run at small air-gaps with correspondingly faster open-loop time constants. The push-pull electromagnets can then be run at relatively low bias currents (only large enough to prevent a dead-zone) and with small air gaps such that the electromagnets are unit-force-per-unit-power efficient, and yet the system open-loop time constants remain slow.

However, the permanent magnets should not be located in the fixed frame, but rather attached to the moving member. If the magnets are located in the fixed frame, then the resultant line of action of the magnet forces only passes through the center of mass of the platen at the nominal operating point. As the platen moves over the large travel envisioned, the platen center of mass moves away from the fixed magnet forces, and thus disturbance torques acting on the platen result. These disturbance torques must be cancelled by the active part of the suspension, and thus result in dissipation in the suspension electromagnets. A better approach is to attach the permanet magnets to the platen, and arrange for them to act on a smooth iron plate which is located in the fixed frame, and is parallel to the long axes of platen travel. In this case the permanet magnets resultant force passes through the platen center of mass independent of platen motion, and thus no disturbance torques result from platen travel. A conceptual design for a suspension incorporating these and other improvements is described in Chapter 8.

4.3.2 Inchworm Drive

The inchworm drive proposed in [Slocum and Eisenhaure 1988] for the purpose of driving the platen in its long axis of travel was not adopted in the current effort. Rather, it is proposed here that it be replaced with a linear motor structure which is capable of controlling two degrees of freedom: the motor air-gap over short travel and linear motion over long travel along the axis of the motor. The design of this linear motor is presented in Chapter 9.

The main reason that the inchworm driver was not used is that it is difficult to see how to make transition between the two piezo-actuators without introducing disturbances onto the wire and consequently the platen. The disadvantage of using the linear motor is that it generates more heat that a piezoelectric driver. However, this thermal problem is not insurmountable if adequate thermal shielding and active temperature control methods are used.

Chapter 5

Dynamics

Before attaching the bearing assemblies to the support brackets, and before gluing the probes into the bearing assemblies, it was appropriate to study the system dynamics in order to develop an appropriate control strategy; the choice of control strategy affects the manner in which the system should be assembled. To this end, the bearings were modeled as applying a force normal to and torques coplanar with the surface of the platen. The force is modeled as being applied at the point where the centerline of the electromagnet intersects the surface of the platen. There are no assumptions made as to how these forces and torques depend on the position of the log or the magnet control currents. The equations of motion are initially derived in their full nonlinear form with no approximations. Then the equations are linearized about the nominal platen operating point.

5.1 Nonlinear Dynamics

In this section, we develop the full non-linear equations of motion for the platen acted upon by the seven support bearings. The equations of motion are derived via the techniques presented in [Kane and Levinson 1985]. I am grateful to Paul Mitiguy for his assistance in teaching me this method, and in formulating these equations with the symbolic dynamics program AUTOLEV. This program largely automates the process of deriving dynamical equations via Kane's method.

First, we describe the unit vectors and reference frames used in the following analysis: $\mathbf{n}_i$, $\mathbf{c}_i$, $\mathbf{d}_i$, and $\mathbf{e}_i$, $i = 1,2,3$ are right-hand sets of orthogonal unit-vectors fixed in reference frames N, C, D, and E, respectively. Figures 5.1, 5.2, and 5.3 show the log dimensions and reference frames N and E. Frame N is the laboratory frame which is considered to be a Newtonian frame, with $\mathbf{n}_2$ directed along the local vertical. The log is fixed in frame E and thus will be referred to

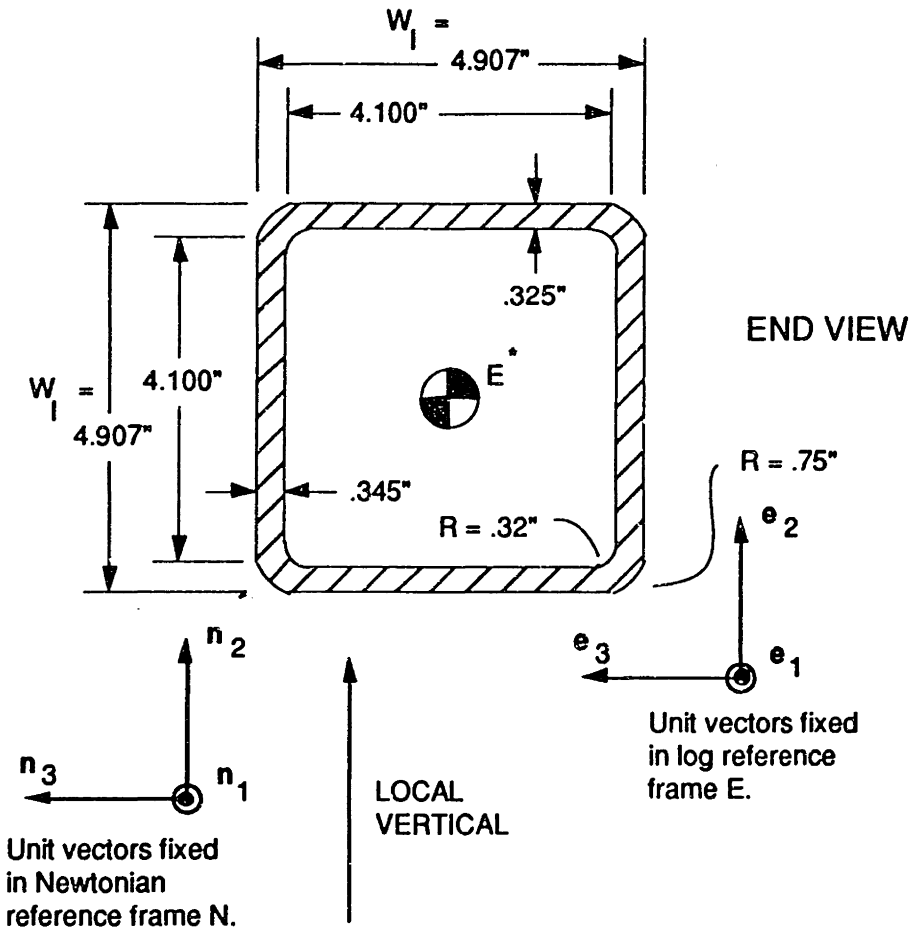

Figure 5.1: End view of log.

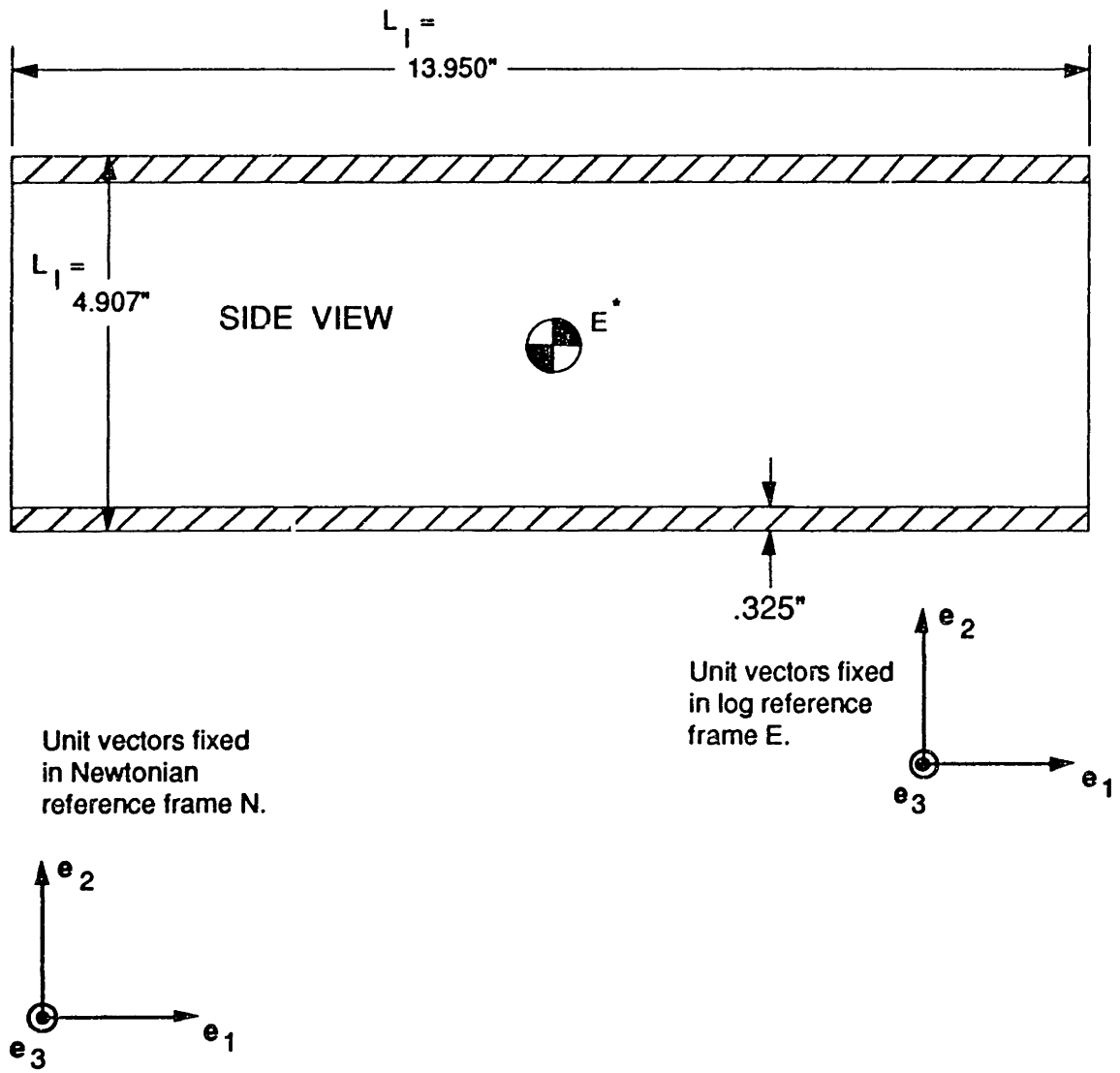

Figure 5.2: Side view of log.

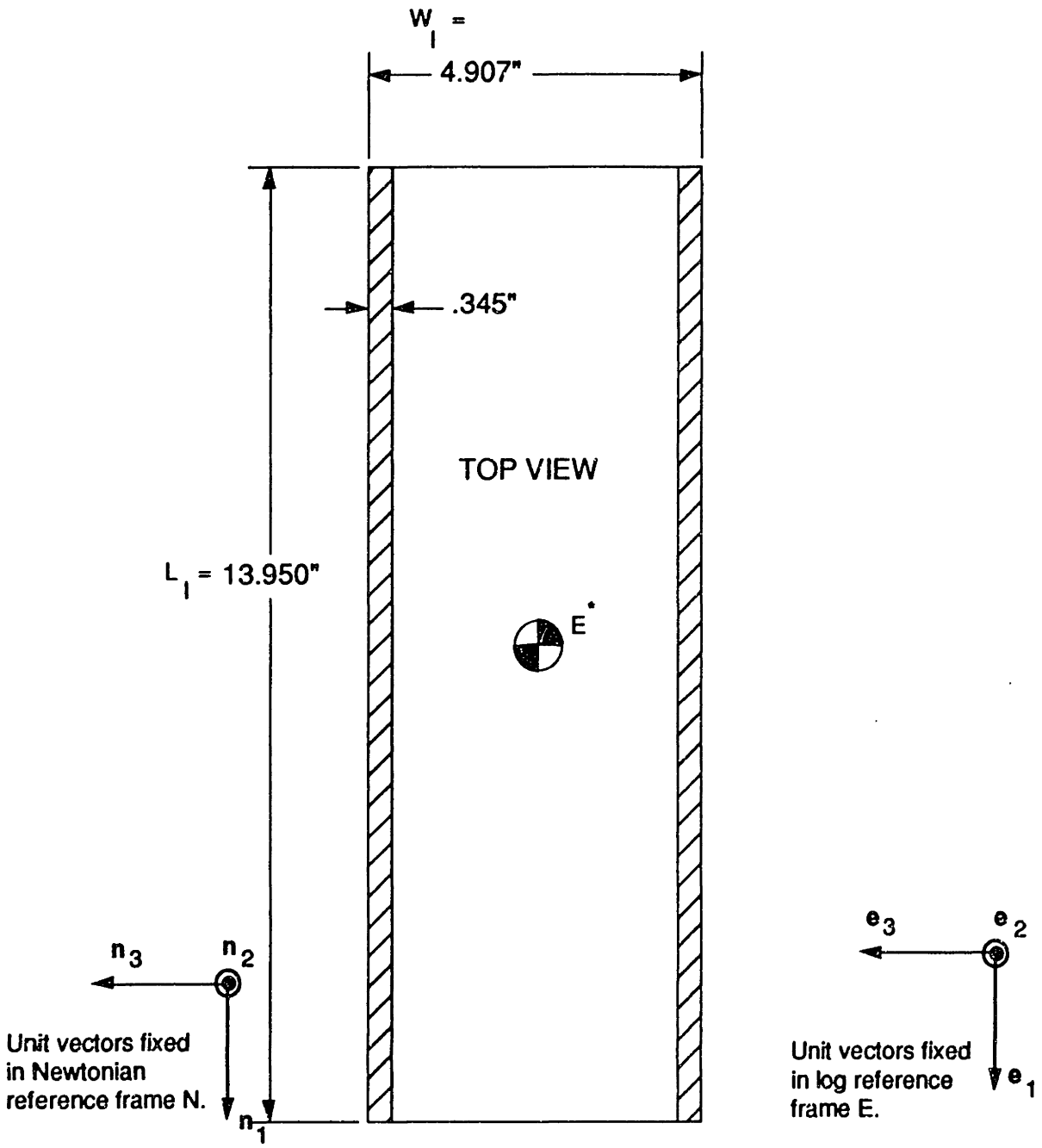

Figure 5.3: Top view of log.

interchangably as the log or as E throughout the remainder of this discussion.[1] $\mathbf{e}_1$ is directed along the long axis of the log, $\mathbf{e}_2$ is perpendicular to the top face of the log, and $\mathbf{e}_3$ is perpendicular to the side face of the log. When the log is at its nominal operating point, $\mathbf{e}_i$ is aligned with $\mathbf{n}_i$, $i = 1, 2, 3$.

The log has length $L_l = 13.95"$ and sides of dimension $W_l = 4.907"$, It has mass M, and its center of mass is referred to as E^*. The log's central principal inertia dyadic (see Section 3.5 in [Kane and Levinson 1985]) is

$$\mathbf{I} = I_1\mathbf{e}_1\mathbf{e}_1 + I_2\mathbf{e}_2\mathbf{e}_2 + I_3\mathbf{e}_3\mathbf{e}_3. \tag{5.1}$$

To calculate numerical values for I_1, I_2, and I_3, we approximate the log as being composed of four rectangular plates as shown in Figure 5.4. The moment of inertia of a rectangular plate of dimensions a, b, c, for an axis through the center of mass and perpendicular to face a-b is $(m/12)(a^2 + b^2)$ where m is the mass of the plate. Using this result, the density of steel 7.88 gm/cm^3, and the parallel axis theorem, the moments of inertia are calculated as $I_1 = 4.76 \times 10^{-2}$ kg m^2, $I_2 = 1.37 \times 10^{-1}$ kg m^2, and $I_3 = 1.35 \times 10^{-1}$ kg m^2. The total mass of the log is calculated as $M = 10.72$ kg.

Frames C and D serve as intermediate frames which are helpful to describe the relative orientations of N and E. C is related to N by first aligning $\mathbf{c}_i$ with $\mathbf{n}_i$, $i = 1, 2, 3$, followed by a simple rotation of C about $\mathbf{n}_1$ by an angle q_1, as shown in Figure 5.5. Thus the direction cosine (rotation) matrix from N to C is

$$^NQ^C = \begin{bmatrix} 1 & 0 & 0 \\ 0 & c_1 & -s_1 \\ 0 & s_1 & c_1 \end{bmatrix} \tag{5.2}$$

where $c_1 = \cos(q_1)$ and $s_1 = \sin(q_1)$. Similar notation will be used throughout this section, i.e., $c_i = \cos(q_i)$ and $s_i = \sin(q_i)$, $i = 1, 2, 3$. The rotation matrix notation is defined such that

$$\begin{bmatrix} \mathbf{n}_1 \\ \mathbf{n}_2 \\ \mathbf{n}_3 \end{bmatrix} = {}^NQ^C \begin{bmatrix} \mathbf{c}_1 \\ \mathbf{c}_2 \\ \mathbf{c}_3 \end{bmatrix} \tag{5.3}$$

or equivalently

$$[\mathbf{c}_1 \;\; \mathbf{c}_2 \;\; \mathbf{c}_3] = [\mathbf{n}_1 \;\; \mathbf{n}_2 \;\; \mathbf{n}_3]\, {}^NQ^C. \tag{5.4}$$

In a similar fashion, D is related to C by first aligning $\mathbf{d}_i$ with $\mathbf{c}_i$, $i = 1, 2, 3$, followed by a simple rotation about $\mathbf{c}_2$ by an angle q_2 as shown in Figure 5.6. Thus the direction cosine (rotation) matrix from C to D is

[1] Rigid bodies are considered to constitute a reference frame. Thus "torque is applied to E" is equivalent to "torque is applied to the log".

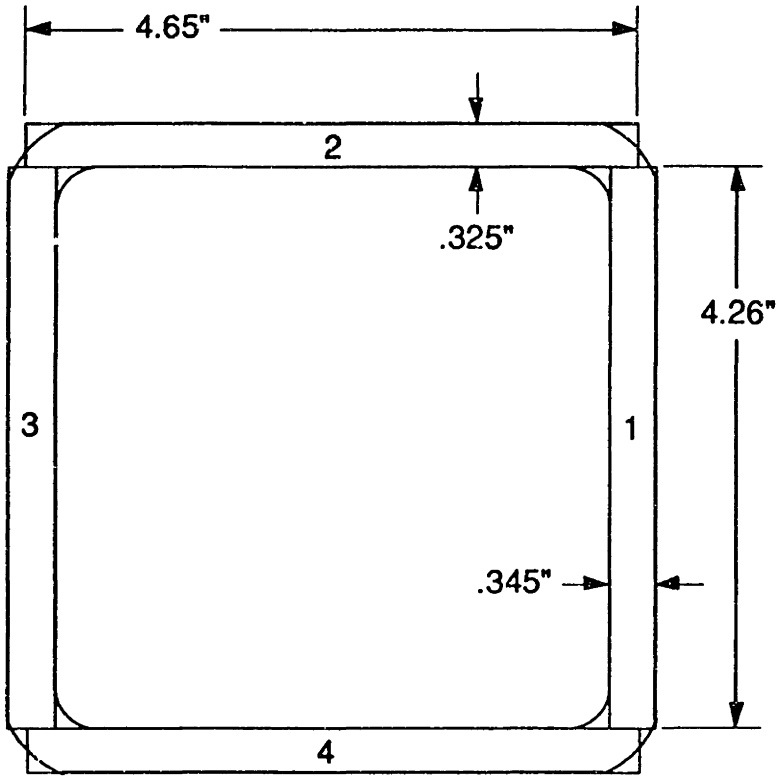

Plates 1 and 3 are identical; plates 2 and 4 are identical. All plates have depth 13.95" into the paper.

Figure 5.4: Showing geometry of four rectangular plates used to approximate the log inertia dyadic.

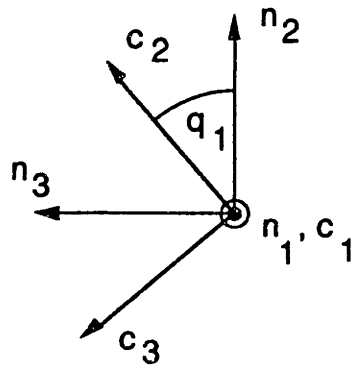

Figure 5.5: Rotation of coordinates from N to C.

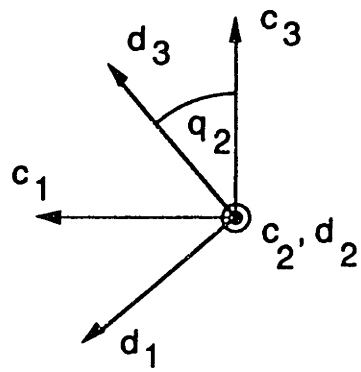

Figure 5.6: Rotation of coordinates from C to D.

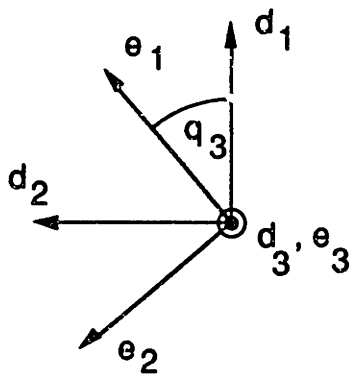

Figure 5.7: Rotation of coordinates from D to E.

$$
{}^{C}Q^{D} = \begin{bmatrix} c_2 & 0 & s_2 \\ 0 & 1 & 0 \\ -s_2 & 0 & c_2 \end{bmatrix} \tag{5.5}
$$

Finally, E is related to D by first aligning $\mathbf{e}_i$ with $\mathbf{d}_i$, $i = 1, 2, 3$, followed by a simple rotation about $\mathbf{d}_3$ by an angle q_3 as shown in Figure 5.7. Thus the direction cosine (rotation) matrix from D to E is

$$
{}^{D}Q^{E} = \begin{bmatrix} c_3 & -s_3 & 0 \\ s_3 & c_3 & 0 \\ 0 & 0 & 1 \end{bmatrix} \tag{5.6}
$$

The rotation matrix from N to E is then given by the product ${}^{N}Q^{E} = {}^{N}Q^{C}{}^{C}Q^{D}{}^{D}Q^{E}$. Carrrying out this multiplication gives

$$
{}^{N}Q^{E} = \begin{bmatrix} c_2c_3 & -c_2s_3 & s_2 \\ s_1s_2c_3 + c_1s_3 & -s_1s_2s_3 + c_1c_3 & -s_1c_2 \\ -c_1s_2c_3 + s_1s_3 & c_1s_2s_3 + s_1c_3 & c_1c_2 \end{bmatrix}. \tag{5.7}
$$

Similarly, ${}^{C}Q^{E} = {}^{C}Q^{D}{}^{D}Q^{E}$, etc.

After defining these successive rotations, the angular velocity of E in N can be written as ${}^{N}\omega^{E} = \dot{q}_1\mathbf{n}_1 + \dot{q}_2\mathbf{c}_2 + \dot{q}_3\mathbf{d}_3$. Using ${}^{N}Q^{E}$, ${}^{C}Q^{E}$, and ${}^{D}Q^{E}$ this may be rewritten in terms of only body-fixed unit vectors as (see [Kane et al (1983)], pg. 427), ${}^{N}\omega^{E} = (\dot{q}_1c_2c_3 + \dot{q}_2s_3)\mathbf{e}_1 + (-\dot{q}_1c_2s_3 + \dot{q}_2c_3)\mathbf{e}_2 + (\dot{q}_1s_2 + \dot{q}_3)\mathbf{e}_3$. Scalar quantities u_1, u_2, and u_3 are then defined as

$$
\begin{aligned}
u_1 &= \dot{q}_1c_2c_3 + \dot{q}_2s_3 \\
u_2 &= -\dot{q}_1c_2s_3 + \dot{q}_2c_3 \\
u_3 &= \dot{q}_1s_2 + \dot{q}_3
\end{aligned} \tag{5.8}
$$

so that the angular velocity of E in N can be rewritten as

$$^N\omega^E = u_1\mathbf{e}_1 + u_2\mathbf{e}_2 + u_3\mathbf{e}_3. \tag{5.9}$$

Let O be a point fixed in N and coincident with E^* when the log is at its nominal operating point. Then, the position vector from O to E^* will be defined as

$$P^{OE^*} \equiv x_1\mathbf{n}_1 + x_2\mathbf{n}_2 + x_3\mathbf{n}_3. \tag{5.10}$$

Then, by definition, the velocity of E^* in N is

$$^N\mathbf{v}^{E^*} = \dot{x}_1\mathbf{n}_1 + \dot{x}_2\mathbf{n}_2 + \dot{x}_3\mathbf{n}_3. \tag{5.11}$$

Introducing scalar quantities

$$\begin{aligned} u_4 &= \dot{x}_1 \\ u_5 &= \dot{x}_2 \\ u_6 &= \dot{x}_3 \end{aligned} \tag{5.12}$$

allows $^N\mathbf{v}^{E^*}$ to be rewritten as

$$^N\mathbf{v}^{E^*} = u_4\mathbf{n}_1 + u_5\mathbf{n}_2 + u_6\mathbf{n}_3. \tag{5.13}$$

The platen's state vector is then formed by the twelve quantities

$$[q_1, q_2, q_3, x_1, x_2, x_3, u_1, u_2, u_3, u_4, u_5, u_6]^T$$

which specify the log's rotational orientation, center-of-mass position, angular velocity, and center-of-mass velocity, relative to N.

Now the kinematical differential equations are obtained by inverting (5.8) and (5.12), yielding

$$\dot{q}_1 = (u_1c_3 - u_2s_3)/c_2 \tag{5.14}$$

$$\dot{q}_2 = u_1s_3 + u_2c_3 \tag{5.15}$$

$$\dot{q}_3 = (-u_1c_3 + u_2s_3)s_2/c_2 + u_3 \tag{5.16}$$

and

$$\dot{x}_1 = u_4 \tag{5.17}$$

$$\dot{x}_2 = u_5 \tag{5.18}$$

$$\dot{x}_3 = u_6 \tag{5.19}$$

These equations form six of the twelve first order nonlinear equations of motion which describe the log dynamics. Note that they involve only kinematics and do

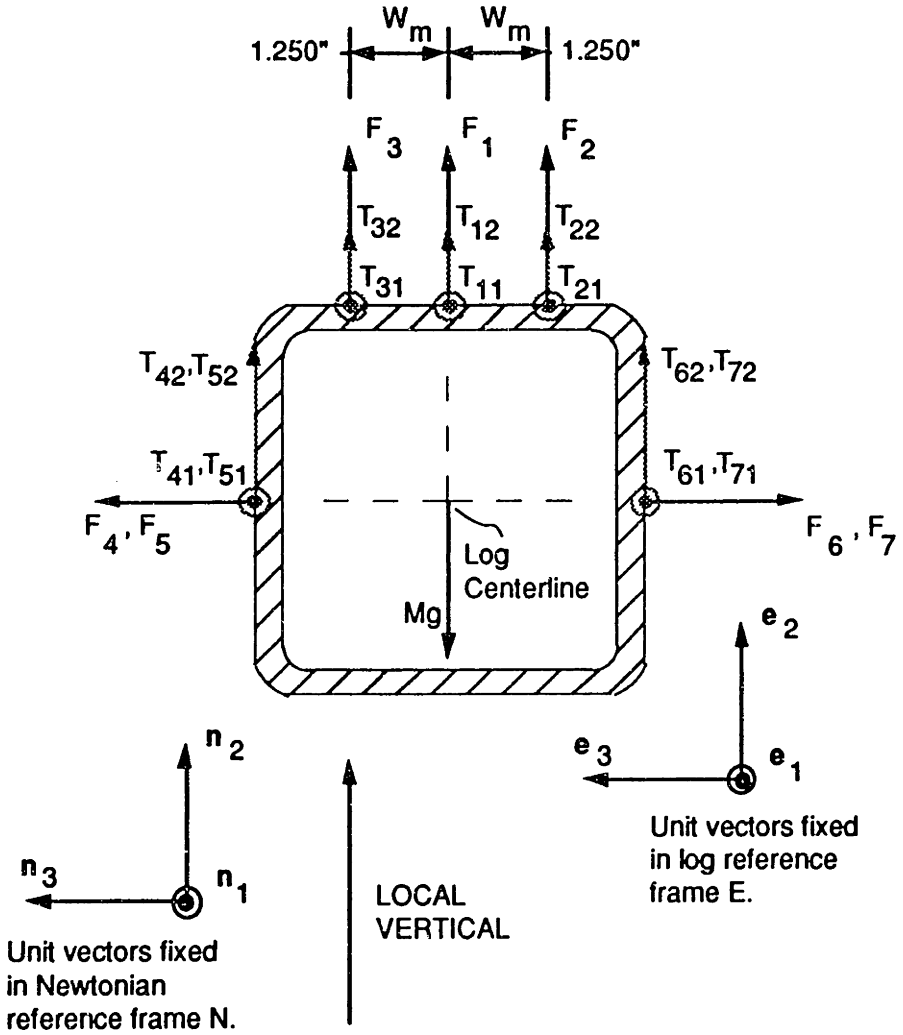

Note: Force and torque vectors are fixed in N. Log is shown at nominal operating point with E and N aligned.

Figure 5.8: End view of forces and torques applied to log.

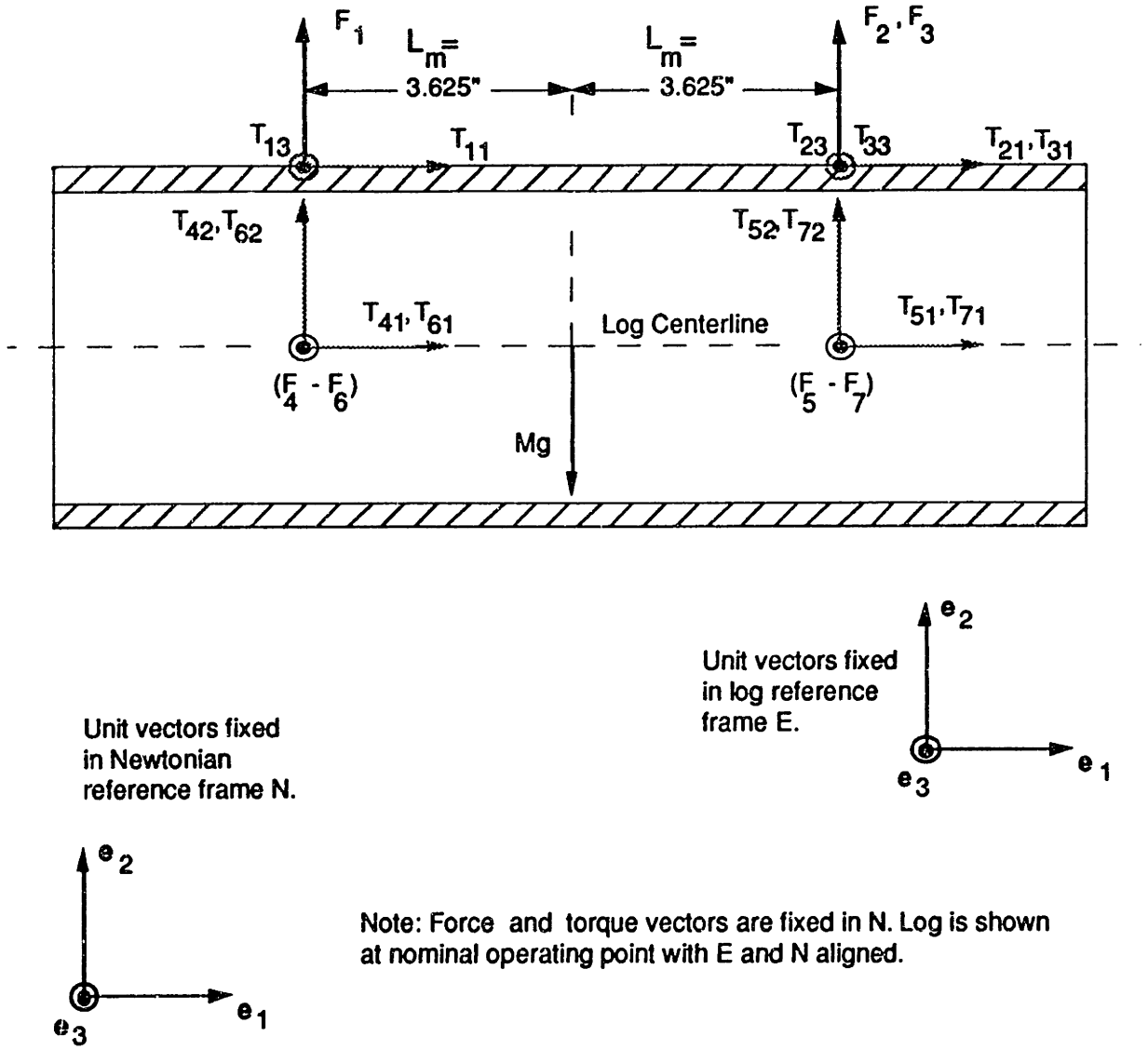

Figure 5.9: Side view of forces and torques applied to log.

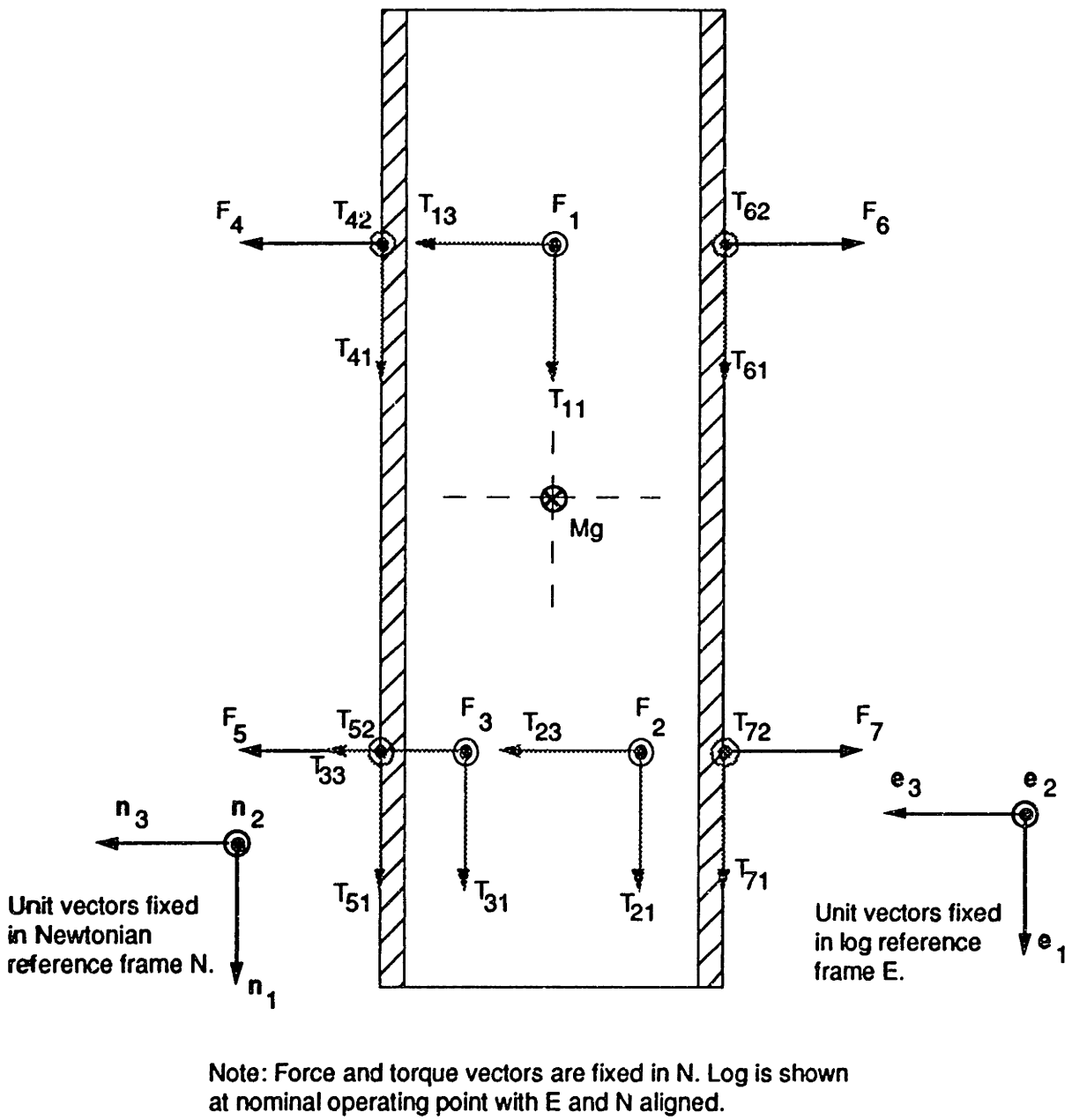

Figure 5.10: Top view of forces and torques applied to log.

not describe any of the log's inertial properties, nor the forces acting on the log. These terms enter the remaining six state equations which we derive next.

The forces and torques applied to the log are shown in Figures 5.8, 5.9, and 5.10. Forces are shown as solid black arrows, and torques are shown as grey arrows. The displacements at the nominal operating point of the magnet forces from E^* are shown in the figures in terms of dimensions L_m and W_m.

To simplify the dynamics, these forces and torques are replaced with an equivalent set consisting of a torque and a resultant whose line of action passes through E^*. To begin, define the position vectors $\mathbf{p}_j$ from E^* to the jth point at which the magnet forces are applied.

$$\mathbf{p}_1 = (-L_m - x_1)\mathbf{n}_1 + (\frac{W_l}{2} - x_2)\mathbf{n}_2 - x_3\mathbf{n}_3 \tag{5.20}$$

$$\mathbf{p}_2 = (L_m - x_1)\mathbf{n}_1 + (\frac{W_l}{2} - x_2)\mathbf{n}_2 + (-W_m - x_3)\mathbf{n}_3 \tag{5.21}$$

$$\mathbf{p}_3 = (L_m - x_1)\mathbf{n}_1 + (\frac{W_l}{2} - x_2)\mathbf{n}_2 + (W_m - x_3)\mathbf{n}_3 \tag{5.22}$$

$$\mathbf{p}_4 = (-L_m - x_1)\mathbf{n}_1 - x_2\mathbf{n}_2 + (\frac{W_l}{2} - x_3)\mathbf{n}_3 \tag{5.23}$$

$$\mathbf{p}_5 = (L_m - x_1)\mathbf{n}_1 - x_2\mathbf{n}_2 + (\frac{W_l}{2} - x_3)\mathbf{n}_3 \tag{5.24}$$

$$\mathbf{p}_6 = (-L_m - x_1)\mathbf{n}_1 - x_2\mathbf{n}_2 + (-\frac{W_l}{2} - x_3)\mathbf{n}_3 \tag{5.25}$$

$$\mathbf{p}_7 = (L_m - x_1)\mathbf{n}_1 - x_2\mathbf{n}_2 + (-\frac{W_l}{2} - x_3)\mathbf{n}_3 \tag{5.26}$$

Note that since the magnets do not move, the point of application remains fixed in N while the log moves under it. The small (.005") air-gap lengths are ignored in this analysis.

The forces applied by the jth magnet are labelled F_j, and are defined as the linearized force applied to the log at each magnet. The torques applied to the log by the jth magnet about the kth direction are labelled T_{jk}. The forces from each magnet are

$$\mathbf{F}_1 = F_1\mathbf{n}_2 \tag{5.27}$$

$$\mathbf{F}_2 = F_2\mathbf{n}_2 \tag{5.28}$$

$$\mathbf{F}_3 = F_3\mathbf{n}_2 \tag{5.29}$$

$$\mathbf{F}_4 = F_4\mathbf{n}_3 \tag{5.30}$$

$$\mathbf{F}_5 = F_5\mathbf{n}_3 \tag{5.31}$$

$$\mathbf{F}_6 = -F_6\mathbf{n}_3 \tag{5.32}$$

$$\mathbf{F}_7 = -F_7\mathbf{n}_3 \tag{5.33}$$

Additionally, gravity applies to E^* a force of

$$\mathbf{F}_g = -Mg\mathbf{n}_2. \tag{5.34}$$

Thus, the total force applied to the log is

$$\mathbf{F}_{tot} = (F_1 + F_2 + F_3 - Mg)\mathbf{n}_2 + (F_4 + F_5 - F_6 - F_7)\mathbf{n}_3. \tag{5.35}$$

The torques at each magnet are

$$\begin{aligned}
\mathbf{T}_1 &= T_{11}\mathbf{n}_1 + T_{13}\mathbf{n}_3 && (5.36)\\
\mathbf{T}_2 &= T_{21}\mathbf{n}_1 + T_{23}\mathbf{n}_3 && (5.37)\\
\mathbf{T}_3 &= T_{31}\mathbf{n}_1 + T_{33}\mathbf{n}_3 && (5.38)\\
\mathbf{T}_4 &= T_{41}\mathbf{n}_1 + T_{42}\mathbf{n}_2 && (5.39)\\
\mathbf{T}_5 &= T_{51}\mathbf{n}_1 + T_{52}\mathbf{n}_2 && (5.40)\\
\mathbf{T}_6 &= T_{61}\mathbf{n}_1 + T_{62}\mathbf{n}_2 && (5.41)\\
\mathbf{T}_7 &= T_{71}\mathbf{n}_1 + T_{72}\mathbf{n}_2 && (5.42)
\end{aligned}$$

Note that the torque vectors for each magnet lie in the plane of the magnet face.

The moments about E^* resulting from the jth magnet forces are labeled M_j and are given by the cross product of the jth position vector and the jth force as shown below

$$\begin{aligned}
\mathbf{M}_1 &= \mathbf{p}_1 \times \mathbf{F}_1 = x_3F_1\mathbf{n}_1 + (-L_m - x_1)F_1\mathbf{n}_3 && (5.43)\\
\mathbf{M}_2 &= \mathbf{p}_2 \times \mathbf{F}_2 = (W_m + x_3)F_2\mathbf{n}_1 + (L_m - x_1)F_2\mathbf{n}_3 && (5.44)\\
\mathbf{M}_3 &= \mathbf{p}_3 \times \mathbf{F}_3 = (-W_m + x_3)F_3\mathbf{n}_1 + (L_m - x_1)F_3\mathbf{n}_3 && (5.45)\\
\mathbf{M}_4 &= \mathbf{p}_4 \times \mathbf{F}_4 = -x_2F_4\mathbf{n}_1 + (L_m + x_1)F_4\mathbf{n}_2 && (5.46)\\
\mathbf{M}_5 &= \mathbf{p}_5 \times \mathbf{F}_5 = -x_2F_5\mathbf{n}_1 + (-L_m + x_1)F_5\mathbf{n}_2 && (5.47)\\
\mathbf{M}_6 &= \mathbf{p}_6 \times \mathbf{F}_6 = x_2F_6\mathbf{n}_1 + (-L_m - x_1)F_6\mathbf{n}_2 && (5.48)\\
\mathbf{M}_7 &= \mathbf{p}_7 \times \mathbf{F}_7 = x_2F_7\mathbf{n}_1 + (L_m - x_1)F_7\mathbf{n}_2 && (5.49)
\end{aligned}$$

The total torque applied to the log is

$$\mathbf{T}_{tot} = \sum_{i=1}^{7}\mathbf{T}_i + \sum_{i=1}^{7}\mathbf{M}_i. \tag{5.50}$$

Substituting from above yields

$$\begin{aligned}
\mathbf{T}_{tot} = \Big[&T_{11} + T_{21} + T_{31} + T_{41} + T_{51} + T_{61} + T_{71} + x_3F_1 + (W_m + x_3)F_2\\
&+ (-W_m + x_3)F_3 - x_2(F_4 - F_6) - x_2(F_5 - F_7)\Big]\mathbf{n}_1
\end{aligned}$$

$$
\begin{aligned}
&+ \Big[T_{42} + T_{52} + T_{62} + T_{72} + (L_m + x_1)(F_4 - F_6) \\
&+ (-L_m + x_1)(F_5 - F_7)\Big]\mathbf{n}_2 \\
&+ \Big[T_{13} + T_{23} + T_{33} + (-L_m - x_1)F_1 + (L_m - x_1)F_2 \\
&+ (L_m - x_1)F_3\Big]\mathbf{n}_3
\end{aligned} \tag{5.51}
$$

At this point we can calculate the generalized active forces $\mathcal{F}_r$. For a rigid body, and using the definition on pg. 106 of [Kane and Levinson 1985], the generalized active force $\mathcal{F}_r$ for the log E in reference frame N is defined as

$$
(\mathcal{F}_r)_E = {}^N\omega_r^E \cdot \mathbf{T}_{tot} + {}^N\mathbf{v}_r^{E^*} \cdot \mathbf{F}_{tot} \tag{5.52}
$$

where ${}^N\omega_r^E$ and ${}^N\mathbf{v}_r^{E^*}$ are, respectively the rth partial angular velocity of E in N and the rth partial velocity of E^* in N (see Section 2.14 in [Kane and Levinson 1985]), and r is the number of system degrees of freedom. The partial angular velocities are found by inspection of the coefficients of u_r in the expression for ${}^N\omega^E$, equation (5.9). For instance, ${}^N\omega_1^E$ is the coefficient of u_1 in (5.9), i.e., $\mathbf{e}_1$. Similarly, the partial velocities are found by inspection of the coefficients of u_r in the expression for ${}^N\mathbf{v}^{E^*}$, equation (5.13). For instance, ${}^N\mathbf{v}_4^{E^*}$ is the coefficient of u_4 in (5.13), i.e., $\mathbf{n}_1$. Following this approach, the remaining partial velocities are calculated and displayed in Table 5.1.

r	${}^N\omega_r^E$	${}^N\mathbf{v}_r^{E^*}$
1	$\mathbf{e}_1$	0
2	$\mathbf{e}_2$	0
3	$\mathbf{e}_3$	0
4	0	$\mathbf{n}_1$
5	0	$\mathbf{n}_2$
6	0	$\mathbf{n}_3$

Table 5.1: Partial velocities.

Using equations (5.9), (5.13), (5.51), and (5.35), and the results in Table 5.1, the generalized active forces are calculated as given below.

$$
\begin{aligned}
\mathcal{F}_1 = &\\
&\Big[(-L_m - x_1)F_1 + (L_m - x_1)F_2 + (L_m - x_1)F_3 + T_{13} + T_{23} \\
&+ T_{33}\Big](-c_1 s_2 c_3 + s_1 s_3)
\end{aligned}
$$

$$
\begin{aligned}
&+\Big[(W_m+x_3)F_2-(W_m-x_3)F_3+F_1x_3-(F_4-F_6)x_2-(F_5-F_7)x_2\\
&+T_{11}+T_{21}+T_{31}+T_{41}+T_{51}+T_{61}+T_{71}\Big]c_2c_3\\
&+\Big[(L_m+x_1)(F_4-F_6)-(L_m-x_1)(F_5-F_7)+T_{42}+T_{52}+T_{62}\\
&+T_{72}\Big](s_1s_2c_3+c_1s_3)
\end{aligned}
\tag{5.53}
$$

$$
\begin{aligned}
\mathcal{F}_2 =\ &\\
&\Big[(-L_m-x_1)F_1+(L_m-x_1)F_2+(L_m-x_1)F_3+T_{13}+T_{23}\\
&+T_{33}\Big](c_1s_2s_3+s_1c_3)\\
&-\Big[(W_m+x_3)F_2-(W_m-x_3)F_3+F_1x_3-(F_4-F_6)x_2-(F_5-F_7)x_2\\
&+T_{11}+T_{21}+T_{31}+T_{41}+T_{51}+T_{61}+T_{71}\Big]c_2s_3\\
&+\Big[(L_m+x_1)(F_4-F_6)-(L_m-x_1)(F_5-F_7)+T_{42}+T_{52}+T_{62}\\
&+T_{72}\Big](-s_1s_2s_3+c_1c_3)
\end{aligned}
\tag{5.54}
$$

$$
\begin{aligned}
\mathcal{F}_3 =\ &\\
&\Big[(-L_m-x_1)F_1+(L_m-x_1)F_2+(L_m-x_1)F_3+T_{13}+T_{23}+T_{33}\Big]c_1c_2\\
&+\Big[(W_m+x_3)F_2-(W_m-x_3)F_3+F_1x_3-(F_4-F_6)x_2-(F_5-F_7)x_2\\
&+T_{11}+T_{21}+T_{31}+T_{41}+T_{51}+T_{61}+T_{71}\Big]s_2\\
&-\Big[(L_m+x_1)(F_4-F_6)-(L_m-x_1)(F_5-F_7)+T_{42}+T_{52}+T_{62}\\
&+T_{72}\Big]c_2s_1
\end{aligned}
\tag{5.55}
$$

$$\mathcal{F}_4 = 0 \tag{5.56}$$

$$\mathcal{F}_5 = F_1+F_2+F_3-Mg \tag{5.57}$$

$$\mathcal{F}_6 = F_4+F_5-F_6-F_7 \tag{5.58}$$

At this point, the generalized inertia forces are evaluated. Following the results given on pg. 125 of [Kane and Levinson 1985], and since the levitation system is holonomic, the generalized inertia forces $\mathcal{F}_r^*$ for the log E in reference frame N are defined as

$$(\mathcal{F}_r^*)_E = {}^N\omega_r^E \cdot (-{}^N\alpha^E \cdot \mathbf{I} - {}^N\omega^E \times \mathbf{I} \cdot {}^N\omega^E) + {}^N\mathbf{v}_r^{E^*} \cdot (-M\,{}^N\mathbf{a}^{E^*}) \tag{5.59}$$

where as before, ${}^N\omega_r^E$ and ${}^N\mathbf{v}_r^{E^*}$ are, respectively the rth partial angular velocity of E in N and the rth partial velocity of E^* in N, from Table 5.1. ${}^N\omega^E$ is the angular velocity of E in N, and $\mathbf{I}$ is the central inertia dyadic of E. Differentiating the angular velocity gives the angular acceleration of the log in N:

$${}^N\alpha^E = \dot{u}_1\mathbf{e}_1 + \dot{u}_2\mathbf{e}_2 + \dot{u}_3\mathbf{e}_3. \tag{5.60}$$

Differentiating the velocity of E^* gives the acceleration of the log center of mass in N:

$${}^N\mathbf{a}^{E^*} = \dot{u}_4\mathbf{n}_1 + \dot{u}_5\mathbf{n}_2 + \dot{u}_6\mathbf{n}_3. \tag{5.61}$$

Applying these results in equation (5.59) yields the generalized inertia forces $\mathcal{F}_r^*$ as

$$\mathcal{F}_1^* = -I_1\dot{u}_1 + I_2u_2u_3 - I_3u_2u_3 \tag{5.62}$$
$$\mathcal{F}_2^* = -I_2\dot{u}_2 - I_1u_1u_3 + I_3u_1u_3 \tag{5.63}$$
$$\mathcal{F}_3^* = -I_3\dot{u}_3 + I_1u_1u_2 - I_2u_1u_2 \tag{5.64}$$
$$\mathcal{F}_4^* = -M\dot{u}_4 \tag{5.65}$$
$$\mathcal{F}_5^* = -M\dot{u}_5 \tag{5.66}$$
$$\mathcal{F}_6^* = -M\dot{u}_6 \tag{5.67}$$

Now, the remaining six nonlinear state equations[2] are derived by setting $\mathcal{F}_r + \mathcal{F}_r^* = 0$ (see Section 6.1 in [Kane and Levinson 1985]). This results in

$$\begin{aligned}
I_1\dot{u}_1 = {} & \\
& I_2u_2u_3 - I_3u_2u_3 + \Big[(-L_m - x_1)F_1 + (L_m - x_1)F_2 + (L_m - x_1)F_3 \\
& + T_{13} + T_{23} + T_{33}\Big](-c_1s_2c_3 + s_1s_3) \\
& + \Big[(W_m + x_3)F_2 - (W_m - x_3)F_3 + F_1x_3 - (F_4 - F_6)x_2 - (F_5 - F_7)x_2 \\
& + T_{11} + T_{21} + T_{31} + T_{41} + T_{51} + T_{61} + T_{71}\Big]c_2c_3 \\
& + \Big[(L_m + x_1)(F_4 - F_6) - (L_m - x_1)(F_5 - F_7) + T_{42} + T_{52} + T_{62} \\
& + T_{72}\Big](s_1s_2c_3 + c_1s_3)
\end{aligned} \tag{5.68}$$

[2]Also known as *Kane's dynamical equations.*

$$
\begin{aligned}
I_2\dot{u}_2 = & \\
& -I_1u_1u_3 + I_3u_1u_3 + \Big[(-L_m - x_1)F_1 + (L_m - x_1)F_2 + (L_m - x_1)F_3 \\
& + T_{13} + T_{23} + T_{33}\Big](c_1s_2s_3 + s_1c_3) \\
& - \Big[(W_m + x_3)F_2 - (W_m - x_3)F_3 + F_1x_3 - (F_4 - F_6)x_2 - (F_5 - F_7)x_2 \\
& + T_{11} + T_{21} + T_{31} + T_{41} + T_{51} + T_{61} + T_{71}\Big]c_2s_3 \\
& + \Big[(L_m + x_1)(F_4 - F_6) - (L_m - x_1)(F_5 - F_7) + T_{42} + T_{52} + T_{62} \\
& + T_{72}\Big](-s_1s_2s_3 + c_1c_3)
\end{aligned} \tag{5.69}
$$

$$
\begin{aligned}
I_3\dot{u}_3 = & \\
& I_1u_1u_2 - I_2u_1u_2 + \Big[(-L_m - x_1)F_1 + (L_m - x_1)F_2 + (L_m - x_1)F_3 \\
& + T_{13} + T_{23} + T_{33}\Big]c_1c_2 \\
& + \Big[(W_m + x_3)F_2 - (W_m - x_3)F_3 + F_1x_3 - (F_4 - F_6)x_2 - (F_5 - F_7)x_2 \\
& + T_{11} + T_{21} + T_{31} + T_{41} + T_{51} + T_{61} + T_{71}\Big]s_2 \\
& - \Big[(L_m + x_1)(F_4 - F_6) - (L_m - x_1)(F_5 - F_7) + T_{42} + T_{52} + T_{62} \\
& + T_{72}\Big]c_2s_1
\end{aligned} \tag{5.70}
$$

$$M\dot{u}_4 = 0 \tag{5.71}$$

$$M\dot{u}_5 = F_1 + F_2 + F_3 - Mg \tag{5.72}$$

$$M\dot{u}_6 = F_4 + F_5 - F_6 - F_7 \tag{5.73}$$

Given the forces and torques, equations (5.14) through (5.19) and (5.68) through (5.73) specify the motion of the log. This completes the derivation of the nonlinear dynamical equations.

5.2 Linear Dynamics

With the nonlinear dynamics in hand, we are now in a position to derive the linear dynamics for small motions about the intended operating point. The linear

dynamics are then used in subsequent analysis and design, since the log dynamics in their full nonlinear form are quite cumbersome, and it is difficult to design and analyze controllers in the nonlinear domain. The log motions are small except in the x_1 direction, and thus a linearized analysis is valid as long as we retain the large possible variations of the operating point value of x_1.

First, each variable is written in terms of an operating point value plus an incremental variation. These two terms are denoted by a overbar and a tilde respectively. That is, $x_1 = \bar{x}_1 + \tilde{x}_1$, where $\bar{x}_1$ is the operating point value of x_1, and $\tilde{x}_1$ is the incremental variation in x_1. The operating plus incremental quantities are substituted into the nonlinear dynamical equations, and the linear analysis is carried out by dropping any terms which are second-order or higher in incremental quantities.

At the operating point, $\bar{x}_1$ is finite and will be retained in the analysis, but the other operating point positions, rotations, velocities and angular velocities are zero. That is, $\bar{x}_2 = \bar{x}_3 = \bar{q}_1 = \bar{q}_2 = \bar{q}_3 = \bar{u}_1 = \bar{u}_2 = \bar{u}_3 = \bar{u}_4 = \bar{u}_5 = \bar{u}_6 = 0$. All magnet torque operating point values are zero since the log is parallel to the magnet faces at the operating point, i.e., $\bar{T}_{jk} = 0$ for all j and k. Also, because the operating point rotations are zero, to first order, $\sin(q_k) \approx \tilde{q}_k$, and $\cos(q_k) \approx 1$.

To support the mass of the log against gravity, and to simultaneously satisfy the conditions that the linear and angular velocities are zero, the operating point values of the magnet forces are chosen such that

$$\bar{F}_1 + \bar{F}_2 + \bar{F}_3 = Mg \tag{5.74}$$

$$\bar{F}_2 = \bar{F}_3 \tag{5.75}$$

$$(-L_m - \bar{x}_1)\bar{F}_1 + (L_m - \bar{x}_1)\bar{F}_2 + (L_m - \bar{x}_1)\bar{F}_3 = 0 \tag{5.76}$$

$$\bar{F}_4 = \bar{F}_6 \tag{5.77}$$

$$\bar{F}_5 = \bar{F}_7 \tag{5.78}$$

Substituting the above operating point conditions into the nonlinear dynamical equations yields the following set of linear dynamics in the incremental quantities. The kinematical differential equations (5.14)–(5.19) become

$$\dot{\tilde{q}}_1 = \tilde{u}_1 \tag{5.79}$$

$$\dot{\tilde{q}}_2 = \tilde{u}_2 \tag{5.80}$$

$$\dot{\tilde{q}}_3 = \tilde{u}_3 \tag{5.81}$$

and

$$\dot{\tilde{x}}_1 = \tilde{u}_4 \tag{5.82}$$

$$\dot{\tilde{x}}_2 = \tilde{u}_5 \tag{5.83}$$

$$\dot{\tilde{x}}_3 = \tilde{u}_6 \tag{5.84}$$

and Kane's equations (5.68)-(5.73) become

$$\begin{aligned} I_1\dot{\tilde{u}}_1 &= Mg\tilde{x}_3 + W_m(\tilde{F}_2 - \tilde{F}_3) \\ &\quad + \tilde{T}_{11} + \tilde{T}_{21} + \tilde{T}_{31} + \tilde{T}_{41} + \tilde{T}_{51} + \tilde{T}_{61} + \tilde{T}_{71} \end{aligned} \tag{5.85}$$

$$\begin{aligned} I_2\dot{\tilde{u}}_2 &= (L_m + \bar{x}_1)(\tilde{F}_4 - \tilde{F}_6) - (L_m - \bar{x}_1)(\tilde{F}_5 - \tilde{F}_7) \\ &\quad + \tilde{T}_{42} + \tilde{T}_{52} + \tilde{T}_{62} + \tilde{T}_{72} \end{aligned} \tag{5.86}$$

$$\begin{aligned} I_3\dot{\tilde{u}}_3 &= (-L_m - \bar{x}_1)\tilde{F}_1 + (L_m - \bar{x}_1)\tilde{F}_2 + (L_m - \bar{x}_1)\tilde{F}_3 \\ &\quad - Mg\tilde{x}_1 + \tilde{T}_{13} + \tilde{T}_{23} + \tilde{T}_{33} \end{aligned} \tag{5.87}$$

$$M\dot{\tilde{u}}_4 = 0 \tag{5.88}$$

$$M\dot{\tilde{u}}_5 = \tilde{F}_1 + \tilde{F}_2 + \tilde{F}_3 \tag{5.89}$$

$$M\dot{\tilde{u}}_6 = \tilde{F}_4 + \tilde{F}_5 - \tilde{F}_6 - \tilde{F}_7 \tag{5.90}$$

It now remains to express the forces F_j and torques T_{jk} in terms of the control currents $i_1, \ldots, i_7$, and the log state variables x_1, x_2, x_3, q_1, q_2, q_3, and $u_1, \ldots, u_6$.

Chapter 6

Development of Bearing Models

The results from the previous chapter express the system dynamics in terms of the magnet forces and torques. No relationship has yet been derived for how these forces and torques depend upon the platen's position and the magnet control currents. This information is needed to complete the modeling of the open-loop plant. This chapter describes the development of accurate models for the open-loop plant including the current drives, electromagnets, platen and position probes. Several alternatives were considered to derive these magnet force characteristics. The approach selected involved developing a crude control strategy which could be empirically tuned to allow suspension in the full five degrees of freedom. The development of this controller is described. The assembly techniques used are described. Several hardware problems were solved in the process of this development, such as mechanical resonances and short circuits in two of the magnet coils. High performance is not a requirement at this stage. Once the system is suspended, more detailed models can be readily developed which allow the refinement of the controller to yield higher performance and stability margins.

6.1 Modeling Alternatives

Due to the low permeablity ($\mu_r \approx 500$) of the stainless steel used in the electromagnets, and the small air gap, the reluctance of the magnetic circuit is comparable to the reluctance of the air gap, and thus the steel's magnetic properties are first-order significant in determining the magnet force. Also, a preliminary finite element analysis of the electromagnets indicates that there is a significant amount of leakage flux. Thus a simple magnetic circuit analysis will not yield accurate results. Such an analysis predicts magnet forces approximately twice what has been measured in the laboratory.

The accuracy of any finite-element analysis also depends upon the accuracy of

the material model for the stainless steel. Magnetic properties for this stainless are not well characterized; thus to undertake a finite element analysis would require laboratory measurement of the steel properties. This would typically be approached by subjecting a toroid of the material to the same processing steps (annealing, etc.) as the electromagnets themselves. Following processing, this material is wound with two coils. One coil is driven by an amplifier with an appropriate sinusoid. Current in this coil is simply related to the magnetic field H in the torus through Ampere's law. The second coil drives an amplifier; if the current drawn by the amplifier is negligable, the voltage in this coil is related through Faraday's law to the derivative of the flux linked by the coil. The voltage can then be integrated (low pass filtered) to yield a measurement of the torus flux density B. The two signals can be used to drive the x-y display of an oscilloscope to plot the material B-H curve. An experiment of this type is described in [Haus and Melcher 1989], pg. 372. The B-H curve is then transferred to the finite element package to allow accurate calculation of the magnet forces and torques. Note however, that the platen is made of a different material than the electromagnets, and thus such a calibration has to be performed for the platen material as well.

Given these properties, the magnet force can be predicted by a 2-dimensional finite-element package. However, due to the lack of symmetry when the platen is rotated, determination of the magnet torques would require the use of a full 3-dimensional finite-element package.

Another approach to determining the magnet force and torques would be through experiment. This would entail building a fixture to hold the electromagnet. The fixture would include three force sensors, three position probes, and three micrometer heads with 0.0001" resolution. The electromagnet would be mounted pole face up in an aluminum base plate. The three position probes would be attached to the base plate, facing upwards, and arranged at the apices of an equilateral triangle centered on the electromagnet. The probes would be mounted such that their faces are coplanar with the face of the electromagnet, and thus they will sense position and two rotations relative to the magnet pole face. The three micrometer heads would also be mounted in the base plate, arranged at the apices of an identical triangle which is rotated by 60 degrees from the original triangle. The force sensors would be sandwiched between the micrometer faces and an iron plate which is attracted by the electromagnet. To yield accurate results, the iron plate should be made of the same material of the same thickness as the platen, and have been subjected to the same processing steps.

The force sensors would be capable of measuring three forces which can be resolved into a normal force and two torques, which are the variables of interest. By adjusting the micrometers, the magnet force and torques as a function of

frequency could then be measured at a number of positions and rotations, yielding the information necessary to model the electromagnetic actuators. The upper frequency limit of measurement accuracy would be set by the resonant frequency of the iron plate acting on the three force sensors' equivalent spring constants. In the vicinity of, or above the resonant frequency, force measurements cannot be made accurately. Thus the iron plate should be made as light as possible within the geometric contstraints of the experimental apparatus.

A third approach, which was adopted for this thesis, is to arrange for the magnetic suspension to serve as the calibration fixture for the electromagnets. The basic idea is to achieve stable suspension by any available means; the stability and performance need not be tremendous, the platen must simply be stably suspended. Once suspension is achieved, then there are many options available for measuring the magnet force-current-frequency parameters. At this stage of the thesis then, the important aspect of this approach is that we need to develop a relatively simple method for achieving active suspension in the full five degrees of freedom, without the need for a highly accurate model of the electromagnets.

As shown in the previous chapter, the dynamics are largely uncoupled between the vertical (pitch, roll, and heave) and the lateral (yaw, and lateral) motions. Thus it is reasonable to begin by studying the vertical motions alone. Thus, initially, only the top two magnet assemblies need to be attached to the primary support bracket. This three magnet, sixth order system can then be tested, and control ideas developed with about half the effort required for the full system. Only three current drives and probes are required. Then, experience gained with this simpler subsystem can be of assistance when the lateral electromagnets and control are added on later.

Another reason for studying this vertical subproblem is that it is advantageous to test the vertical system with the side magnet assemblies not installed onto the support brackets. If the side assemblies are uncontrolled, their permanent magnets will introduce destabilizing lateral forces, and their close proximity to the platen will create mechanical interferences. Both of these factors would make development of the vertical controller difficult. Thus, the approach used in assembling the system is intimately connected with the development of suspension control algorithms.

6.2 Vertical System Assembly

Following the strategy elucidated above, this section describes the manner in which the two top electromagnet assemblies were accurately attached to the primary support bracket, as well as the technique used for mounting the three top capacitance probes into the centers of their respective electromagnets.

6.2.1 Magnet Assemblies

In order to keep the bearing pole faces coplanar within a fraction of a thousandth of an inch, the top magnet assemblies were bolted to the primary support bracket while magnetically clamped to the top surface of the platen. Thus, the accurately ground top face of the platen defines the plane of the top magnet pole faces to the extent allowed by the mechanical accuracy of the magnet assemblies and support brackets. As noted in the previous chapter, these were machined to the required accuracy. The platen was shimmed up to the operating-point height using stacks of brass shim stock and aluminum foil under the three landing pad table legs. Care was taken not to mechanically constrain roll motions[1] of the platen as the six assembly bolts were tightened. This is important because it is the alignment of the top magnet assemblies to the support bracket which determines this degree of freedom. This decoupling was achieved by resting the platen on two 1" long, 0.030" diameter wires which were set parallel to the long axis of the platen and touched the platen on the centerline of its bottom face, thus allowing freedom in the roll mode. Note that because of this support arrangement, the landing pad supported the weight of the platen and top magnet assemblies as the bolts were tightened. Thus there was no lateral loading on these bolts, allowing them to freely center the platen in roll. Also, the magnetic clamping forces were thereby not required to support any gravity related forces as the system was assembled. Magnetic clamping was achieved by setting the three current drives to source one ampere through each of the three top electromagnets. The current drive design is described in detail in a subsequent section.

This approach was quite successful. Following assembly, the platen was fully supported by clamping to the top magnets, and the pole-face/platen interface was checked for any significant airgaps. There were no spots where a 0.001" feeler gauge could be inserted, indicating alignment to better than this figure. The resulting alignment has been satisfactory throughout all following work and has never required readjustment. If even higher stability of the alignment were required, the system could be assembled with a thin layer of adhesive placed in the joints between the magnet assemblies and the support brackets. This is a technique which has been used in the precision machines area. Personal communication with Prof. Slocum indicates that if low-bond (5 min. cure time) epoxy is used, these type of joints can be broken with a blow from a nylon-faced hammer, if this is required. In the current work, I did not feel comfortable with such a semi-permanet attachment method, unless it were experimentally determined that the joints without epoxy were mechanically unstable. However, experiment has indicated them to be sufficiently stable for the purposes of this research. In a production environment, where there was little need to disassemble the system,

[1] We define roll motions as rotations about the long axis of the platen.

this technique would be valuable for maintaining accuracy of alignment over time.

Following assembly, initial tests indicated that even though the pole faces had been ground on the two small top electromagnets, they were capable of supporting the platen with an undesirably small coil current (on the order of 0.2 A). The magnet safe full scale current set by thermal limits is on the order of 1.5 Amps. For large-signal response, it is desirable to run the magnets at about one half of this current in the steady state. Thus the effective magnet air gap was increased by applying three pieces of Scotch tape to each of the three top magnet faces. On each pole face, the three pieces were applyed radially, separated by 120 degrees, and not overlapping. The thickness of the tape is about 0.0025", and it is nonmagnetic, thus the magnet effective air gap is increased by this amount, while motion of the platen is stopped 0.0025" from the actual pole face. Operating farther from the pole faces further attenuates the undesired effect of the permanent magnets, and reduces the frequency of the unstable open-loop time constant.

6.2.2 Probes

The probes were installed with their faces coplanar with the surface of the tape. Thus the operating point for the platen was set to 0.005" away from the probe face, yet 0.0075" away from the magnet pole face. Since the probes are flush with the tape they are protected from damage. When the platen strikes the electromagnet it hits the tape, and forces can not be concentrated on the probe. Such forces might result in shifts in probe position or damage to the probe itself. The manner in which the probes were installed is described next.

In order to accurately align the probe faces with the surface of the tape on each of the three top magnets, the current drives were set to 1 Ampere in order to clamp the platen firmly against the tape surface. The three probes were then inserted into the central hole in the three top magnets such that their faces were resting against the platen surface. Thus the platen was used to accurately define the plane of the tape surface. The probes were permanently installed into the electromagnets by gluing them with epoxy. It was important here that the magnet and probe faces remain free of epoxy, in order to prevent contamination of their accurately ground surfaces.

The technique used for gluing the probes prevented any such contamination. Fresh 5 minute epoxy was mixed for each probe. After the epoxy was mixed, a 1/8" fillet of epoxy was formed in the annular region at the interface between the top of the aluminum probe holder and the outer surface of the cable end of the probe. At this point the probe face was still in contact with the platen top surface.

After the fillet had been formed, the probe was retracted from the electro-

magnet by about 1/4", allowing epoxy to coat the probe outer surface as it was withdrawn. This process was repeated several times to ensure a uniform coating, then the probe was reinserted and pressed firmly against the platen, thereby aligning its front surface with the surface of the tape. The probe was held in this position by gravity; while the epoxy cured, care was taken to apply no disturbance forces to the probe or its cable. In this fashion, the back 1/4"–1/2" of the ≈0.003" clearance between the probe and the probe holder was filled with epoxy, while keeping the face area clear of any contamination. This process was repeated for each of the three top probes. This method of attaching the probes has proven entirely adequate in maintaining the probe alignment.

6.3 Current Source Design

This section describes the magnet electrical parameters, short-circuits which developed in two of the electromagnets, and the two types of current drives which were designed to control the magnet coil currents.

6.3.1 Magnet Electrical Parameters

The large magnet has a coil resistance $R_{cl} = 4.4\ \Omega$, and inductance $L_{cl} = 48$ mH at the nominal operating point. The small magnet has a coil resistance $R_{cs} = 2.9\ \Omega$, and inductance $L_{cs} = 19$ mH at the nominal operating point.

On testing the magnets before assembly, it was discovered that two of the magnets had developed internal short-circuits. One of the side magnets had an intermittent short between one of its leads and the body of the electromagnet. The body of the electromagnet is necessarily grounded, thus this short forms a connection to ground on that side of the coil. A more serious problem was found in the large top electromagnet; an intermittent short was found between *both* coil leads and the magnet body, thereby shorting out the coil. In both cases, the shorts are believed to have occured through nicks in the magnet wire enamel where the wire feeds into the inner end of the coil access hole in the magnet body. The inner end of this hole was not chamfered, and no supplemental insulation was used on the coil wires in this area. In retrospect, these are obvious ommissions.

With some effort, by wiggling the coil leads on the large magnet, an arrangement was found whereby only one lead was shorted to the magnet body; the leads were epoxied in this postion. With only one side of the coil grounded, the magnets could be used with a current drive which was designed for a grounded load. Thus, the two magnets with shorts are driven single-ended, while the remaining five magnets are driven as floating loads. Two different current source designs were thus required; these are described in the next sections.

6.3.2 Current Source for Floating Load

The current source used to drive the five floating coils is shown in Figure 6.1. Current is sensed with a 1 Ω power resistor, and controlled via the IRF510 power FET. The coil is protected with a 2 amp fuse, and the series combination of the MUR1560 diode and 5 Ω resistor form a flyback network to allow coil current to continue to flow even when the FET is turned off suddenly. The 0.01 μF capacitor connected between the FET drain and ground was empirically selected to damp a closed-loop oscillation at about 500 kHz. A shown in the schematic, the +12 return, analog ground, and chassis ground were connected at only one point, in ord ensure that no coil currents flowed in the analog ground; the common point is at the ground end of the current sense resistor. In parallel with the 1 Ω current sense resistor, a 50 μA meter in series with a 37.5 kΩ resistor provides a front-panel indication of coil current.

The OP-27 op amp was used as the current controller for its low noise (especially in the 0.1–10 Hz band), high slew rate, and wide frequency response. The network at the noninverting input allows setting the DC current level through a 10 kΩ, 10 turn potentiometer, and couples current input signals through a lead network with a DC attenuation of 15, and unity gain at high frequencies. This lead network is included here because all anticipated position controller designs required lead compensation in the vicinity of crossover, and this allowed saving an additional stage in the position controller circuitry. Such savings are important, as five position control channels need to be constructed. With the input attenuation of 15 and the 1 Ω current sense resistor, the amplifier has a closed-loop response of 15 Volts input per ampere of coil current output. The 47 Ω resistor at the inverting input of the OP-27 allows the injection of disturbances into the current loop and is of the correct resistance to be driven by a standard signal generator. An AD581 voltage reference supplies 10 Volts to bias the upper end of the potentiometer.

6.3.3 Current Source for Grounded Load

The current source used to drive the two single-ended coils is shown in Figure 6.2. It is very similar to the floating load current source, with the exception that a p-channel IRF9520 power FET is used to invert the power portion of the circuit in order to arrange for the magnet coil to be tied to ground on one end. Also the OP-27 differential amplifier is used to translate the floating current sense resistor voltage into a single-ended signal. The four 10 kΩ resisors in the differential amplifier a matched to 0.02% in order to guarantee high common-mode rejection, and the 100 pf feedback capacitor assures stability of the relatively wide-band OP-27.

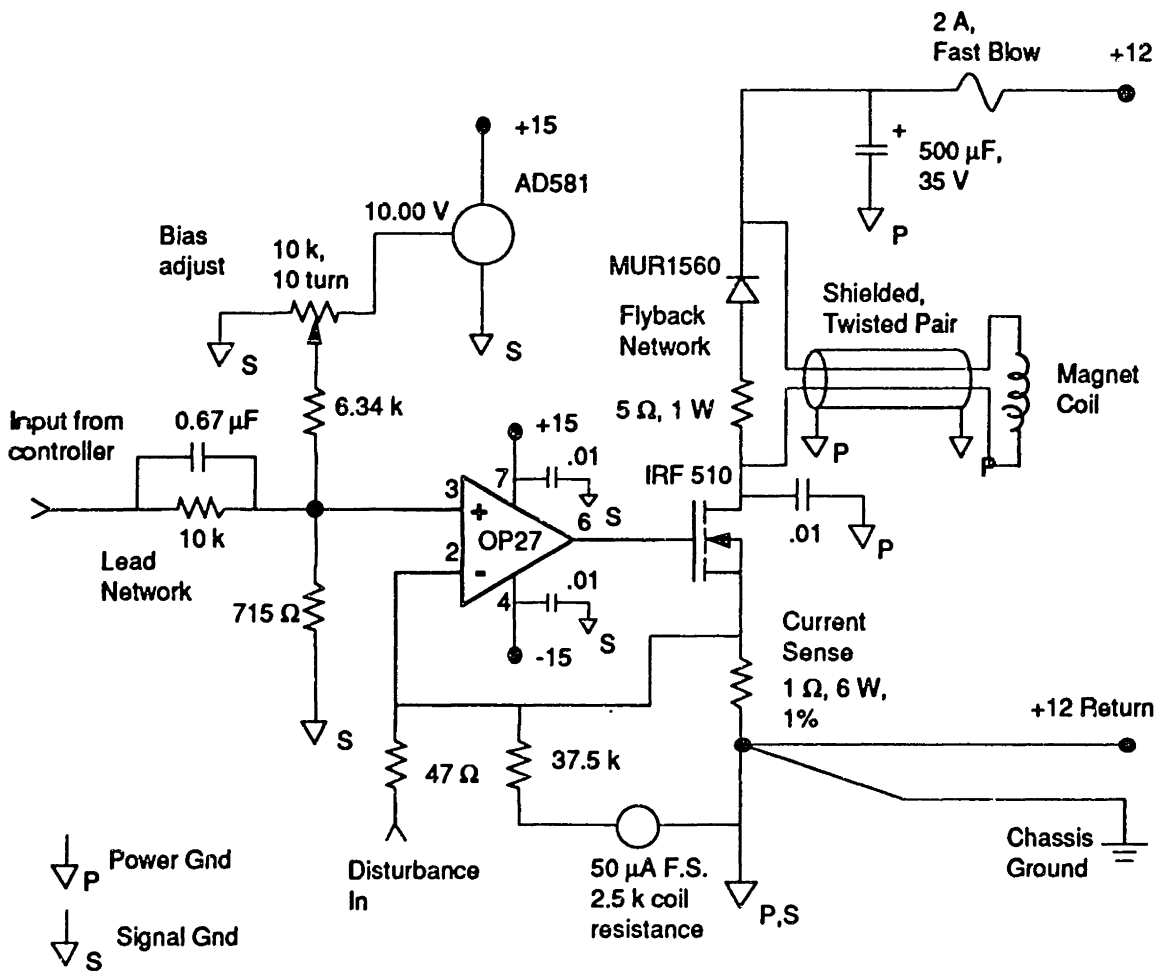

Figure 6.1: Current source for driving floating load.

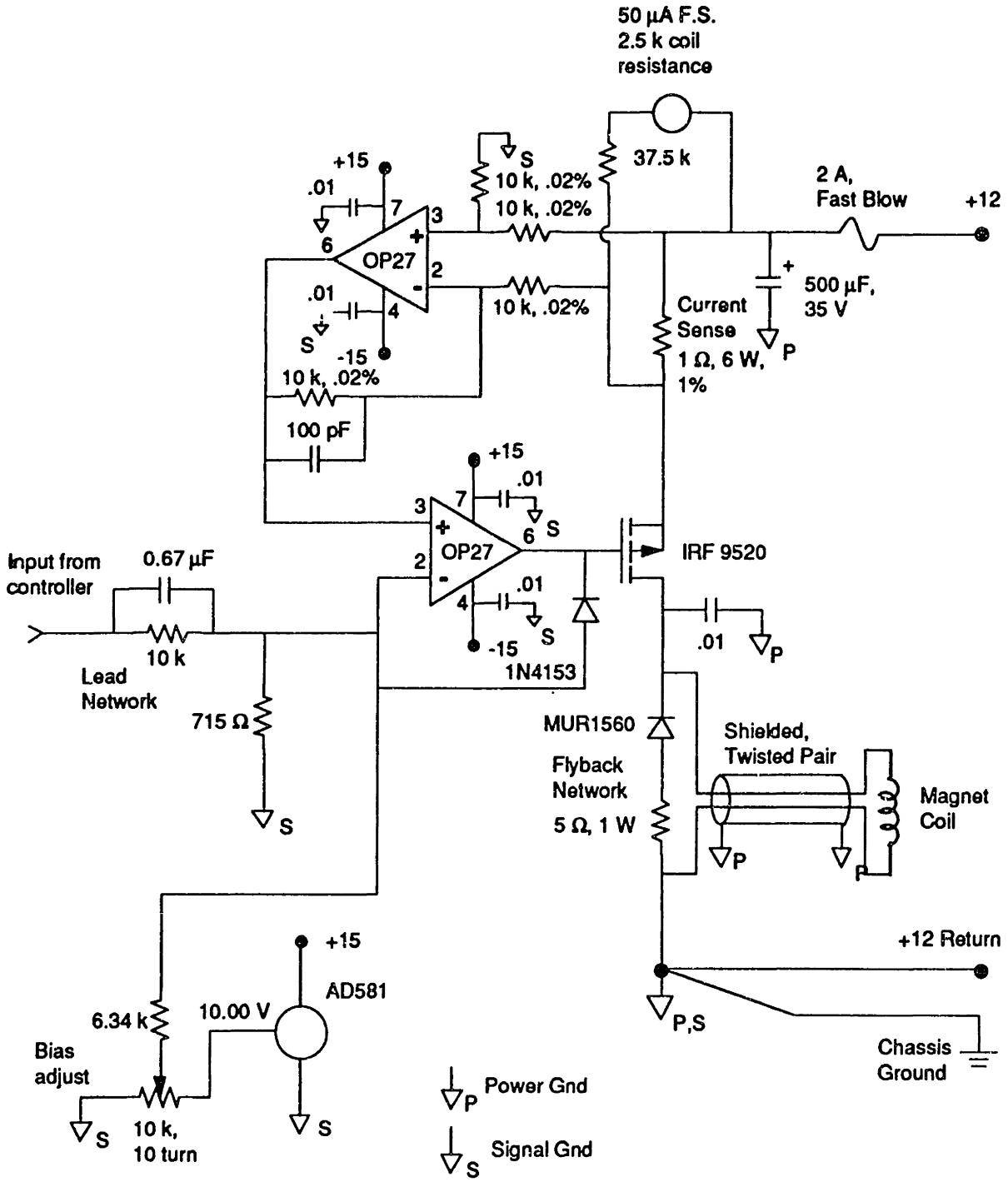

Figure 6.2: Current source for driving grounded load.

The 1N4153 diode acts as a clamp to prevent the application of excessively negative signals to the gate of the FET; with the given supply voltages, if the op amp output was allowed to pull down to -15 volts, the FET maximum gate-source voltage spec would be exceeded. The clamp diode prevents the output from going more than 0.6 volts below the amplifier input voltage, which is never more than about +2/-1 volts away from ground.

6.4 Magnet Force Measurements

In order to design a preliminary controller for the purpose of achieving levitation of the platen, rough measurements were made of the magnet force characteristics. This allowed a ball park controller design which was then empirically tuned.

A linear model for the magnet characteristics about some operating point is

$$\tilde{F} = k_i\tilde{i} + k_g\tilde{g}$$

where $\tilde{F}$ is the magnet incremental force of attraction in Newtons, $\tilde{i}$ is the incremental coil current, $\tilde{g}$ is the incremental motion in the direction of $\tilde{F}$, and k_i, k_g are constants of proportionality. Development of a linear model requires the measurement of k_i and k_g for both the small and the large bearings.

These constants were measured via the following experiment. Two thin wires of 0.005" diameter were stretched across the top surface of the platen perpendicular to its long axis, and intersecting the centerline of the small bearings and the large bearing, respectively. The ends of the wire were taped to the sides of the platen such that the wires were taught. Then the platen was clamped up against the pole faces of the three top magnets by setting the current drives to a sufficiently high value. In this fashion, the wires were sandwiched between the platen and the electromagnets, with the magnet/platen air gap thereby determined by the wire diameter. Only two current drives were used, one for the large electromagnet, and one for the two small electromagnets, which were wired in series.

At this point, the current in one of the current drives was reduced until the corresponding end of the platen dropped away from the magnet. Then an additional weight was added resting on the inside surface of the bottom of the platen immediately below the centerline of the magnet(s) being measured, and the experiment was repeated. The drop current was recorded for several different weights on both ends of the platen. Then 0.0075" wires were substituted for the 0.005" wires, and the full set of experiments repeated at this larger air gap. The resulting data is summarized in Table 6.1.

This data was taken before the mylar tape was attached to the bearing pole faces, and thus the gap is relative to the bearing pole face. In the case of the

	Large Bearing		Small Bearing	
Gap(in)	Current(mA)	Weight(gm)	Current(mA)	Weight(gm)
0.005"	203.5	30	343.4	120
0.005"	215.0	340	361.0	270
0.005"	231.0	490	380.5	480
0.005"	248.0	1220	423.6	1070
0.0075"	342.9	70	595.0	170
0.0075"	364.0	370	632.0	450
0.0075"	386.3	670	656.2	720

Table 6.1: Bearing force data.

small magnets, the additional weight is the total carried by the two top magnets; thus each magnet is carrying half this amount. The experiments were not highly repeatable; this is believed to be due to the variability of the magnet/wire/platen interface which had the opportunity to shift after each experiment. Another potential source of error is hysteresis in the magnetic materials. Higher accuracy measurements can be made once the platen is suspended.

These sets of measurements allowed the calculation of the linear magnet models for the large and the small bearings. The numerical results for the large magnet are $k_{gl} = 4.2 \times 10^5$N/m, and $k_{il} = 137$ N/A. The numerical results for the small magnets are $k_{gs} = 1.9 \times 10^5$N/m, and $k_{is} = 39$ N/A. The additional subscripts s and l refer to the small and large bearings respectively.

At this point a single degree of freedom controller was designed based upon these magnet parameters. The controller implemented integral and lead compensation. This controller was successfully used to float the large magnet end of the platen under the condition where the small bearing end of the platen was clamped up against one of the wires used in the previous experiment. In this context the wire served as a pivot which only allowed motion about the pitch degree of freedom. With retuning, the controller was also used to suspend the small bearing end of the platen by driving the two small magnets in series, with the large bearing end of the platen clamped against a thin pivot wire as before. These experiments served to verify the linear parameters for the large and small magnets.

I also attempted to use this single degree of freedom suspension to experimentally measure the transfer function from coil current to platen position, but this effort was not successful. The transfer function was measured with an HP3562A dynamic analyzer, but was not repeatable. The measured transfer function displayed a resonance in the vicinity of 40 Hz. The damping and center frequency of

this resonance varied significantly each time the experiment was repeated. After trying different support arrangements, it became apparent that the resonance was due to the interaction of the platen mass with the support wire clamped against the small bearing faces. Thus it was not possible to use the single degree of freedom suspension to develop a dynamic model for the bearings. At this point it was clear that suspension in the full five degrees of freedom was required in order to develop models for the bearing dynamics.

6.5 Approximate Model for Vertical Dynamics

In this section an open-loop model for the vertical suspension dynamics is developed which incorporates the linear bearing models developed in the previous section. The object is to develop a simple model for the dynamics which will allow the design of a control strategy for suspension. A number of assumptions are made in order to simplify this process without losing any essential details. The vertical dynamics are viewed as uncoupled from the horizontal dynamics, and translations in the x_1 and x_3 directions are set to zero. As the bearing torque terms are as yet unknown, they are ignored. Applying these assumptions to the linear dynamical equations developed in Section 5.2, and focusing on the three vertical degrees of freedom yields the following sixth order set of state equations.

$$\dot{\tilde{q}}_1 = \tilde{u}_1 \tag{6.1}$$
$$\dot{\tilde{q}}_3 = \tilde{u}_3 \tag{6.2}$$
$$\dot{\tilde{x}}_2 = \tilde{u}_5 \tag{6.3}$$
$$I_1\dot{\tilde{u}}_1 = W_m(\tilde{F}_2 - \tilde{F}_3) \tag{6.4}$$
$$I_3\dot{\tilde{u}}_3 = L_m(-\tilde{F}_1 + \tilde{F}_2 + \tilde{F}_3) \tag{6.5}$$
$$M\dot{\tilde{u}}_5 = \tilde{F}_1 + \tilde{F}_2 + \tilde{F}_3 \tag{6.6}$$

where we have set $\tilde{T}_{jk} = 0$, $\tilde{x}_3 = 0$, and $\tilde{x}_1 = 0$.

These equations are expressed in terms of the state variables used in Chapter 5. However, the bearing forces depend on the pole face air gap. Define $\tilde{g}_j$ as the incremental change in the jth air gap in the direction of the jth force. Then, using the results of the previous section, the incremental forces for the three top electromagnets are given by

$$\tilde{F}_1 = k_{il}\tilde{i}_1 + k_{gl}\tilde{g}_1 \tag{6.7}$$
$$\tilde{F}_2 = k_{is}\tilde{i}_2 + k_{gs}\tilde{g}_2 \tag{6.8}$$
$$\tilde{F}_3 = k_{is}\tilde{i}_3 + k_{gs}\tilde{g}_3 \tag{6.9}$$
$$\tag{6.10}$$

To linear terms, the three top magnet incremental air gaps are related to the state variables as

$$\tilde{g}_1 = \tilde{x}_2 - L_m \tilde{q}_3 \tag{6.11}$$
$$\tilde{g}_2 = \tilde{x}_2 + L_m \tilde{q}_3 + W_m \tilde{q}_1 \tag{6.12}$$
$$\tilde{g}_3 = \tilde{x}_2 + L_m \tilde{q}_3 - W_m \tilde{q}_1 \tag{6.13}$$

Combining equations 6.1 through 6.13, and substituting in the numerical values for the constants which have been calculated earlier, yields the rough numerical model for the vertical suspension dynamics as

$$\dot{w}_v = A_v w_v + B_v i_v \tag{6.14}$$
$$y_v = C_v w_v \tag{6.15}$$

where $w_v = [\ \tilde{q}_1\ \tilde{q}_3\ \tilde{x}_2\ \tilde{u}_1\ \tilde{u}_3\ \tilde{u}_5\ ]'$, $i_v = [\ \tilde{i}_1\ \tilde{i}_2\ \tilde{i}_3\ ]'$, $y_v = [\ \tilde{q}_1\ \tilde{q}_3\ \tilde{x}_2\ ]'$,

$$A_v = \begin{bmatrix} 0 & 0 & 0 & 1 & 0 & 0 \\ 0 & 0 & 0 & 0 & 1 & 0 \\ 0 & 0 & 0 & 0 & 0 & 1 \\ 8.05 \times 10^3 & 0 & 0 & 0 & 0 & 0 \\ 0 & 5.01 \times 10^4 & -2.52 \times 10^4 & 0 & 0 & 0 \\ 0 & -3.18 \times 10^2 & 7.43 \times 10^4 & 0 & 0 & 0 \end{bmatrix}, \tag{6.16}$$

$$B_v = \begin{bmatrix} 0 & 0 & 0 \\ 0 & 0 & 0 \\ 0 & 0 & 0 \\ 0 & 26.0 & -26.0 \\ -93.4 & 26.6 & 26.6 \\ 12.8 & 3.64 & 3.64 \end{bmatrix}, \tag{6.17}$$

and

$$C_v = \begin{bmatrix} 1 & 0 & 0 & 0 & 0 & 0 \\ 0 & 1 & 0 & 0 & 0 & 0 \\ 0 & 0 & 1 & 0 & 0 & 0 \end{bmatrix}. \tag{6.18}$$

In this section, the matrices above are shown with three significant figures, but the intermediate computations are carried out with higher precision.

These state equations describe the open-loop linearized dynamics of the suspension under the assumptions given at the beginning of this section. An eigenanalysis of these dynamics gives insight into the plant behavior. The eigenvalues

of A_v are

$$\begin{bmatrix} \lambda_1 \\ \lambda_2 \\ \lambda_3 \\ \lambda_4 \\ \lambda_5 \\ \lambda_6 \end{bmatrix} = \begin{bmatrix} 89.7 \\ -89.7 \\ -273 \\ 273 \\ 223 \\ -223 \end{bmatrix}, \tag{6.19}$$

and the corresponding right eigenvectors are $[\ v_1\ v_2\ v_3\ v_4\ v_5\ v_6\ ] =$

$$\begin{bmatrix} 1.11 \times 10^{-2} & 1.11 \times 10^{-2} & 0 & 0 & 0 & 0 \\ 0 & 0 & 2.62 \times 10^{-3} & -2.62 \times 10^{-3} & 4.48 \times 10^{-3} & -4.48 \times 10^{-3} \\ 0 & 0 & -2.56 \times 10^{-3} & 2.56 \times 10^{-3} & 5.79 \times 10^{-5} & -5.79 \times 10^{-5} \\ 1.00 & -1.00 & 0 & 0 & 0 & 0 \\ 0 & 0 & -7.16 \times 10^{-1} & -7.16 \times 10^{-1} & 1.00 & 1.00 \\ 0 & 0 & 6.98 \times 10^{-1} & 6.98 \times 10^{-1} & 1.29 \times 10^{-2} & 1.29 \times 10^{-2} \end{bmatrix}.$$

Terms which are numerically small have been replaced with zeros to make the eigenstructure more apparent.

Examination of the structure of the eigenvalues and eigenvectors indicates that there are three pairs of modes which are each similar to the pair of modes which were investigated for the one degree of freedom suspension in Chapter 3. The entries in the first pair of eigenvectors v_1 and v_2 indicate that the pair of eigenvalues ± 89.7 sec^{-1} correspond to rotations q_1, i.e., in the roll mode. The entries, v_3 and v_4 indicate that the pair of eigenvalues ± 273 sec^{-1} correspond to about equal amounts of rotations q_3, and translations x_2 . Finally, v_5 and v_6 indicate that the pair of eigenvalues ± 223 sec^{-1} correspond to almost pure rotations q_3 . The system is of course open-loop unstable.

There is a mode in pure roll because the two small top bearings are assumed to be matched. The modes in pitch q_3 and translation x_2 interact because k_{gl} is not exactly equal to $2k_{gs}$. If the magnet parameters were perfectly matched, then there would be modes in pure pitch and translation as well. Of course in any actual hardware, matching can never be perfect, and thus the mode shapes will always exhibit some degree of cross-coupling. To the extent that the hardware is carefully constructed, this cross-coupling can be reduced to a negligible level.

6.6 Local Control of Vertical System

In this section the model developed above is used to design a controller which makes the current in each bearing depend only upon that bearing's local position measurement. This strategy is used to design local controllers for the three top bearings which set the frequency and damping of the heave mode. This is a

very simple control strategy; however, it was found to be inadequate. On paper, the heave mode is well controlled, but the roll and pitch modes are found to be unacceptably lightly damped.

6.6.1 Theory

The local controller is designed such that the heave mode natural frequency and damping ratio are set to reasonable values. This approach to designing magnetic bearings via their closed-loop natural frequency and damping ratio has frequently been adopted in the literature. For the purposes of this section the controller is designed to regulate the incremental gap to zero, and thus has no explicit setpoint input. Additionally, as purpose of this design is primarily instructive, and it does not result in a successful system, neither the current drives nor the probe electronics are modeled here, in order to reduce the complexity of the presentation. These factors are addressed in the section on modal design.

The viewpoint is that the log is composed of three independent masses of $M/2$, $M/4$, and $M/4$ suspended by the large bearing and the two small top bearings, respectively. These masses are assumed free to move only in the heave mode. In terms of their open-loop natural frequencies, each of these masses can be thought of as being acted upon by a negative spring $-k_m$, such that all three have the same natural frequency. The controller for each mass is designed to create the equivalent of a positive spring k_c in parallel with a viscous damper b_c. A mass acted upon by these three factors is shown in Figure 6.3. The closed-loop combination will be stable as long as the damping coefficient b_c is greater than zero, and the positive spring rate k_c is greater in magnitude than the open-loop negative spring rate $-k_m$. This statement has its corresponding images in the root-locus and Nyquist domains as developed in more detail in Chapter 3.

It seemed reasonable that if the heave mode was well-behaved, the pitch and roll modes would have acceptable dynamics as well. This turns out not to be the case, but it is instructive to follow through the design process.

The natural frequency for the system of Figure 6.3 is $\omega_n = \sqrt{(k_c - k_m)/M}$ and the damping ratio is $\zeta = (b_c/2M\omega_n)$. As reasonable design values, the controller is designed to set $\omega_n = 628$ rad/sec and $\zeta = 1$. The mass of the platen is 10.72 kg. Thus for the large bearing, $M = 5.36$ and for each of the two small bearings, $M = 2.68$. From earlier results, for the large bearing $k_m = k_{gl} = 4.2 \times 10^5$ N/m, and for the small bearings $k_m = k_{gs} = 1.9 \times 10^5$ N/m. To set the desired natural frequencies and damping ratios then the controller for the large bearing must have $k_{cl} = 2.53 \times 10^6$ N/m and $b_{cl} = 6.73 \times 10^3$ N-sec/m. The controller for the small bearing must have $k_{cs} = 1.25 \times 10^6$ N/m and $b_{cs} = 3.37 \times 10^3$ N-sec/m.

Skipping over some numerical details, these values can be implemented by letting $\tilde{i}_1 = -1.84 \times 10^4 \tilde{g}_1 - 49.0\dot{\tilde{g}}_1$, $\tilde{i}_2 = -3.20 \times 10^4 \tilde{g}_2 - 86.3\dot{\tilde{g}}_2$, and $\tilde{i}_3 =$

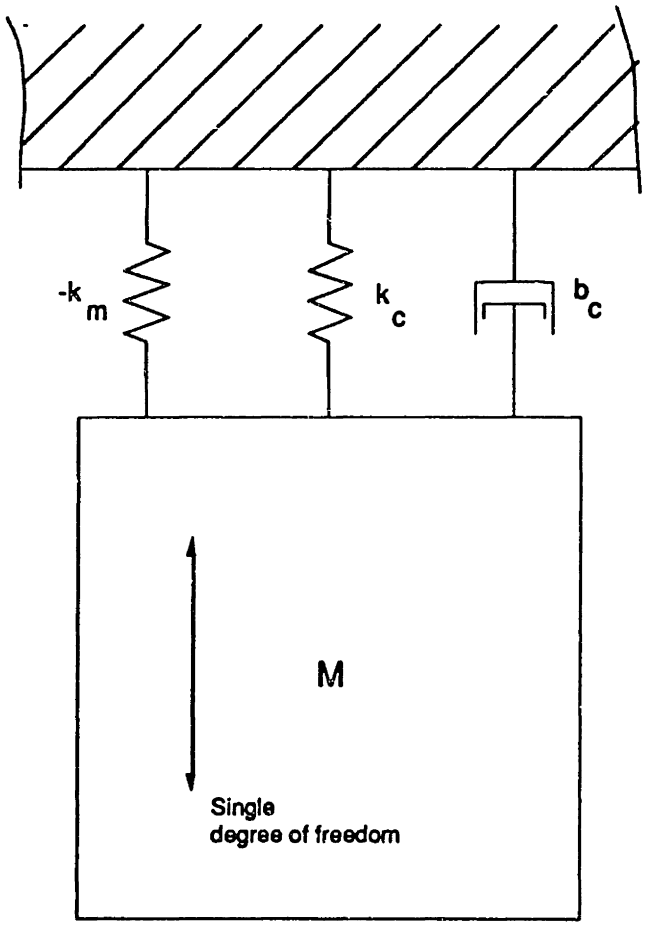

Figure 6.3: A mass acted upon by the open-loop unstable magnetic spring constant $-k_m$, and the controller equivalent spring and damping terms k_c and b_c.

$-3.20 \times 10^4 \tilde{g}_3 - 86.3\dot{\tilde{g}}_3$. That is, the controller should implement proportional plus derivative control. In transfer function form, these compensators consist of a single zero.

The derivative of the gaps can not be directly measured. Thus it is not physically possible to implement the free differentiator implied by these equations. Therefore a pole is added to the compensators a factor of 100 farther from the origin than the compensator zeros, changing the compensator to proportional plus lead. This unrealistically large lead factor is chosen so that the calculated results for the closed-loop modes come out close to those for the ideal proportional plus derivative control. If a factor of only 10 is used, the resulting closed-loop singularities are not close to the design values. Incorporating this pole and putting the results in matrix form gives the compensator state equation

$$\dot{z}_v = A_{vc} z_v + B_{vc} g_v \tag{6.20}$$

$$i_v = C_{vc} z_v + D_{vc} g_v. \tag{6.21}$$

where z_v is the three element compensator state vector, $g_v = [\ \tilde{g}_1\ \tilde{g}_2\ \tilde{g}_3\ ]'$, $i_v = [\ \tilde{i}_1\ \tilde{i}_2\ \tilde{i}_3\ ]'$ as before, and

$$A_{vc} = \begin{bmatrix} -3.76 \times 10^3 & 0 & 0 \\ 0 & -3.70 \times 10^3 & 0 \\ 0 & 0 & -3.70 \times 10^3 \end{bmatrix}, \tag{6.22}$$

$$B_{vc} = \begin{bmatrix} 1 & 0 & 0 \\ 0 & 1 & 0 \\ 0 & 0 & 1 \end{bmatrix}, \tag{6.23}$$

$$C_{vc} = \begin{bmatrix} 6.24 \times 10^8 & 0 & 0 \\ 0 & 1.07 \times 10^9 & 0 \\ 0 & 0 & 1.07 \times 10^9 \end{bmatrix}, \tag{6.24}$$

and

$$D_{vc} = \begin{bmatrix} -1.84 \times 10^5 & 0 & 0 \\ 0 & -3.20 \times 10^5 & 0 \\ 0 & 0 & -3.20 \times 10^5 \end{bmatrix}. \tag{6.25}$$

Note that because the controller transfer functions are not proper, there is a direct feedthrough D_{vc} from input to output.

The compensator equations are expressed in terms of the incremental gap variations g_v, whereas the plant model (6.14)-(6.15) has the state variables y_v as outputs. These two sets of quantities are related to linear terms through (6.11)-(6.13); re-expressed in matrix form as

$$g_v = T_{gy} y_v \tag{6.26}$$

where

$$T_{gy} = \begin{bmatrix} 0 & -L_m & 1 \\ W_m & L_m & 1 \\ -W_m & L_m & 1 \end{bmatrix} = \begin{bmatrix} 0 & -0.0921 & 1 \\ 0.0318 & 0.0921 & 1 \\ -0.0318 & 0.0921 & 1 \end{bmatrix} \tag{6.27}$$

This transformation is used to express the compensator inputs in terms of the plant outputs. The closed-loop state equation is then written by combining the plant and compensator state vectors into a single state vector. As there are no inputs or outputs for the purposes of this exercise, the closed-loop state equation is simply of the form

$$\begin{bmatrix} \dot{w}_v \\ \dot{z}_v \end{bmatrix} = A_{vcl} \begin{bmatrix} w_v \\ z_v \end{bmatrix} \tag{6.28}$$

where

$$A_{vcl} = \begin{bmatrix} (A_v + B_v D_{vc} T_{gy} C_v) & B_v C_{vc} \\ B_{vc} T_{yg} C_v & A_{vc} \end{bmatrix} =$$

$$\begin{bmatrix} 0 & 0 & 0 & 1.00 & 0 & 0 & 0 & 0 & 0 \\ 0 & 0 & 0 & 0 & 1.00 & 0 & 0 & 0 & 0 \\ 0 & 0 & 0 & 0 & 0 & 1.00 & 0 & 0 & 0 \\ -5.27 \times 10^6 & 0 & 0 & 0 & 0 & 0 & 0 & 3.05 \times 10^{12} & -3.05 \times 10^{12} \\ 0 & -3.15 \times 10^7 & 2.25 \times 10^6 & 0 & 0 & 0 & -6.42 \times 10^{12} & 3.12 \times 10^{12} & 3.12 \times 10^{12} \\ 0 & 2.81 \times 10^4 & -4.68 \times 10^7 & 0 & 0 & 0 & 8.78 \times 10^{11} & 4.27 \times 10^{11} & 4.27 \times 10^{11} \\ 0 & -9.21 \times 10^{-2} & 1.00 & 0 & 0 & 0 & -3.76 \times 10^{04} & 0 & 0 \\ 3.18 \times 10^{-2} & 9.21 \times 10^{-2} & 1.00 & 0 & 0 & 0 & 0 & -3.70 \times 10^4 & 0 \\ -3.18 \times 10^{-2} & 9.21 \times 10^{-2} & 1.00 & 0 & 0 & 0 & 0 & 0 & -3.70 \times 10^4 \end{bmatrix} \tag{6.29}$$

The eigenvalues of A_{vcl} are

$$\begin{bmatrix} \lambda_1 \\ \lambda_2 \\ \lambda_3 \\ \lambda_4 \\ \lambda_5 \\ \lambda_6 \\ \lambda_7 \\ \lambda_8 \\ \lambda_9 \end{bmatrix} = \begin{bmatrix} -3.69 \times 10^4 \\ -3.66 \times 10^4 \\ -3.59 \times 10^4 \\ -7.08 \times 10^1 + 1.99 \times 10^2 j \\ -7.08 \times 10^1 - 1.99 \times 10^2 j \\ -4.27 \times 10^2 + 2.97 \times 10^2 j \\ -4.27 \times 10^2 - 2.97 \times 10^2 j \\ -7.16 \times 10^2 \\ -5.69 \times 10^2 \end{bmatrix}, \tag{6.30}$$

and the corresponding right eigenvectors are $[\ v_1\ v_2\ v_3\ v_4\ v_5\ v_6\ v_7\ v_8\ v_9\ ] =$

$$\begin{bmatrix} -2.70 \times 10^{-5} & 0 & 0 & -1.35 \times 10^{-3} + 4.51 \times 10^{-3} j & -1.35 \times 10^{-3} - 4.51 \times 10^{-3} j & 0 & 0 & 0 & 0 \\ 0 & 2.72 \times 10^{-5} & -2.68 \times 10^{-5} & 0 & 0 & 0 & 0 & 1.34 \times 10^{-3} - 1.36 \times 10^{-3} j & 1.34 \times 10^{-3} + 1.36 \times 10^{-3} j & 3.61 \times 10^{-5} & 4.56 \times 10^{-5} \\ 0 & -1.86 \times 10^{-6} & -7.49 \times 10^{-6} & 0 & 0 & 0 & 0 & -4.07 \times 10^{-7} + 4.06 \times 10^{-7} j & -4.07 \times 10^{-7} - 4.06 \times 10^{-7} j & 1.39 \times 10^{-3} & 1.75 \times 10^{-3} \\ 1.00 & 0 & 0 & -8.06 \times 10^{-1} - 5.91 \times 10^{-1} j & -8.06 \times 10^{-1} + 5.91 \times 10^{-1} j & 0 & 0 & 0 & 0 & 0 & 0 \\ 0 & -9.97 \times 10^{-1} & 9.63 \times 10^{-1} & 0 & 0 & -1.69 \times 10^{-1} + 9.85 \times 10^{-1} j & -1.69 \times 10^{-1} - 9.85 \times 10^{-1} j & -2.58 \times 10^{-2} & -2.59 \times 10^{-2} \\ 0 & 6.82 \times 10^{-2} & 2.69 \times 10^{-1} & 0 & 0 & 5.32 \times 10^{-5} - 2.95 \times 10^{-4} j & 5.32 \times 10^{-5} + 2.95 \times 10^{-4} j & -9.99 \times 10^{-1} & -9.99 \times 10^{-1} \\ 0 & -4.38 \times 10^{-9} & -2.94 \times 10^{-9} & 0 & 0 & -3.31 \times 10^{-9} + 3.42 \times 10^{-9} j & -3.31 \times 10^{-9} - 3.42 \times 10^{-9} j & 3.77 \times 10^{-8} & 4.73 \times 10^{-8} \\ -6.07 \times 10^{-9} & 1.48 \times 10^{-9} & -8.70 \times 10^{-9} & -1.14 \times 10^{-9} + 3.88 \times 10^{-9} j & -1.14 \times 10^{-9} - 3.88 \times 10^{-9} j & 3.34 \times 10^{-9} - 3.45 \times 10^{-9} j & 3.34 \times 10^{-9} + 3.45 \times 10^{-9} j & 3.84 \times 10^{-8} & 4.82 \times 10^{-8} \\ 6.07 \times 10^{-9} & 1.48 \times 10^{-9} & -8.70 \times 10^{-9} & 1.14 \times 10^{-9} - 3.88 \times 10^{-9} j & 1.14 \times 10^{-9} + 3.88 \times 10^{-9} j & 3.34 \times 10^{-9} - 3.45 \times 10^{-9} j & 3.34 \times 10^{-9} + 3.45 \times 10^{-9} j & 3.84 \times 10^{-8} & 4.82 \times 10^{-8} \end{bmatrix} \tag{6.31}$$

Terms which are numerically insignificant have been replaced with zeros to make the eigenstructure more apparent.

The first three eigenvalues are very high frequency, and are associated with the open-loop poles of the controller. They are thus not of primary interest here. The last pair of eigenvalues λ_8 and λ_9 are centered about the design value of -628. That the poles are not exactly located at the design location is due to the addition of the poles to the compensator, in order to make it proper. If the compensator poles are placed a factor of 1000 above the compensator zeros, then this pair of eigenvalues are closer to coinciding at the design value. The associated eigenvectors v_8 and v_9 are almost completely in the direction of motion in x_2, as designed for.

The remaining eigenvalues are significant modes which were not explicitly determined in the design process. The eigenvalues λ_6 and λ_7 are associated with primarily pitching motions in q_3, as shown by their associated eigenvectors. These modes are moderately damped. The eigenvalues λ_4 and λ_5 are associated with

pure roll motions in q_1, as shown by their associated eigenvectors. These modes are lightly damped, and therefore exhibit dynamics which may not be acceptable in a precision motion control system. As an example, in the case of scanned probe microscopy, overshoot is clearly undesirable, as it may result in the probe crashing into the surface. The design process used in this section offers no direct handle on this problem. One can see that the damping of the roll mode needs to be increased; this can be accomplished by increasing the coefficients b_{c_s} associated with the two small bearings.

Certainly then, this design can be improved by a cut and try process. This approach is somewhat akin to the tuning of an automobile suspension. In the passive suspensions which have primarily been used in automobiles to date, the suspension components act on each wheel locally, as do the bearings here. In the case of a mechanical suspension, by proper tuning of spring rates and damping ratios, a reasonable compromise can be achieved where the various modes have acceptable dynamics. In the current case, because the design is electronic, the individual bearing responses can readily be made to depend on *all* the position measurements. In this manner, the modal responses can be individually tuned to have desirable dynamics without degrading one at the expense of another.

In the current design, the heave translation mode was designed to have a given natural frequency and damping ratio. In this sense the design goals have been achieved. This design process was attractive in the sense that we could think physically in terms of spring and damping coefficients, and only three second-order dynamical systems needed to be considered. The multi-variable nature of the plant was ignored. The penalty paid is that the other two modes were essentially free parameters, with only the hope that they would turn out to have reasonable dynamics when the design was complete. Also, the design results in a proportional plus derivative controller which can only be implemented approximately. The closed-loop dynamics depend sensitively upon the quality of the approximation. That is, the additional controller poles had to be located a factor of 100 higher in frequency than the controller zeros in order that the closed-loop translation poles were close to the design value of $s = -628$. However, this factor of 100 results in a physically unrealistic controller. A design technique which requires these types of approximations is clearly undesirable.

The bottom line is that to use the controllers in a purely local mode is to give up powerful degrees of freedom. Also, the design technique should result in physically realizable controllers without built-in approximations. For these reasons, a slightly more sophisticated controller architecture was adopted in which the modal responses can be approximately decoupled and independently compensated for good dynamic response. This architecture is described in the next section.

6.7 Modal Control of Vertical System

The design of a controller which attempts to decouple and independently compensate the modes is described in this section. The decoupling design is based upon physical reasoning, and is implemented in analog electronics. This controller was designed based upon the plant model developed in Section 6.5; empirical tuning in the laboratory resulted in successful suspension in the three vertical degrees of freedom. The nominal design process is described in the next section, the controller design is described in Section 6.7.1, and the experimental results are given in Section 6.7.2.

6.7.1 Theory

The models used up to this point do not incorporate the current-drive dynamics, nor the relationship between platen position and the probe output voltages. Also, the modal controller design includes a network at the input of the plant which serves to convert from modal control signals to individual current setpoints and a network at the output of the plant which converts from the individual probe voltages to signals which represent the modal motions. A block diagram showing this control architecture is given in Figure 6.4. All the data paths carry three-vectors, although they are shown as single lines in the figure.

The open-loop dynamics, current-drive dynamics and controller dynamics are given by their associated system matrices. The matrix T_{py} transforms the state variables y into the probe voltages v_p. The matrix T_{mp} transforms the the probe voltages v_p into voltages v_m which represent motions in the roll, pitch and heave modes. The voltages v_m are subtracted from the modal setpoints v_s to give the modal errors v_e. These three errors are processed by the three independent modal controllers to give the control voltages v_u which represent drives to the three modes. The matrix T_{iu} transforms the control voltages v_u into voltages v_i which control the current setpoints for the three current drives. The current drives establish currents i which act as inputs to the plant, thereby driving the state variables y.

The position probes have a sensitivity of 5 volts per 0.001" or 1.97×10^5 volts per meter, increasing as $\tilde{g}_j$ increases. Thus the matrix T_{py} is given by

$$T_{py} = 1.97 \times 10^5 T_{gy} = \begin{bmatrix} 0 & -1.81 \times 10^4 & 1.97 \times 10^5 \\ 6.25 \times 10^3 & 1.81 \times 10^4 & 1.97 \times 10^5 \\ -6.25 \times 10^3 & 1.81 \times 10^4 & 1.97 \times 10^5 \end{bmatrix} \tag{6.32}$$

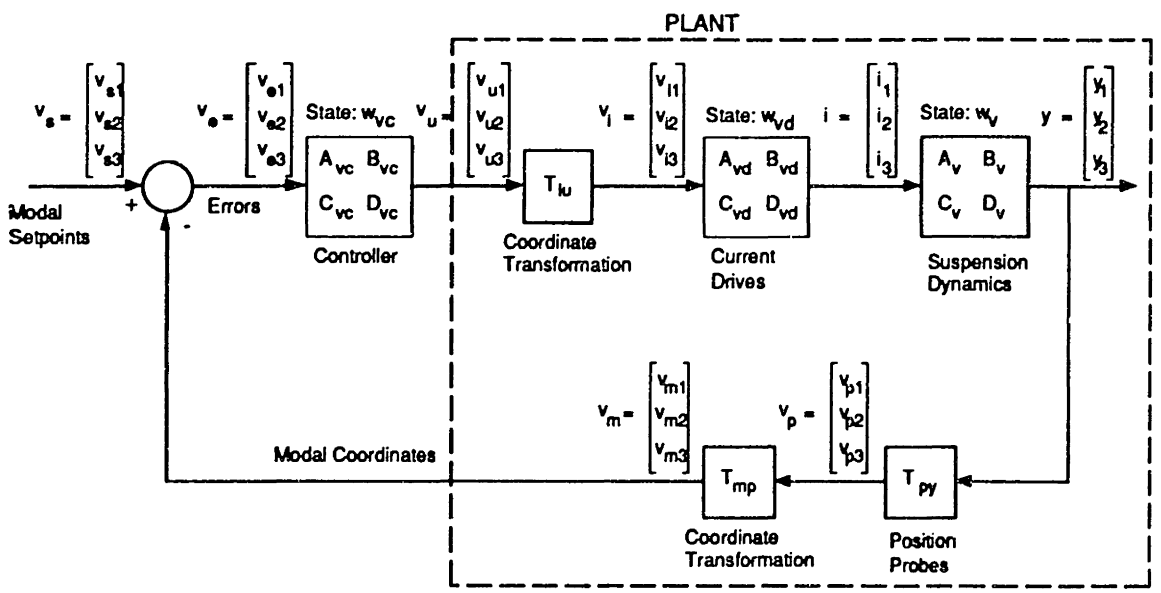

Figure 6.4: Block diagram for the vertical control loop.

Then T_{mp} is defined as

$$T_{mp} = \begin{bmatrix} 0 & 0.5 & -0.5 \\ -0.5 & 0.25 & 0.25 \\ 0.5 & 0.25 & 0.25 \end{bmatrix} \tag{6.33}$$

The relative scaling of the elements in the array is dictated by the suspension geometry. The absolute levels are chosen so that the voltages v_m saturate[2] only when all three probe outputs are saturated.

T_{iu} is defined as

$$T_{iu} = \begin{bmatrix} 0 & -0.57 & 0.57 \\ 1 & 1 & 1 \\ -1 & 1 & 1 \end{bmatrix} \tag{6.34}$$

The relative scaling of the elements in the array is dictated the ratio of the large and small magnet current constants. That is, the magnitude ratio of the 1-2 and 1-3 entries to the 2-2, 3-2, 2-3, and 3-3 entries is equal to $2 * k_{is}/k_{il}$ The absolute levels are chosen so that as many of the entries as possible are of unity magnitude. This allows an easier circuit implementation and is such that a single modal control signal can saturate the current drives.

The current drive circuits have been presented in Section 6.3. Each of the current drives has a transfer function from input v_{ij} to output i_j given by

$$\frac{i_j(s)}{v_{ij}(s)} = \frac{1}{\alpha}\frac{\alpha\tau s + 1}{\tau s + 1} \tag{6.35}$$

where $\alpha = 15$ and $\tau = 4.47 \times 10^{-4}$. Combining the three current drives in parallel yields the current source system equations as

$$\dot{w}_{vd} = A_{vd}w_{vd} + B_{vd}v_i \tag{6.36}$$
$$i = C_{vd}w_{vd} + D_{vd}v_i \tag{6.37}$$

where

$$A_{vd} = \mathrm{diag}(-2.24 \times 10^3,\ -2.24 \times 10^3,\ -2.24 \times 10^3) \tag{6.38}$$
$$B_{vd} = \mathrm{diag}(1,\ 1,\ 1) \tag{6.39}$$
$$C_{vd} = \mathrm{diag}(-2.09 \times 10^3,\ -2.09 \times 10^3,\ -2.09 \times 10^3) \tag{6.40}$$
$$D_{vd} = \mathrm{diag}(1,\ 1,\ 1) \tag{6.41}$$

For the purposes of design, the region contained within the dashed line in Figure 6.4 is considered to be the plant which is controlled by the controller.

[2]Recall that the probe outputs and the op amps used to implement these coordinate transformations saturate at about ± 13 volts.

Combining all the information developed above yields the plant system matrices as

$$\dot{w}_{vp} = A_{vp} w_{vp} + B_{vp} v_u \tag{6.42}$$

$$v_m = C_{vp} w_{vp} + D_{vp} v_u \tag{6.43}$$

where $w_{vp} = [\ w_v'\ w_{vd}'\ ]'$ and

$$A_{vp} = \begin{bmatrix} A_v & B_v C_{vd} \\ 0 & A_{vd} \end{bmatrix} \tag{6.44}$$

$$B_{vp} = \begin{bmatrix} B_v D_{vd} T_{iu} \\ B_{vd} T_{iu} \end{bmatrix} \tag{6.45}$$

$$C_{vp} = \begin{bmatrix} T_{mp} T_{py} C_v & 0 \end{bmatrix} \tag{6.46}$$

$$D_{vp} = [0] \tag{6.47}$$

where the indicated zero blocks are of the appropriate dimensions.

A copy of the Matlab output for the numerical values of the system matrices is given in Figure 6.5. D_{vp} is not shown because it is identically zero.

Bode plots for the plant transfer functions from the controller output v_u to the coordinate transformation output v_m are shown in Figures 6.6, 6.7, and 6.8. This design results in near-diagonalization of the plant. There is no cross-coupling to the first output from the second and third inputs, nor from the first input to the second and third outputs. The transfer function from the first input (roll) to the first output is shown in Figure 6.6. The transfer functions from the second input (pitch) to the second and third outputs are shown in Figure 6.7. Note that the cross-coupling from the pitch input to the heave mode is attenuated at low frequencies by a factor of about 20 relative to the coupling into the pitch mode. In the vicinity of cross-over at 100 Hz, the relative coupling is attenuated by a factor of about 130. The transfer functions from the third input (heave) to the second and third outputs are shown in Figure 6.8. Note that the cross-coupling from the heave input to the pitch mode is attenuated at low frequencies by a factor of about 20 relative to the coupling into the heave mode. In the vicinity of cross-over at 100 Hz, the relative coupling is attenuated by a factor of about 180. The greater attenuation at cross-over is due to the fact that the platen mass-properties are becoming significant at this frequency.

That there is any cross-coupling is due to the fact that the magnet incremental force-position constants k_{gs} and k_{gl} are not exactly in the ratio of two to one. The coordinate transformation T_{iu} has only been designed to account for the relative size of k_{is} and k_{il}. At this stage, since the magnet models are not highly accurate, this level of cross-coupling is unimportant. The controller described in the next section is designed as though the system were perfectly decoupled, under the assumption that the small amount of cross-coupling will be insignificant.

```
Avp =
  Columns 1 through 6

         0         0         0  1.0000e+00         0         0
         0         0         0         0  1.0000e+00         0
         0         0         0         0         0  1.0000e+00
 8.0476e+03         0         0         0         0         0
         0  5.0056e+04 -2.5237e+04         0         0         0
         0 -3.1781e+02  7.4347e+04         0         0         0
         0         0         0         0         0         0
         0         0         0         0         0         0
         0         0         0         0         0         0

  Columns 7 through 9

         0         0         0
         0         0         0
         0         0         0
         0 -5.4387e+04  5.4387e+04
 1.9536e+05 -5.5615e+04 -5.5615e+04
-2.6719e+04 -7.6061e+03 -7.6061e+03
-2.2371e+03         0         0
         0 -2.2371e+03         0
         0         0 -2.2371e+03
Bvp =

         0         0         0
         0         0         0
         0         0         0
 5.2092e+01 -5.7836e-15 -5.7836e-15
 5.9137e-15  1.0654e+02  1.7573e-15
 8.0881e-16  1.7000e-16  1.4570e+01
         0 -5.6934e-01  5.6934e-01
 1.0000e+00  1.0000e+00  1.0000e+00
-1.0000e+00  1.0000e+00  1.0000e+00
Cvp =
  Columns 1 through 6

 6.2500e+03         0         0         0         0         0
         0  1.8126e+04         0         0         0         0
         0         0  1.9685e+05         0         0         0

  Columns 7 through 9

         0         0         0
         0         0         0
         0         0         0
```

Figure 6.5: Vertical plant numerical values output from Matlab.

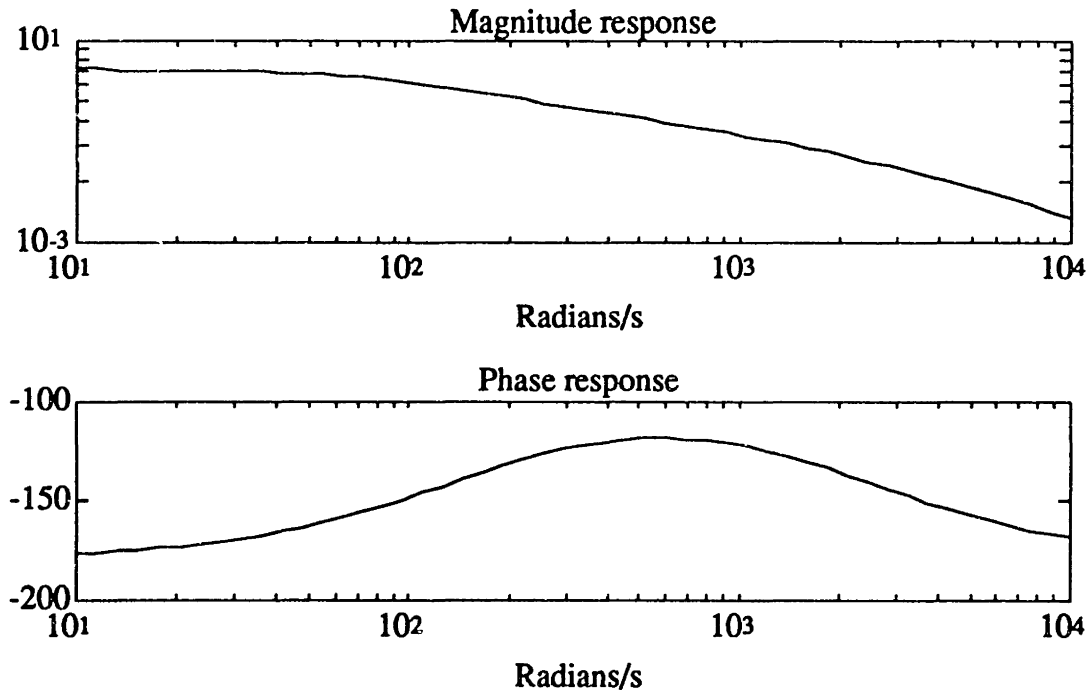

Figure 6.6: Transfer function $v_{m1}(s)/v_{u1}(s)$.

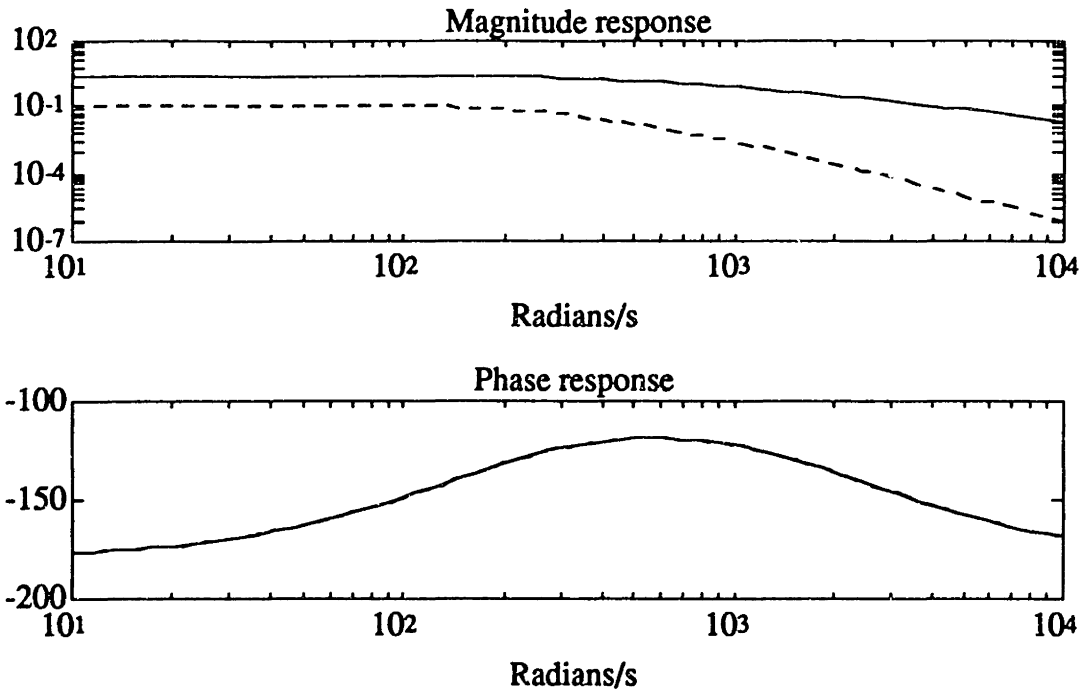

Figure 6.7: Transfer function $v_{m2}(s)/v_{u2}(s)$ (solid line) and $v_{m3}(s)/v_{u2}(s)$ (dashed line).

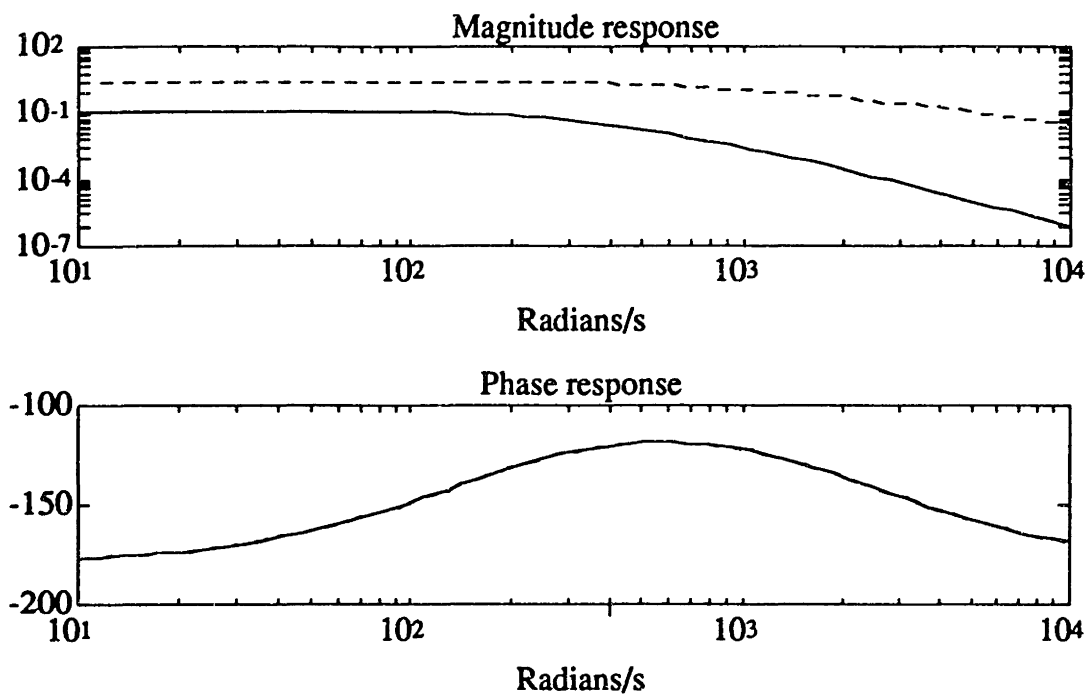

Figure 6.8: Transfer function $v_{m3}(s)/v_{u3}(s)$ (dashed line) and $v_{m2}(s)/v_{u3}(s)$ (solid line).

Controller Design

The controller is designed under the assumption that the plant is decoupled. That is, the roll controller is designed to control the transfer function $v_{m1}(s)/v_{u1}(s)$, the pitch controller is designed to control the transfer function $v_{m2}(s)/v_{u2}(s)$, and the heave controller is designed to control the transfer function $v_{m3}(s)/v_{u3}(s)$. All three controllers take the form of lag compensators designed for a 100 Hz crossover. Recall that the current drives already implement lead compensation with a phase maximum at about 100 Hz.

The lag network parameters for each controller are fixed, but the controller DC gain is adjustable, such that the controller can be conveniently tuned in the laboratory. For the plant transfer functions shown above, the nominal controller designs are

$$\frac{v_{ui}(s)}{v_{ei}(s)} = k_i \frac{\tau_a s + 1}{\tau_b s + 1} \qquad i = 1, 2, 3 \tag{6.48}$$

where $\tau_a = 8.6$ milliseconds, $\tau_b = 62$ milliseconds, $k_1 = 31.6$, $k_2 = 5.88$, and $k_3 = 4.20$.

Closed loop stability of the controlled system is determined by the multivariable Nyquist criterion. That is the system is stable if the number of clockwise encirclements of the origin by $\det(I+T(s))$ as s traces the normal Nyquist contour D_R in the s-plane is equal to the negative of the number of open-loop unstable poles of $T(s)$. In standard notation, this statement appears as

$$N(0, \det(I + T(s)), D_R) = -P_u \tag{6.49}$$

This can also be put in terms of encirclements of the -1 point as

$$N(-1, -1 + \det(I + T(s)), D_R) = -P_u \tag{6.50}$$

Here $T(s)$ is the control system loop transfer function matrix; in the current case this is given by the series combination of the compensator transfer matrix and the plant transfer matrix. The Nyquist contour which results for the vertical control loop is shown in Figure 6.9.

Applying this criterion to the vertical loop gives the result that the system is stable, since the contour encircles the -1 point -3 times in the clockwise direction. This is indeed equal to the negative of the number of open-loop unstable poles.

At this point, it has been demonstrated that the nominal design successfully stabilizes the vertical plant. Further, since the three loops are close to decoupled, we anticipate that they can be empirically tuned in the laboratory in order to stabilize each modal response independently. The next section describes the laboratory implementation of the control system and the experimental results.

This is the Nyquist plot from 100 to 10000 rad/sec. Note that there are three counterclockwise encirclements of the -1 point. Since there are three open-loop unstable poles, the closed-loop is thus stable. More detail in the vicinity of the origin is shown in the panel below.

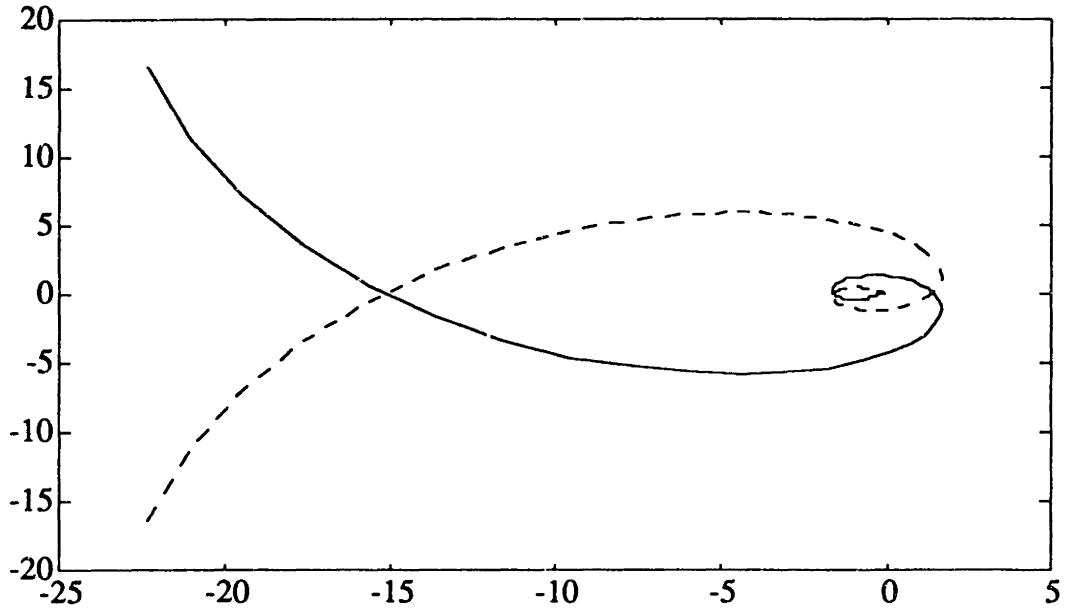

This shows the Nyquist plot from 200 to 10000 rad/sec to give more detail in the vicinity of the -1 point.

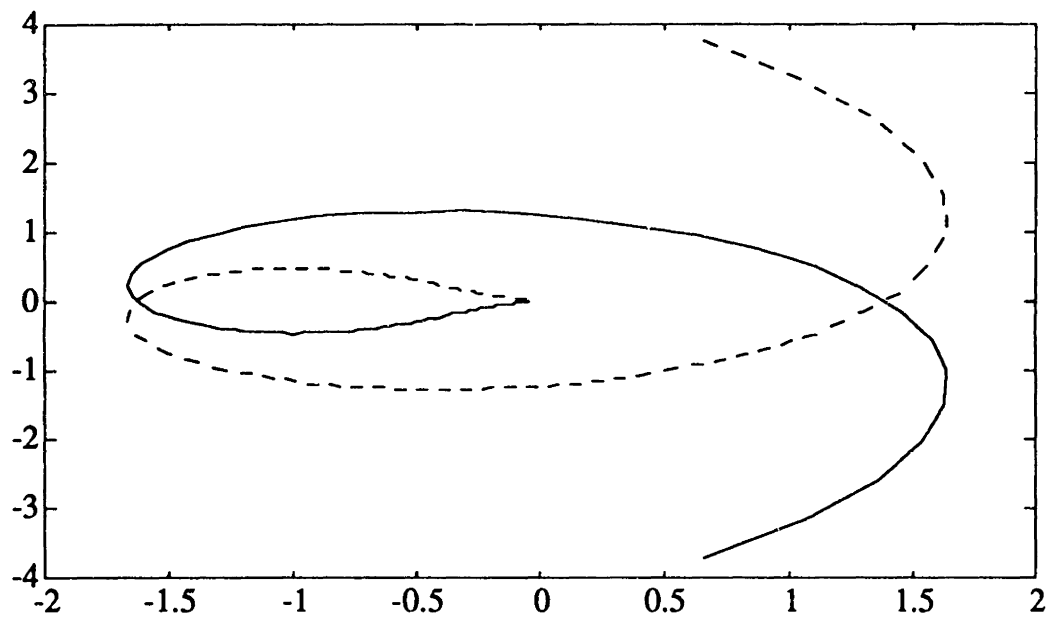

Figure 6.9: Multivariable Nyquist plot for vertical control loop, showing that system is stable.

6.7.2 Vertical control system experimental results

The three vertical controllers were tuned sequentially by constraining the platen such that motion was allowed in only the single degree of freedom associated with the controller being tuned. The lateral and axial degrees of freedom were eliminated by attaching Mylar tape under tension between the ends of the platen and the sides of the primary and secondary support brackets. Recall that at this point, the lateral magnets were not yet assembled onto the support brackets.

Roll mode tuning

The roll control loop was tuned first by eliminating the heave and pitch degrees of freedom. This was accomplished by placing a one inch length of #24 wire under the bottom face of each end of the platen. The wire was arranged on the centerline of the bottom face, parallel to the long axis of the platen. The two wires in this manner acted as a pair of hinges to carry the weight of the platen and allow only rotational motion about their centerlines. Though these centerlines are about 2.5" below the centerline of the platen, and thus the rotations do couple to the lateral translation mode, such rotations *do not* couple to the pitch or heave modes; thus the roll controller could be tuned independently in this configuration. It was experimentally far easier to constrain the platen here than about the true centerline.

The active range of the three top position probes is only $\pm 50\mu$m. In order to place the platen within this active range, once the platen was resting on the two wires as described above, shims were placed under the three legs of the landing pad in order to raise the combined system into place. Once the probes were within their active range, the controller was tuned by adjusting the gain term k_1. The controllers and decoupling networks were implemented in analog electronics; their circuit designs are very similar to the final controller and decoupling network designs given in the next chapter and will not be presented here.

When the gain term is too low, the system exhibits a low frequency limit cycle, indicating that the cross-over frequency is occuring at a frequency low enough that the lag network is contributing more negative phase shift than the positive phase shift of the lead network. As the gain is increased, the frequency of oscillation increases as well until the point is reached that the phase is more positive than -180 degrees at crossover, and the loop becomes stable, although with a lightly damped low frequency oscillation present in the step response. As the gain is increased further, the frequency of this oscillation increases at the same time that it becomes better damped. Still higher gains eventually lead back to high-frequency instabilty as the phase drops below -180 degrees at crossover due to the inevitable higher-frequency dynamics which as of yet have not been modeled. The roll loop gain was adjusted for the best-looking step response

within the stable range.

Several other dynamic effects were encountered as the roll loop was tuned. First, the small top magnet assembly exhibited a resonance in the vicinity of 300 Hz. The resonance is a cantilever mode of the magnet assembly which is only supported at the primary support bracket end. The resonance was sufficiently lightly damped to cause the system to break into oscillation as the roll gain was increased to a value which gave a good step response. The damping of this mode was significantly increased by attaching a 100 gram weight with double-faced sticky tape to the top surface of the end of the magnet assembly. This additional damping allowed the gain to be increased to the desired level. The idea behind this approach is that at the resonant frequency, the weight is remaining approximately fixed in inertial space, while the magnet assembly moves under it. Thus, the tape is being deformed, and because it is a visco-elastic material, this cyclic deformation adds loss to the mode, thereby reducing the magnitude of the resonant peak. Certainly the mass is too small to shift the frequency of the resonance, but a reduction of amplitude is all that is required. In section 6.11 a more permanent solution to the resonance problem is described; the use of the mass on tape solution provided a means to rapidly continue the main experimental work.

The second problem encountered at this point was a resonance in the platen itself at about 1 kHz. As the platen is hollow, it acts like a tubular bell with a resonant mode at 1 kHz. This mode is very lightly damped, and thus can be pumped by the roll controller. Again the solution was to place weights on sticky tape, in this case inside the platen on the bottom surface of its interior. Crude experiments with a screwdriver used as a probing rod determined that the centerline of each platen face was a node for this resonance, with the largest motion at the corners of the platen. Accordingly, a pair of weights were placed at diagonally opposite corners of the interior bottom face. These weights reduced the magnitude of the resonance to below the necessary level.

Pitch mode tuning

After the roll mode was satisfactorily adjusted, the pitch mode was tuned. To constrain all but the pitch mode, a single #24 wire was placed under the platen, perpendicular to its long axis, and directly below the platen center of mass. In this configuration the pitch controller gain was adjusted in a manner similar to the roll controller gain. As the pitch gain was increased, the large magnet assembly exhibited a resonance at about 300 Hz. This was damped as before with a 100 gm weight on sticky tape at the free end of the assembly, allowing the pitch gain to be increased to the desired value.

Heave mode tuning

The heave mode gain was adjusted by trial and error. Initializing the system into suspension in all three vertical modes is difficult. The problem is that the probes have an active range of $\pm 50\mu$m, while this active range is centered at the magnet air gap of 125μm. Thus the active range represents a tiny window out in free space. When the platen is resting on the landing pad the air gap has the large value of about 1200μm. In order to initialize the system, the platen needs to be held in the active range of all three probes with a low enough velocity that the controller electronics can settle to the proper values.

Such initialization proved impossible until the following approach was developed. With the electronics powered down, the heave mode setpoint is adjusted to an air gap value of about 100μm. Slips of folded drafting paper were chosen to have a thickness of 125μm. With the platen resting on the landing pad, a slip of this paper is placed at either end of the top surface of the platen such that the pieces of paper are immediately under the small magnets and the large magnet respectively. Then power is applied to the controller and coil power amplifiers, and the platen lifted until it is pulled up by the suspension magnets, clamping the paper shims against their faces. The paper is clamped because it is thicker than the setpoint air gap.

Then, the heave setpoint is slowly reduced until it coincides with the position of the platen, allowing the controller to settle out. As the setpoint is further reduced, the platen gradually moves away from the slips of paper until they are free to be drawn out of the air gap, and the platen is in free suspension. This initialization experiment was repeated with different values of the heave mode gain until stable suspension was achieved in the three vertical modes. At this point, the three loop gains were fine tuned for the best overall step responses.

The resulting tuned gain values are $k_1 = 36.0$, $k_2 = 14.4$, and $k_3 = 5.9$. These values are not far from the nominal design values of $k_1 = 31.6$, $k_2 = 5.9$, and $k_3 = 4.2$. Discrepancies are accounted for by the fact that the model we have used is only approximate at this point.

The suspended system demonstrates position stability on the order of 5 nm when the optical table is undisturbed. This stability is documented in Figure 6.10.

6.8 Lateral System Assembly

This section describes the manner in which the four side electromagnets were mounted to the support brackets, as well as the techniques used to mount the two lateral capacitance probes into the centers of their respective electromagnets. The adjustment of the relative positions of the two support brackets is also described.

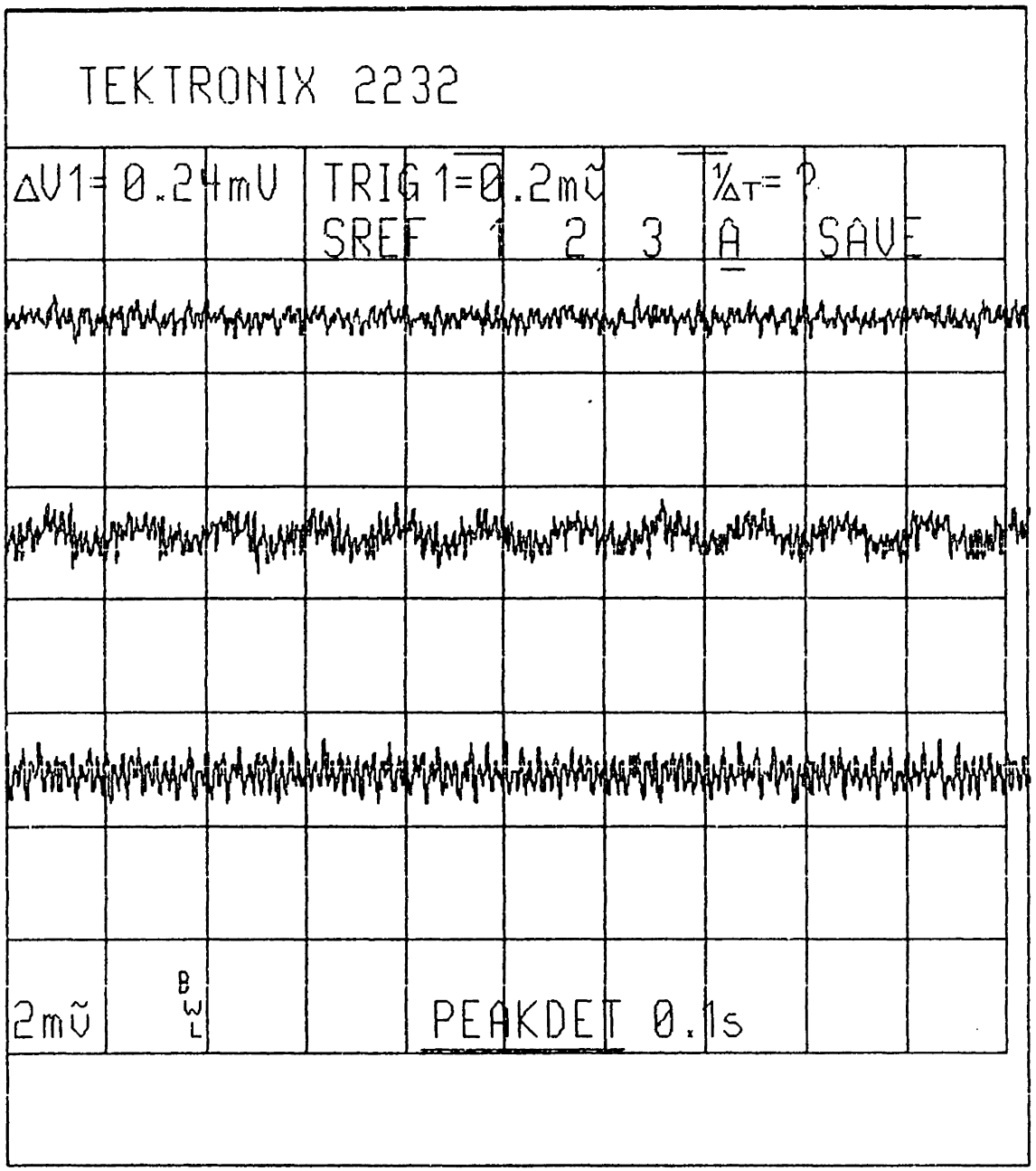

Figure 6.10: Vertical system suspension stability. Three traces show output voltages of probes #1, #2, and #3 from top to bottom respectively. One millivolt corresponds to approximately 5 nm.

This adjustment was crucial in order to determine the lateral air gaps.

The lateral system is somewhat simpler to assemble than the vertical system. This is so because the only degrees of freedom of the side magnet assemblies lie in the plane of the vertical face of the support brackets. The distance from the support bracket surface to the side-magnet pole-faces is accurately set by the surface grinding operation described in an earlier chapter. This operation also assures that the pole face plane is accurately parallel to the support bracket plane. Therefore, the pole faces of the two side magnets mounted on a support bracket are guaranteed to be coplanar simply by attaching the magnet assemblies to the support bracket. Then, assuming that the support brackets are resting on a flat surface, e.g., the optical table, it is assured the pole-face planes of the two opposing pairs of magnets are accurately parallel.

As in the case of the vertical system, the effective magnet air gap was increased by applying three pieces of Scotch tape to each of the four side magnet faces. On each pole face, the three pieces were applyed radially, separated by 120 degrees, and not overlapping. The thickness of the tape is about 0.0025", and it is nonmagnetic, thus the magnet effective air gap is increased by this amount, while motion of the platen is stopped 0.0025" from the actual pole face. Operating farther from the pole faces further attenuates the undesired effect of the permanent magnets, and reduces the frequency of the unstable open-loop time constant.

As in the vertical system, the two side probes were installed with their faces coplanar with the surface of the tape. Thus the operating point for the platen is set to 0.005" away from the probe face, yet 0.0075" away from the magnet pole face.

Unlike the vertical system, the back side of the probe mounting hole is inacessable after the electromagnets are attached to the support brackets. Thus, the two side probes were installed into their respective electromagnets *prior* to mounting the electromagnets onto the primary support bracket. In order to accurately align the probe faces with the surface of the tape on each of the two side magnets, the current drives were set to 1 Ampere and the electromagnets were then magnetically clamped to the platen top surface.

The two probes were then inserted into the central hole in the two side magnets such that their faces were resting against the platen surface. Thus the platen was used to accurately define the plane of the tape surface. The probes were permanently installed into the electromagnets by gluing them with epoxy in a manner identical to that used in the vertical probe installation.

Following the probe installation and sufficient epoxy cure time, the four side magnet assemblies were bolted onto their respective support brackets. The only critical dimension which is not determined when the magnet mounting bolts are tightened is the distance between the primary and secondary support brackets.

This distance was set by attaching 125μm brass shims to the faces of all four side magnets. The primary support bracket was first bolted down to the optical table. The platen was then placed in position between the opposing pairs of side magnets and the secondary support bracket was forced up against the platen to clamp it between the opposing pole faces and their associated shims. At this point the bolts holding down the secondary support bracket were tightened. In this manner, the shims set the air gaps of all four side magnets to the desired value of 125μm. The shims were then removed, completing the lateral system assembly.

6.9 Approximate Model for Lateral Dynamics

In this section an open-loop model for the lateral suspension dynamics is developed which incorporates the linear bearing models developed in Section 6.4. The object is to develop a simple model for the lateral dynamics which will facilitate the lateral controller design. A number of assumptions are made in order to simplify this process. The vertical dynamics are viewed as uncoupled from the horizontal dynamics, and translation in the x_1 direction is set to zero. As the bearing torque terms are as yet unknown, they are ignored. Applying these assumptions to the linear dynamical equations developed in Section 5.2, and focusing on the two lateral degrees of freedom yields the following fourth order set of state equations.

$$\dot{\tilde{q}}_2 = \tilde{u}_2 \tag{6.51}$$

$$\dot{\tilde{x}}_3 = \tilde{u}_6 \tag{6.52}$$

$$I_2\dot{\tilde{u}}_2 = L_m(\tilde{F}_4 - \tilde{F}_5 - \tilde{F}_6 + \tilde{F}_7) \tag{6.53}$$

$$M\dot{\tilde{u}}_6 = \tilde{F}_4 + \tilde{F}_5 - \tilde{F}_6 - \tilde{F}_7 \tag{6.54}$$

where we have set $\tilde{T}_{jk} = 0$, and $\tilde{x}_1 = 0$.

These equations are expressed in terms of the state variables used in Chapter 5. However, the bearing forces depend on the pole face air gap. Define $\tilde{g}_j$ as the incremental change in the jth air gap in the direction of the jth force. Then, the incremental forces for the four side electromagnets are given by

$$\tilde{F}_4 = k_{is}\tilde{i}_4 + k_{gs}\tilde{g}_4 \tag{6.55}$$

$$\tilde{F}_5 = k_{is}\tilde{i}_5 + k_{gs}\tilde{g}_5 \tag{6.56}$$

$$\tilde{F}_6 = k_{is}\tilde{i}_6 + k_{gs}\tilde{g}_6 \tag{6.57}$$

$$\tilde{F}_7 = k_{is}\tilde{i}_7 + k_{gs}\tilde{g}_7 \tag{6.58}$$

To linear terms, the four side magnet incremental air gaps are related to the state

variables as

$$\tilde{g}_4 = \tilde{x}_3 + L_m \tilde{q}_2 \tag{6.59}$$
$$\tilde{g}_5 = \tilde{x}_3 - L_m \tilde{q}_2 \tag{6.60}$$
$$\tilde{g}_6 = -\tilde{g}_4 \tag{6.61}$$
$$\tilde{g}_7 = -\tilde{g}_5 \tag{6.62}$$

The lateral open-loop dynamics are described in state-varible form as

$$\dot{w}_l = A_l w_l + B_l i_l \tag{6.63}$$
$$y_l = C_l w_l \tag{6.64}$$

where $w_l = [\ \tilde{q}_2\ \tilde{x}_3\ \tilde{u}_2\ \tilde{u}_6\ ]'$, $i_l = [\ \tilde{i}_4\ \tilde{i}_5\ \tilde{i}_6\ \tilde{i}_7\ ]'$, and $y_v = [\ \tilde{q}_2\ \tilde{x}_3\ ]'$.

Combining equations 6.51 through 6.62, and substituting in the numerical values for the constants which have been calculated in earlier sections, yields the numerical values for the lateral open-loop system matrices as shown in Matlab output format in Figure 6.11.

The system eigenvalues and eigenvectors are also listed. These indicate a pair of modes in pure yaw and pure lateral translation with time constants on the order of 4 msec. The modes are pure because all four side magnets are assumed to be identical.

6.10 Modal Control of Lateral System

6.10.1 Theory

A block diagram showing the lateral control architecture is given in Figure 6.12. Most of the data paths carry two-vectors, however, since there are four side magnets, the data paths associated with the current drives carry four-vectors.

In the previous section, we derived the system matrices A_l, B_l, C_l, and D_l. The coordinate transformations S_{py}, S_{mp}, and S_{iu}, and the lateral current drive system matrices A_{ld}, B_{ld}, C_{ld}, and D_{ld} are developed in this section, and the controller design is given in the next section.

The position probes have a sensitivity of 1.97×10^5 volts per meter, increasing as $\tilde{g}_j$ increases. The side probes are contained in magnets 6 and 7; probe #4 is located in magnet #6, and probe #5 is located in magnet #7.

Thus the matrix S_{py} which relates the lateral state variables to probe voltages v_{p4} and v_{p5} is given by

$$S_{py} = 1.97 \times 10^5 \begin{bmatrix} -L_m & -1 \\ L_m & -1 \end{bmatrix} = \begin{bmatrix} -1.81 \times 10^4 & -1.97 \times 10^5 \\ 1.81 \times 10^4 & -1.97 \times 10^5 \end{bmatrix} \tag{6.65}$$

```
System matrices:

Al =

   1.0e+04 *

         0         0    0.0001         0
         0         0         0    0.0001
    4.7035         0         0         0
         0    7.0896         0         0

Bl =

         0         0         0         0
         0         0         0         0
   26.2126  -26.2126  -26.2126   26.2126
    3.6381    3.6381   -3.6381   -3.6381

Cl =

     1     0     0     0
     0     1     0     0

Dl =

     0     0
     0     0

Eigen-analysis:

evec =

    0.0046    0.0046         0         0
    0.0000   -0.0000   -0.0038   -0.0038
    1.0000   -1.0000   -0.0000   -0.0000
         0         0   -1.0000    1.0000


eval =

  216.8762         0         0         0
         0 -216.8762         0         0
         0         0  266.2621         0
         0         0         0 -266.2621
```

Figure 6.11: Lateral open-loop system matrix and eigen-analysis numerical values output from Matlab.

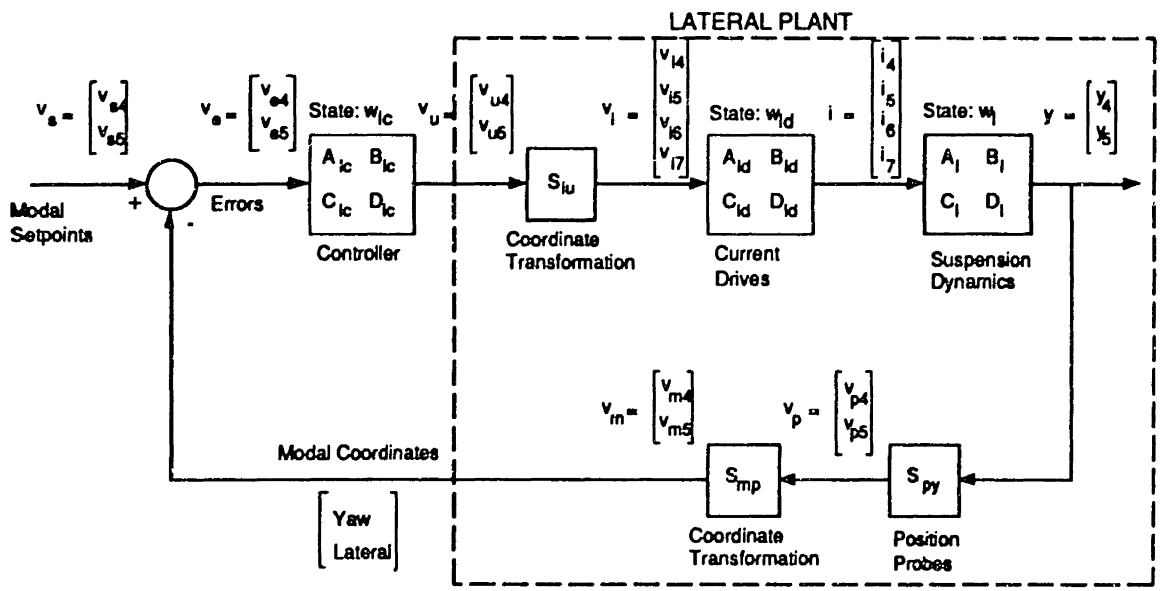

Figure 6.12: Block diagram for the lateral control loop.

Then S_{mp} is defined as

$$S_{mp} = \begin{bmatrix} -.5 & .5 \\ -.5 & -.5 \end{bmatrix} \tag{6.66}$$

The relative scaling of the elements in the array is dictated by the suspension geometry. The absolute levels are chosen so that the voltages v_m saturate[3] only when both probe outputs are saturated.

S_{iu} is defined as

$$S_{iu} = \begin{bmatrix} 1 & 1 \\ -1 & 1 \\ -1 & -1 \\ 1 & -1 \end{bmatrix} \tag{6.67}$$

This matrix converts from the two modal controller drive signals to the four current-drive inputs. All entries are of equal magnitude since the four side magnets are assumed to be identical. The absolute levels are chosen so that all of the entries are of unity magnitude. This allows an easier circuit implementation and is such that a single modal control signal can saturate the current drives.

The current drive circuits have been presented in Section 6.3. Each of the current drives has a transfer function from input v_{ij} to output i_j given by

$$\frac{i_j(s)}{v_{ij}(s)} = \frac{1}{\alpha}\frac{\alpha\tau s + 1}{\tau s + 1} \tag{6.68}$$

where $\alpha = 15$ and $\tau = 4.47 \times 10^{-4}$. Combining the four lateral current drives in parallel yields the current source system equations as

$$\dot{w}_{ld} = A_{ld}w_{ld} + B_{ld}v_i \tag{6.69}$$

$$i = C_{ld}w_{ld} + D_{ld}v_i \tag{6.70}$$

where

$$\begin{aligned} A_{vd} &= \mathrm{diag}(-2.24 \times 10^3,\ -2.24 \times 10^3,\ -2.24 \times 10^3,\ -2.24 \times 10^3) \\ B_{vd} &= \mathrm{diag}(1,\ 1,\ 1,\ 1) \\ C_{vd} &= \mathrm{diag}(-2.09 \times 10^3,\ -2.09 \times 10^3,\ -2.09 \times 10^3,\ -2.09 \times 10^3) \\ D_{vd} &= \mathrm{diag}(1,\ 1,\ 1,\ 1) \end{aligned}$$

For the purposes of design, the region contained within the dashed line in Figure 6.12 is considered to be the plant which is controlled by the controller.

[3]Recall that the probe outputs and the op amps used to implement these coordinate transformations saturate at about ± 13 volts.

Combining all the information developed above yields the plant system matrices as

$$\dot{w}_{lp} = A_{lp}w_{lp} + B_{lp}v_u \tag{6.71}$$

$$v_m = C_{lp}w_{lp} + D_{lp}v_u \tag{6.72}$$

where $w_{lp} = [\ w_l'\ w_{ld}'\ ]'$ and

$$A_{lp} = \begin{bmatrix} A_l & B_lC_{ld} \\ 0 & A_{ld} \end{bmatrix} \tag{6.73}$$

$$B_{lp} = \begin{bmatrix} B_lD_{ld}S_{iu} \\ B_{ld}S_{iu} \end{bmatrix} \tag{6.74}$$

$$C_{lp} = \begin{bmatrix} S_{mp}S_{py}C_l & 0 \end{bmatrix} \tag{6.75}$$

$$D_{lp} = [0] \tag{6.76}$$

where the indicated zero blocks are of the appropriate dimensions.

A copy of the Matlab output for the numerical values of the lateral plant system matrices is given in Figure 6.13. D_{lp} is not shown since it is a two by two matrix of zeros.

Bode plots for the plant transfer functions from the controller output v_u to the coordinate transformation output v_m appear very similar to the plots shown in Section 6.7.1, and thus will not be shown here. Due to the symmetry between the identical side magnets, the plant is completely decoupled. This simplifies the controller design described in the next section.

6.10.2 Controller Design

The yaw controller is designed to stabilize the transfer function $v_{m4}(s)/v_{u4}(s)$. The lateral translation controller is designed to stabilize the transfer function $v_{m5}(s)/v_{u5}(s)$. Both controllers take the form of lag compensators designed for a 100 Hz crossover. Recall that the current drives already implement lead compensation with a phase maximum at about 100 Hz.

The lag network parameters for each controller are fixed, but the controller DC gain is adjustable, such that the controller can be conveniently tuned in the laboratory. The controllers are identical in form to those presented in Section 6.7.1, that is the controller transfer functions are given by

$$\frac{v_{ui}(s)}{v_{ei}(s)} = k_i\frac{\tau_a s + 1}{\tau_b s + 1} \qquad i = 4, 5 \tag{6.77}$$

where $\tau_a = 8.6$ milliseconds, $\tau_b = 62$ milliseconds, $k_4 = 5.92$, and $k_5 = 4.14$.

```
Alp =
   1.0e+04 *
  Columns 1 through 7

         0         0    0.0001         0         0         0         0
         0         0         0    0.0001         0         0         0
    4.7035         0         0         0   -5.4732    5.4732    5.4732
         0    7.0896         0         0   -0.7596   -0.7596    0.7596
         0         0         0         0   -0.2237         0         0
         0         0         0         0         0   -0.2237         0
         0         0         0         0         0         0   -0.2237
         0         0         0         0         0         0         0

  Column 8

         0
         0
   -5.4732
    0.7596
         0
         0
         0
   -0.2237

Blp =
         0         0
         0         0
  104.8502         0
         0   14.5522
    1.0000    1.0000
   -1.0000    1.0000
   -1.0000   -1.0000
    1.0000   -1.0000

Clp =
  1.0e+05 *
  Columns 1 through 7

    0.1814         0         0         0         0         0         0
         0    1.9700         0         0         0         0         0

  Column 8

         0
         0
```

Figure 6.13: Lateral plant numerical values output from Matlab.

Closed loop stability of the controlled system is determined by the multivariable Nyquist criterion as described in Section 6.7.1. Applying this criterion to the lateral loop gives the result that the system is stable, since the contour encircles the -1 point -2 times in the clockwise direction. This is indeed equal to the negative of the number of open-loop unstable poles of the lateral system.

At this point, it has been demonstrated that the nominal design successfully stabilizes the lateral plant. Further, since the two loops are decoupled, we anticipate that they can be empirically tuned in the laboratory in order to stabilize each modal response independently. The next section describes the laboratory implementation of the lateral control system and the experimental results.

6.10.3 Experimental Results

Unlike the vertical system, the lateral system is self-initializing. This is so as a result of several factors. First, the small air-gaps on both sides of the platen restrict its motion to no more than $\pm 125\mu$m motion from the centered nominal operating point. Secondly, there is no gravity component to overcome in the lateral direction. Finally, when the lateral loops are initialized, the platen is out of suspension and resting on the landing pad. This mechanical contact provides a damping term which aids the initialization process.

The lateral controller gains were set to the values derived in the previous section, and the closed-loop system was stable with these values. As indicated above, the lateral loops are self-initializing at power-up. Once power is on, and the lateral loops stabilized, the vertical system is initialized using slips of paper as described in Section 6.7.2. In this manner all five degrees of freedom are brought into suspension.

Once the platen was suspended in all five degrees of freedom, it became apparent that the system had a slight tilt toward the small top bearing end, as the platen slowly tries to slide in this direction. To restrain this motion, a rubber band was stretched between the landing pad and the 'uphill' end of the bottom of the platen. The low stiffness of the rubber band assures that it does not appreciably interfere with the system dynamics.

At this point the controller gain terms were adjusted to achieve the best step response. The actual gain terms were higher than those predicted in the previous section by about a factor of two, e.g., $k_4 = k_5 = 10.4$. This difference may be ascribed to the coarseness of the model used to derive the nominal values.

With the system in suspension, it was observed that there was a significant imbalance between the currents of the opposing pairs of side magnets. This is likely due to the fact that the pole-face grinding operation described in Section 4.3.1 did not remove equal amounts of material from the individual pole-faces. This imbalance was corrected by attaching ferrite magnets to the sides of bearing as-

semblies #5 and #7. The ferrite magnets have dimensions 1" × 2" × 0.5". Initial placement was maintained with double-faced sticky tape. The magnet air gap was adjusted relative to the log until the opposing coil currents were brought into balance. At this point, the magnet air gaps were about 1 cm. Finally, an aluminum clamp bracket was used to attach the magnet rigidly to the magnet assembly.

6.11 Resonance Elimination

In order to eliminate the resonances of the two top magnet assemblies, aluminum blocks and side plates were fabricated. The stiffening blocks are shown in Figure 6.14, and the side plates are shown in Figure 6.15.

These blocks were epoxied into place between the secondary support bracket and the free end of the two top magnet assemblies as shown in Figure 6.16 and Figure 6.17.

Twenty four hour cure-time epoxy was used in order to allow sufficient working time, and while the epoxy was curing the side plates were held in place with C-clamps.

This solution was very effective in eliminating the resonances, as evidenced by the frequency response curves shown in Figure 6.18, which show the heave mode frequency response before and after the installation of the stiffening blocks.

With the resonances eliminated, the control task is greatly simplified. If possible it is best to solve this type of problem with a hardware solution such as the stiffening blocks described above. Compensation techniques such as notch filters have the disadvantage of rendering the resonant mode near-unobservable/uncontrollable. Additionally, it is difficult to make the notch precisely coincide with and thus cancel the resonant mode. If the resonance is well above the crossover frequency, then notch filters can be applied successfully, however in the current situation, the resonant modes are located only a factor of 2–3 above crossover. Thus the mechanical solution described above is the best approach.

6.12 Accurate Model Development

Having achieved suspension in all five controlled axes, it is possible to accurately measure the magnet incremental parameters k_{il}, k_{is}, k_{gl}, and k_{gs}, as well as the contribution of the torque terms T_{ij} which have heretofore been ignored. To this end, two sets of experiments were conducted; one set to measure the force constants as described in the next section, and another set to measure the torque constants, as described in Section 6.12.2.

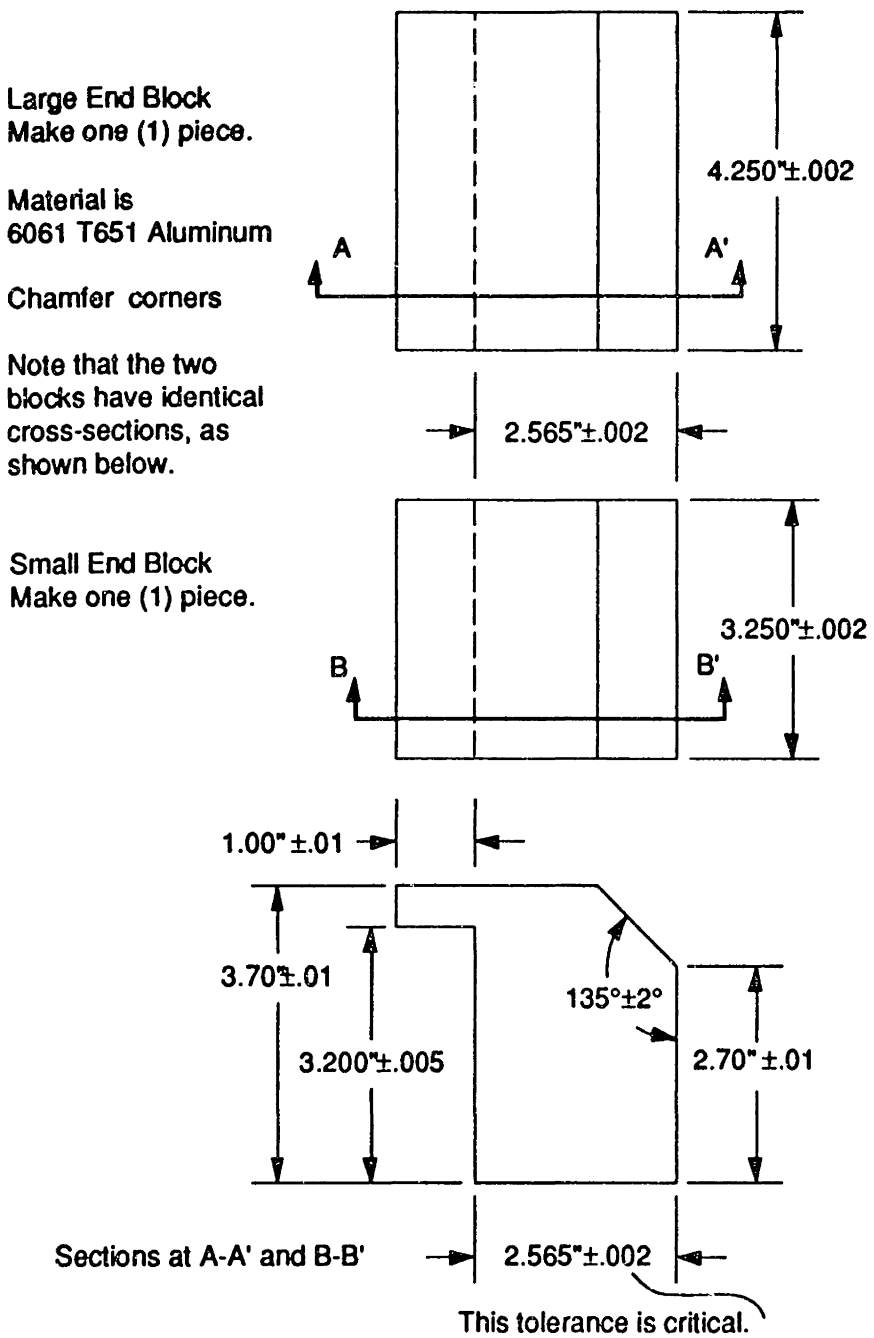

Figure 6.14: Large and small stiffening blocks.

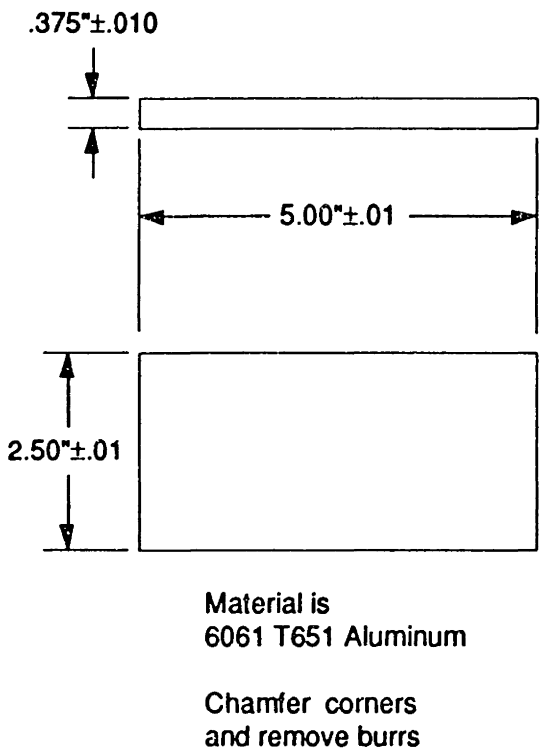

Figure 6.15: Side plates

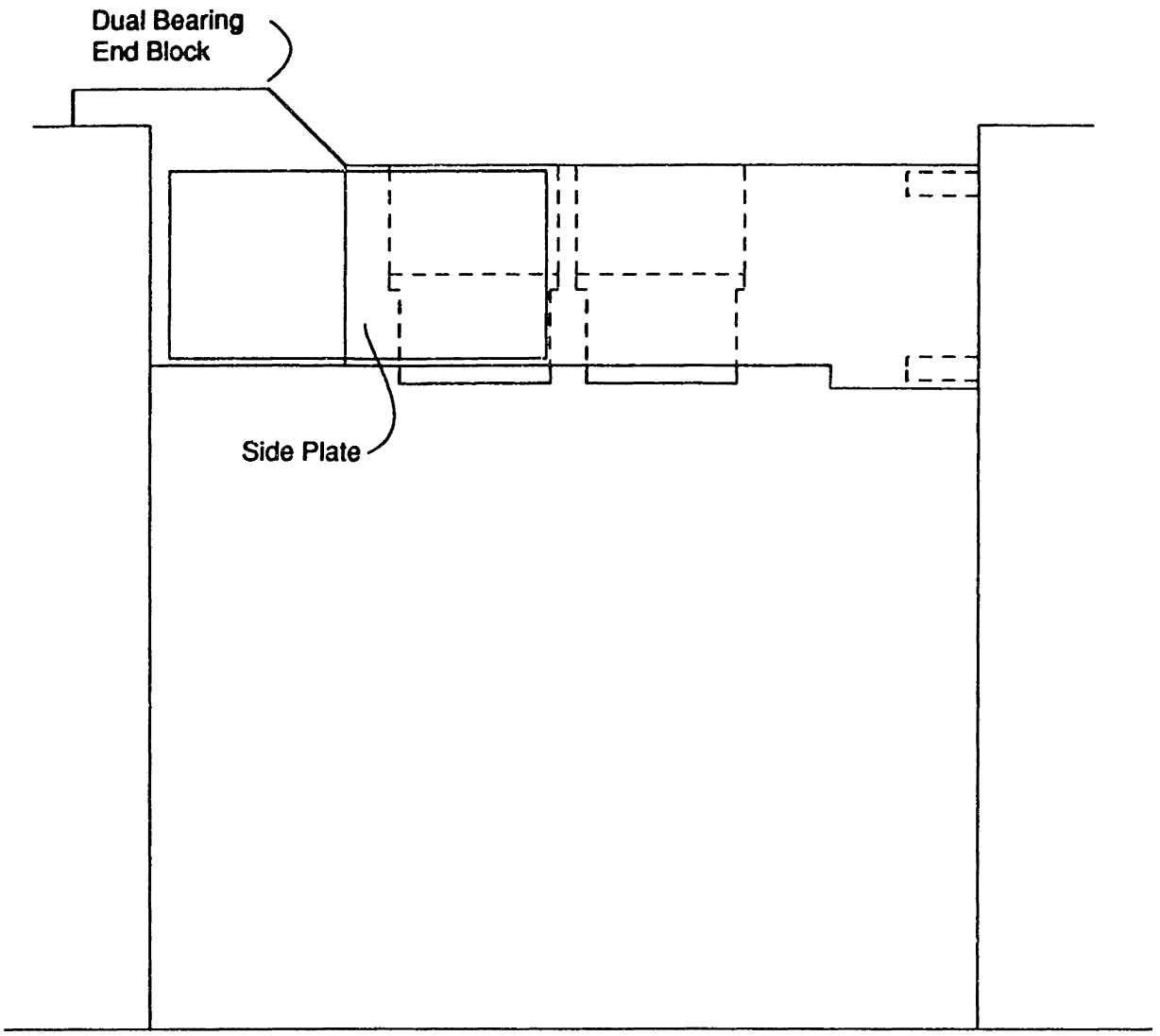

Figure 6.16: End view of stiffening block and side plates in-place between small top magnet assembly and secondary support bracket.

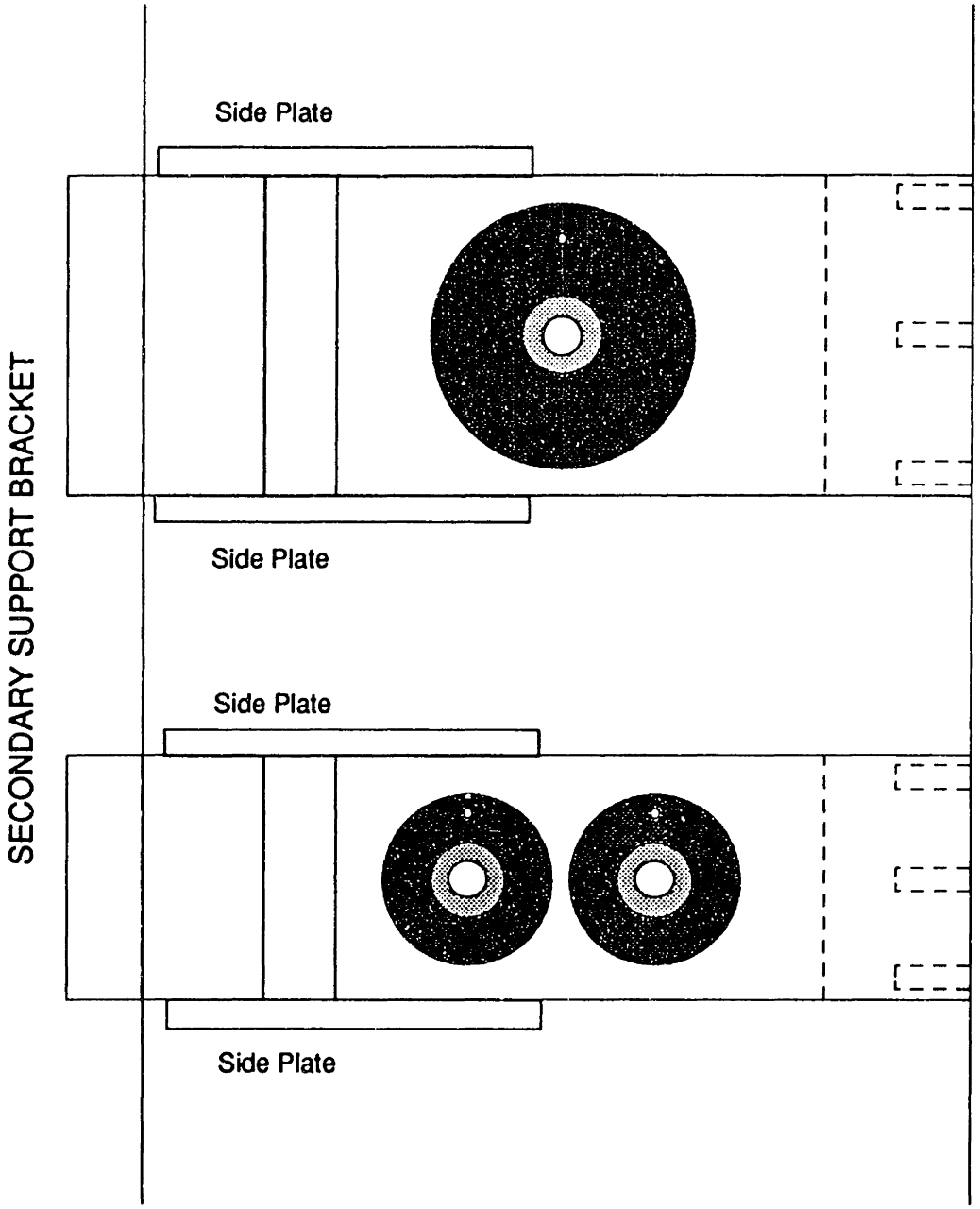

Figure 6.17: Top view of stiffening blocks and side plates in-place between magnet assemblies and secondary support bracket.

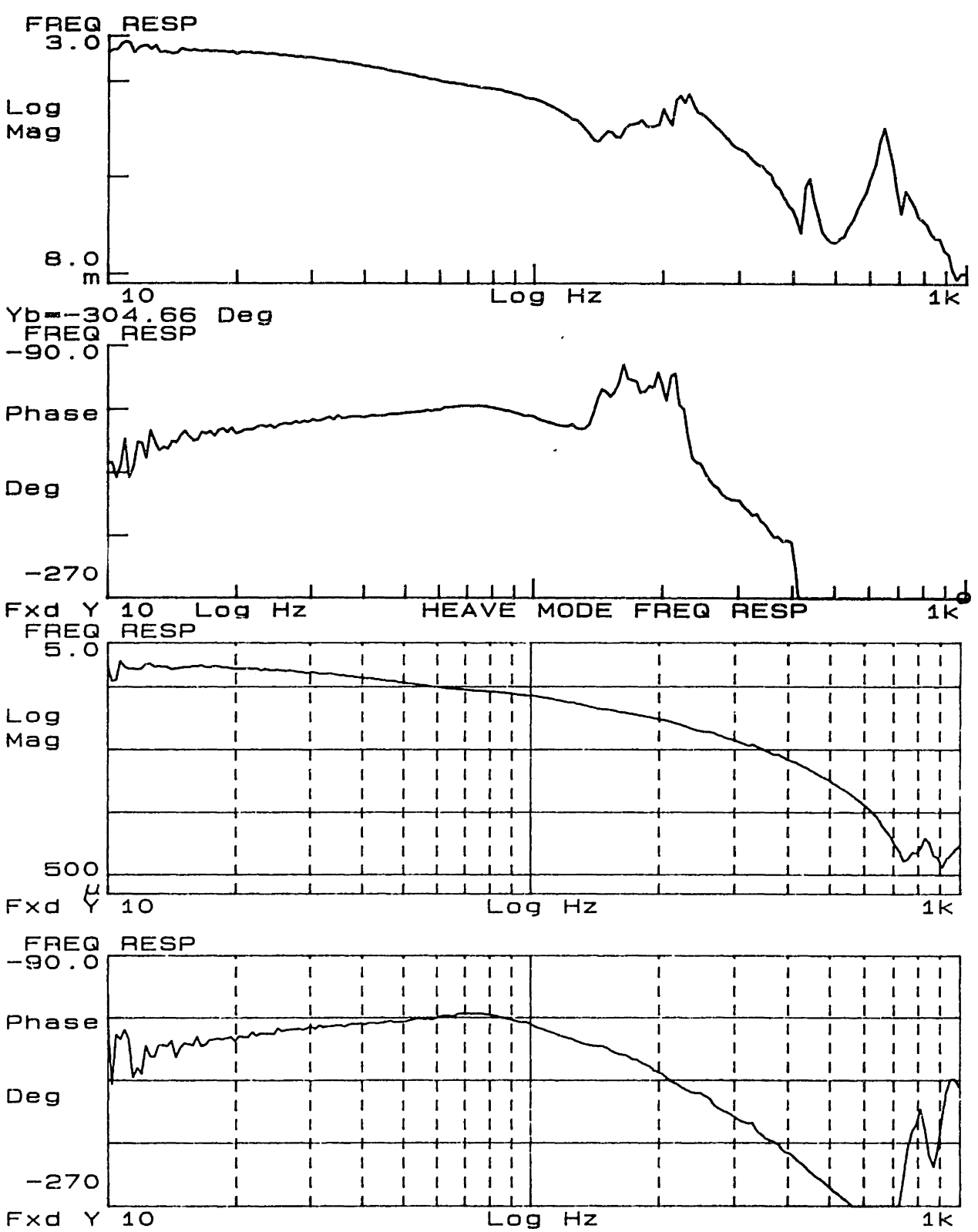

Figure 6.18: The upper trace shows the heave mode magnitude and phase frequency response $v_{m3}(j\omega)/v_{u3}(j\omega)$ before the stiffening blocks were attached. The lower trace shows the frequency response after the attachment of the stiffening blocks.

6.12.1 Force measurements

The platen was suspended at the nominal operating point (zero volts on each position probe), and the seven current drive bias potentiometers were adjusted so that the five modal control signals were approximately zero. That is, in this state, the DC component of current in each drive is supplied by the bias potentiometer setting. An additional mass was placed inside the platen, resting on the center of the bottom face of the interior of the platen. In this manner, the additional mass is directly below the platen center of mass. Thus, an additional force of mg was applied to the platen, with no resulting torques about the platen center of mass. Four masses were used: 50, 100, 200, and 500 grams, respectively. For each mass value, the platen was cycled through a range of approximately $\pm 17\mu$m in heave translation. At about 20 points in this range, the three top magnet coil currents and the three top probe voltages were measured. The resulting data for the three top magnets is shown in Figures 6.19, 6.20, and 6.21.

The data shown in the figures was fitted in the least squares sense to the linearized force model

$$i = mx + cF + d, \tag{6.78}$$

or

$$F = \frac{1}{c}i - \frac{m}{c}x - \frac{d}{c}, \tag{6.79}$$

where F is the additional force applied to the magnet, i is the coil current, x is the probe voltage, and m, c, and d are constants to be determined by the least squares fit. Note that d represents the operating point bias current. Further, using our earlier notation from Section 6.4, it is apparent that $k_i = \frac{1}{c}$ and $k_g = -\frac{m}{c}$. A small hysteresis effect is present in the magnet force curves. The curves do not form closed loops; this is believed to be due to the fact that the set of measurements for each loop required approximately 30 minutes to complete. For the development of the linearized model, this hysteresis is absorbed by the averaging process, as all data points are given equal weight in the least squares fit. This is equivalent to taking the centerline of the hysteresis curve.

Two models were developed, one for the large magnet and one for the small magnets. The two top magnets are assumed to be identical, and their characteristics were averaged before fitting parameters. Note that the large magnet carries half the additional load, and each of the small magnets carry one fourth of the additional load. For the large magnet, the least squares fit is given by the parameters $m = -1.68 \times 10^{-2}$ amps/volt, $c = 1.36 \times 10^{-4}$ amps/gram, and $d = 2.58 \times 10^{-1}$ amps. For the small magnet, the least squares fit is given by the parameters $m = -1.94 \times 10^{-2}$ amps/volt, $c = 2.81 \times 10^{-4}$ amps/gram, and $d = 5.04 \times 10^{-1}$ amps. These constants are not in SI units; putting the data in SI units gives values for the magnet constants $k_{il} = 7.21 \times 10^{1}$ new-

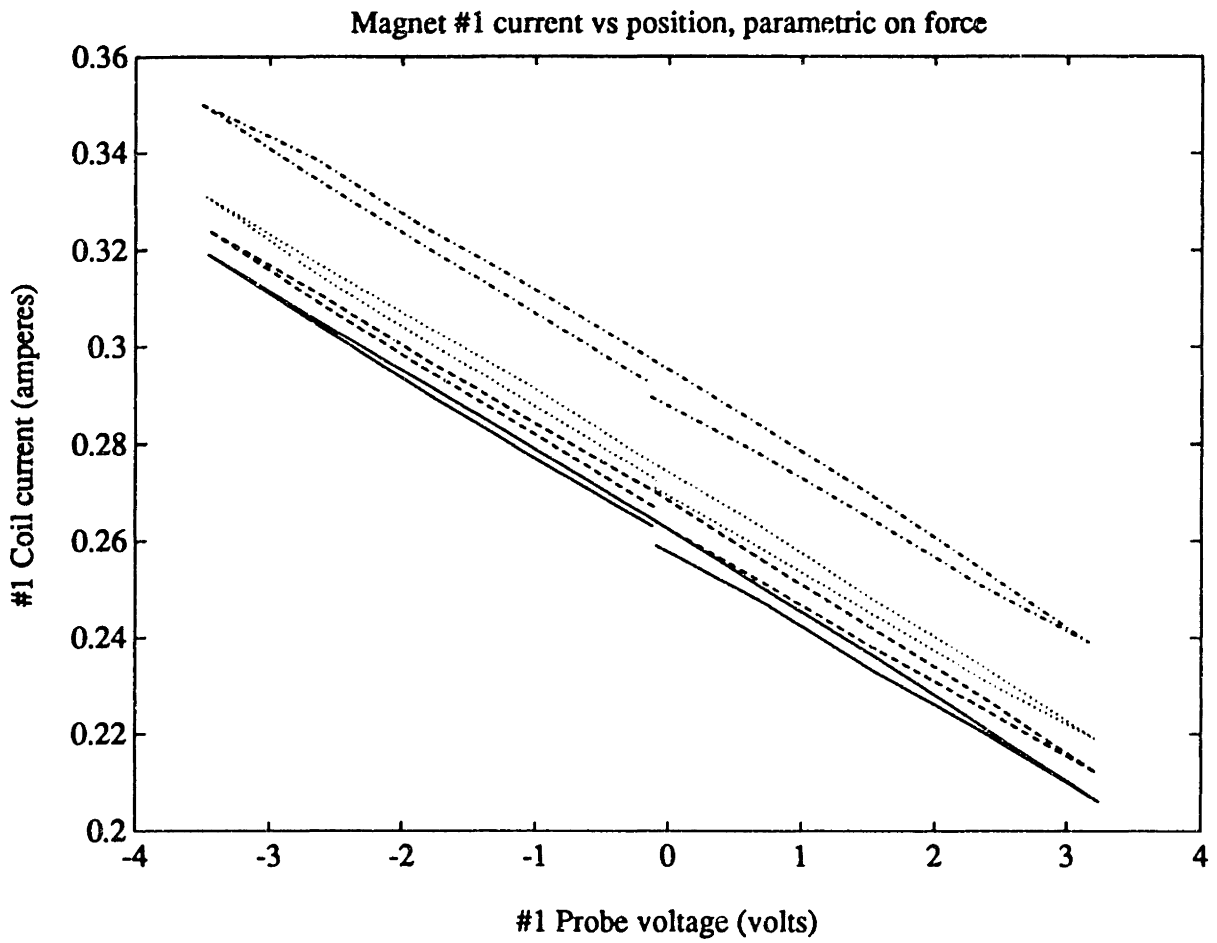

Figure 6.19: Magnet #1 coil current vs. position probe voltage, for four additional mass values: 50, 100, 200, and 500 grams respectively from bottom to top.

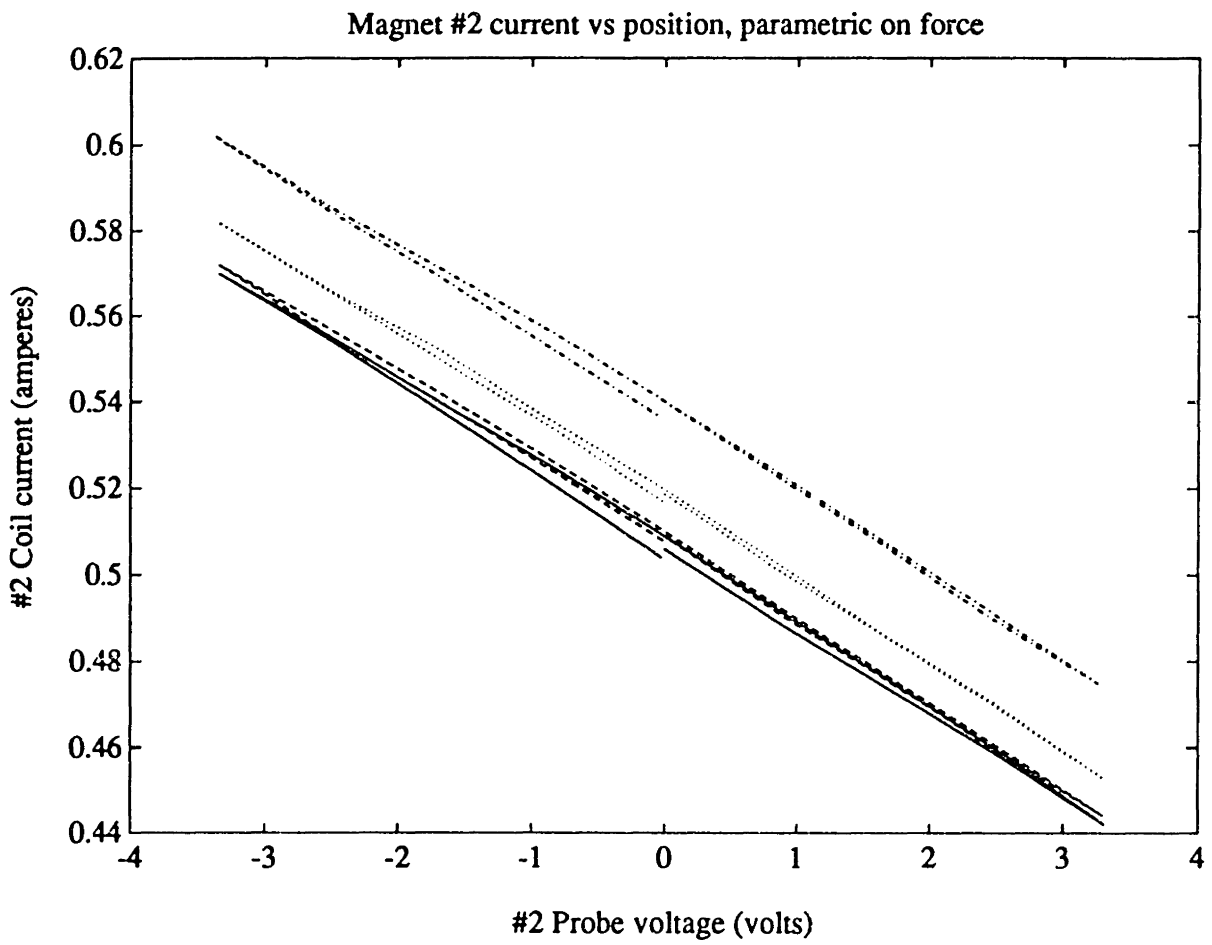

Figure 6.20: Magnet #2 coil current vs. position probe voltage, for four additional mass values: 50, 100, 200, and 500 grams respectively from bottom to top.

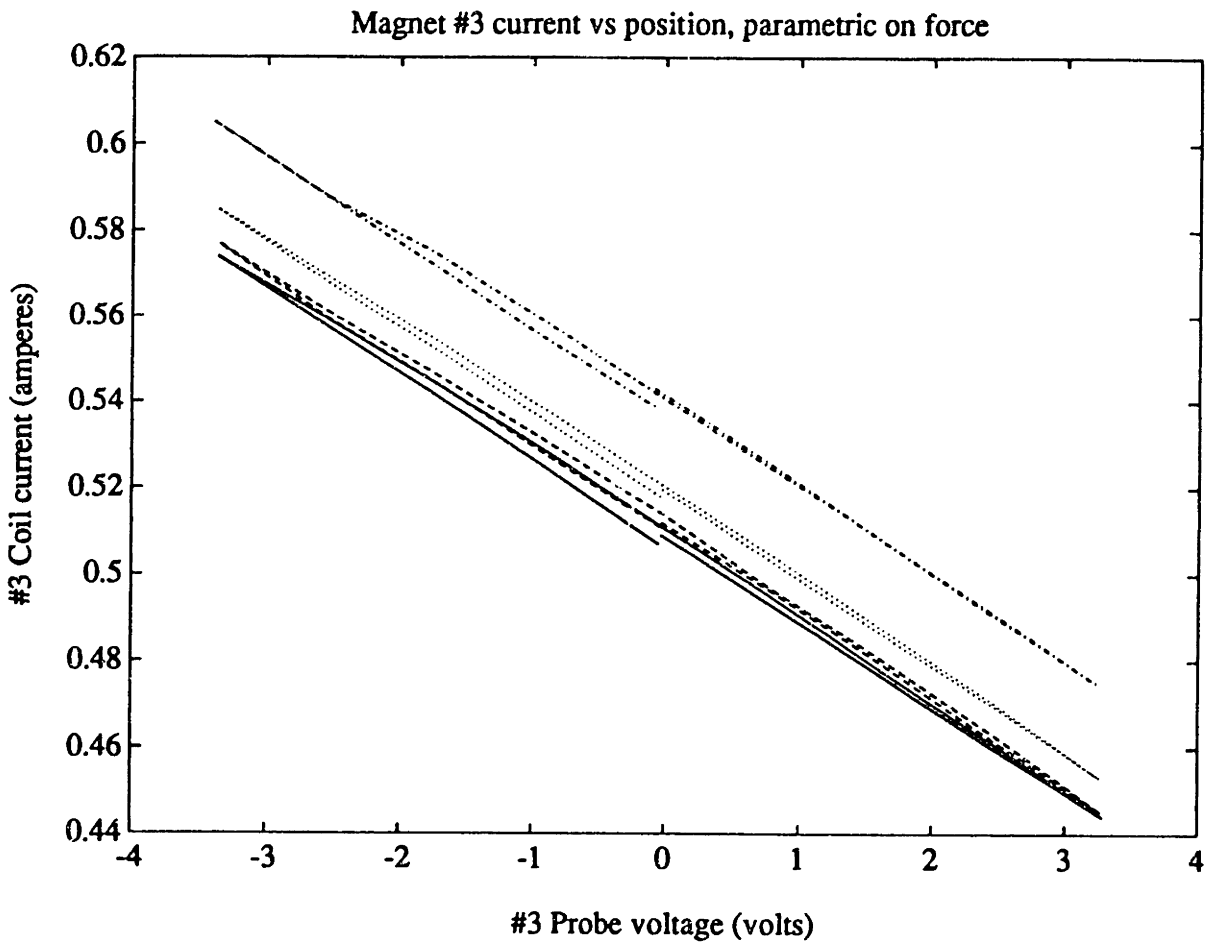

Figure 6.21: Magnet #3 coil current vs. position probe voltage, for four additional mass values: 50, 100, 200, and 500 grams respectively from bottom to top.

tons/amp, $k_{gl} = 2.38 \times 10^5$ newtons/meter, $k_{is} = 3.49 \times 10^1$ newtons/amp, and $k_{gs} = 1.33 \times 10^5$ newtons/meter. Note that these values are significantly different from the cruder estimates developed in Section 6.4. These values are used to represent the magnets in the accurate model which is developed below.

Since the four lateral magnets are operated at approximately the same bias currents and air gaps as the two small top magnets, the parameters developed here apply to the lateral magnets as well. Thus, we have developed accurate models for the force constants of all seven electromagnets.

6.12.2 Torque measurements

Until this point, the incremental torque terms $\tilde{T}_{ij}$ in the linear dynamical model developed in Section 5.2 have gone unmodeled. These terms represent the rotational instability present when a magnet pole piece of finite extent is held in proximity to a plane of permeable material. Holding a flat magnet in close proximity and parallel to a sheet of steel will convince one that this system is unstable in the rotational degrees of freedom as well as the normal-translation degree of freedom.

It can be argued that the only terms which have great significance are the torques about the $\mathbf{e}_1$ axis, i.e., $\tilde{T}_{i1}, \quad i = 1, 2, \ldots, 7$. This is so for two reasons. First, all seven magnets contribute to these terms whereas only magnets 4 through 7 contribute to torque instabilities about the $\mathbf{e}_2$ axis and only magnets 1 through 3 contribute to torque instabilities about the $\mathbf{e}_3$ axis. Secondly, the moment arm by which the $\tilde{T}_{i1}, \quad i = 1, 2, \ldots, 7$ torques are controlled is $W_m = 3.175 \times 10^{-2}$ meters, which is much smaller than $L_m = 9.208 \times 10^{-2}$ meters. For these reasons, only the $\mathbf{e}_1$ torque terms will be modelled, and we will assume $\tilde{T}_{i2} = 0, \quad i = 4, 5, \ldots, 7$, and $\tilde{T}_{i3} = 0, \quad i = 1, 2, 3$.

This section describes an experiment which allows the estimation of the sum of the torque terms about the $\mathbf{e}_1$ axis. The individual dependencies are not identified. That is, we estimate the quantity

$$\tilde{T}_1(q_1) \triangleq \sum_{i=1}^{7} \tilde{T}_{i1}(q_1) \tag{6.80}$$

as a linear function of q_1, i.e.,

$$\tilde{T}_1(q_1) = k_t q_1 \tag{6.81}$$

The term k_t is identified by a least squares fit to data taken from the suspended system as described below.

With the system in suspension, and no additional load on the platen, the roll setpoint was varied such that the platen was rotated through a range of about

$\pm 2.5 \times 10^{-4}$ radians (about 1/5 of the full range). At about 20 points in this range, the coil currents i_2 and i_3, and position transducer voltages v_{p2} and v_{p3} were recorded. To linear terms, the difference $v_{p2} - v_{p3}$ is proportional to the angle q_1. Specifically,

$$q_1 \approx \frac{v_{p2} - v_{p3}}{2W_m 1.97 \times 10^5} \tag{6.82}$$

The incremental force model (6.79) from the previous section was applied using the linear parameters c, d, m for the small magnets to predict the incremental forces $\tilde{F}_2$ and $\tilde{F}_3$ in Newtons applied to the platen by bearings #2 and #3. Note that only these forces can control torques about the $\mathbf{e}_1$ axis. These incremental forces are multiplied by the moment arm W_m to calculate the incremental torque applied to the platen by the bearings as a function of rotation q_1. The torque term $\tilde{T}_1$ is equal to the negative of the torque applied to the platen by the bearings. This is so because in static suspension, the bearings are balancing out the term $\tilde{T}_1$. Specifically, we calculate

$$\tilde{T}_1 = W_m(\tilde{F}_3 - \tilde{F}_2) \tag{6.83}$$

The torque $\tilde{T}_1$ in Newton-meters is plotted versus the angle q_1 in radians as shown in Figure 6.22. Note that there is a torque offset of -3.29×10^{-2} Newton-meters in the data. This offset is first subtracted out and then the data is fitted to the model (6.81). The resulting parameter estimate is $k_t = 300$ Newton-meters/radian.

6.13 Eddy Currents

The suspension transfer functions were calculated using the parameters derived above. Then the five principal system transfer functions were measured using an HP3562A dynamic analyser. The measured and predicted transfer functions were in good agreement at low- to mid-frequencies within a factor of 1.3 in the vertical system and a factor of 1.5 in the lateral system in terms of DC gain and suspension unstable pole location.

However, the measured transfer functions showed a significant phase and magnitude roll-off at frequencies above 100 Hz. This roll-off is believed to be due to eddy currents in the electromagnet structure, which is not laminated. The roll-off can be matched by adding a pair of poles with time constants of 0.6 msec and 0.2 msec respectively in series with each current input. This raises the order of the vertical plant from sixth order to twelfth order, and the lateral plant from fourth order to twelfth order.

The predicted and measured transfer functions are presented graphically and discussed in more detail in section 6.16. In the next section, the pair of eddy-

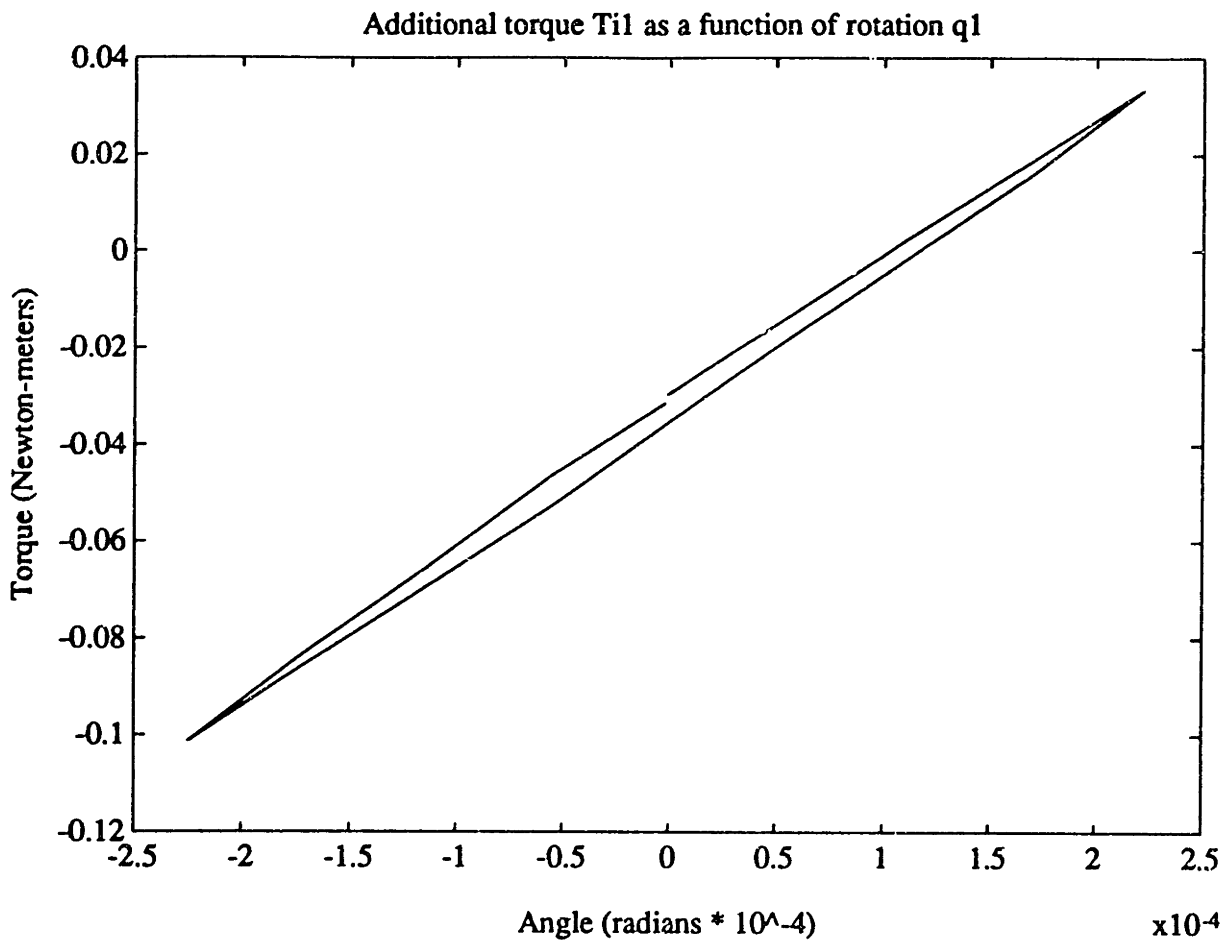

Figure 6.22: Incremental torque $\tilde{T}_1$ in Newton-meters versus rotation q_1 in radians.

current poles described above are added in series with each of the coil-current inputs in order to more accurately model the plant high-frequency behavior.

6.14 Suspension Models

In this section, the results derived in previous sections are combined to yield models for the vertical and lateral suspension dynamics. The important changes relative to the results from section 6.7.1 are the numerical change in the magnet incremental parameters k_{is}, k_{gs}, k_{il}, and k_{gl}, and the inclusion of the eddy-current and roll torque terms as developed from experimental data in the previous three sections. Combining all these results gives the numerical values for the vertical suspension system matrices shown below.

```
Matlab numerical values for vertical suspension system matrices.

Av =

  Columns 1 through 6

  -6.6667e+03  -8.3333e+06           0           0           0           0
   1.0000e+00           0           0           0           0           0
           0           0  -6.6667e+03  -8.3333e+06           0           0
           0           0   1.0000e+00           0           0           0
           0           0           0           0  -6.6667e+03  -8.3333e+06
           0           0           0           0   1.0000e+00           0
           0           0           0           0           0           0
           0           0           0           0           0           0
           0           0           0           0           0           0
           0           0           0   1.9399e+08           0  -1.9399e+08
           0  -4.0981e+08           0   1.9537e+08           0   1.9837e+08
           0   5.6048e+07           0   2.7130e+07           0   2.7130e+07

  Columns 7 through 12

           0           0           0           0           0           0
           0           0           0           0           0           0
           0           0           0           0           0           0
           0           0           0           0           0           0
           0           0           0           0           0           0
           0           0           0           0           0           0
           0           0           0   1.0000e+00           0           0
           0           0           0           0   1.0000e+00           0
           0           0           0           0           0   1.0000e+00
   1.1936e+04           0           0           0           0           0
           0   3.1654e+04   1.9098e+04           0           0           0
           0   2.4051e+02   4.7015e+04           0           0           0

Bv =

     1     0     0
     0     0     0
     0     1     0
     0     0     0
     0     0     1
     0     0     0
     0     0     0
```

```
     0     0     0
     0     0     0
     0     0     0
     0     0     0
     0     0     0

Cv =

     0     0     0     0     0     0     1     0     0     0     0     0
     0     0     0     0     0     0     0     1     0     0     0     0
     0     0     0     0     0     0     0     0     1     0     0     0

Dv =

     0     0     0
     0     0     0
     0     0     0
```

The numerical results for the lateral suspension dynamics including the effect of eddy currents are shown below.

```
Matlab numerical values for lateral suspension system matrices.

Al =

  Columns 1 through 6

  -6.6667e+03  -8.3333e+06           0           0           0           0
   1.0000e+00           0           0           0           0           0
           0           0  -6.6667e+03  -8.3333e+06           0           0
           0           0   1.0000e+00           0           0           0
           0           0           0           0  -6.6667e+03  -8.3333e+06
           0           0           0           0   1.0000e+00           0
           0           0           0           0           0           0
           0           0           0           0           0           0
           0           0           0           0           0           0
           0           0           0           0           0           0
           0   1.9547e+08           0  -1.9547e+08           0  -1.9547e+08
           0   2.7130e+07           0   2.7130e+07           0  -2.7130e+07

  Columns 7 through 12

           0           0           0           0           0           0
           0           0           0           0           0           0
           0           0           0           0           0           0
           0           0           0           0           0           0
           0           0           0           0           0           0
           0           0           0           0           0           0
  -6.6667e+03  -8.3333e+06           0           0           0           0
   1.0000e+00           0           0           0           0           0
           0           0           0           0   1.0000e+00           0
           0           0           0           0           0   1.0000e+00
           0   1.9547e+08   3.2925e+04           0           0           0
           0  -2.7130e+07           0   4.9627e+04           0           0

Bl =

     1     0     0     0
     0     0     0     0
     0     1     0     0
     0     0     0     0
```

```
     0     0     1     0
     0     0     0     0
     0     0     0     1
     0     0     0     0
     0     0     0     0
     0     0     0     0
     0     0     0     0
     0     0     0     0

C1 =

     0     0     0     0     0     0     0     0     1     0     0     0
     0     0     0     0     0     0     0     0     0     1     0     0

D1 =

     0     0     0     0
     0     0     0     0
```

6.15 Decoupled Plant Models

Models for the vertical and lateral plants including the current drives and decoupling networks are developed in this section. These models are used to predict the expected frequency response of the decoupled plant. In the next section, experimental measurements of the plant frequency response are compared with those predicted from the models developed in this section. The measured frequency responses are then used as the final models for the principal frequency responses which are used to design the controllers in the next chapter.

6.15.1 Vertical Decoupling Network Design

For the new values of the magnet incremental parameters developed in the previous sections, the transformation matrix T_{iu} is re-defined as

$$T_{iu} = \begin{bmatrix} 0 & -1 & 1 \\ 1 & 1 & 1 \\ -1 & 1 & 1 \end{bmatrix}. \tag{6.84}$$

The relative scaling of the elements in the array is dictated by the ratio of the large and small magnet current constants. That is, the magnitude ratio of the 1-2 and 1-3 entries to the 2-2, 3-2, 2-3, and 3-3 entries is equal to $2 * k_{is}/k_{il}$. Due to the symmetry of the measured parameters, this ratio is approximately unity to within the expected accuracy of the experimental measurement.

The matrices T_{py} and T_{mp} remain unchanged from the values used in the

previous chapter, i.e.,

$$T_{py} = 1.97 \times 10^5 T_{gy} = \begin{bmatrix} 0 & -1.81 \times 10^4 & 1.97 \times 10^5 \\ 6.25 \times 10^3 & 1.81 \times 10^4 & 1.97 \times 10^5 \\ -6.25 \times 10^3 & 1.81 \times 10^4 & 1.97 \times 10^5 \end{bmatrix} \tag{6.85}$$

and

$$T_{mp} = \begin{bmatrix} 0 & 0.5 & -0.5 \\ -0.5 & 0.25 & 0.25 \\ 0.5 & 0.25 & 0.25 \end{bmatrix}. \tag{6.86}$$

The transformation T_{mp} is implemented in op-amp circuitry as shown in Figure 6.23. The transformation T_{iu} is implemented in op-amp circuitry as shown in Figure 6.24.

6.15.2 Vertical plant system matrices

As before, the current drives implement lead compensation. Each of the current drives has a transfer function from input v_{ij} to output i_j given by

$$\frac{i_j(s)}{v_{ij}(s)} = \frac{1}{\alpha}\frac{\alpha\tau s + 1}{\tau s + 1} \tag{6.87}$$

where $\alpha = 15$ and $\tau = 4.47 \times 10^{-4}$. Combining the three current drives in parallel yields the current source system equations as

$$\dot{w}_{vd} = A_{vd} w_{vd} + B_{vd} v_i \tag{6.88}$$

$$i = C_{vd} w_{vd} + D_{vd} v_i \tag{6.89}$$

where

$$A_{vd} = \mathrm{diag}(-2.24 \times 10^3,\ -2.24 \times 10^3,\ -2.24 \times 10^3) \tag{6.90}$$

$$B_{vd} = \mathrm{diag}(1,\ 1,\ 1) \tag{6.91}$$

$$C_{vd} = \mathrm{diag}(-2.09 \times 10^3,\ -2.09 \times 10^3,\ -2.09 \times 10^3) \tag{6.92}$$

$$D_{vd} = \mathrm{diag}(1,\ 1,\ 1) \tag{6.93}$$

For the purposes of design, the region contained within the dashed line in Figure 6.4 is considered to be the plant which is controlled by the controller. Combining all the information developed above yields the plant system matrices as

$$\dot{w}_{vp} = A_{vp} w_{vp} + B_{vp} v_u \tag{6.94}$$

$$v_m = C_{vp} w_{vp} + D_{vp} v_u \tag{6.95}$$

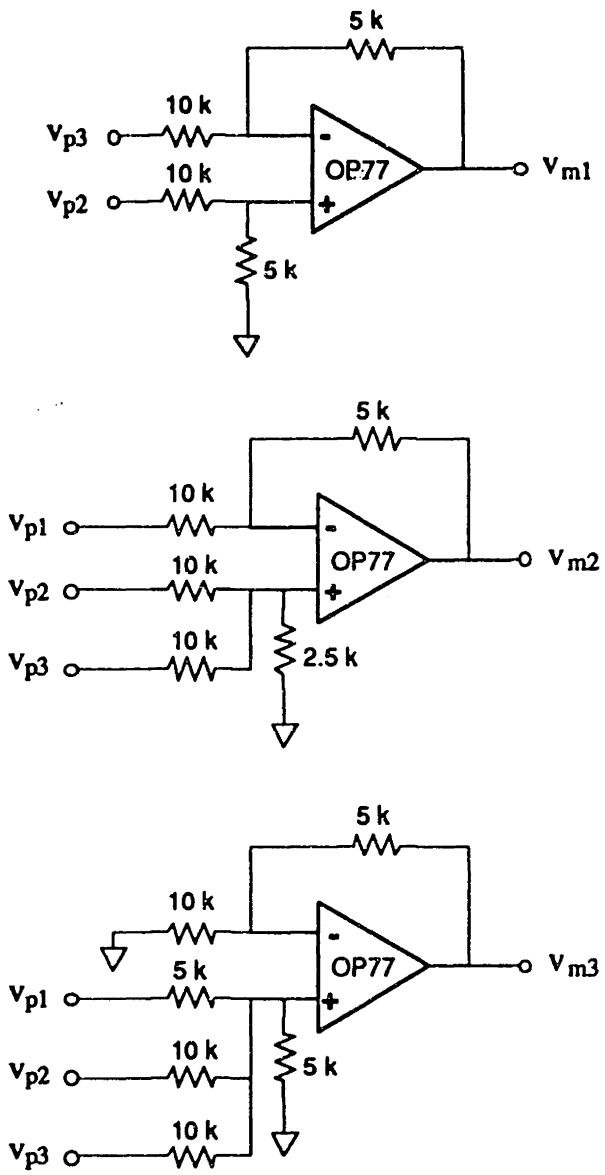

Figure 6.23: Circuit implementation of the transformation T_{mp}.

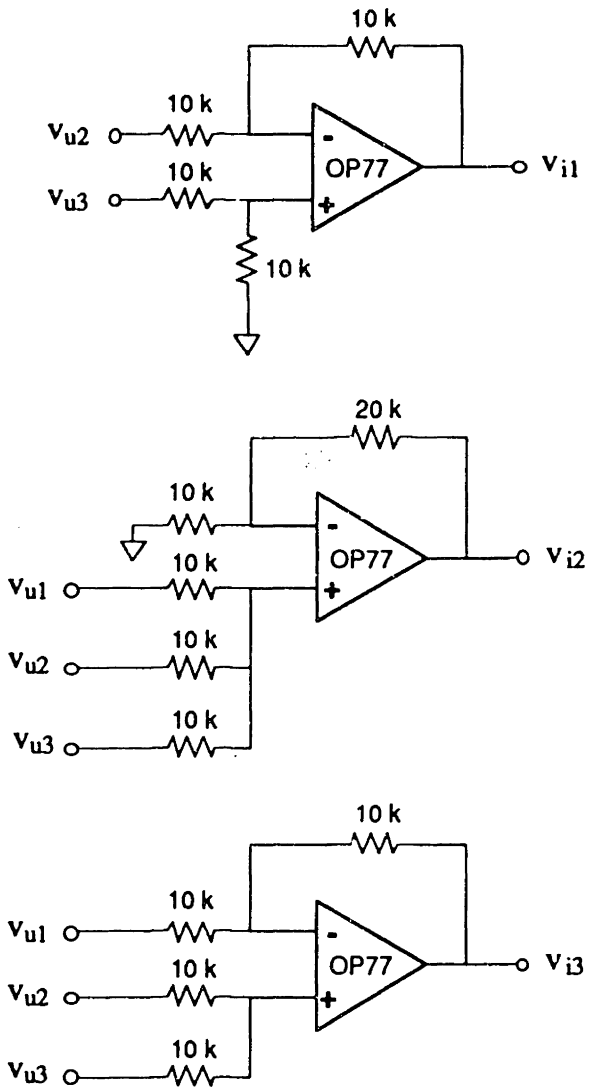

Figure 6.24: Circuit implementation of the transformation T_{iu}.

where $w_{vp} = [\ w_v'\ w_{vd}'\ ]'$ and

$$A_{vp} = \begin{bmatrix} A_v & B_v C_{vd} \\ 0 & A_{vd} \end{bmatrix} \tag{6.96}$$

$$B_{vp} = \begin{bmatrix} B_v D_{vd} T_{iu} \\ B_{vd} T_{iu} \end{bmatrix} \tag{6.97}$$

$$C_{vp} = \begin{bmatrix} T_{mp} T_{py} C_v & 0 \end{bmatrix} \tag{6.98}$$

$$D_{vp} = [0] \tag{6.99}$$

where the indicated zero blocks are of the appropriate dimensions.

The numerical values of the vertical system matrices are shown below.

```
Avp =

  Columns 1 through 6

  -6.6667e+03  -8.3333e+06           0           0           0           0
   1.0000e+00           0           0           0           0           0
           0           0  -6.6667e+03  -8.3333e+06           0           0
           0           0   1.0000e+00           0           0           0
           0           0           0           0  -6.6667e+03  -8.3333e+06
           0           0           0           0   1.0000e+00           0
           0           0           0           0           0           0
           0           0           0           0           0           0
           0           0           0           0           0           0
           0           0           0   1.9399e+08           0  -1.9399e+08
           0  -4.0981e+08           0   1.9837e+08           0   1.9837e+08
           0   5.6048e+07           0   2.7130e+07           0   2.7130e+07
           0           0           0           0           0           0
           0           0           0           0           0           0
           0           0           0           0           0           0

  Columns 7 through 12

           0           0           0           0           0           0
           0           0           0           0           0           0
           0           0           0           0           0           0
           0           0           0           0           0           0
           0           0           0           0           0           0
           0           0           0           0           0           0
           0           0           0   1.0000e+00           0           0
           0           0           0           0   1.0000e+00           0
           0           0           0           0           0   1.0000e+00
   1.1936e+04           0           0           0           0           0
           0   3.1654e+04   1.9098e+04           0           0           0
           0   2.4051e+02   4.7015e+04           0           0           0
           0           0           0           0           0           0
           0           0           0           0           0           0
           0           0           0           0           0           0

  Columns 13 through 15

  -2.0880e+03           0           0
           0           0           0
           0  -2.0880e+03           0
```

```
            0            0            0
            0            0  -2.0880e+03
            0            0            0
            0            0            0
            0            0            0
            0            0            0
            0            0            0
            0            0            0
            0            0            0
  -2.2371e+03            0            0
            0  -2.2371e+03            0
            0            0  -2.2371e+03

Bvp =

            0  -1.0000e+00   1.0000e+00
            0            0            0
   1.0000e+00   1.0000e+00   1.0000e+00
            0            0            0
  -1.0000e+00   1.0000e+00   1.0000e+00
            0            0            0
            0            0            0
            0            0            0
            0            0            0
            0            0            0
            0            0            0
            0            0            0
            0  -1.0000e+00   1.0000e+00
   1.0000e+00   1.0000e+00   1.0000e+00
  -1.0000e+00   1.0000e+00   1.0000e+00

Cvp =

  Columns 1 through 6

            0            0            0            0            0            0
            0            0            0            0            0            0
            0            0            0            0            0            0

  Columns 7 through 12

   6.2548e+03            0            0            0            0            0
            0   1.8140e+04            0            0            0            0
            0            0   1.9700e+05            0            0            0

  Columns 13 through 15

            0            0            0
            0            0            0
            0            0            0

Dvp =

     0     0     0
     0     0     0
     0     0     0
```

The plant is fifteenth order, i.e., six state variables in the suspension dynamics without eddy currents, six state variables in the eddy current model, and three

state variables in the current drive lead terms.

6.15.3 Lateral Decoupling Network Design

The lateral decoupling transformations are unchanged from the transformations used earlier in this chapter. The specific numerical values of S_{py}, S_{mp}, and S_{iu} are given in section 6.10.1. No change is required, since all four lateral suspension magnets are identical; this symmetry makes it simple to design the decoupling transformations.

The operational-amplifier circuits which implement the transformations S_{mp} and S_{iu} are shown in Figures 6.25 and 6.26.

6.15.4 Lateral plant system matrices

The current drive design is unchanged from that used earlier in this chapter. Specifically, the numerical values of the matrices A_{ld}, B_{ld}; C_{ld}, and D_{ld} are the same as given in section 6.10.1

For the purposes of design, the region contained within the dashed line in Figure 6.12 is considered to be the plant which is controlled by the controller. Combining all the information developed above yields the plant system matrices as

$$\dot{w}_{lp} = A_{lp} w_{lp} + B_{lp} v_u \tag{6.100}$$

$$v_m = C_{lp} w_{lp} + D_{lp} v_u \tag{6.101}$$

where $w_{lp} = [\ w_l'\ w_{ld}'\ ]'$ and

$$A_{lp} = \begin{bmatrix} A_l & B_l C_{ld} \\ 0 & A_{ld} \end{bmatrix} \tag{6.102}$$

$$B_{lp} = \begin{bmatrix} B_l D_{ld} S_{iu} \\ B_{ld} S_{iu} \end{bmatrix} \tag{6.103}$$

$$C_{lp} = \begin{bmatrix} S_{mp} S_{py} C_l & 0 \end{bmatrix} \tag{6.104}$$

$$D_{lp} = [0] \tag{6.105}$$

where the indicated zero blocks are of the appropriate dimensions.

A copy of the output for the numerical values of the lateral plant system matrices including the effect of eddy currents is shown below.

```
Alp =

  Columns 1 through 6
```

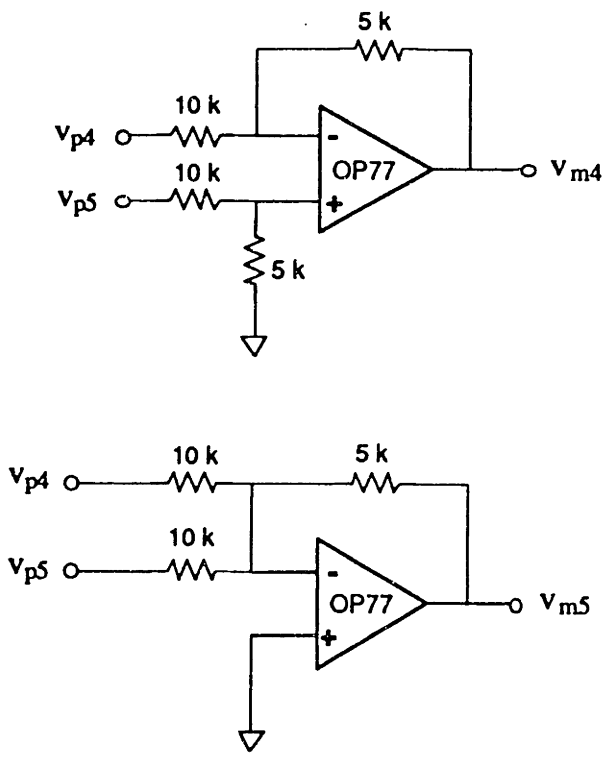

Figure 6.25: Circuit implementation of the transformation $S_{m\rho}$.

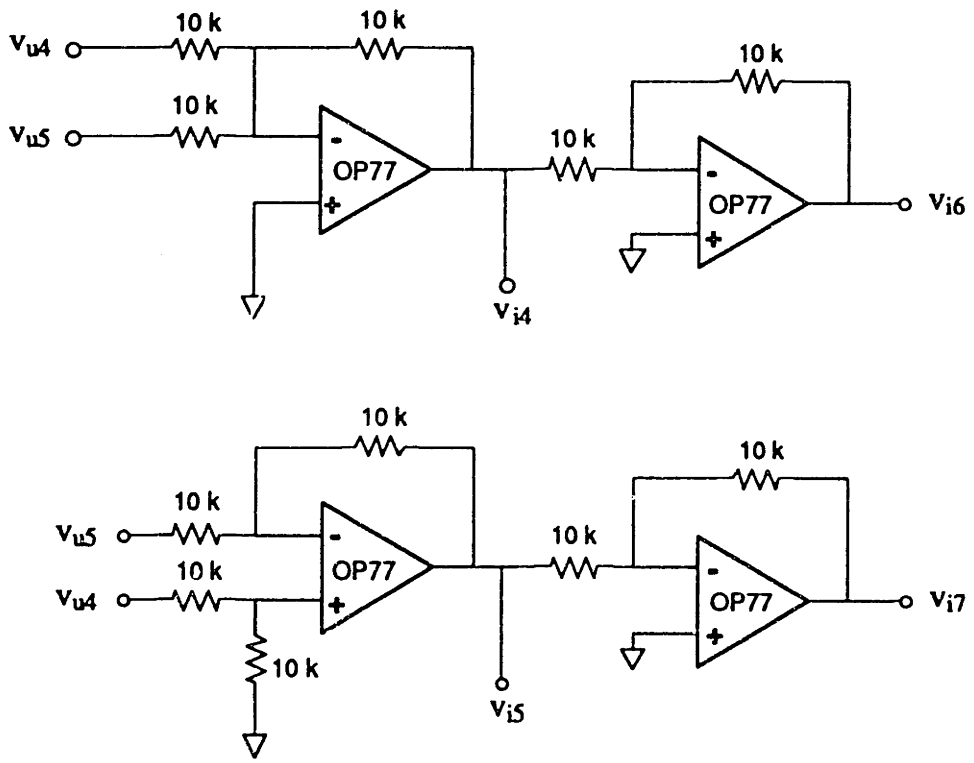

Figure 6.26: Circuit implementation of the transformation S_{iu}.

-6.6667e+03	-8.3333e+06	0	0	0	0
1.0000e+00	0	0	0	0	0
0	0	-6.6667e+03	-8.3333e+06	0	0
0	0	1.0000e+00	0	0	0
0	0	0	0	-6.6667e+03	-8.3333e+06
0	0	0	0	1.0000e+00	0
0	0	0	0	0	0
0	0	0	0	0	0
0	0	0	0	0	0
0	0	0	0	0	0
0	1.9547e+08	0	-1.9547e+08	0	-1.9547e+08
0	2.7130e+07	0	2.7130e+07	0	-2.7130e+07
0	0	0	0	0	0
0	0	0	0	0	0
0	0	0	0	0	0
0	0	0	0	0	0

Columns 7 through 12

0	0	0	0	0	0
0	0	0	0	0	0
0	0	0	0	0	0
0	0	0	0	0	0
0	0	0	0	0	0
0	0	0	0	0	0
-6.6667e+03	-8.3333e+06	0	0	0	0
1.0000e+00	0	0	0	0	0
0	0	0	0	1.0000e+00	0
0	0	0	0	0	1.0000e+00
0	1.9547e+08	3.2925e+04	0	0	0
0	-2.7130e+07	0	4.9627e+04	0	0
0	0	0	0	0	0
0	0	0	0	0	0
0	0	0	0	0	0
0	0	0	0	0	0

Columns 13 through 16

-2.0880e+03	0	0	0
0	0	0	0
0	-2.0880e+03	0	0
0	0	0	0
0	0	-2.0880e+03	0
0	0	0	0
0	0	0	-2.0880e+03
0	0	0	0
0	0	0	0
0	0	0	0
0	0	0	0
0	0	0	0
-2.2371e+03	0	0	0
0	-2.2371e+03	0	0
0	0	-2.2371e+03	0
0	0	0	-2.2371e+03

Blp =

1.0000e+00	1.0000e+00
0	0
-1.0000e+00	1.0000e+00
0	0
-1.0000e+00	-1.0000e+00

```
         0            0
 1.0000e+00  -1.0000e+00
         0            0
         0            0
         0            0
         0            0
         0            0
 1.0000e+00   1.0000e+00
-1.0000e+00   1.0000e+00
-1.0000e+00  -1.0000e+00
 1.0000e+00  -1.0000e+00

Clp =

  Columns 1 through 6

         0            0            0            0            0            0
         0            0            0            0            0            0

  Columns 7 through 12

         0            0   1.8140e+04            0            0            0
         0            0            0   1.9700e+05            0            0

  Columns 13 through 16

         0            0            0            0
         0            0            0            0

Dlp =

    0    0
    0    0
```

This completes the vertical and lateral suspension modeling process.

6.16 Comparison of predicted and measured frequency responses

In this section, the transfer functions predicted by the models developed in the previous section are compared with the transfer functions which were measured on the actual hardware using a dynamic analyser. As mentioned before, the predicted and measured transfer functions agree within 30% in the vertical system and 50% in the lateral system. The measured transfer functions are used for further design work, as they represent the most accurate model of the system.

The transfer functions were measured using an HP3562A dynamic analyser in swept-sine, log-resolution mode. The analyzer source signal amplitude was set to a low value of 75 mV maximum, so that the response of the system was linear. This corresponds to a maximum platen translation of 375 nm.

The vertical transfer functions are presented in the next section, and the lateral transfer functions in the section following that.

6.16.1 Vertical system transfer functions

The three principal vertical plant transfer functions are defined as the transfer functions from the ith input of the transformation T_{iu} to the ith output of the transformation T_{mp}. In other words the three principal vertical plant transfer functions represent the transfer functions seen by the three vertical modal controllers.

Figure 6.27 shows the predicted transfer function and the measured transfer function in roll motion $v_{m1}(s)/v_{u1}(s)$. As shown in the figure, the predicted DC gain is higher than the measured DC gain by a factor of 1.1, and the predicted suspension break-frequency is higher than the measured break-frequency by a factor of 1.3. Also it can be seen that at high frequencies, the measured transfer function falls off in magnitude even faster than the predicted transfer function. In other words, a higher order model must be used at high frequencies. However, the pair of poles with 0.2 and 0.6 millisecond time constants suffice to model the transfer function in the vicinity of crossover, and thus no higher-order model will be developed for this or the other four modal transfer functions which follow.

The measured transfer function is fit to a model of the form

$$\frac{v_{m1}(s)}{v_{u1}(s)} = \frac{k_1}{(\tau_1 s+1)(\tau_1 s-1)} \cdot \frac{1}{15} \frac{6.71\times 10^{-3}s+1}{4.47\times 10^{-4}s+1} \cdot \frac{1}{(6\times 10^{-4}s+1)(2\times 10^{-4}s+1)} \tag{6.106}$$

where the second term represents the current-drive lead term, and the third term models eddy-current behavior to frequencies above crossover. The first term models the DC gain and break-frequency. The measured data is well fit if these paramters are chosen as $k_1 = 1.5$ and $\tau_1 = 1/80$ seconds.

Figure 6.28 shows the quality of fit between measured data and the transfer function given by (6.106). At all but the highest frequencies the fit is quite good. This transfer function (6.106) will be used in the next chapter to design the roll modal controller and to predict its performance.

Figure 6.29 shows the predicted transfer function and the measured transfer function in pitch motion $v_{m2}(s)/v_{u2}(s)$. As shown in the figure, the predicted DC gain is higher than the measured DC gain by a factor of 1.3, and the predicted suspension break-frequency is higher than the measured break-frequency by a factor of 1.3.

The measured transfer function is fit to a model of the form

$$\frac{v_{m2}(s)}{v_{u2}(s)} = \frac{k_2}{(\tau_2 s+1)(\tau_2 s-1)} \cdot \frac{1}{15} \frac{6.71\times 10^{-3}s+1}{4.47\times 10^{-4}s+1} \cdot \frac{1}{(6\times 10^{-4}s+1)(2\times 10^{-4}s+1)} \tag{6.107}$$

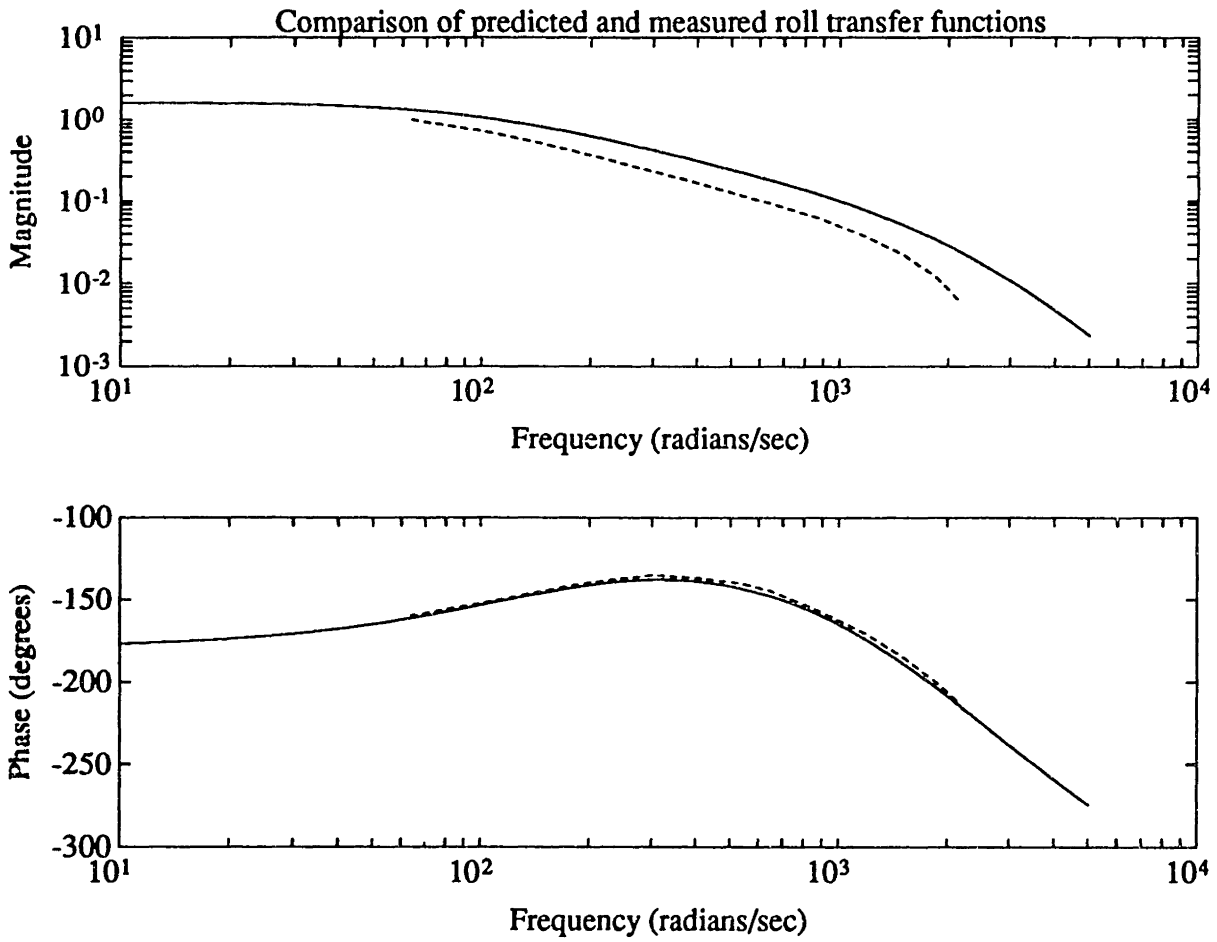

Figure 6.27: Predicted (solid line) versus measured (dashed line) roll transfer functions $v_{m1}(s)/v_{u1}(s)$.

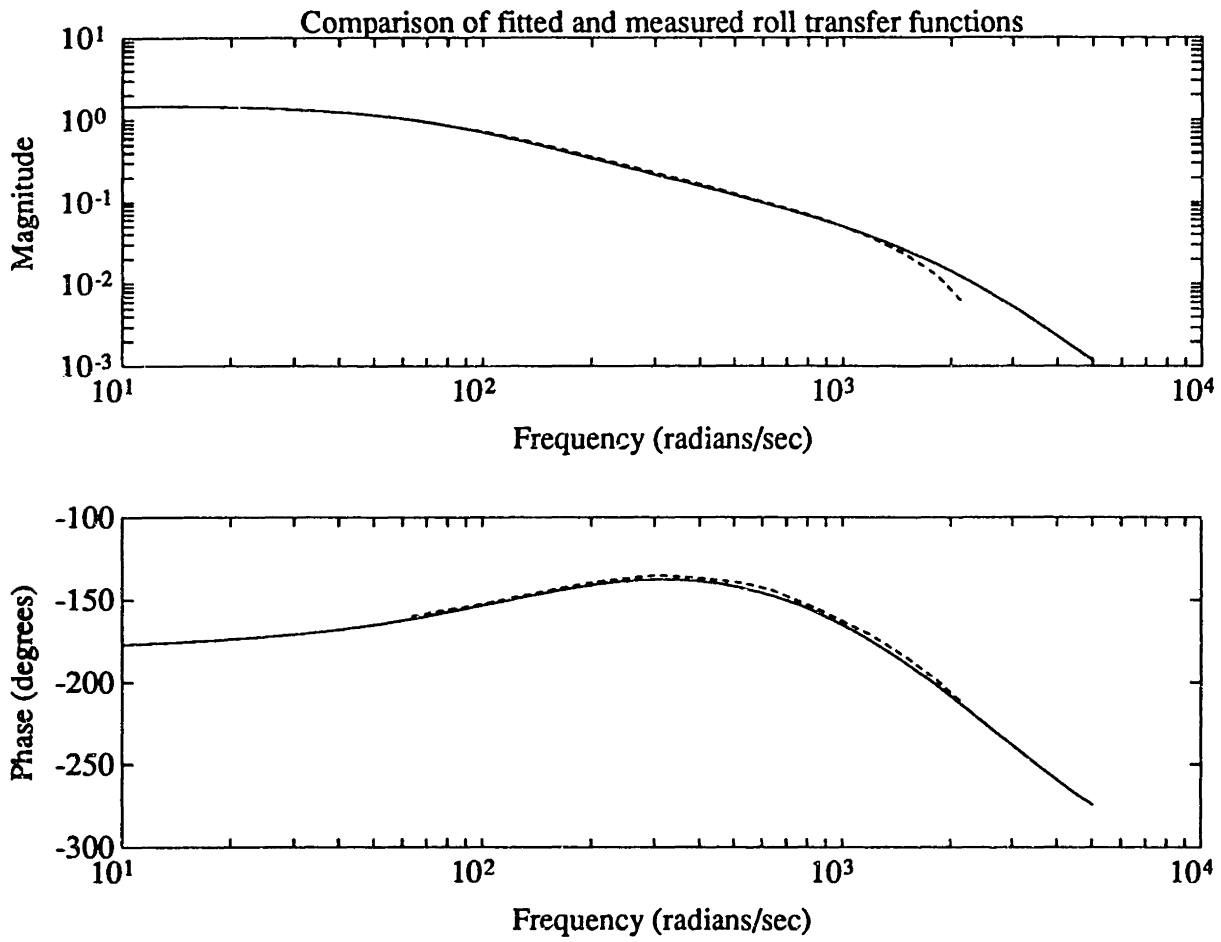

Figure 6.28: Showing the quality of fit between the transfer function of equation (6.106) (solid line) and the measured roll transfer function(dashed line).

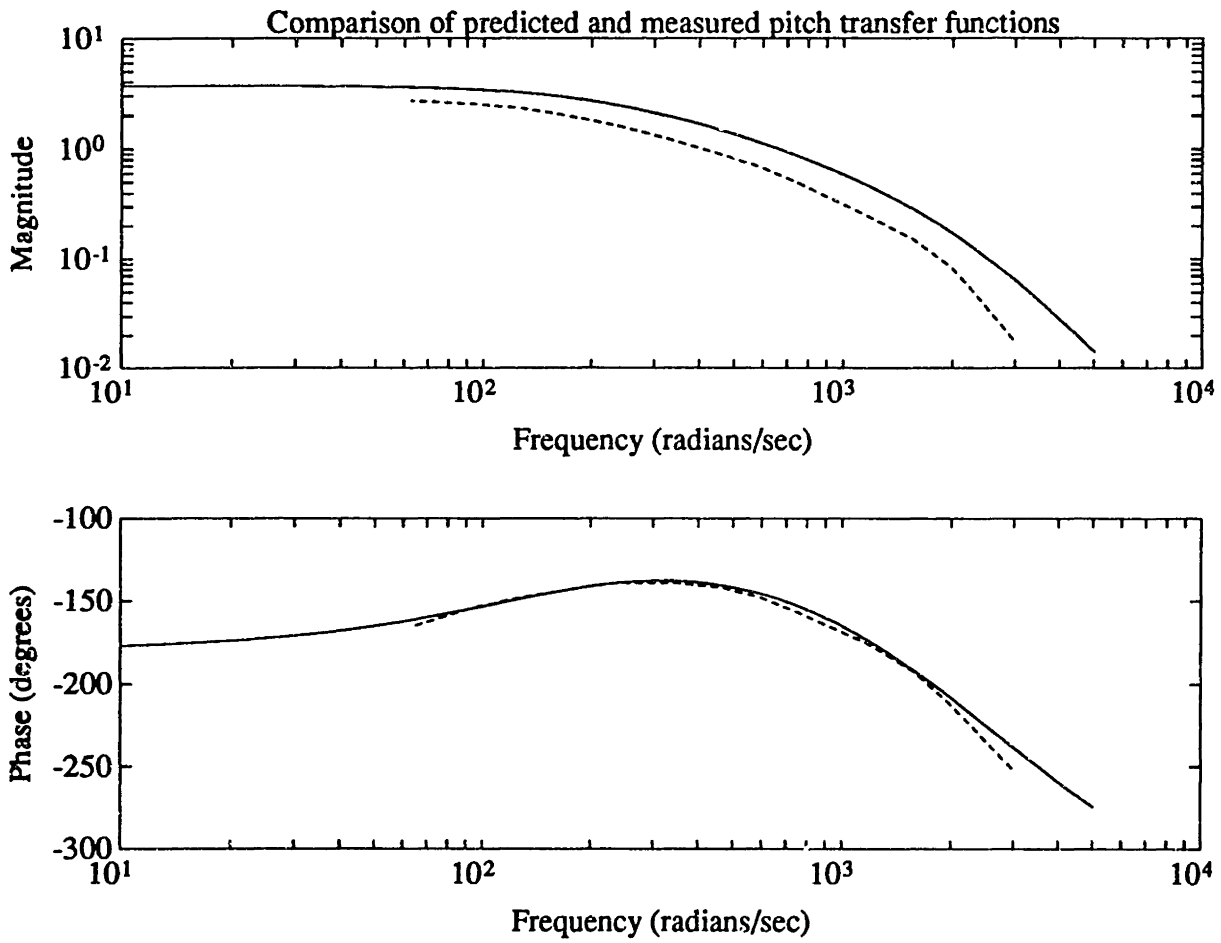

Figure 6.29: Predicted (solid line) versus measured (dashed line) pitch transfer functions $v_{m2}(s)/v_{u2}(s)$.

The measured data is well fit if these paramters are chosen as $k_2 = 2.9$ and $\tau_2 = 1/150$ seconds.

Figure 6.30 shows the quality of fit between measured data and the transfer function given by (6.107). At all but the highest frequencies the fit is quite good. This transfer function (6.107) will be used in the next chapter to design the pitch modal controller and to predict its performance.

Figure 6.31 shows the predicted transfer function and the measured transfer function in heave motion $v_{m3}(s)/v_{u3}(s)$. As shown in the figure, the predicted DC gain is higher than the measured DC gain by a factor of 1.2, and the predicted suspension break-frequency is higher than the measured break-frequency by a factor of 1.4.

The measured transfer function is fit to a model of the form

$$\frac{v_{m3}(s)}{v_{u3}(s)} = \frac{k_3}{(\tau_3 s + 1)(\tau_3 s - 1)} \cdot \frac{1}{15} \frac{6.71 \times 10^{-3} s + 1}{4.47 \times 10^{-4} s + 1} \cdot \frac{1}{(6 \times 10^{-4} s + 1)(2 \times 10^{-4} s + 1)} \tag{6.108}$$

The measured data is well fit if these paramters are chosen as $k_3 = 3.2$ and $\tau_3 = 1/175$ seconds.

Figure 6.32 shows the quality of fit between measured data and the transfer function given by (6.108). At all but the highest frequencies the fit is quite good. This transfer function (6.108) will be used in the next chapter to design the heave modal controller and to predict its performance.

Discussion of errors

Clearly, there are systematic errors between the predicted principal vertical transfer functions and the measured principal vertical transfer functions. In all three cases, the predicted DC gain is higher than the measured DC gain (by factors of 1.1 in roll and 1.3 in pitch and heave), and the predicted break-frequency is higher than the measured break-frequency by factors of about 1.3 in all three transfer functions. These discrepancies can be accounted for by errors on the order of 30% in the platen moments of inertia and in the magnet incremental parameters. This has been verified numerically, and a good fit to the measured data can be achieved by tweaking the plant paramters by this amount.

However, it is not highly meaningful to blindly adjust numerical parameters to achieve this fit. The present errors of about 30% are not overly large; the fact that the predicted and measured transfer functions agree to this extent gives confidence in the analysis presented in this chapter. To further refine the paper model will require additional experiments in order to identify which parameters are in error. For instance, the platen moments of inertia have been calculated, but never measured. These can be simply measuring the platen period of rotational oscillation on a torsion balance. Such a measurement can be carried out simply by

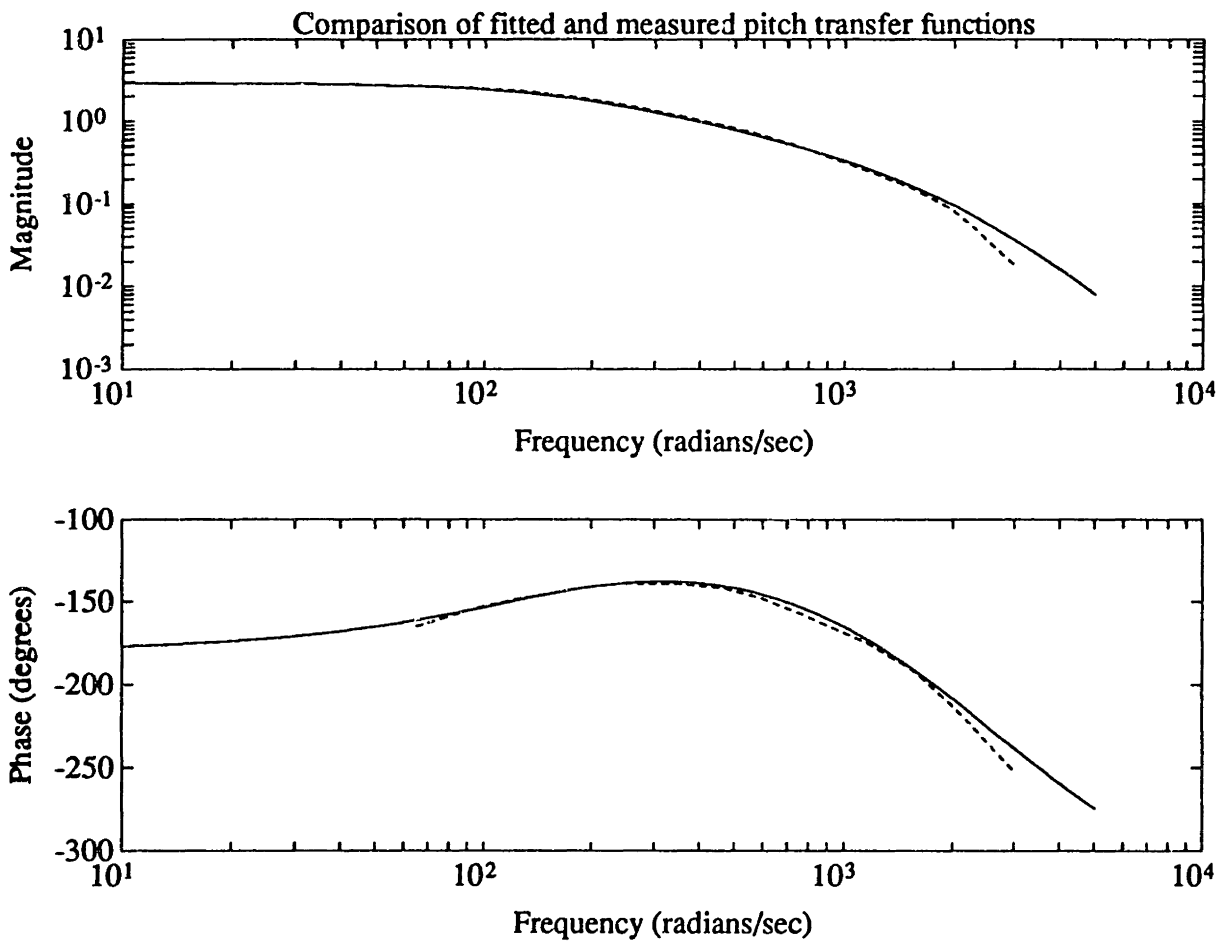

Figure 6.30: Showing the quality of fit between the transfer function of equation (6.107) (solid line) and the measured pitch transfer function (dashed line).

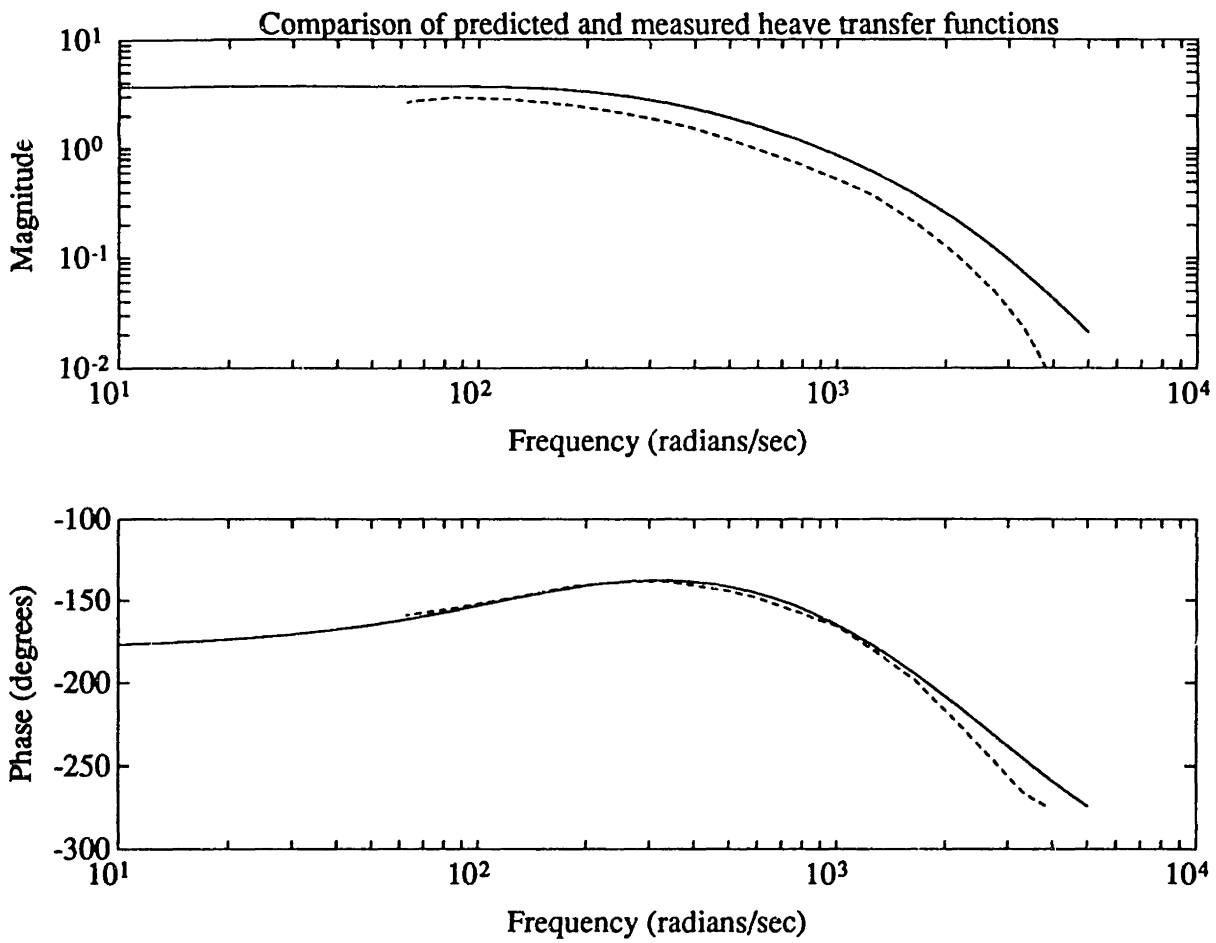

Figure 6.31: Predicted (solid line) versus measured (dashed line) heave transfer functions $v_{m3}(s)/v_{u3}(s)$.

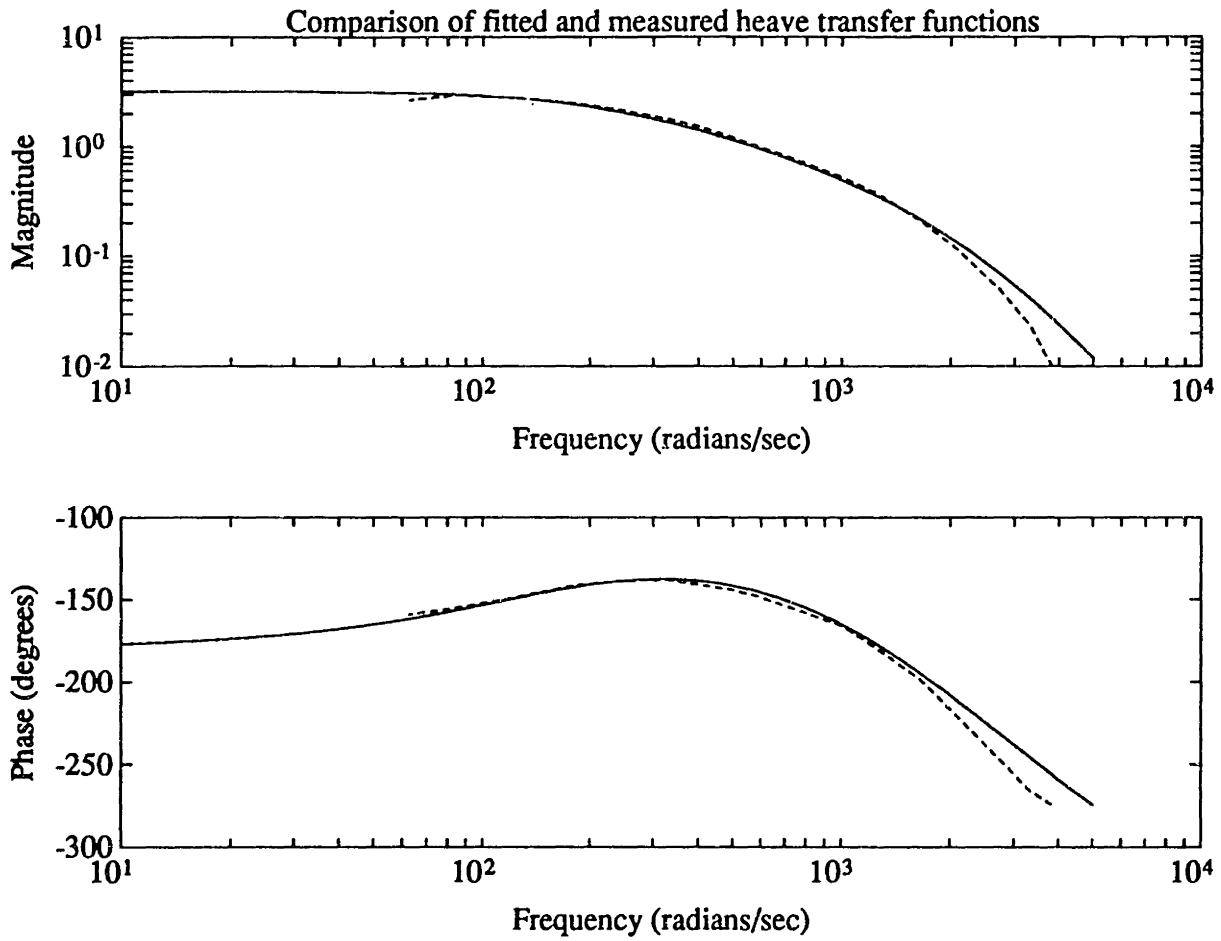

Figure 6.32: Showing the quality of fit between the transfer function of equation (6.108) (solid line) and the measured heave transfer function (dashed line).

hanging the platen from a piece of piano wire[4]. The two 100 gm damping weights added to the platen to damp its resonance are not included in the moments of inertia calculation, and do increase the moments of inertia, thereby lowering the break-frequency of all three principal vertical transfer functions. The magnet force experiments could be improved by building a fixture to directly measure the forces on the platen as a function of platen position, magnet currents, and frequency.

Time constraints have prevented me from undertaking any of these additional experiments. For the current purposes, the measured transfer functions serve as an accurate model with which to design controllers in the next chapter.

6.16.2 Lateral system transfer functions

The two principal lateral plant transfer functions are defined as the transfer functions from the ith input of the transformation S_{iu} to the ith output of the transformation S_{mp}. In other words the two principal lateral plant transfer functions represent the transfer functions seen by the two lateral modal controllers.

Figure 6.33 shows the predicted transfer function and the measured transfer function in yaw motion $v_{m4}(s)/v_{u4}(s)$. As shown in the figure, the predicted DC gain is higher than the measured DC gain by a factor of 1.5, and the predicted suspension break-frequency is higher than the measured break-frequency by a factor of 1.4.

The measured transfer function is fit to a model of the form

$$\frac{v_{m4}(s)}{v_{u4}(s)} = \frac{k_4}{(\tau_4 s+1)(\tau_4 s-1)} \cdot \frac{1}{15} \frac{6.71\times 10^{-3}s+1}{4.47\times 10^{-4}s+1} \cdot \frac{1}{(6\times 10^{-4}s+1)(2\times 10^{-4}s+1)} \tag{6.109}$$

The measured data is well fit if these paramters are chosen as $k_4 = 2.3$ and $\tau_4 = 1/145$ seconds.

Figure 6.34 shows the quality of fit between measured data and the transfer function given by (6.109). At all but the highest frequencies the fit is quite good. This transfer function (6.109) will be used in the next chapter to design the yaw modal controller and to predict its performance.

Figure 6.35 shows the predicted transfer function and the measured transfer function in lateral motion $v_{m5}(s)/v_{u5}(s)$. As shown in the figure, the predicted DC gain is higher than the measured DC gain by a factor of 1.4, and the predicted suspension break-frequency is higher than the measured break-frequency by a factor of 1.4.

[4]Thanks to Prof. Roberge for pointing out this method of measuring moments of inertia.

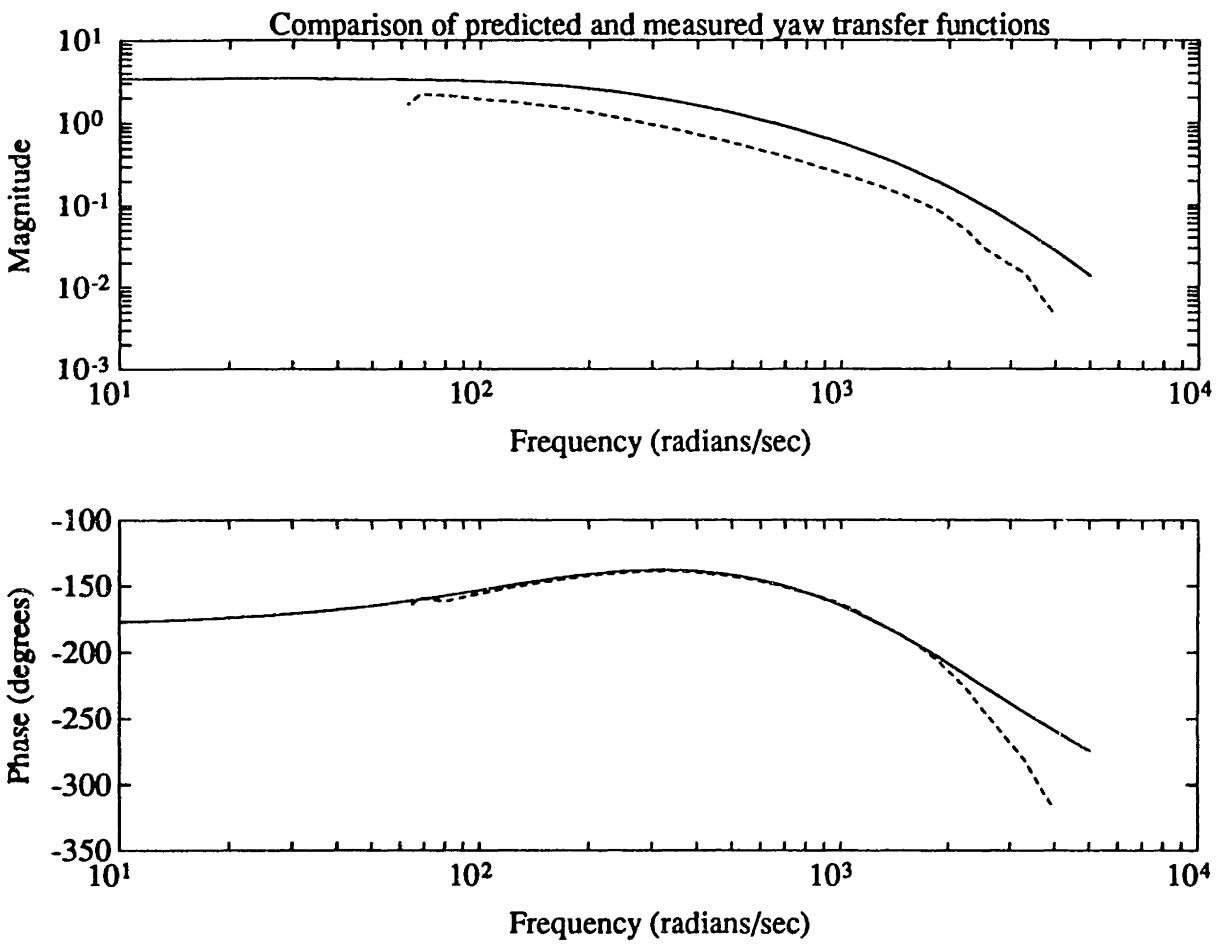

Figure 6.33: Predicted (solid line) versus measured (dashed line) yaw transfer functions $v_{m4}(s)/v_{u4}(s)$.

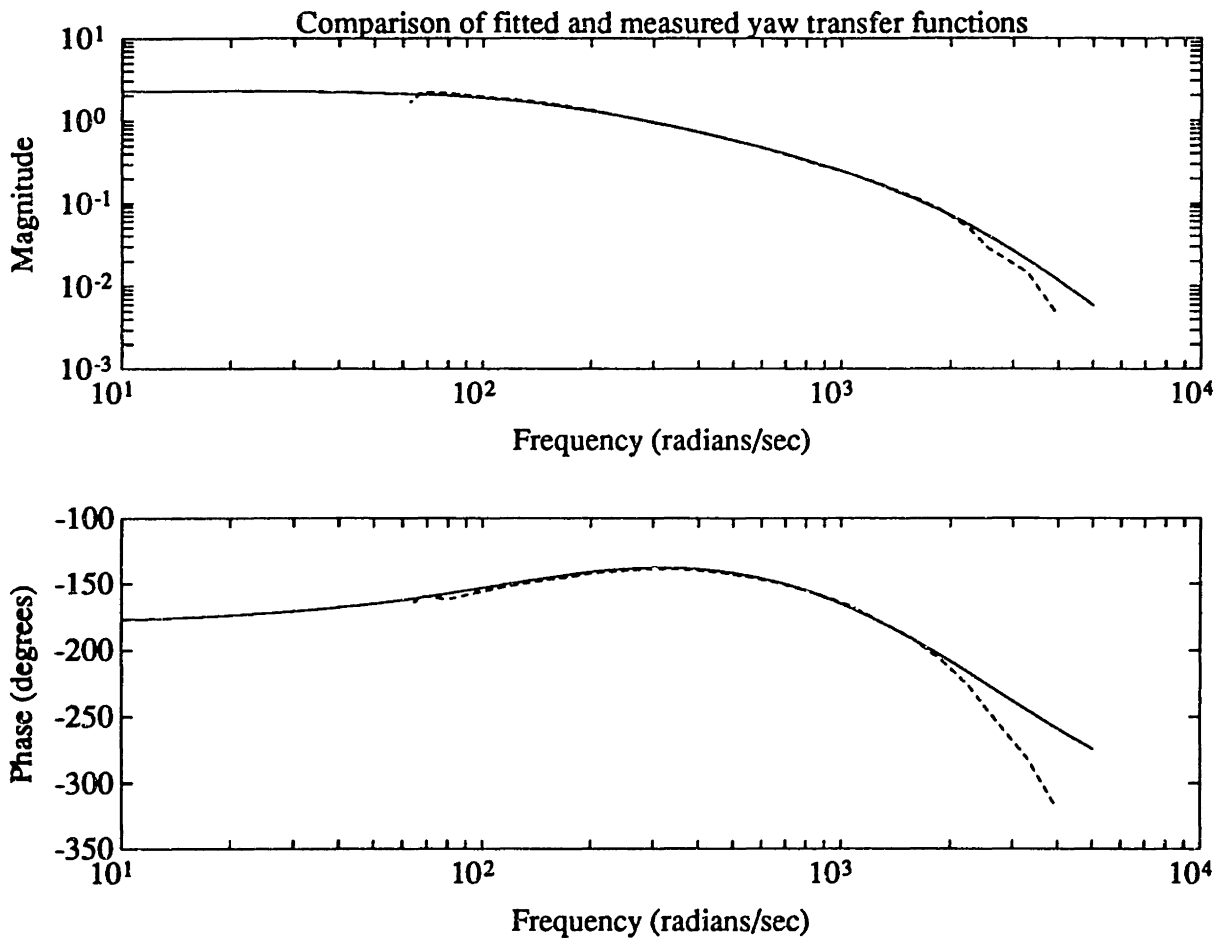

Figure 6.34: Showing the quality of fit between the transfer function of equation (6.109) (solid line) and the measured yaw transfer function (dashed line).

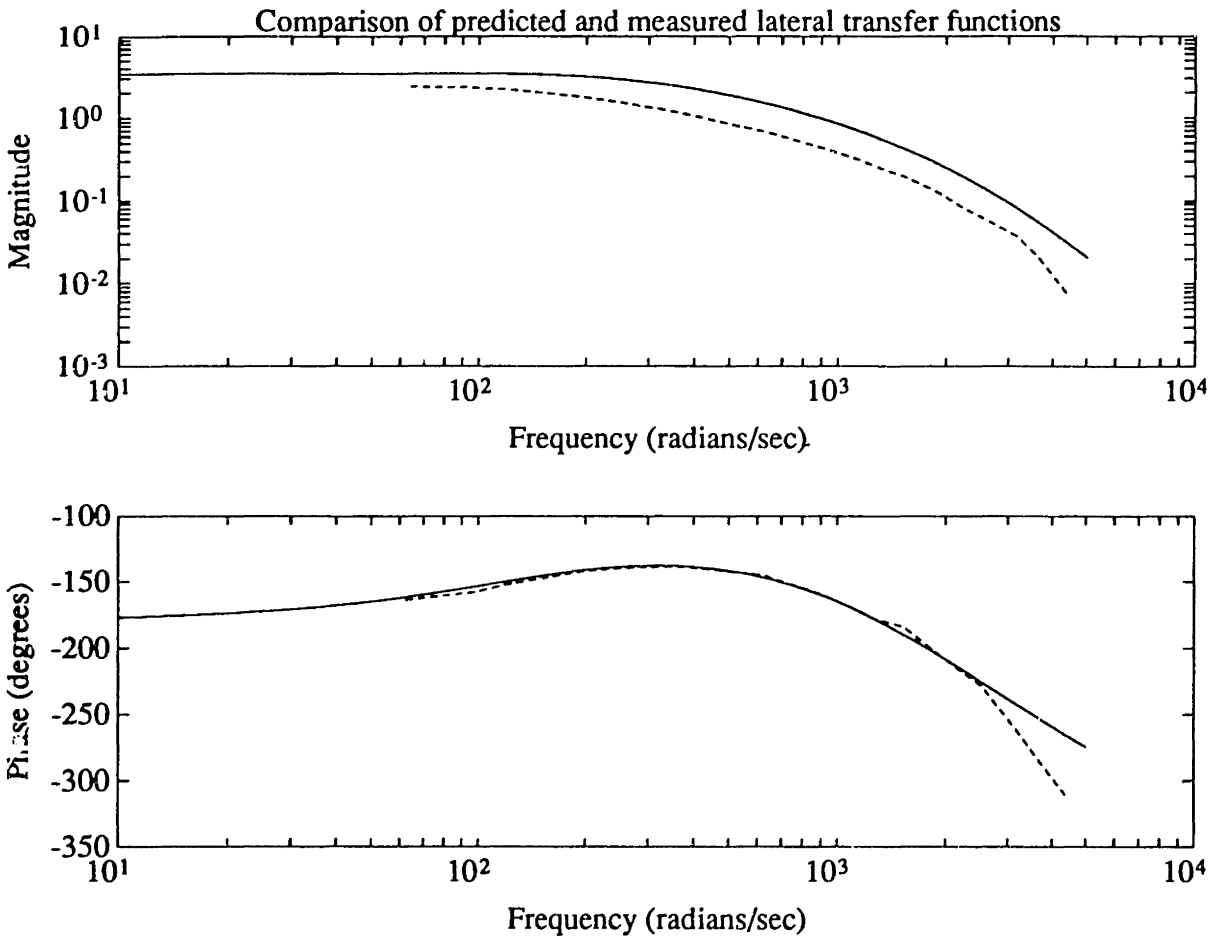

Figure 6.35: Predicted (solid line) versus measured (dashed line) lateral transfer functions $v_{m5}(s)/v_{u5}(s)$.

The measured transfer function is fit to a model of the form

$$\frac{v_{m5}(s)}{v_{u5}(s)} = \frac{k_5}{(\tau_5 s + 1)(\tau_5 s - 1)} \cdot \frac{1}{15} \frac{6.71 \times 10^{-3} s + 1}{4.47 \times 10^{-4} s + 1} \cdot \frac{1}{(6 \times 10^{-4} s + 1)(2 \times 10^{-4} s + 1)} \tag{6.110}$$

The measured data is well fit if these paramters are chosen as $k_5 = 2.5$ and $\tau_5 = 1/180$v seconds.

Figure 6.36 shows the quality of fit between measured data and the transfer function given by (6.110). At all but the highest frequencies the fit is quite good. This transfer function (6.110) will be used in the next chapter to design the pitch modal controller and to predict its performance.

Discussion of errors

Clearly, as with the vertical system, there are systematic errors between the predicted principal lateral transfer functions and the measured principal lateral transfer functions. In both cases, the predicted DC gain is higher than the measured DC gain (by factors of about 1.5), and the predicted break-frequency is higher than the measured break-frequency by factors of about 1.4 in both transfer functions. These discrepancies can be accounted for by errors on the order of 40% in the platen moments of inertia and in the magnet incremental parameters. This has been verified numerically, and a good fit to the measured data can be achieved by tweaking the plant parameters by this amount.

As discussed earlier in connection with the vertical transfer functions, there are a number of possible causes for the lack of agreement between the predicted and measured transfer functions. However for the purposes of design, the two results are close enough that we can be confident in the basic analysis and use the measured transfer functions for accurate design in the next chapter.

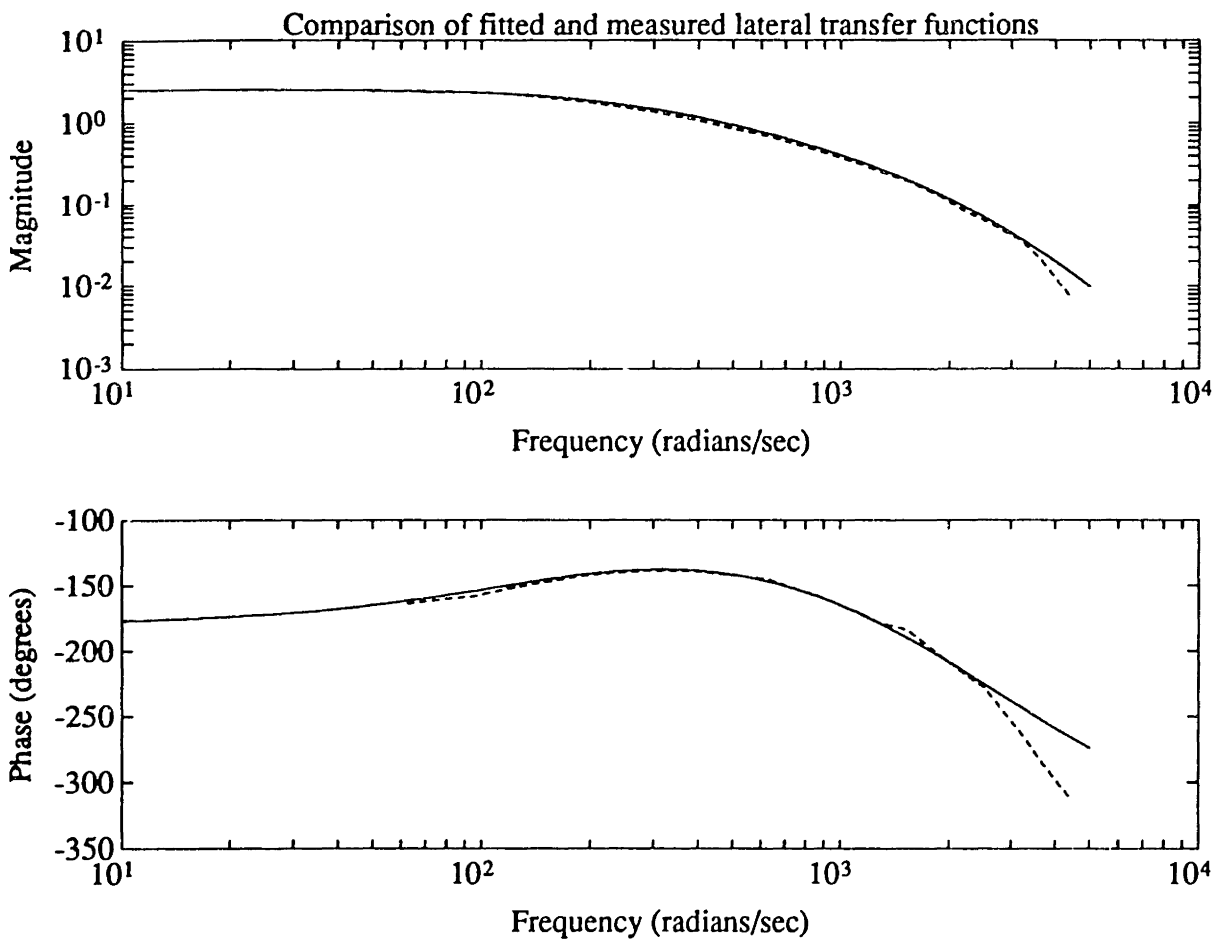

Figure 6.36: Showing the quality of fit between the transfer function of equation (6.110) (solid line) and the measured lateral transfer function (dashed line).

Chapter 7

Final Controller Design

The controllers developed in the previous chapter did not depend upon an accurate knowledge of the plant dynamic model. They were empirically tuned in order to achieve active suspension of the platen. In this section we develop the final controller design which exploits the measurements and accurate models developed in the previous chapter. The vertical system uses lead/lag compensation which is identical in form to the compensation used in the initial design given in the previous chapter. The lateral system uses a double-lead/lag compensator to achieve higher performance.

7.1 Vertical Controller Design

The three vertical system controllers take the form of lag-compensators. Lag compensation is used to develop higher disturbance rejection. Recall that the current drives already implement lead compensation; the lead term is necessary in order to stabilize the loops. The controllers in this section use lag networks with a lag factor of only ten. This does not allow as good disturbance rejection as the controllers studied in Chapter 3 which place the lag pole at the origin by using an integrator. However it has been found experimentally that it is very difficult to initialize the suspension if integrators are used in the compensator. This difficulty is due to integrator windup. The best solution is to use a dual-mode controller which gates-out the integral term until the suspension is initialized.

The controllers are designed under the assumption that the plant is decoupled. That is, the roll controller is designed to control the transfer function $v_{m1}(s)/v_{u1}(s)$, the pitch controller is designed to control the transfer function $v_{m2}(s)/v_{u2}(s)$, and the heave controller is designed to control the transfer function $v_{m3}(s)/v_{u3}(s)$. All three controllers take the form of lag compensators designed for a 100 Hz crossover.

The controller designs are

$$\frac{v_{ui}(s)}{v_{ei}(s)} = k_i \frac{\tau_a s + 1}{\tau_b s + 1} \qquad i = 1,2,3 \tag{7.1}$$

where τ_a = 9.1 milliseconds, τ_b = 100 milliseconds, k_1 = 111, k_2 = 17, and k_3 = 12. The circuit implementation of the transfer functions (7.1) is shown in Figure 7.1.

The only difference among the three controllers is in the value of the DC gain which is set by the resistor R_i'. The roll controller has R_1' = 1 k, the pitch controller has R_2' = 6.5 k, and the heave controller has R_3' = 9.6 k, as shown in the figure.

7.1.1 Vertical loop transmissions and step-responses

This section shows the vertical principal loop-transmissions and predicted and measured step-responses. The measured step-responses are very close to the step-responses predicted by the models developed from the measured transfer functions in the previous chapter. This confirms the accuracy of the models we have developed. The measured step-responses also show cross-coupling into other modes. It is clear that some of the cross-coupling is due to nonlinear terms which are important given the large transient signals at the step-edge.

Roll

The loop transmission in roll is shown in Figure 7.2 and the predicted step-response in roll is shown in Figure 7.3. The measured roll step response shown in Figure 7.4 matches the predicted response very closely. Specifically, the time from the beginning of the step to the first peak is about 5 msec in both the predicted and measured responses, and the peak-overshoot value is about 1.75 times the final value.

The second trace in Figure 7.4 shows the cross-coupling into the platen pitch motion. The pitch response is not symmetric with respect to the two step edges; this indicates that even at these small signal-levels, nonlinear terms are significant. This is supported by the observation that at the step-edge, the coil currents have discontinuities of several tenths of an ampere.

Pitch

The loop transmission in pitch is shown in Figure 7.5 and the predicted step-response in pitch is shown in Figure 7.6. The measured pitch step response shown in Figure 7.7 matches the predicted response very closely. Specifically, the

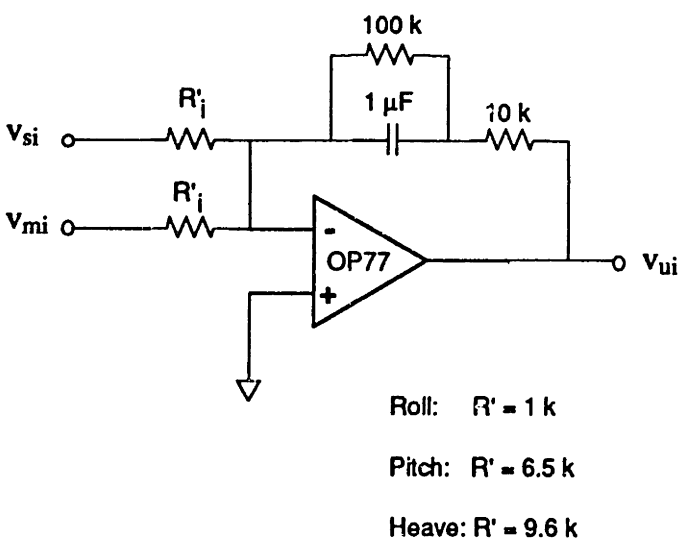

Figure 7.1: Vertical controller circuit implementation.

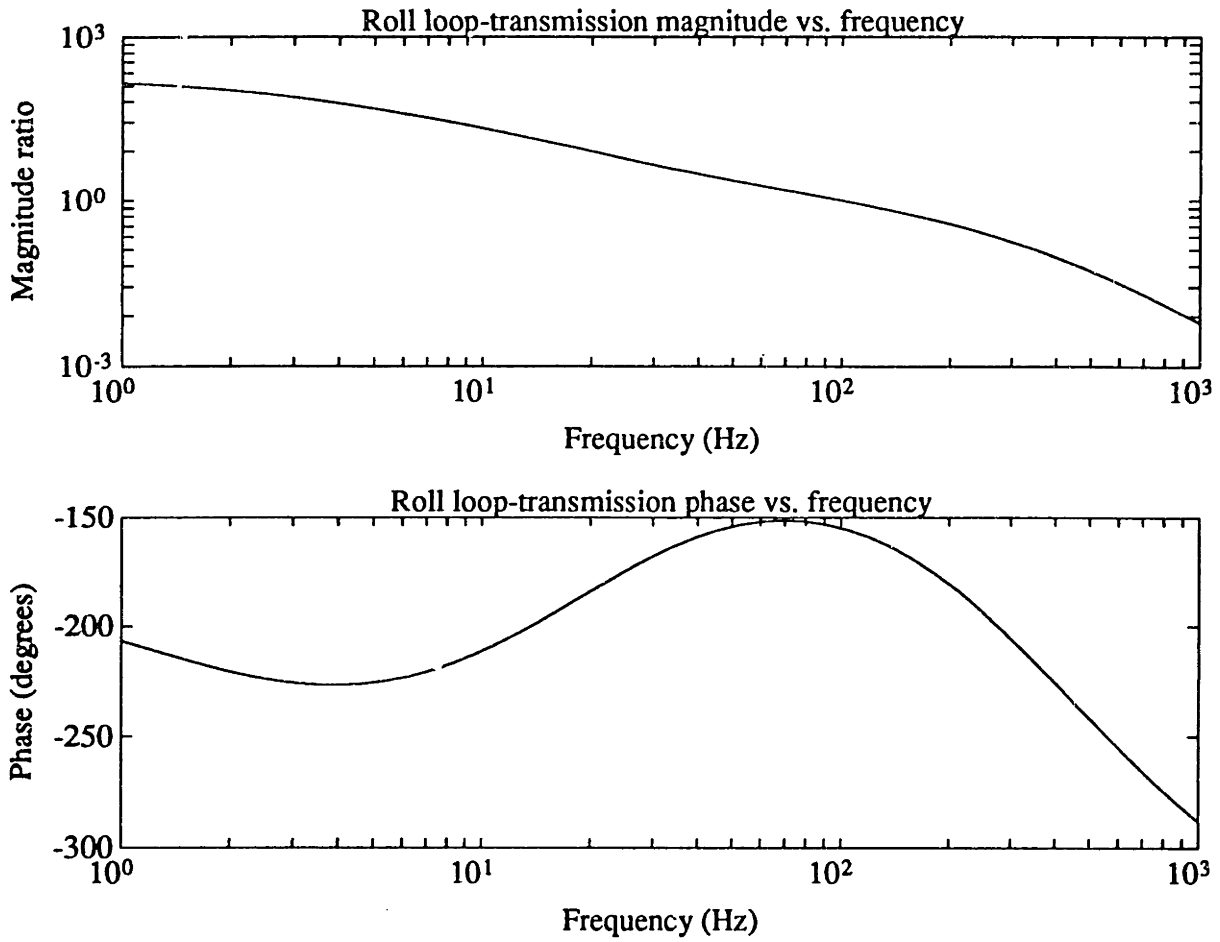

Figure 7.2: Roll loop-transmission $v_{m1}(s)/v_{e1}(s)$ magnitude and phase versus frequency.

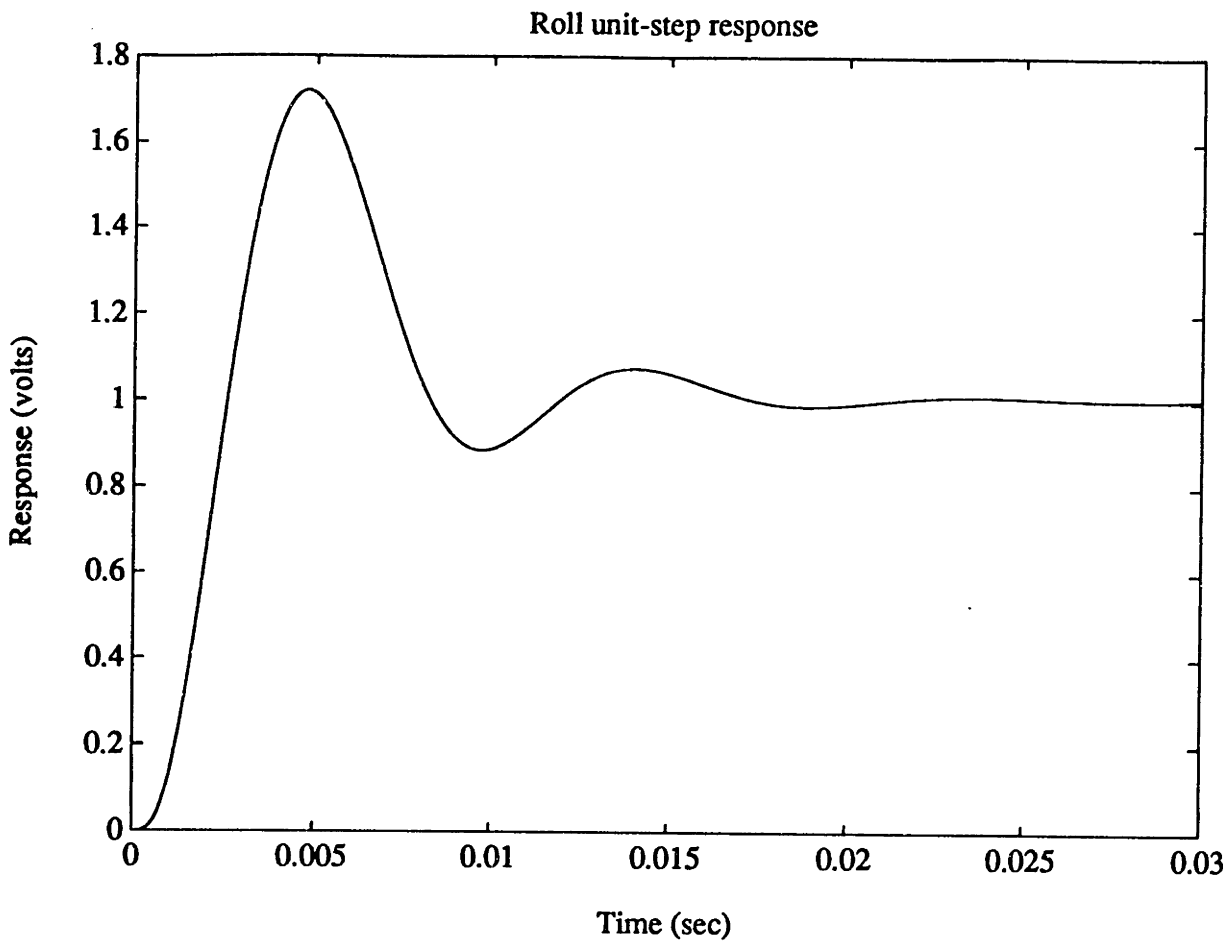

Figure 7.3: Roll unit-step response predicted by models.

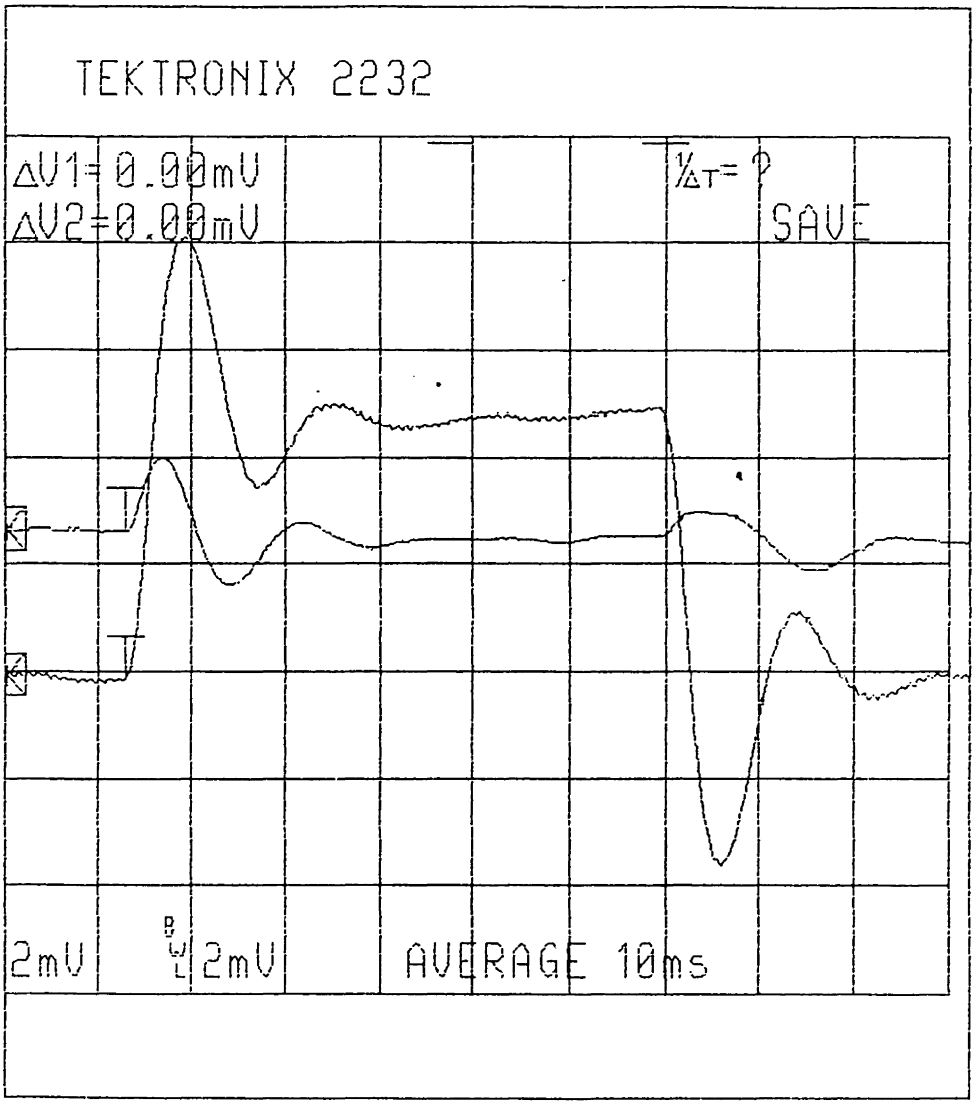

Figure 7.4: Actual roll step-response $v_{m1}(t)$. Second trace shows undesired cross-coupling response in pitch $v_{m2}(t)$.

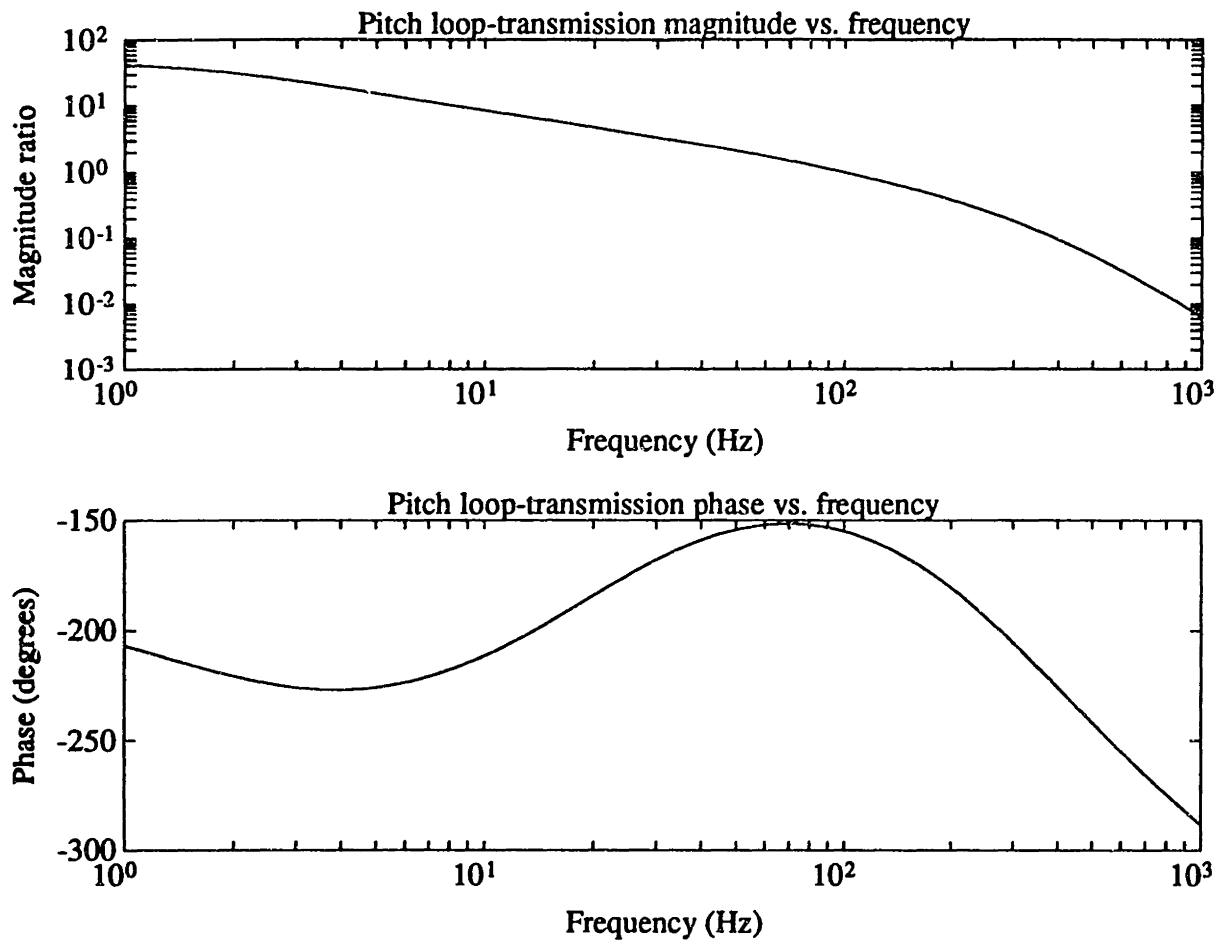

Figure 7.5: Pitch loop-transmission $v_{m2}(s)/v_{e2}(s)$ magnitude and phase versus frequency.

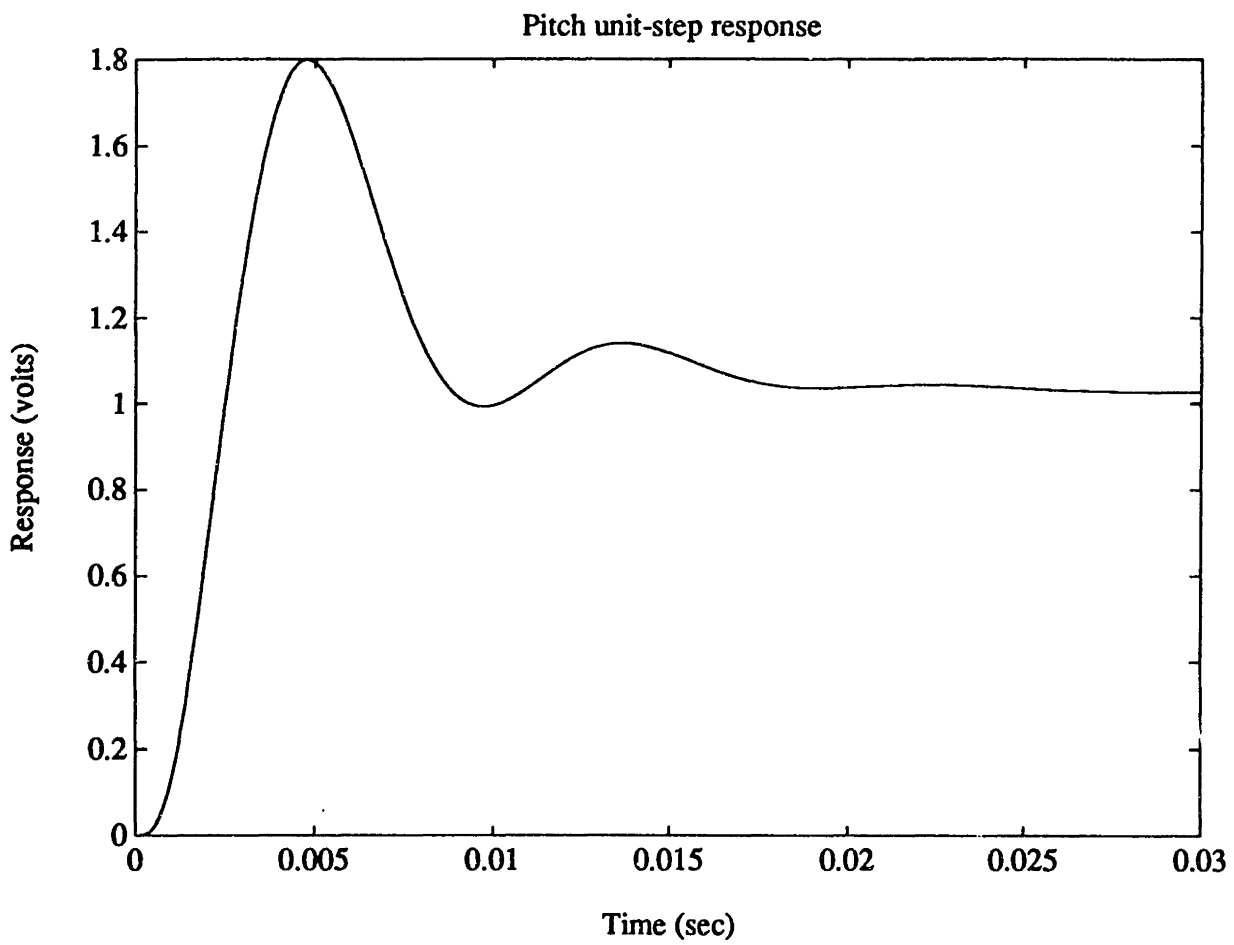

Figure 7.6: Pitch unit-step response predicted by models.

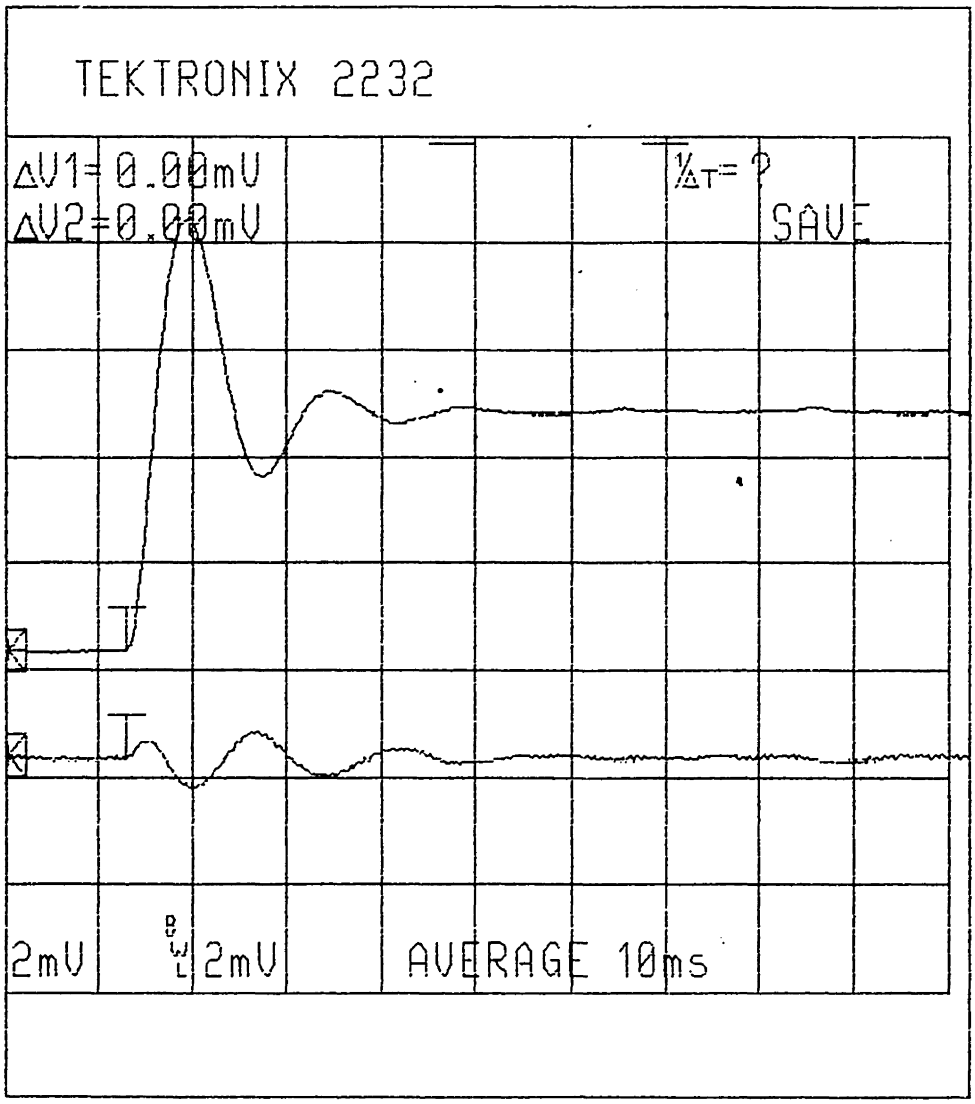

Figure 7.7: Actual pitch step-response $v_{m2}(t)$. Second trace shows undesired cross-coupling response in heave $v_{m3}(t)$.

time from the beginning of the step to the first peak is about 5 msec in both the predicted and measured responses, and the peak-overshoot value is about 1.75 times the final value.

The second trace in Figure 7.7 shows the cross-coupling into the platen heave motion.

Heave

The loop transmission in heave is shown in Figure 7.8 and the predicted step-response in heave is shown in Figure 7.9. The measured heave step response shown in Figure 7.10 matches the predicted response very closely. Specifically, the time from the beginning of the step to the first peak is about 5 msec in both the predicted and measured responses, and the peak-overshoot value is about 1.85 times the final value.

The second trace in Figure 7.10 shows the cross-coupling into the platen pitch motion.

7.2 Lateral Controller Design

The two lateral system controllers take the form of lag/lead-compensators. Lag compensation is used to develop higher disturbance rejection. Recall that the current drives already implement a single lead compensation term. The lateral controllers add a second lead term in order to allow higher system bandwidth and thus a faster response time.

The controllers are designed under the assumption that the plant is decoupled. That is, the yaw controller is designed to control the transfer function $v_{m4}(s)/v_{u4}(s)$, and the lateral translation controller is designed to control the transfer function $v_{m5}(s)/v_{u5}(s)$.

The design is arranged such that the two lead-zeros and the single lag-zero approximately coincide at about -500 in the s-plane. This requires changing the four lateral current drive lead networks. To achieve this, an 0.22 μF capacitor is substituted for the 0.67 μF capacitor shown in the current-drive schematics in the previous chapter.

The controller designs are

$$\frac{v_{ui}(s)}{v_{ei}(s)} = k_i \frac{(\tau_c s + 1)(1.1\tau_c s + 1)}{(11\tau_c s + 1)(0.1\tau_c s + 1)} \qquad i = 4, 5 \tag{7.2}$$

where $\tau_c = 2.1$milliseconds, $k_4 = 43$, and $k_5 = 26$.

The circuit implementation of the transfer functions (7.2) is shown in Figure 7.11. The only difference among the two controllers is in the value of the DC

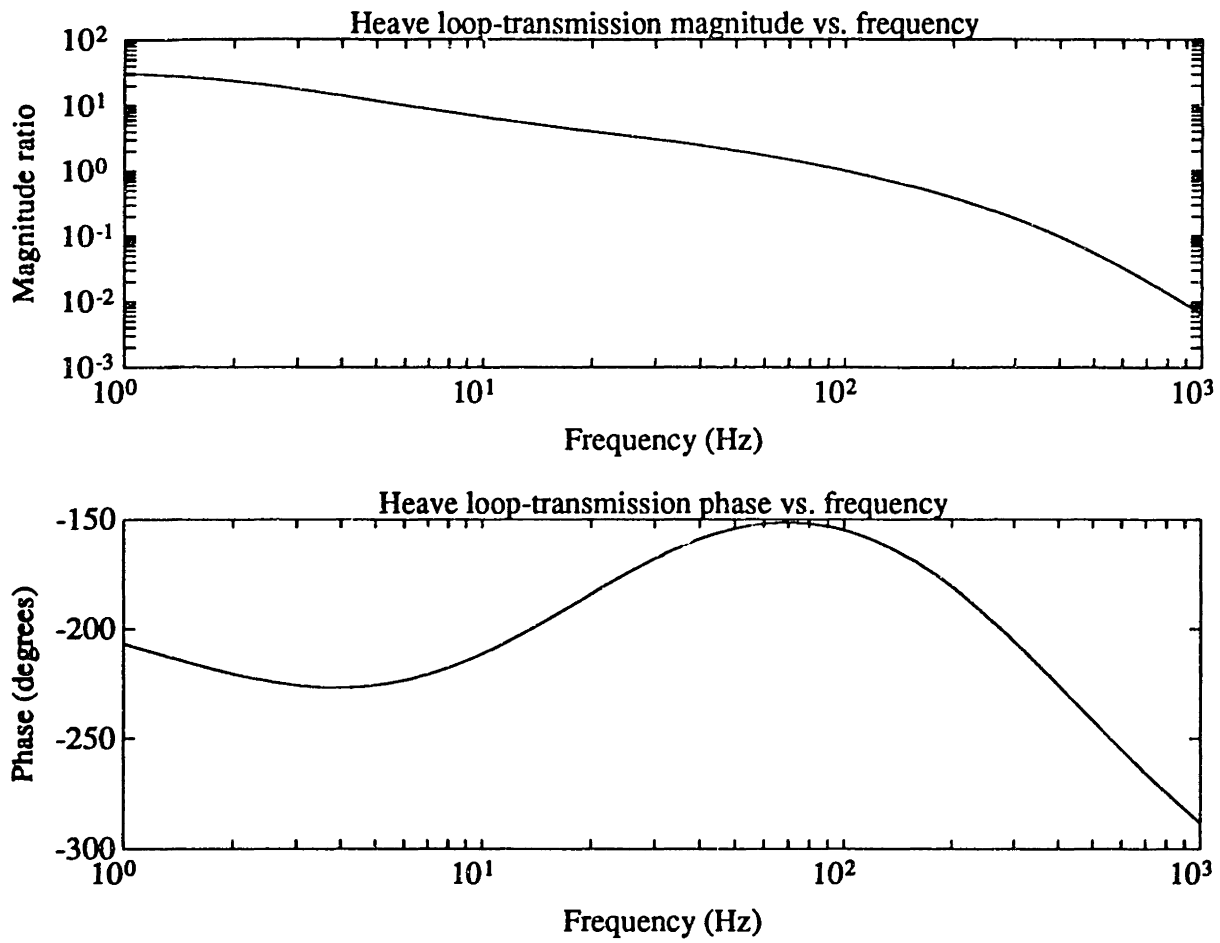

Figure 7.8: Heave loop-transmission $v_{m3}(s)/v_{e3}(s)$ magnitude and phase versus frequency.

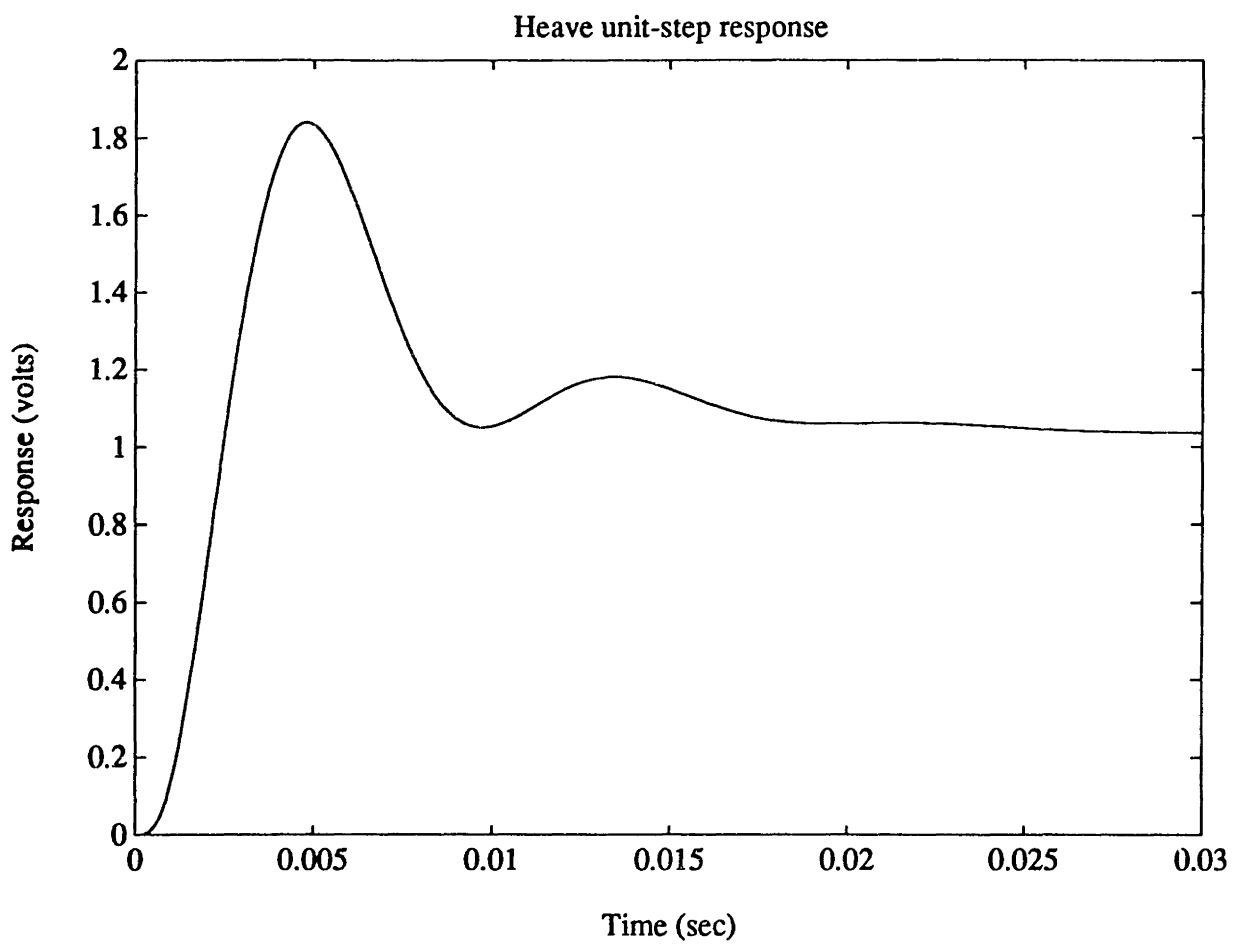

Figure 7.9: Heave unit-step response $v_{m3}(t)$ predicted by models.

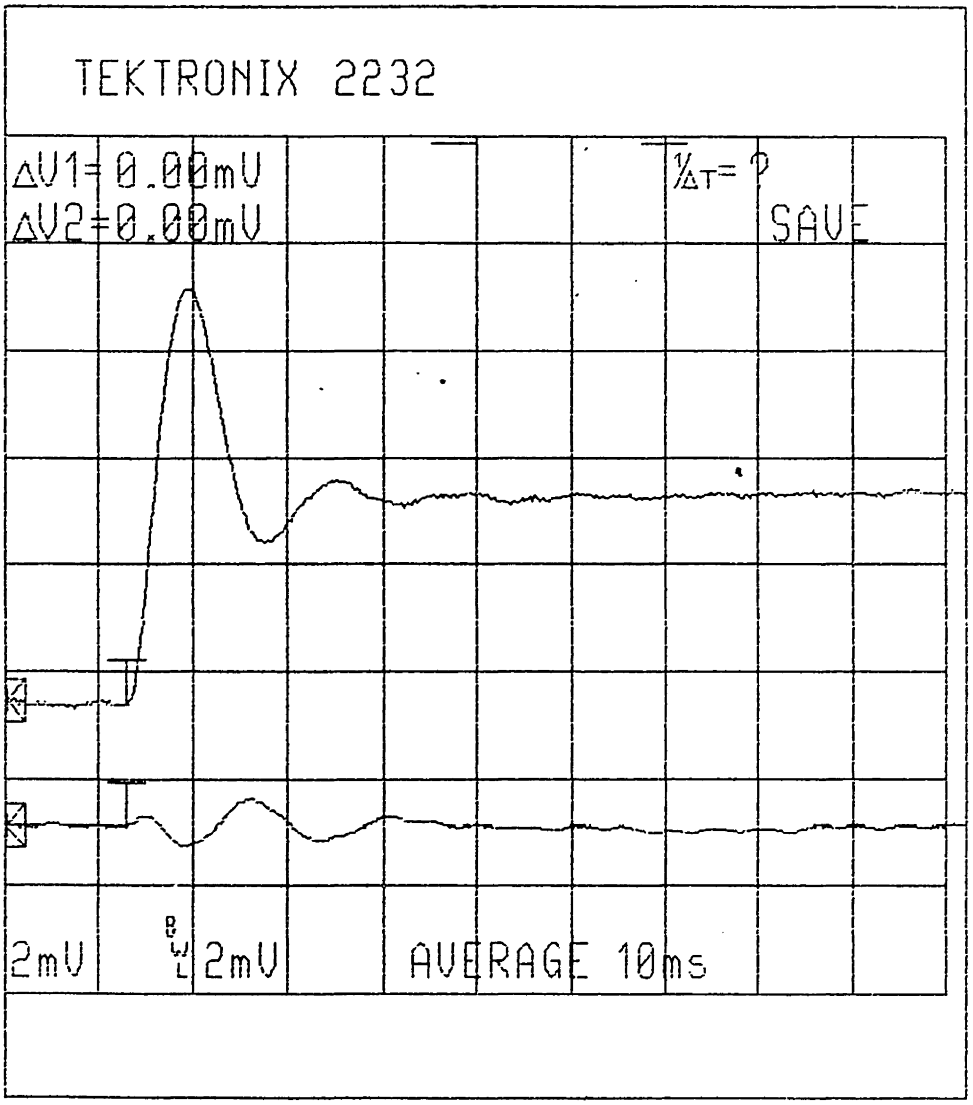

Figure 7.10: Actual heave step-response $v_{m3}(t)$. Second trace shows undesired cross-coupling response in pitch $v_{m2}(t)$.

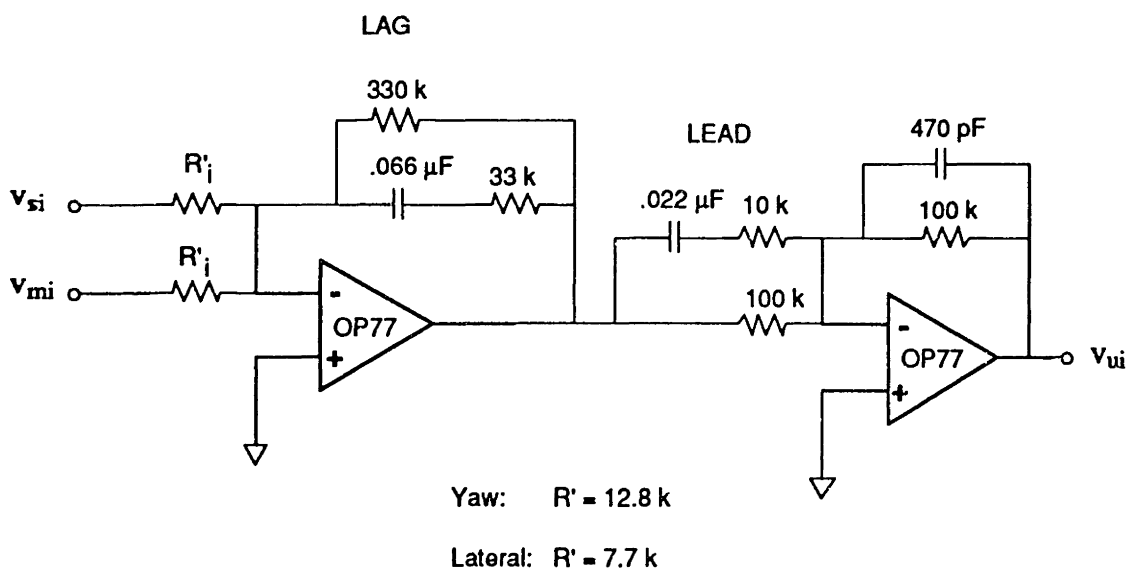

Figure 7.11: Lateral controller circuit implementation.

gain which is set by the resistor R_i'. The yaw controller has $R_4' = 12.8$ k, and the lateral controller has $R_5' = 7.7$ k, as shown in the figure.

7.2.1 Lateral loop transmissions and step-responses

This section shows the lateral principal loop-transmissions and predicted and measured step-responses. The measured step-responses are very close to the step-responses predicted by the models developed in the previous chapter. This confirms the accuracy of the models we have developed. The measured step-responses also show cross-coupling into other modes. It is clear that some of the cross-coupling is due to nonlinear terms which are important given the large transient signals at the step-edge.

Yaw

The loop transmission in yaw is shown in Figure 7.12 and the predicted step-response in yaw is shown in Figure 7.13. The measured yaw step response shown in Figure 7.14. The time to peak is somewhat slower than expected (4.5 versus 3 msec), and the resonant frequency is correspondingly lower. It seems clear that this loop is crossing over near 120 Hz, rather than the designed-for 160 Hz. Examination of the loop-transmission Bode plots shows that small changes in gain can result in relatively large changes in crossover frequency. This is because of the small slope of the magnitude plot in the vicinity of crossover. Numerical simulation shows that this error could be acounted for by a 30% reduction in gain. It is possible that the gain-setting potentiometer on the yaw controller channel was mis-adjusted when the scope-trace was taken.

The second trace in Figure 7.14 shows the cross-coupling into the platen lateral motion.

Lateral translation

The loop transmission in lateral translation is shown in Figure 7.15 and the predicted step-response in lateral translation is shown in Figure 7.16. The measured lateral step response shown in Figure 7.17 matches the predicted response very closely. Note the faster response-time and lower overshoot values achieved with the dual-lead compensation. There is however a sharp peak on the initial response which is not predicted by our model. This is believed to be due to bending modes in the platen.

The second trace in Figure 7.17 shows the cross-coupling into the platen yaw motion.

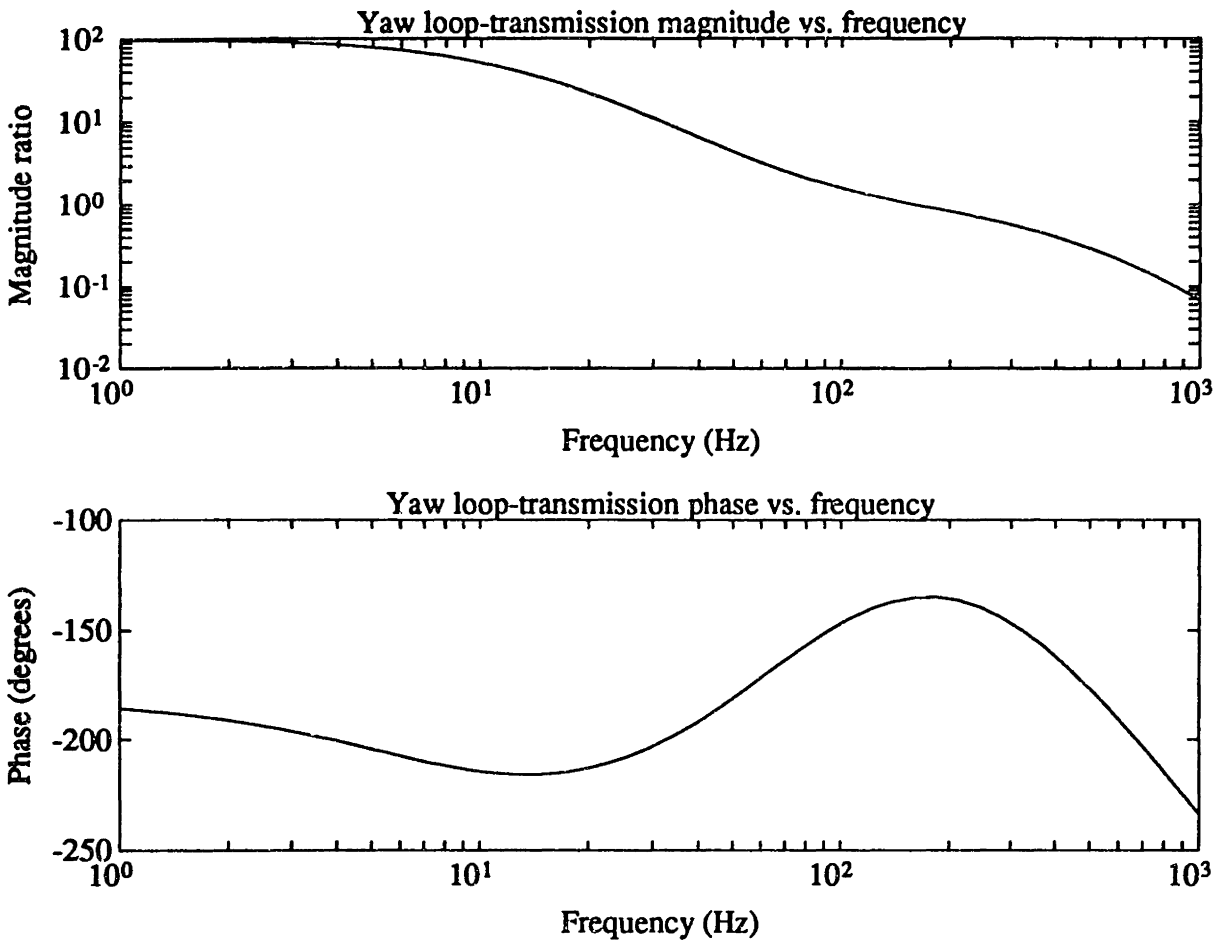

Figure 7.12: Yaw loop-transmission $v_{m4}(s)/v_{e4}(s)$ magnitude and phase versus frequency.

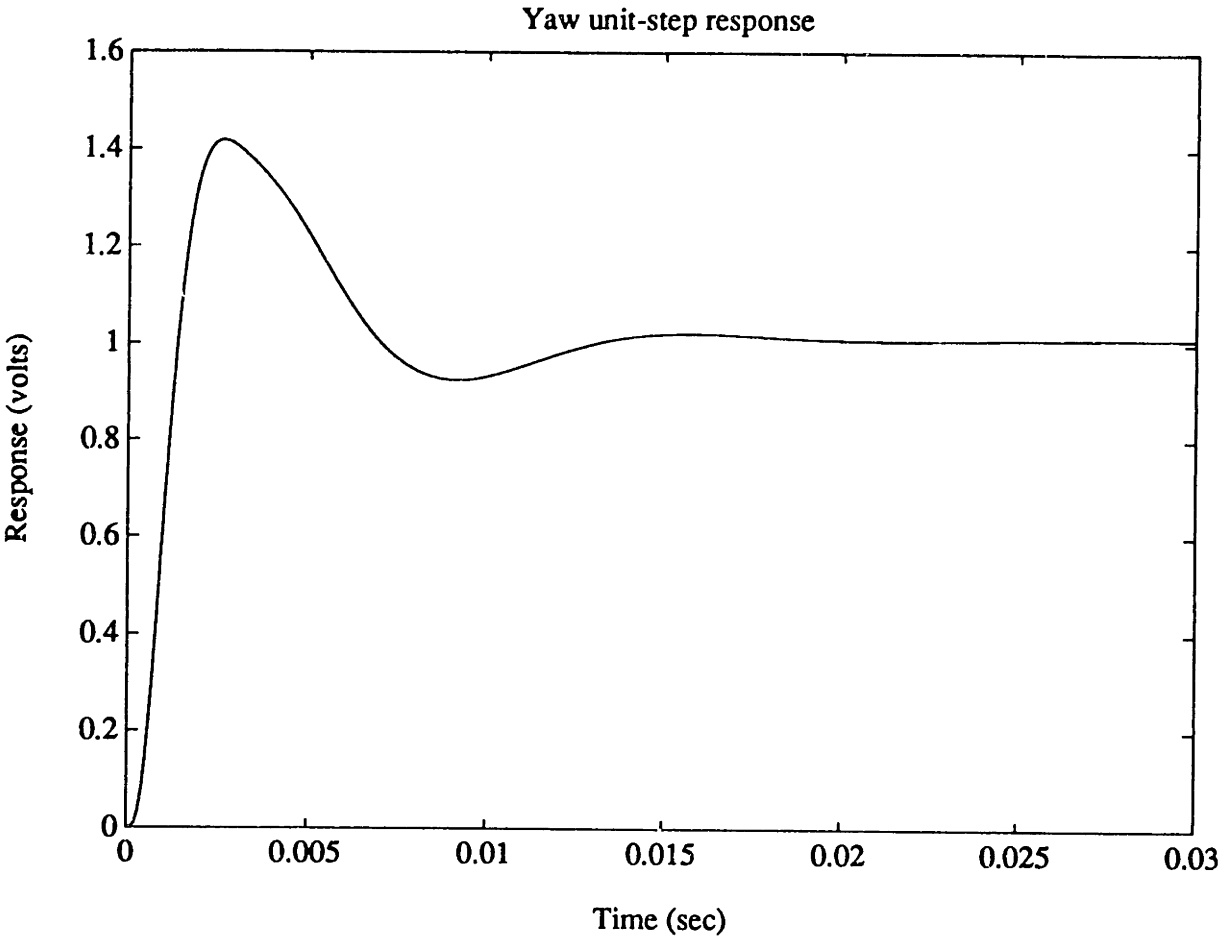

Figure 7.13: Yaw unit-step response predicted by models.

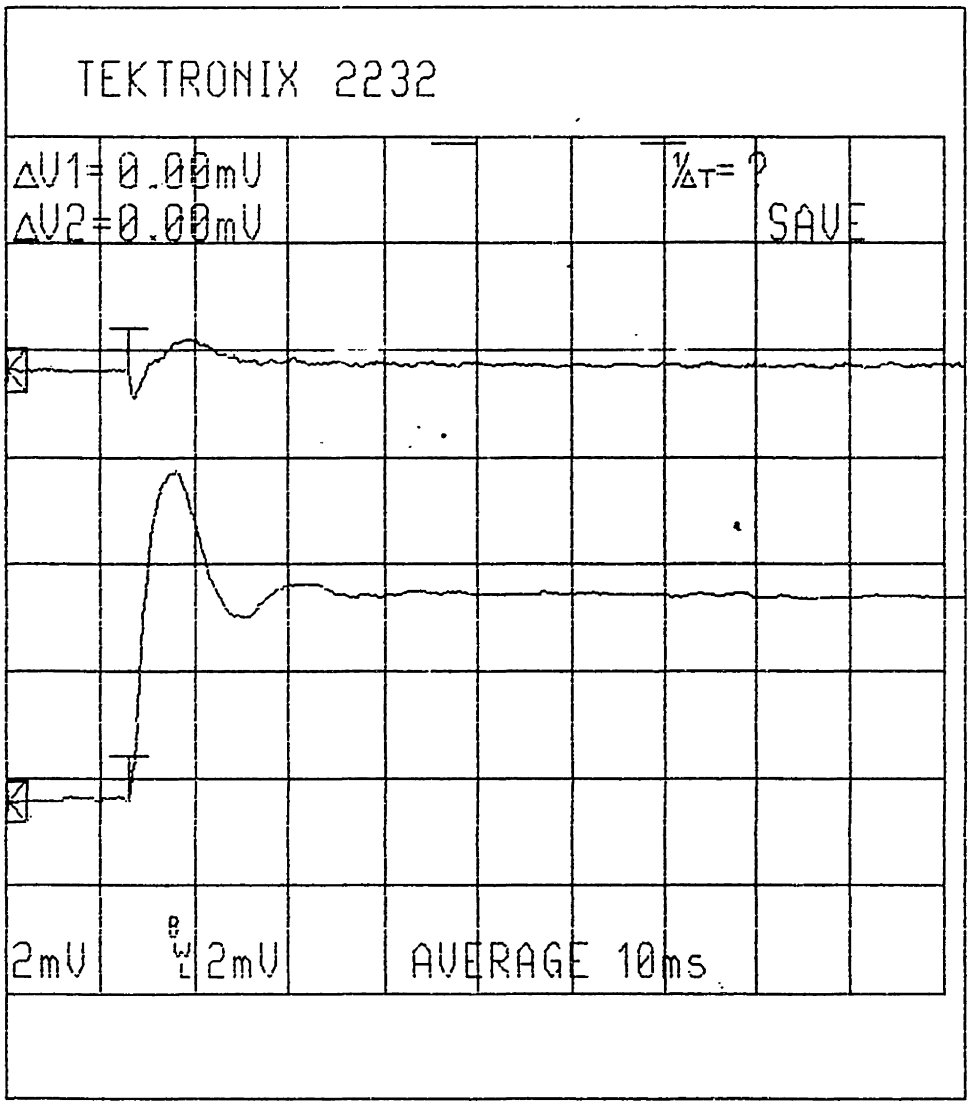

Figure 7.14: Actual yaw step-response $v_{m4}(t)$. Second trace shows undesired cross-coupling response in lateral translation $v_{m5}(t)$.

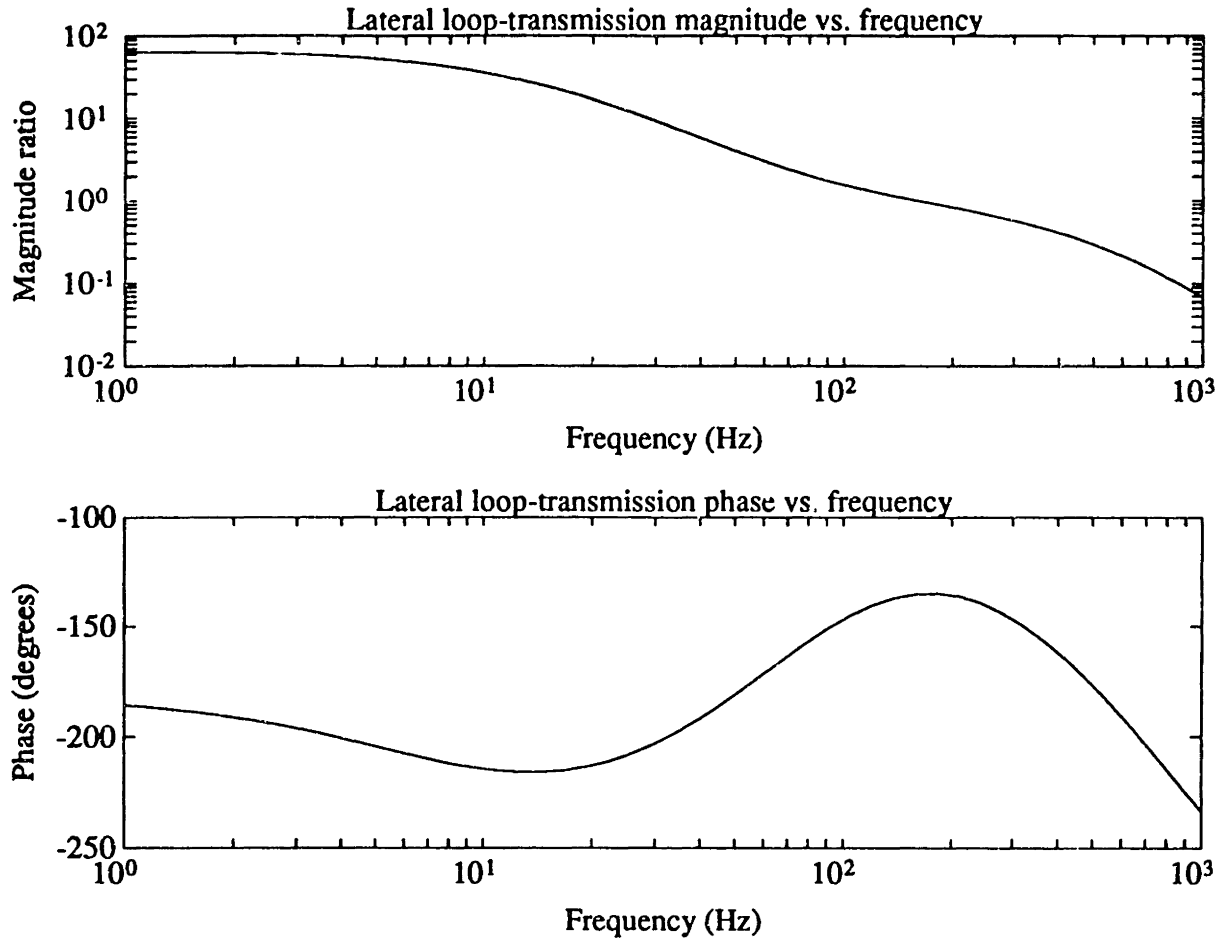

Figure 7.15: Lateral loop-transmission $v_{m5}(s)/v_{e5}(s)$ magnitude and phase versus frequency.

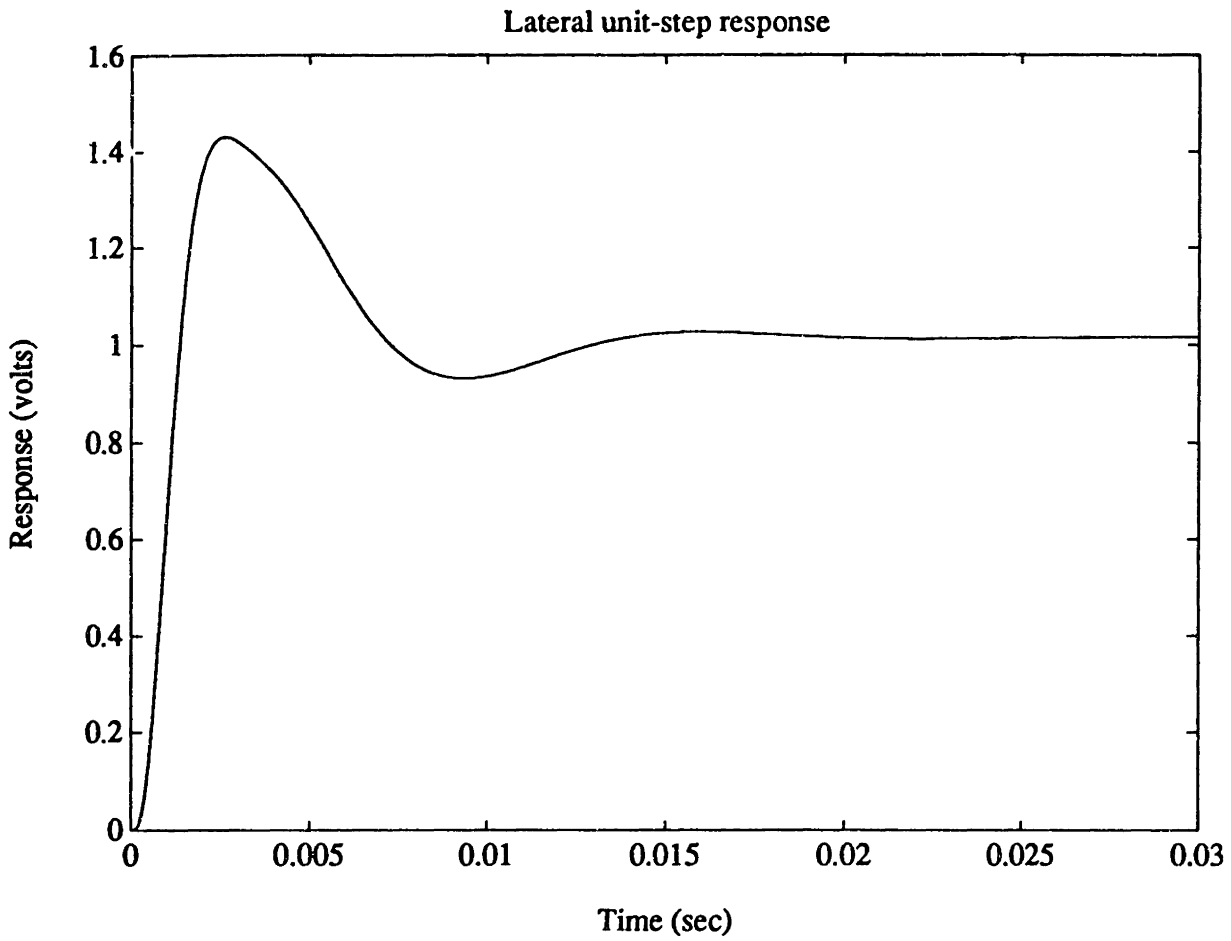

Figure 7.16: Lateral unit-step response predicted by models.

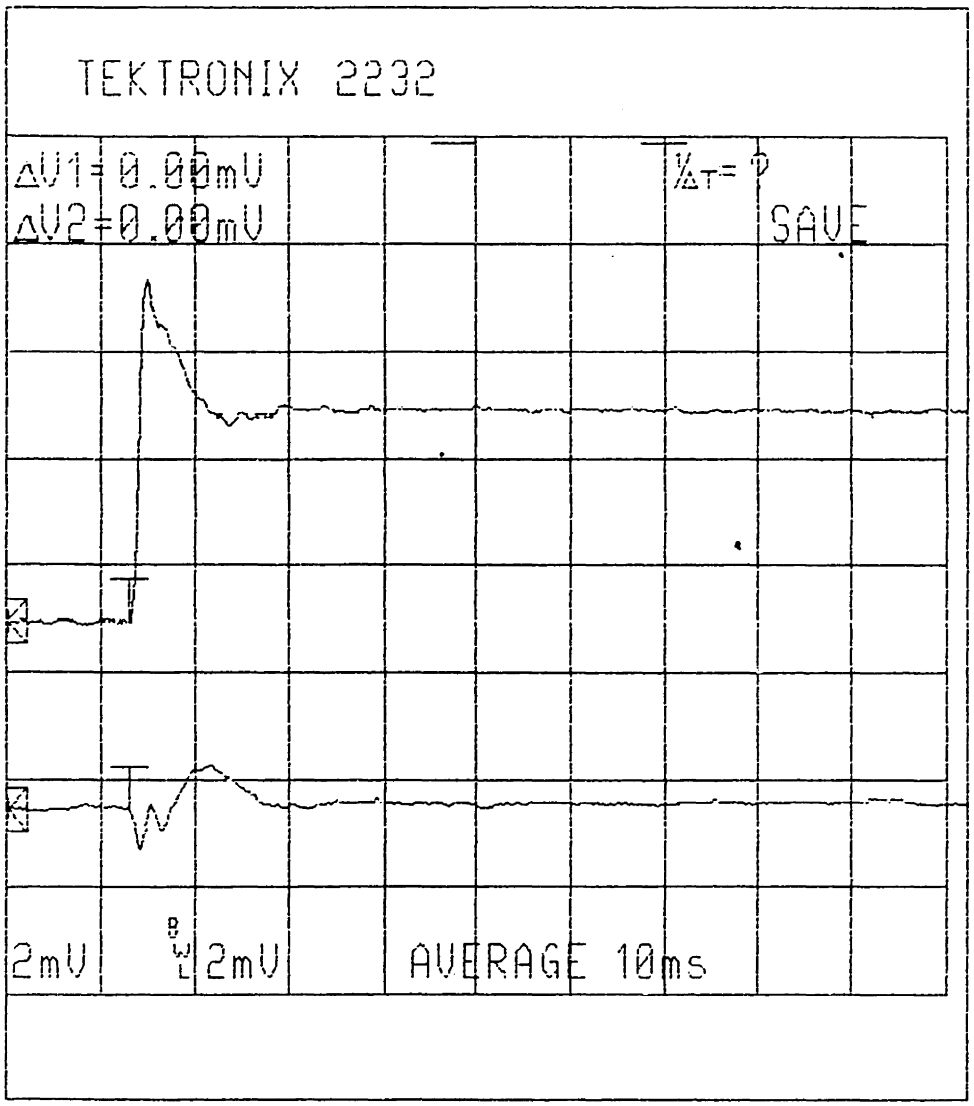

Figure 7.17: Actual lateral step-response $v_{m5}(t)$. Second trace shows undesired cross-coupling response in yaw $v_{m4}(t)$.

Chapter 8

Suggestions for an improved linear bearing

This chapter provides suggestions for incremental improvements to the linear bearing which has been described in the previous chapters. Additionally, we present a completely revised linear bearing design. This design addresses many of the problems which have been encountered in the course of this study, but which could not be addressed by incremental changes to the existing slide design.

8.1 Incremental changes to the the existing design

This section suggests ways to improve the current hardware design. The suggestions are listed as items in the bulleted list below.

- **All magnets should be arranged in push/pull pairs.** One problem with the current topology is that the three top electromagnets are only opposed by gravity. Thus it is easy to saturate the top electromagnets at zero current if disturbance torques or upward forces are applied to the platen. Whenever the system saturates, it goes unstable and needs to be reinitialized.

- **All magnets should be identical.** One major design error in the current system is the use of three top magnets, two small and one large. Using physically different support magnets makes the design of the decoupling networks far more complicated, since physically different magnets will not match in their static or dynamic characteristics. As in analog circuit design, it makes far more sense to use matched devices, such that when they are arranged in differential connections, their static and dynamic characteristics

inherently match. Thus taking note of the previous bulleted comment, the bearing should be designed with four identical magnets pulling up on the top of the platen, and four identical magnets pulling down on the bottom of the platen. Using four magnets rather than three will also afford better control of the roll mode, which currently can only be controlled by the two small top magnets.

- **Electromagnet structure should be laminated.** The current design uses solid stainless steel for the electromagnet bodies and solid cold-rolled steel nickel-plated for the platen. The use of stainless steel is a poor choice in terms of its magnetic properties. Also, using solid materials greatly reduces the high-fequency capabilities of the suspension. To achieve stiffness it is necessary to have high suspension bandwidth, thus laminating the magnet structure is quite important. Also, stainless steel has very poor magnetic characteristics as opposed to iron, and thus the magnets are quite inefficient in terms of their leakage-flux component. Stainless was initially chosen in order to avoid corrosion, but this can be readily accomplished in an iron magnet through the use of proper coatings.

- **The magnets should be run at air gaps larger than 0.005", or at lower bias currents.** As discussed in the chapter on suspension fundamentals, if the suspension is supporting the platen gravity load, running the suspension at small air gaps raises the unstable frequency of the suspension thereby making the control problem far more difficult and greatly constraining the freedom one has in compensating the suspension control loop.

  The current design value of 0.005" was chosen to match the operating point air-gap of the capacitance probes. This was necessary in order to protect the probe faces from mechanical contact with the platen, given the present 'through-the-bearing' measurement topology. This location is neither necessary or desirable, as described in a subsequent item. An air gap on the order of 0.030" would allow much easier control of the platen suspension, as well as simplifying the mechanical assembly issues.

  Alternatively, if permanent magnets are used to carry the gravity load, and if the system is arranged so that all magnets are in push/pull pairs, then the suspension can be run at small air gaps but reduced bias currents. At small operating point currents, the suspension open-loop time constants can be made sufficiently large even at small air gaps. This allows the efficiency of force production associated with small air gaps while retaining the advantages of slow unstable time constants. To make this approach work, it is essential that the platen gravity load be carried by a permanent

magnet with a large air gap as was suggested in Chapter 3.

- **Permanent magnets should not be located in the suspension magnets.** If the platen gravity load is to be carried by permanent magnets, these magnets should be separate from the suspension magnets. Further, they should not be located in the fixed electromagnet frame. Rather, the permanent magnets should be mounted on the moving platen, facing a smooth sheet of iron mounted in the fixed frame. In this manner, the magnet force vectors remain fixed in the platen frame, and thus fixed relative to the platen center of mass. This is essential, since if the magnets are fixed in the support frame, disturbance toques will be applied to the platen as it moves.

  Another reason for not including the permanent magnets in the suspension electromagnets is that this increases the size of the electromagnet structure and thereby reduces the efficiency of the magnet. This is discussed in more detail in the next item.

- **The capacitance probes should not be located in the center of the suspension magnets.** Placing the capacitance probes in the center of the suspension electromagnets is attractive in the sense that position is being sensed at the same point that it is being controlled. However, this approach is a carryover from thinking of the magnetic suspension as though it were the same as a mechanical suspension contacting the platen at each of the bearing locations. It is for this reason that three top suspension magnets were used in the original design. The design was arranged on the basis of kinematic principles of machine design. In the case of magnetic suspensions, this type of approach is not required, since there is no mechanical contact with the platen, and thus no possibility of the mechanical overconstraint which kinematic design seeks to avoid.

  Another disadvantage of locating the probes in the electromagnets is that this increases the size of the electromagnets for a given pole-face area and thereby increases the length of the magnet coil. This is also an effect of locating the permanent magnets in the electromagnet structure. This reduces the magnet efficiency in terms of force per watt of coil power. As an example, for the large electromagnet in the present design, the inner pole-face area is $0.91 in^2$, while the average coil major diameter is 2.58 inches. By removing the permanent magnet and the capacitance probe, this same pole face area could be achieved with a coil major diameter of 1.30 inches, thereby decreasing the coil resistance by a factor of two and increasing the magnet power efficiency by this same factor at a given force level. This represents a significant improvment in power efficiency. Further, the elec-

tromagnet structure becomes more compact, simplifying the mechanical design issues.

As an additional remark, if the frequencies of interest are high enough that modal deflections of the platen become important, then the probe locations need to be carefully considered in order to reduce the sensitvity of the system to modes which are not controlled. It is desirable to locate the probes at nodes of any such modes.

- **Some form of position sensing is needed over the full travel of the suspension.** A major problem with the current design is initialization. As described earlier, initalization is a manual operation involving inserting pieces of paper in the magnet air-gaps. Clearly, this technique is not desirable in a suspension which is used for other than academic purposes.

  One principal reason for this initialization problem is the extremely small active sensing range of the position probes (± 0.002 in). When the platen travels outside of this range, observability is lost. As mentioned before, this loss of suspension is permanent.

  This situation can be rectified by including some form of coarse position sensing which is capable of measuring the platen position over the full range of positions which are mechanically possible. This would allow a design which would not readily lose suspension.

- **Platen should not be a hollow-tube structure.** The current platen structure exhibits a significant resonance in the vicinity of 1 kHz. This resonance results because of the hollow-tube structure of the platen, which allows it to act like a tubular bell.

  To alleviate this problem, the platen should be designed to be as light and stiff as possible, with good damping characteristics. This points to the use of a composite/honeycomb structure with laminated iron inserts where magnetic forces must be applied.

- **A fixture should be constructed to measure the magnet force characteristics directly.** The modeling errors described earlier can be addressed by constructing a fixture to measure the magnet force characteristics. Such a fixture would allow accurate characterization of the magnet model to be used in the controller design. This becomes especially important in the case where nonlinear control is used to correct for the magnet force nonlinearities.

- **Experiments should be devised to measure the platen moments of inertia.** One possible source of error described in the earlier chapter

is that the platen moments of inertia were caculated but never measured. One possible approach to measurement of the platen principal moments of inertia is to suspend the platen in a torsion balance. The moment of inertia can be deduced by measuring the period of the torsional oscillation. The balance can be calibrated by using a test mass with an easily calculated or known moment of inertia.

8.1.1 Illustrative linear bearing design

Figures 8.1, 8.2, and 8.3 present end, top, and side schematic views of a linear bearing design which incorporates some of the changes proposed above. The electromagnets are laminated E-core transformer components chosen because of their wide commercial availability. These electromagnets face and act on strips of laminated magnetic material which run the length of the platen as shown in the figure. The outboard location of the support magnets gives good control of the platen roll motion. All iron components are shown as light gray. For simplicity, the electromagnet coils are not explicitly shown, but fill the E-core coil windows in the conventional fashion. Also, support for the E-core electromagnets is not explicitly shown.

I envision the platen iron as being contained in a composite structure, perhaps graphite honeycomb. Such materials should allow a weight reduction of the platen by at least a factor of two. Magnetically soft materials are also mechanically soft, and thus the nonmagnetic part of the platen must supply all mechanical strength. Further, the iron pieces must be protected from any high-force mechanical contact.

A pair of permanent magnets are located on the centerline at each end of the platen top surface as shown in the figure. These magnets face a smooth laminated iron sheet fixed to the electromagnet frame and thus serve to carry the platen gravity load. The magnets are used with a comparatively large air gap so that their associated unstable time constant is made large compared to the designed-for closed-loop time constants. As stated above, designing for large open-loop time constants reduces the difficulty of the control design problem.

The location of the position probes is not shown in the figure, but the probes can be located essentially as in the previous design.

This example serves to illustrate that the current design can be improved in many aspects, allowing higher performance, and a simpler mechanical design.

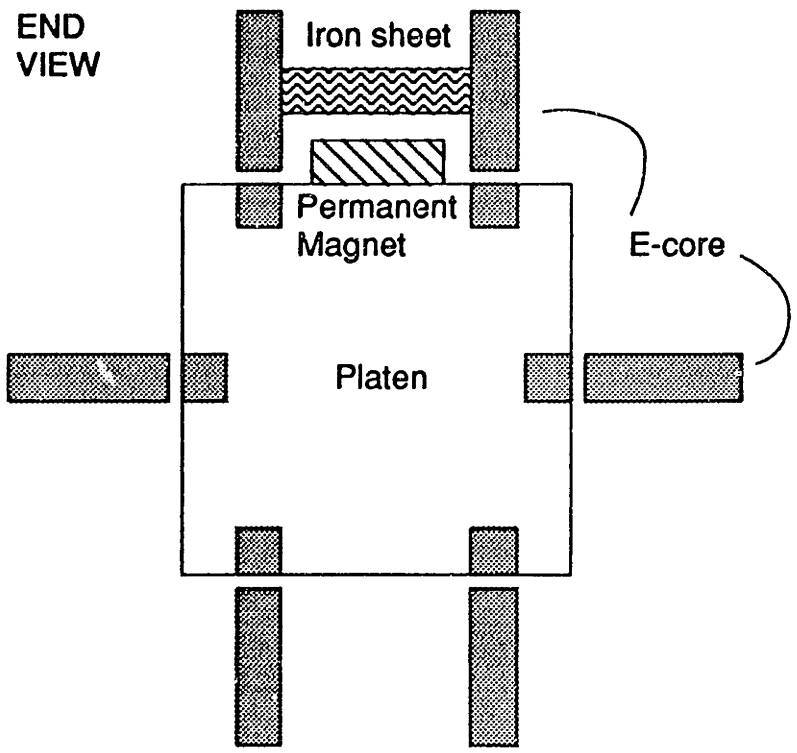

Figure 8.1: End view of proposed improved bearing.

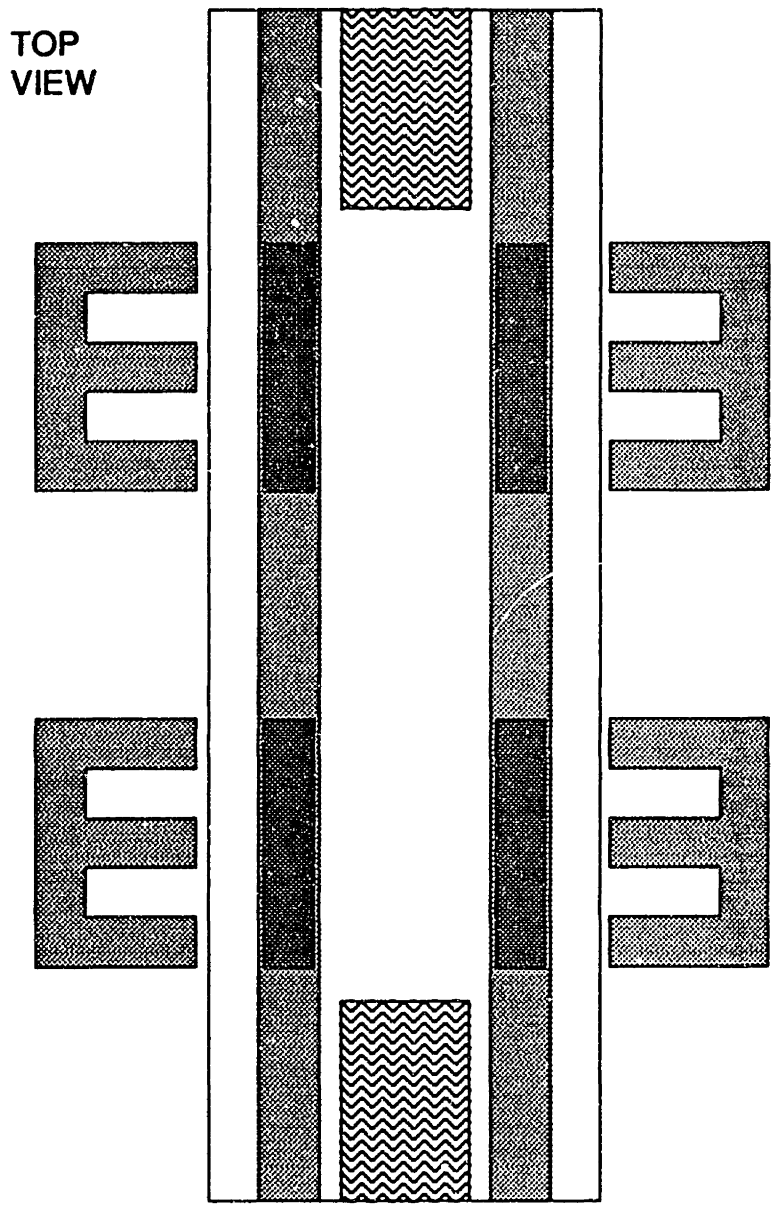

Figure 8.2: Top view of proposed improved bearing.

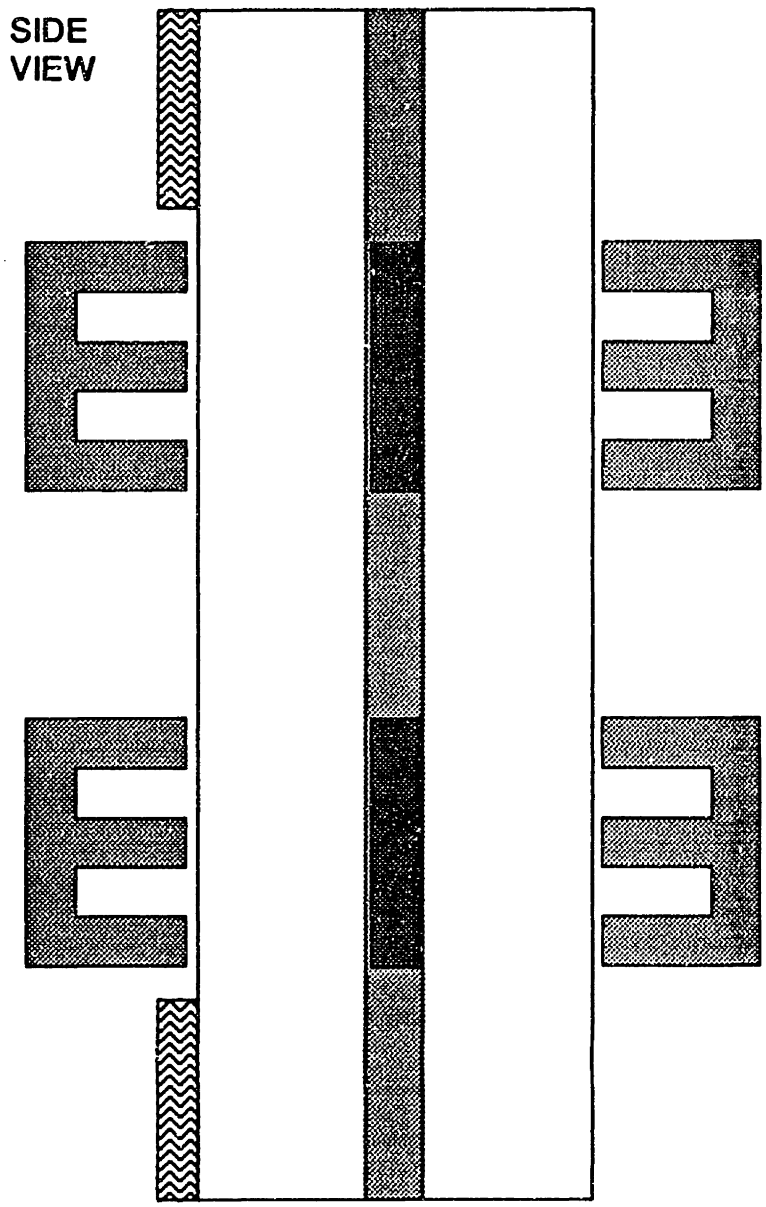

Figure 8.3: Side view of proposed improved bearing.

Chapter 9

Magnetically Suspended X-Y Stage

The previous chapters have investigated the issues associated with the design, construction, and testing of a precision linear bearing which provided large travel in a single degree of freedom and small travel in the remaining five degrees of freedom. In this chapter we present the design of a precision X-Y stage which has the advantage of providing control of large planar travel, and small travel in the remaining four platen degrees of freedom. This travel is provided using only a single moving element. The design has been developed on paper only; implementing this design in hardware will be the goal of future efforts.

One important application for the X-Y stage design is as the motion control subsystem in a photolithographic machine for producing semiconductor wafers. Current wafer stepping machines such as those produced by GCA in Andover, Mass., use compound axes and a coarse/fine topology to achieve travels of about 200 mm in X and Y with resolution better than 100 nm. Additionally, the camera head is moved on flexures to provide Z-axis focusing motions. This head contains an arc-source, cooling system, interferometer optics, and a heavy lens for imaging patterns onto the wafer; the assembly weighs on the order of 100 lbs. A schematic view of this type of wafer stepping system is shown in Figure 9.1.

The stages on the existing wafer stepper position the wafer in six degrees of freedom through the use of numerous actuators including rack and pinion or ball screws for the coarse motion in X and Y, and piezoelectric and miniature hydraulic actuators driving elements mounted on flexures. The overall system is quite complex, using on the order of 100 parts. It is especially difficult to design such a stage to be free of resonances, and thus to design for a fast settling time as the stepper moves from one chip-site to the next.

In contrast with this design is the magnetically-suspended X-Y stage shown in Figure 9.2. This stage will provide travel of 300 mm in X and Y and capabilities

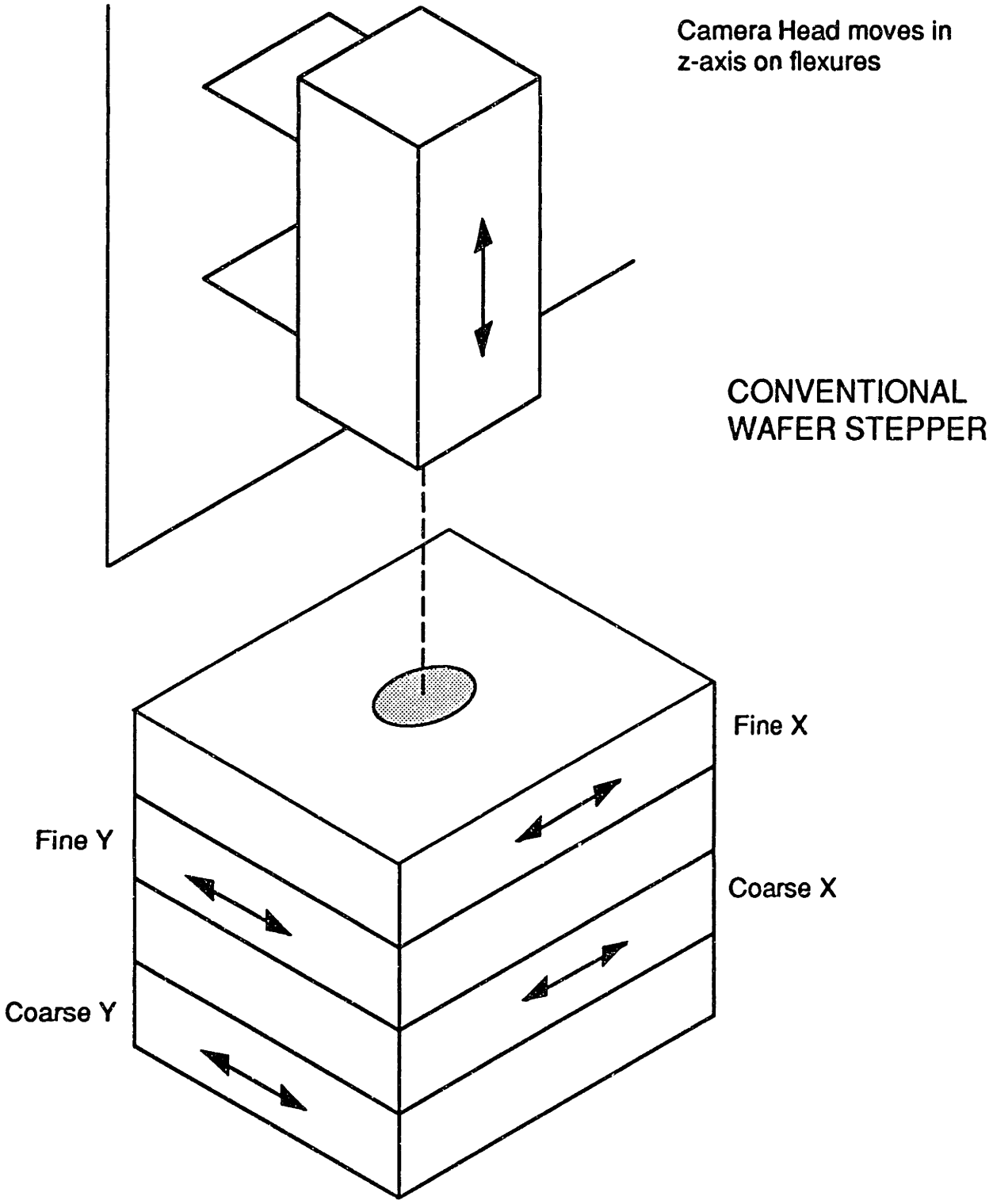

Figure 9.1: Schematic view of current wafer-stepper design which uses stacked coarse and fine stages in X and Y.

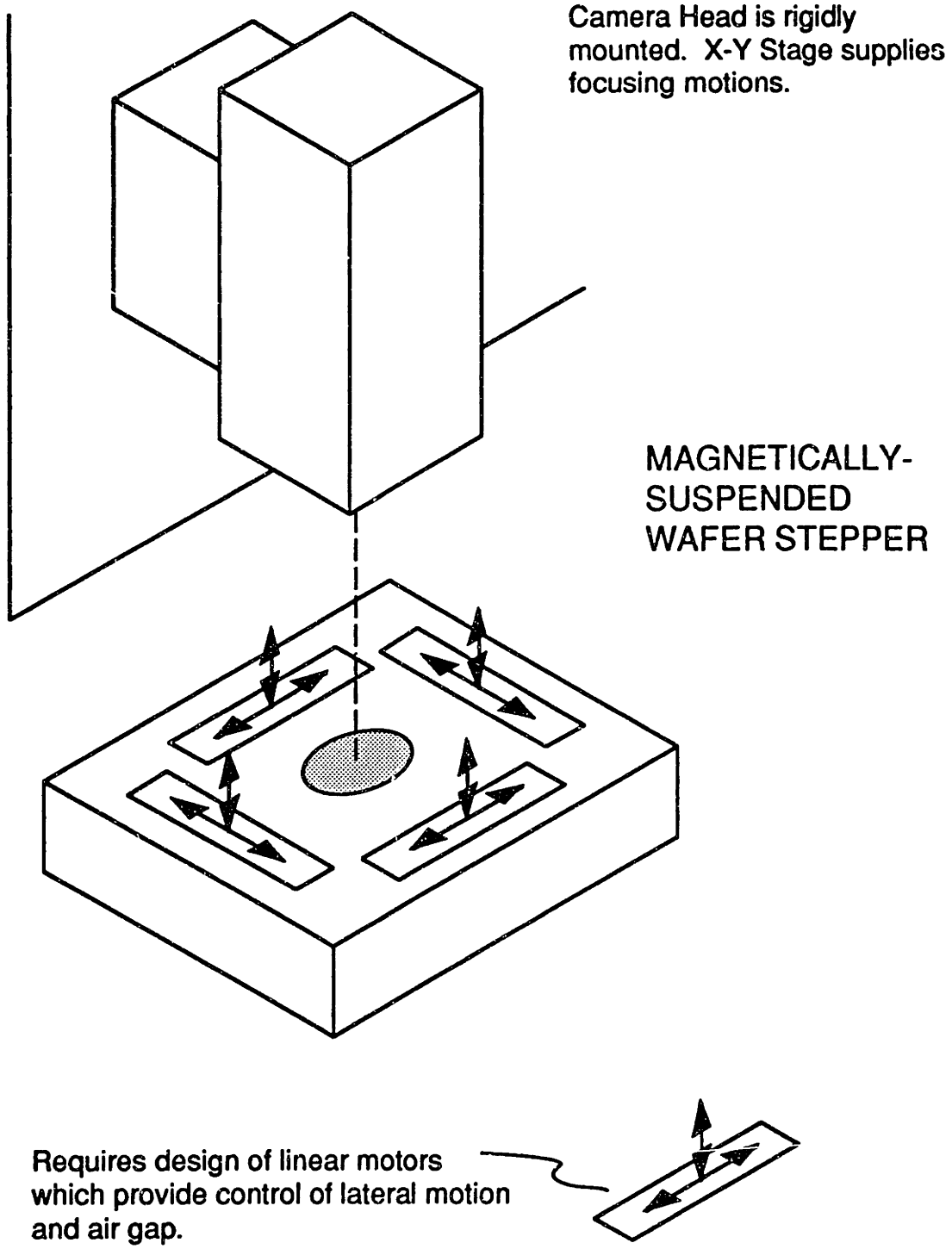

Figure 9.2: Schematic view of magnetically-suspended wafer-stepper design which uses only a single stage to implement all wafer motions, including Z-axis focusing.

for the required motions of focusing (Z) and alignment in the three rotational degrees of freedom. We envision accelerations of 0.5 g and settling times for a 15 mm step on the order of 200 msec to an accuracy of 10 nm. The moving stage will have dimensions on the order of 1 meter square. Position in all six degrees of freedom will be measured via laser interferometry using systems such as are available commericially from Hewlett-Packard, Zygo, and other vendors. Capacitive probes can be used to provide measurement of the platen home position.

Since the platen is monolithic and provides all required stepping and alignment motions, this design will greatly reduce the production costs associated with the stepper stage (perhaps by a factor of 10), while at the same time increasing the positioning performance of the stage in terms of accuracy and settling time. An approach utilizing magnetic bearings also opens up the possiblity of driving the stage in a scanning mode at high resolution, allowing new wafer production techniques. Additionally, magnetic suspension systems are inherently suitable for vacuum environments, which may be of interest in new wafer production techniques such as X-ray lithography.

A side benefit of this project is that the technology developed here is also suitable for implementing the stepper vibration isolation system, which currently uses passive pneumatic supports. This offers the possibility of solving the problems which exist with the current stepper isolation system.

To achieve the required level of performance necessitates new developments in both the magnetic system and its associated control electronics. As shown in the figure, the essential stage subsystem is a linear motor capable of controlling its axial and normal degrees of freedom. A number of these linear motor subsystems are arrayed on the platen, allowing control of its six degrees of freedom. The design issues and force/current characteristics of such linear motors are considered in the next section. The stage control architecture is presented in the section following that.

9.1 Linear Motor Design

In this section we describe the linear motor and derive the field equations for an idealized geometry which represents the essential operation of the linear motor subsystem.

The linear motor subsystem must be capable of controlling forces along the axis of the motor and normal to its air-gap. An array of permanent magnets are attached to the moving platen. An array of stator coils are mounted in the fixed machine-frame so as to interact with the permanent magnet array. The stator windings consist of at least two phases such that by independently controlling the amplitude of the phase currents, the required axial and normal components

of force can be controlled.

A schematic view of one possible motor topology is shown from above in Figure 9.3, and in cross-section in Figure 9.4. The stator shown in the figure is wound with three phases, but this choice is for the purpose of illustration only; the exact number of phases will be decided as the detailed design is developed. The motor is designed such that the attraction of the permanent magnets to the back iron will support the gravity load of the platen. In this manner, the stator coils will supply only the forces required to stabilize the equilibrium and to move the platen in the required trajectories. Under static conditions the power dissipated in the stator coils will be near zero. An advantage of this design is that no power is dissipated in the platen; power is only dissipated in the fixed frame. There are however, significant thermal design issues still to be resolved.

The linear motor design will be developed on paper and then verified via finite-element magnetics modeling software. Once the design appears to be satisfactory, a hardware prototype will be constructed. Initially, we will use ferrite magnets to reduce the cost of the prototype, but the final linear motor will use rare earth magnets to increase the force by about a factor of four.

The motor will then be placed in a test-stand which we will have constructed in order to map the motor force/current/displacement characteristics. I envision this test stand as consisting of a dedicated vertical milling machine wherein the spindle-head carries the stator coils, and the bed carries the permanent magnet platen. The platen will be mounted on a force sensor which is capable of simultaneously measuring force in the normal and axial directions. The milling machine carriages will be used to translate the motor platen throughout its operating space as the stator coil currents are varied. In this manner, the motor characteristics can be mapped and its performance verified.

Once the motor force characteristics are measured, a nonlinear controller can be designed which provides control of the axial and normal forces independent of the motor motion. This nonlinear controller is contained within the block labeled 'Motor Commutation and Power Amp' in Figure 9.6 shown in the next section. The performance of this controller can then be verified with the milling-machine test stand.

9.1.1 Field/Force solution

In this section we analyze an idealized geometry which represents the essential operating characteristics of the linear motor which drives the X-Y Stage. This geometry is shown in Figure 9.5. Coordinate directions x, y, and z are defined in the figure. The sides of each boundary are indicated with the letters c through h in parentheses. The upper region in the figure is a half-infinite space of material where the permeability is assumed to approach infinity. This region models

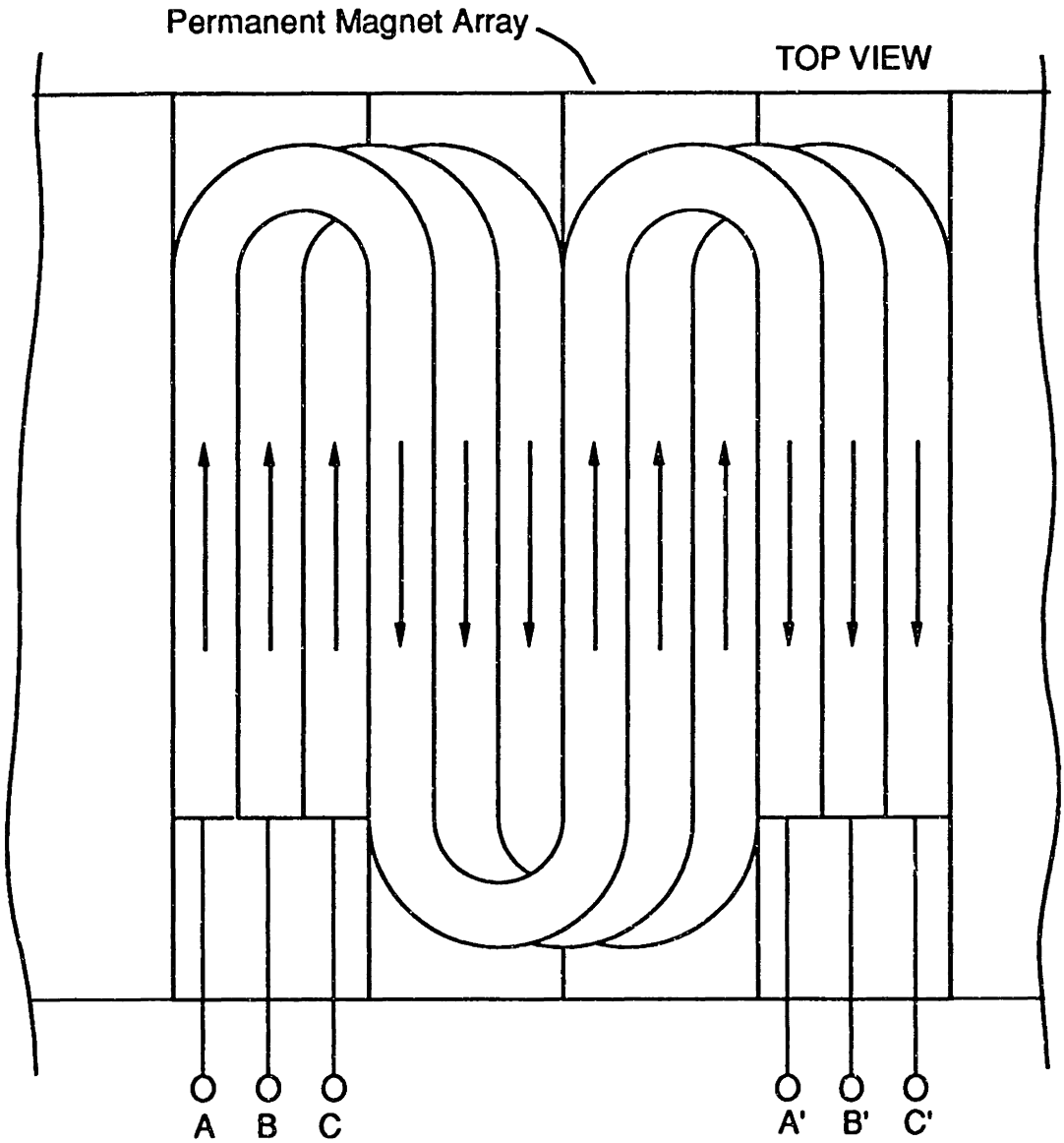

Figure 9.3: Linear motor top view.

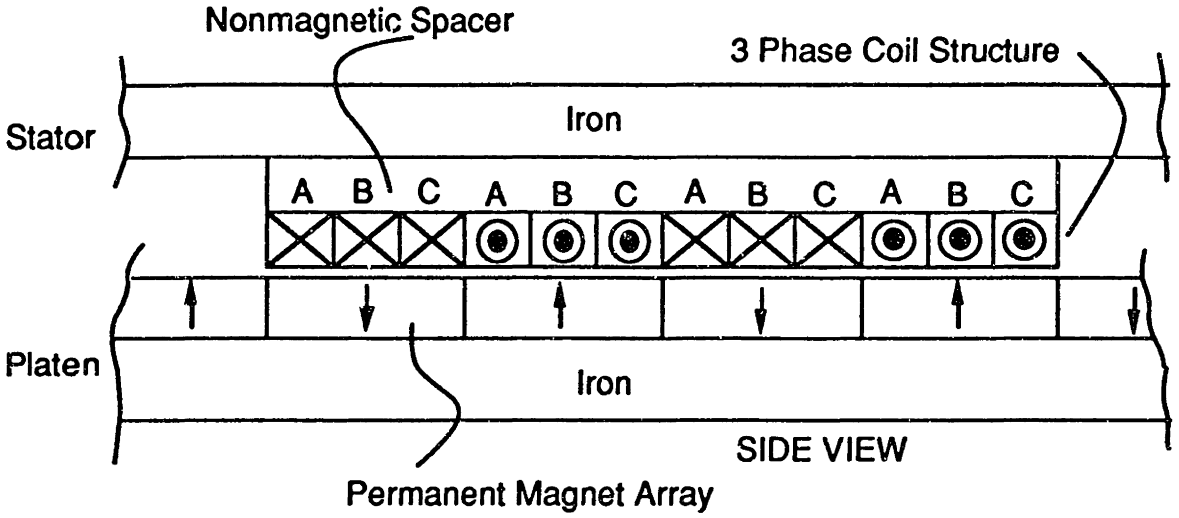

Figure 9.4: Linear motor section view.

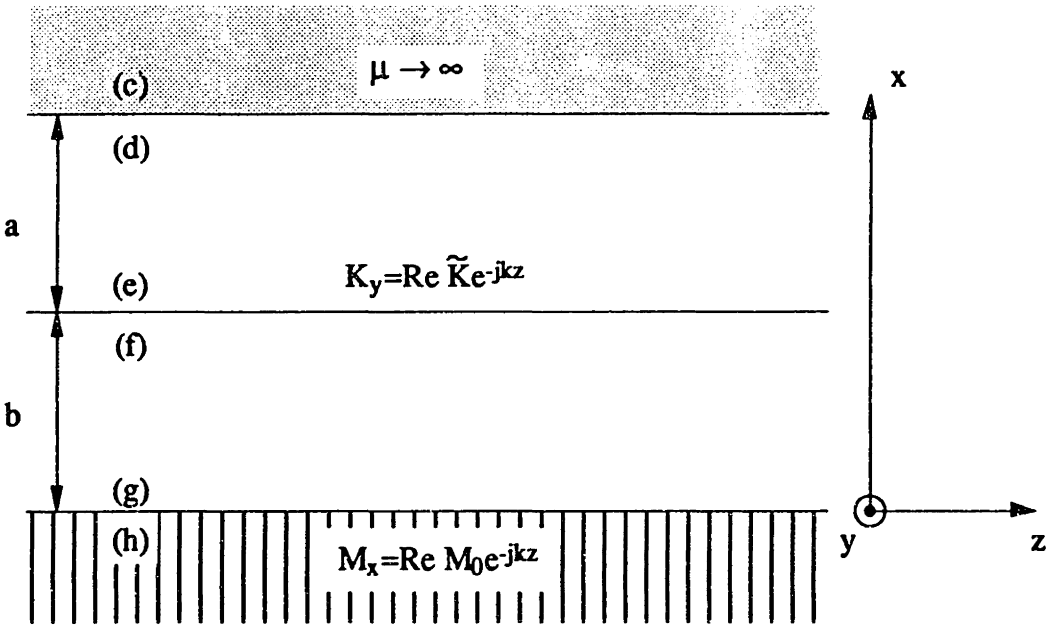

Figure 9.5: Geometry which represents model of linear motor.

the stator back iron. Separated a distance a from this high-permeability region is a current sheet carrying a sinusoidally distributed, y-directed surface current $K_y = \mathrm{Re}\tilde{K}e^{-jkz}$, where $\tilde{K}$ is the surface current complex amplitude, which represents time variations in both the current amplitude and spatial phase . Separated a distance b from this current sheet is a half-infinite space of x-directed magnetization $M_x = \mathrm{Re}M_0e^{-jkz}$. Here, for notational simplicity, M_0 is considered to be purely real, and represents the magnetization intensity, which is considered constant. The structure has a depth w into the paper, and is assumed to extend indefinitely in the $\pm z$-direction. We will use this model to calculate the force per spatial wavelength of the motor. End effects and fringing fields are neglected.

The model is idealized in several ways. First, while the stator current in the real motor occupies a region of finite thickness, and is distributed down the axis of the motor in a spatial square-wave, in the model we represent this stator current as a current-sheet of zero thickness, distributed sinusoidally in space at the spatial fundamental of the actual stator current distribution. Further, although the real magnets are of finite thickness and distributed in a spatial square-wave of magnetization, we model the magnetized region as of half-infinite extent and with the magnetization distributed sinusoidally in space at the spatial fundamental of the actual magnetization distribution. It is reasonable to model only the fundamental components of magnetization and current, as these are responsible for the bulk of the motor force production. Further, modeling the current as a sheet and the magnets as half-infinite greatly simplifies the analysis while retaining the essential features of the motor operation. Given these simplifications, analysis of the motor fields and forces is quite straightforward, though somewhat algebra intensive. I will skip some of the algebraic details and present the essential results below. This analysis follows the techniques and notation set forth in [Melcher 1981], chapters 2, 3, and 4.

The magnetic field is given as the gradient of the magnetic scalar potential $\mathbf{H} = -\nabla\psi$. Vector quantities are indicated in boldface. At the boundaries, we have the following conditions on the potential and field complex amplitudes. Because of the infinite permeability of the upper layer, $\tilde{\psi}^d = 0$; this is equivalent to $\tilde{H}_z^d = 0$. That is, the field is purely normal at the boundary of the region of high permeability. At the current sheet, normal H is continuous, $\tilde{H}_x^e = \tilde{H}_x^f$, and the tangential field is discontinuous by the value of the surface current, $\tilde{H}_z^e - \tilde{H}_z^f = -\tilde{K}$, or alternatively $\tilde{\psi}^e - \tilde{\psi}^f = j\frac{\tilde{K}}{k}$. At the magnetization boundary the potential is continuous, $\tilde{\psi}^g = \tilde{\psi}^h$, and the normal field is discontinuous by the magnetization, $\tilde{H}_x^g - \tilde{H}_x^h = M_0$. These boundary conditions are summarized below

$$\tilde{\psi}^d = 0 \tag{9.1}$$

$$\tilde{H}_x^e = \tilde{H}_x^f \tag{9.2}$$

$$\tilde{\psi}^e - \tilde{\psi}^f = j\frac{\tilde{K}}{k} \tag{9.3}$$

$$\tilde{\psi}^g = \tilde{\psi}^h \tag{9.4}$$

$$\tilde{H}_x^g - \tilde{H}_x^h = M_0 \tag{9.5}$$

Applying the transfer relations from Section 2.16 of [Melcher 1981] gives the following five equations among the field and potential complex amplitudes at the boundaries.

$$\tilde{H}_x^d = -k\coth(ka)\,\tilde{\psi}^d + \frac{k}{\sinh(ka)}\,\tilde{\psi}^e \tag{9.6}$$

$$\tilde{H}_x^e = \frac{-k}{\sinh(ka)}\,\tilde{\psi}^d + k\coth(ka)\,\tilde{\psi}^e \tag{9.7}$$

$$\tilde{H}_x^f = -k\coth(kb)\,\tilde{\psi}^f + \frac{k}{\sinh(kb)}\,\tilde{\psi}^g \tag{9.8}$$

$$\tilde{H}_x^g = \frac{-k}{\sinh(kb)}\,\tilde{\psi}^f + k\coth(kb)\,\tilde{\psi}^g \tag{9.9}$$

$$\tilde{H}_x^h = -k\,\tilde{\psi}^h \tag{9.10}$$

Together, equations (9.1)–(9.10) form a set of ten equations in ten unknowns, which are driven by the sources M_x and K_y. Since our interest is in finding the force on the permanent magnets which are attached to the platen, we eliminate variables to solve for the normal and tangential magnetic fields at the boundary (g) which is just above the magnetized layer. Solving (9.1)–(9.10) yields

$$\tilde{H}_x^g = M_0 e^{-k(a+b)}\cosh k(a+b) + j\tilde{K}e^{-k(a+b)}\cosh ka \tag{9.11}$$

and

$$\tilde{\psi}^g = \frac{M_0}{k}e^{-k(a+b)}\sinh k(a+b) - j\frac{\tilde{K}}{k}e^{-k(a+b)}\cosh ka. \tag{9.12}$$

The tangential field $\tilde{H}_z^g$ is related to the potential $\tilde{\psi}^g$ via the negative of the gradient with respect to z. Thus $\tilde{H}_z^g = jk\tilde{\psi}^g$, and thus

$$\tilde{H}_z^g = jM_0 e^{-k(a+b)}\sinh k(a+b) + \tilde{K}e^{-k(a+b)}\cosh ka. \tag{9.13}$$

The force acting on one spatial wavelength of the platen is given by the spatial average over this wavelength of the stress tensor multiplied by the area of the platen over one spatial wavelength. Specifically, $F_x = A_m\langle T_{xx}\rangle_z$, and $F_z = A_m\langle T_{zx}\rangle_z$, where F_x is the force acting on the platen in the x-direction, F_z is the force acting on the platen in the z-direction, $A_m = w2\pi/k$ is the area of one wavelength, T_{xx} and T_{zx} are the xx- and zx-components of the Maxwell

stress tensor, and the expression $\langle\cdot\rangle_z$ stands for the spatial average with respect to z.

The stress tensor for magnetically-linear materials derived from the Korteweg-Helmholtz force density [Melcher 1981, section 3.10] is $T_{ij} = \mu H_i H_j - \frac{\mu}{2}\delta_{ij} H_k H_k$ using the Einstein summation convention where since the k's appear twice in the same term they are to be summed from one to three. A final identity is the averaging theorem [Melcher 1981, section 2.15]

$$\left\langle \mathrm{Re}\tilde{A}e^{-jkz}\mathrm{Re}\tilde{B}e^{-jkz}\right\rangle_z = \frac{1}{2}\mathrm{Re}\tilde{A}\tilde{B}^* \tag{9.14}$$

where the * indicates complex conjugation. Applying these results to (9.11) and (9.13) yields the forces acting on the platen as

$$F_x = \frac{A_m\mu_0}{4}\left(M_0^2 e^{-2k(a+b)} - M_0\mathrm{Im}(\tilde{K})e^{-kb}(1+e^{-2ka})\right) \tag{9.15}$$

and

$$F_z = \frac{A_m\mu_0}{4}M_0\mathrm{Re}(\tilde{K})e^{-kb}(1+e^{-2ka}) \tag{9.16}$$

This completes the derivation of the motor force equations.

The first term in (9.15) is the attraction of the permanent magnets to the iron stator backing. The exponent of e involves a multiple of two times the air gap $(a+b)$ since the magnet's effect must cross the air-gap, induce magnetic surface charge on the iron, which effect must cross the air-gap again to interact with the magnet. This term is used to balance the gravity load on the platen by adjusting the parameter a which is the distance from the iron to the current sheet. The second term in (9.15) gives the force normal to the air gap resulting from the interaction of the current sheet with the permanent magnets. The imaginary component of $\tilde{K}$ drives this term. The real component of $\tilde{K}$ drives the lateral component of force on the platen in a symmetrical term in (9.16). These two components of current are of course just the spatial quadrature components of the sinusoidally distributed current sheet. If the current sheet is distributed in a more complex spatial function, this function can be built up in a Fourier series from the fundamental solution derived above. This comment also applies to more complex spatial distributions of the magnetization.

The exponential term e^{-kb} shows that the force decreases exponentially with separation between the magnets and the current sheet. Thus, for maximum force, the stator windings need to be positioned as close to the permanent magnet plane as possible. The exponential term e^{-2ka} represents the effect of the iron backing; the force decreases by a factor of two as a is varied from zero to infinity. In a practical design, b will be minimized, and a will be adjusted to balance the platen gravity load.

If the back iron is closely coupled to the magnetic circuit then its material properties will have a significant effect on motor performance. To allow good high-frequency response, the iron backing must be laminated. Perhaps more significantly, the iron's nonlinear magnetization and hysteresis characteristics will render the motor forces nonlinear with stator current. This poses significant problems with regard to achieving decoupling among the platen modal motions. Specifically, a transient such as a step in position in one degree of freedom will inevitably couple into the other degrees of freedom through the nonlinear magnetization curve of the back iron. At low frequencies this will be rejected by the modal controllers but the high-frequency transient response will be uncontrolled. For these reasons, it may make sense to give up the factor of two in (9.15) and (9.16) by removing ($a \rightarrow \infty$) the back iron entirely from the portion of the magnetic circuit driven by the stator coils. This iron could then be put in a separate location such that it attracts the platen magnets sufficiently to carry the gravity loads but does not significantly interact with the stator currents. This would render the motor response much more nearly linear and thus simplify the task of achieving decoupling of the platen modal motions.

In any case, it is clear that the motor design satisfies its goals of allowing the gravity load to be balanced by the permanent magnets, and independent control over the normal and lateral forces by proper weighting of the quadrature components of K_y. It is also a good feature of the design that the two components enter with equal control authority in x and z.

As an example of the performance which can be expected from this motor design, assume that the stator is 10 cm wide and 20 cm long with a magnet pitch of 5 cm. Thus $w = 0.1\text{m}$, $k = 1.26 \times 10^2\text{m}^{-1}$, and $A_m = 0.02\text{m}^2$. Further assume that the stator winding is 1 mm thick and carries a peak surface current density of 10^4 A/m. Assume that the center of this winding is separated 0.8 mm from both the back iron and the platen magnet plane, i.e., $a = b = 8 \times 10^{-4}$ m. Also assume that the platen magnets are rare-earth magnets with a remanence $\mu_0 M_0 = 1.2$ Tesla. For these values we calculate a peak force capability of about 100 Newtons for the 10 by 20 cm stator in both the normal and lateral directions, with a steady-state force capability of perhaps one quarter of this amount.

In the next section the integration of this motor design with the platen control algorithm is presented.

9.2 XY Stage Design

A block diagram for the X-Y stage control system is shown in Figure 9.6. The inner blocks labeled Motor Commutation and Power Amp contain the stator coil-current drives, and a local controller which, given the platen position and force

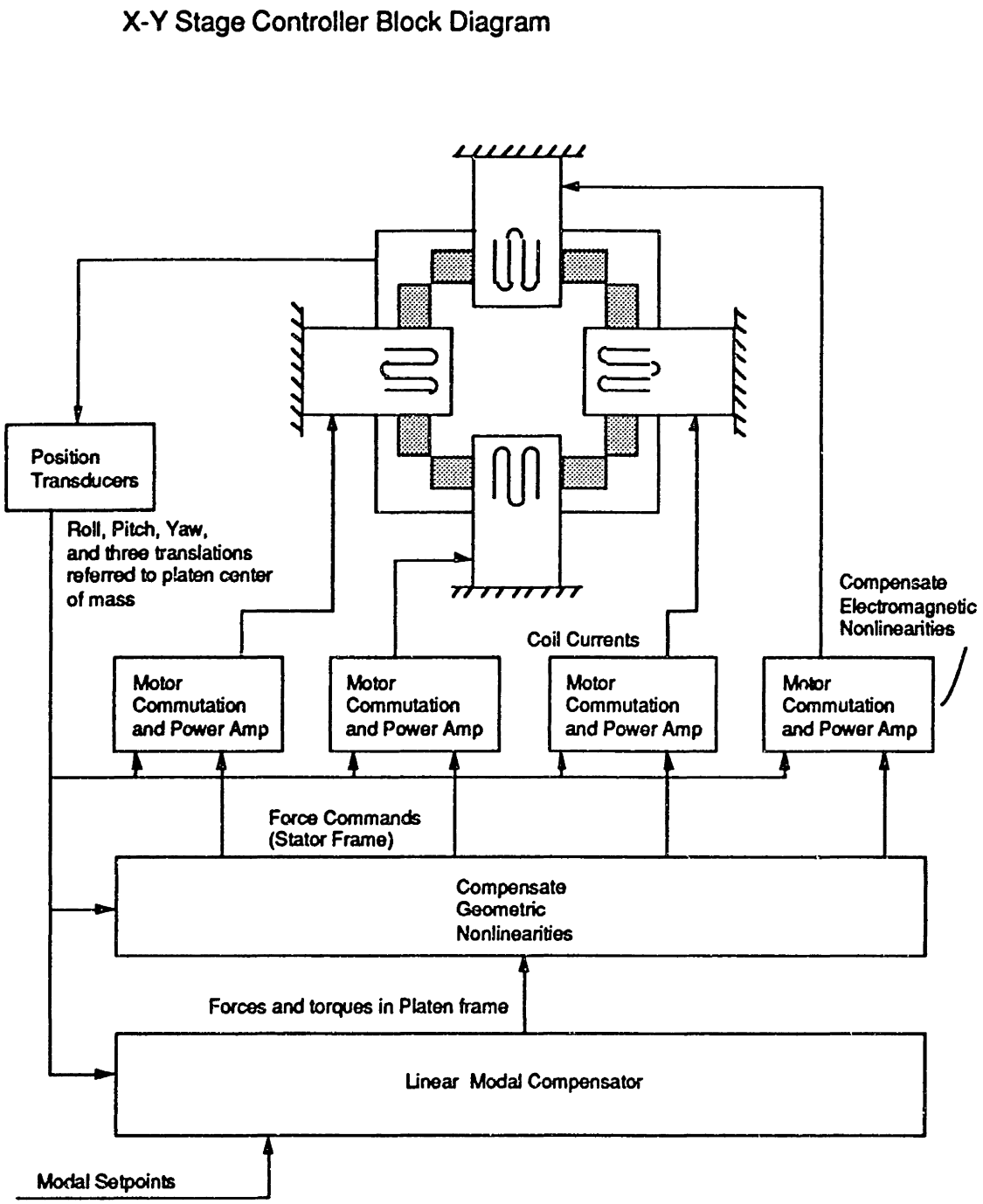

Figure 9.6: X-Y stage control architecture.

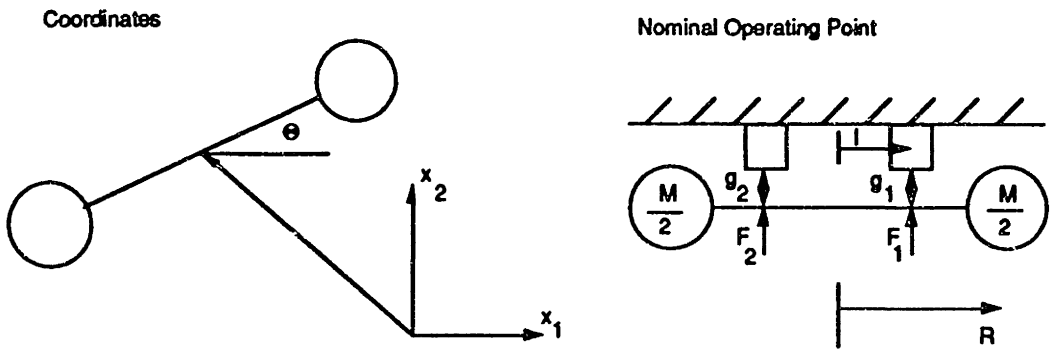

Figure 9.7: A three degree of freedom magnetically suspended system.

setpoints in the normal and axial directions is responsible for adjusting the stator coil-currents such that the motor forces are equal to the setpoints. That is, given desired normal and lateral forces, inverting (9.15) and (9.16) allows solution for the components of K_y required to realize these forces.

The desired forces are specified in the stator frame which is fixed in the laboratory. However, for linear control of the platen, forces should be specified in the platen frame. The block labelled Compensate Geometric Nonlinearities is responsible for translating forces and torques specified in the platen frame into forces specified in the various stator frames. This is essential since the platen moves relative to the stator frame.

As a simple example of the ideas presented in the previous two paragraphs, consider the system shown in Figure 9.7. This represents a three degree of freedom system in which two of the degrees of freedom x_2 and θ are to be controlled. These degrees of freedom are controlled through the currents in two electromagnets which apply forces F_1 and F_2 to the levitated member which is in the shape of a barbell having masses of $M/2$ at each end. The third degree of freedom x_1 is considered to be an idependent variable with the limits $-l < x_1 < l$. The object of this example is to demonstrate tranformations which linearize and decouple the system such that the transformed model is independent of variations in x_1, therby demonstrating the concepts to be applied to the full X-Y stage system.

The equations of motion are

$$\tau = F_1(l - x_1) - F_2(l + x_1) = MR^2\ddot{\theta}$$

and

$$F = F_1 + F_2 - Mg = M\ddot{x}_2$$

For a typical magnetic circuit $F_1 = C(i_1/g_1)^2$ and $F_2 = C(i_2/g_2)^2$ where i_1 and i_2 are the respective electromagnet coil currents. Letting

$$i_1 = g_1\sqrt{\frac{F_{s1}}{C}}$$

$$i_2 = g_2\sqrt{\frac{F_{s2}}{C}}$$

gives $F_1 = F_{s1}$ and $F_2 = F_{s2}$. Setting

$$F_{s1} = \frac{Mg(l + x_1)}{2l} + \frac{\tau_S}{2l} + \frac{F_S(l + x_1)}{2l}$$

and

$$F_{s2} = \frac{Mg(l - x_1)}{2l} - \frac{\tau_S}{2l} + \frac{F_S(l - x_1)}{2l}$$

gives

$$\tau = \tau_S = MR^2\ddot{\theta}$$

$$F = F_S = M\ddot{x}_2$$

a linear, decoupled system with inputs τ_S and F_S, and outputs θ and x_2. The terms τ_S and F_S may be though of as setpoints for desired torque and force applied to the suspended member. These setpoints exist at the input to the nonlinear compensator, which adjusts the coil currents to match the requested components. Because the torque and force are specified in the frame of the barbell, rather than in the frame of the suspension magnets, the system is linear in these terms.

This example shows the utility of linearizing what I would refer to as geometric or kinematic nonlinearities. These appear simply because the point of application of the forces F_1 and F_2 remains fixed in space while the suspended member moves relative to these points. Such terms should be easy to model accurately and also highly repeatable and are thus excellent candidates for linearization.

The block labeled Linear Modal Compensator is a linear controller which compares the actual platen position to the desired position and specifies the appropriate forces and torques in the platen frame. In this frame the system appears linear and decoupled. The block labeled Position Transducers contains the laser interferometers and the capacitance probes. The various controller blocks will be implemented on one or several DSP boards such as the floating point TMS320C30 board manufactured by Atlanta Signal Processors, Inc., at sampling rates of several kHz in each degree of freedom.

Assume that the platen has four linear motors attached to its top surface and four linear motors attached to its bottom surface and that half of these motors are oriented to act in the X-direction and half are oriented to act in the Y-direction. For the example numbers used for the linear motor in the previous section, this gives a peak force capability of 400 Newtons in X and Y, with a steady-state capability of 100 Newtons in X and Y. For a 40 kg platen steady accelerations of one quarter gee would then be possible, with peak accelerations on the order of one gee. These values are in the proper range to satisfy the acceleration requirements in wafer stepping applications.

This completes the discussion of the XY-stage design.

Chapter 10

Summary, Conclusions, and Suggestions for Further Work

This thesis has experimentally demonstrated that the control of nanometer scale motion is possible using magnetic suspension techniques. It has further proposed linear bearing and X-Y stage designs and techniques for their control.

The linear bearing system which has been constructed has provided a useful tool for understanding the issues which are important to the implementation of magnetic bearing supported motion control. The 5 nm position stability which it has demonstrated is the finest postion stability yet reported in the literature for a magnetic bearing system.

The X-Y stage design which has been proposed is novel in its use of linear motors to both suspend and translate the platen with large travel in two degrees of freedom. This novel design provides fine motion control and large travel in X and Y using a single stage with one moving element. Also, the ability to position in the Z-axis over small travels opens up application areas such as wafer stepping which are more difficult to address with conventional solutions such as mechanical, fluid, or gas bearings. The X-Y stage design is currently under patent application.

Another contribution of this thesis is an investigation of fundamental issues important to magnetic suspension control, such as the minimum crossover frequency for any practical control loop, and the manner in which nonlinear compensation techniques can be applied.

Much of what has been learned has grown out of the experimental implementation of the linear bearing system. As pointed out in Chapter 8, there are many ways in which the linear bearing can be improved. These areas can provide the focus for future efforts in precision suspensions. To this end, a linear bearing incorporating the proposed changes from Chapter 8 could be constructed. This second linear bearing should incorporate the approach of using a permanent mag-

net operating at a large air-gap to carry the gravity load on the platen, while the suspension electromagnets operate at small air-gaps and low bias currents. This approach allows the suspension open-loop time constants to be made slow without sacrificing power efficiency of the actuators, and is believed to be novel.

The actuators should by arranged in a symmetric configuration of identical electromagnets. The combination of symmetry and matched electromagnets greatly simplifies the task of designing for decoupling of the platen modes. It is far better to solve this problem in the electromechanical system than to try to compensate for it with the control algorithm. This lesson was driven home by experience with the linear bearing where two different types of actuators were used on the top of the platen.

Another area which requires further effort is in the modeling of the actuator nonlinearities. The nonlinearity of the electromagnet magnetization curve is one such nonlinearity. If the suspension controller does not account for this term, then it is impossible to decouple the modal motions during large transients. Using the nonlinear compensation techniques described in Chapter 3, controllers which compensate for the bearing nonlinearity can readily be designed. Another reason for using only a single type of actuator is that the modeling process is simplified since only one type of device needs to be tested.

On the other hand, hysteresis is more troubling than nonlinear but single-valued magnetization characteristics, and was not specifically addressed in this thesis. From the magnet force/current data taken earlier it is clear that the electromagnets exhibit hysteresis. The approach taken in the current work is to assume that the effects of hysteresis are small for small motions about an operating point. However, for large transients, this assumption does not hold. Thus, models for the electromagnet hysteresis need to be developed along with methods to accurately control the system in spite of hysteresis. One possible technique is to use a high-frequency dither signal, as is done in magnetic tape recording. The dither signal must be at a frequency high enough so as not to couple significantly to the platen.

As a performance goal for the second-generation bearing, if position sensors with Ångstrom resolution can be developed, it seems reasonable to attempt to build a magnetic suspension which demonstrates Ångstrom resolution. The capacitive sensors used in this thesis are within a factor of 50 of this resolution in a 1 kHz bandwidth. [Donaldson and Patterson 1983] claim 5 Ångstrom resolution for the custom capacitance probes designed for their diamond turning machine. Thus it seems reasonable that with careful design, a capacative probe with Ångstrom resolution can be designed, allowing the achievement of this goal.

The linear motor subsystem is the key element of the X-Y stage. Its essential operating characteristics have been derived in Chapter 9. These characteristics can be used to develop the detailed design of the motor. This design can then

be verified using finite-element magnetic modeling software. Then a single motor can be constructed and tested for its force/current/position characteristics and thermal limitations.

This information will allow the development of the nonlinear controller associated with the motor. This controller is responsible for driving the motor phases such that specified lateral and normal forces are maintained on the permanent magnet array. Once a single linear motor and its associated controller are successfully designed, then multiple copies of the motor can be constructed in order to implement the X-Y stage. The concept of controlling each motor with an individual controller which implements two-axis force control is believed to be novel.

Several significant elements of the X-Y stage design which were not addressed are the laser interferometric position transducer which must measure at least three degrees of freeedom of the platen and the implementation of the stage control algorithms. It may be possible to use capacitance probes to measure the three axes with small travel. The interferometric position measurements would be required in the three axes with long travel, i.e., X-translation, Y-translation and rotation about the Z-axis. The design of the interferometer measurement system sets the postion resolution and thus the performance limits long travel axes of the suspension. The interferometer optics carried on the platen need to be light and stiff; and arranged so as not to interfere with the suspension electromagnets. The implementation of control algorithms will involve total data rates on the order of 20,000 samples per second. These data rates necessitate the use of high-speed signal processing hardware, with the algorithms implemented in machine language. Programming control algorithms in machine language requires a significant investment of time.

The above discussion details the contributions of this thesis. The linear bearing system studied herein has demonstrated position stability in the laboratory which is the best yet reported. The X-Y stage design opens up application areas which have been addressed only poorly in the past. However, as we have described, there are many ways to improve the systems which have been constructed. Also, the X-Y stage design currently exists on paper only; there will be much to be learned in implementing this stage in hardware. By advancing the current state of the art, and by pointing to ideas for additional study, this thesis establishes a foundation on which to base future efforts in precision magnetic suspensions.

Chapter 11

Bibliography

Adamiak et al (1987): "The Switched Reluctance Motor as a Low-Speed Linear Drive," IEEE Int'l Conf. on Maglev and Linear Drives, Las Vegas, May 19-21, 1987 pp. 39-43.

Anschutz-Kaempfe, H. (1923): "Improvements in or relating to gyroscopes," British Patent #193397 of 1923.

Anschutz-Kaempfe, H. (1926): "Gyroscope Apparatus," US Patent #1589039 of 1926.

Arnold, S., and Folan L.M. (1987): "Spherical Void Electrodynamic Levitator," *Review of Scientific Instruments* , Vol. 58, No. 9, pp. 1732–1735, Sept., 1987.

Azukizawa, T., Morishita, M., Kanda, S., Tamura, N., Yokohama, T. (1986): A Linear Induction Motor Control System for Magnetically Levitated Carrier System," IEEE Int'l Conf. on Maglev and Linear Drives, Vancouver, B.C., May 14-16, 1986, pp. 205-210.

Basore, P.A. (1980): "Passive Stabilization of Flywheel Magnetic Bearings," M.S. Thesis, M.I.T., Camb., Mass., 1980.

Basore, P.A. (1982): "Self-Stabilizing Magnetic Bearings for Flywheels," Ph.D. Thesis, M.I.T., Camb., Mass., 1982.

Beams, J.W., Young, J.L., and Moore, J.W. (1946): "The Production of High Centrifugal Fields," *Journal of Applied Physics*, Vol. 17, Nov., 1946, pp. 886–890.

Beams, J.W. (1947): "Rotors Driven by Light Pressure," *Physical Review*, series 2, vol. 72, No. 10, Nov. 15, 1947, pp. 987–988.

Beams, J.W. (1950): "Magnetic Suspension for Small Rotors," *Review of Scientific Instruments,* 21, 1959, pp. 182-184.

Beams, J.W. (1954): "Magnetic-Suspension Ultracentrifuge Circuits," *Electronics*, Vol. 27, Mar., 1954, pp. 152–155.

Beams, J.W., Hulburt, C.W., Lotz, W.E., and Montague, R.M. (1955): "Magnetic Suspension Balance," *Review of Scientific Instruments*, Vol. 26, No. 12, Dec., 1955, pp. 1181–1185.

Beams, J.W. (1963): "Double Magnetic Suspension," *Review of Scientific Instruments*, Vol. 34, No. 10, Oct., 1963, pp. 1071–1074.

Benjamin, D. (1988): "Floating Trains: What a Way to Go!," *Time Magazine*, Aug. 22, 1988, pp. 58-59.

Bloom, H.L., et al. (1982): "Design Concepts and Cost Studies for Magnetic Suspension and Balance Systems." NASA-CR-165917.

Braunbek, W. (1939): "Freely Suspended Bodies in Electric and Magnetic Fields," *Zeitschrift fur Physik,* 112, p. 753, 1939. (English translation by R. Durham.)

Britcher, C.P., Fortescue, P.W., Allcock, G.A., and Goodyer, M.J. (1979): "Preliminary Investigations of Design Philosophies and Features Applicable to Large Magnetic Suspension and Balance Systems." NASA-CR-162433, Nov., 1979.

Britcher, C.P. (1983): "Some Aspects of Wind Tunnel Magnetic Suspension Systems with Special Application at Large Physical Scales". NASA-CR-172154.

Britcher, C.P. (1984): "Progress Toward Magnetic Suspension and Balance Systems for Large Wind Tunnels," *J. Aircraft*, Vol. 22, No. 4, pp. 264–269.

Britcher, C., Goodyer, M.J., Scurlock, R.G., and Wu, Y.Y. (1984): "A Flying Superconducting Magnet and Cryostat for Magnetic Suspension of Wind-Tunnel Models," *Cryogenics*, Vol. 24, Apr., 1984, pp. 185–189.

Britcher, C.P., Goodyer, M.J., Eskins, J., Parker, D., and Halford, R.J. (1987): "Digital Control of Wind Tunnel Magnetic Suspension and Balance Systems," Int'l Conf. on Instr. in Aerospace Simulation Facilities, Williamsburg, VA, June 22-25, 1987.

Carmichael, A.T., Hinchliffe, S., Murgatroyd, P.N., and Williams, I.D. (1986): "Magnetic Suspension Systems with Digital Controllers," *Review of Scientific Instruments*, Vol. 57, No. 8, Aug., 1986, pp. 1611–1615.

Clark, J.W. (1947): " An Electronic Analytical Balance," *Review of Scientific Instruments,* 18, 1947, pp. 915-918.

Covert, E.E., Vlajinac, M., Stephens, T., and Finston, M. (1973): "Magnetic Balance and Suspension Systems for Use with Wind Tunnels," *Progress in Aerospace Sciences*, Vol. 14, ed. D. Kuchemann, pp. 27–107, Pergamon Press.

Covert, E.E., Haldeman, C.W., Ramohalli, G., and Way, P. (1982): "Development of Closed-Loop Roll Control for Magnetic Balance Systems." NASA-CR-166017.

Donaldson, R.R., and Patterson, S.R. (1983): "Design and Construction of a Large, Vertical-Axis Diamond Turning Machine," SPIE 27th Annual Int'nl Technical Symposium and Instrument Display, Aug. 21–26, 1983.

Doyle, J.C., and Stein, G. (1981): "Multivariable Feedback Design: Concepts for a Classical-Modern Synthesis," *IEEE Transactions on Automatic Control*, Vol. AC-26, Feb., 1981, pp. 4-16.

Downer, J. R. (1980): "Analysis of a Single Axis Magnetic Suspension System," M.S. Thesis, M.I.T., Camb., Mass., 1980.

Downer, J. R. (1986): "Design of Large-Angle, Magnetic Suspensions," Sc.D. Thesis, M.I.T., Camb., Mass., 1986.

Ellis, R.W., and Mote, C.D., (1979): "A Feedback Vibration Controller for Circular Saws," *ASME Journal of Dynamic Systems, Measurement, and Control*, Vol. 101, Mar., 1979, pp. 44–49.

Earnshaw, S. (1842): "On the Nature of the Molecular Forces Which Regulate the Constitution of the Luminiferous Ether," *Transactions of the Cambridge Philosophical Society,* 7, p. 97, 1842.

Eskins, J. (1986): "Further Investigation into Calibration Techniques for a Magnetic Suspension and Balance System," NASA-CR-178056, Feb., 1986.

de Ferranti, S.Z., (1890): *Electric Meters*, British Patent #2653 of 1890, (Appl. Feb. 18, 1890, Pat. Jan. 10, 1891).

Franklin, G. F., Powell, J. D., and Emami-Naeini, A. (1986): *Feedback Control of Dynamic Systems.* Addison-Wesley Publishing Co., Reading, MA, 1986.

Franklin, G. F., and Powell, J. D. (1980): *Digital Control of Dynamic Systems.* Addison-Wesley Publishing Co., Reading, MA, 1980.

Frazier, R.H., Gilinson, P.J., and Oberbeck, G.A. (1974): *Magnetic and Electric Suspensions.* MIT Press, Cambridge, Mass., 1974.

Fortescue, P.W., and Bouchalis, C. (1981): "Digital Controllers for the Vertical Channels of a Magnetic Suspension System." NASA-CR-165684.

Fosque, H.S., and Miller, G. (1959): "Electromagnetic Support Arrangement with Three Dimensional Control—Part II, Experimental," *Journal of Applied Physics*, Supplement to Vol. 30, No. 4, Apr., 1959, pp. 240S–241S.

Geary, P.J. (1964): "Magnetic and Electric Suspensions — A Survey of their Design, Construction, and Use." British Scientific Instrument Research Association, Research Report R-314, 1964.

Graeminger, B. (1912): "Improvements in or Relating to Electromagnetic Suspension Devices," British Patents #24499 and #24541 of 1912.

Gondhalekar, V., and Holmes, R. (1984): "Design of a Radial Electromagnetic Bearing for the Vibration Control of a Supercritical Shaft," *Proc. Instn. Mech. Engrs.*, Vol. 198C, No. 16, 1984.

Gottzein, E., Brok, K.H., Schneider, E., and Pfefferl, J. (1977): "Control Aspects of a Tracked Magnetic Levitation High Speed Test Vehicle," *Automatica*, Vol. 13, pp. 205–223.

Groom, N.J., and Waldeck, G.C. (1979): "Magnetic Suspension System for a Laboratory Model Annular Momentum Control Device," AIAA Paper No. 79-1755, 1979.

Hansma, P.K. et al (1988): "Scanning Tunneling Microscopy and Atomic Force Microscopy: Application to Biology and Technology," *Science*, Vol. 242, No. 4876, Oct. 14, 1988, pp. 209–216.

Haberman, H. and Liard, G. (1979): "Practical Magnetic Bearings," *IEEE Spectrum,* Sept. 1979, p. 26.

Histani, M., Inoue, Y., and Mitsui, J. (1986): "Development of Digitally Controlled Magnetic Bearing (1st Report, Single Axis Control Method)," *Bulletin of JSME*, Vol. 29, No. 247, Jan., 1986, pp. 214–220.

Holmes, F.T. (1937): "Axial Magnetic Suspensions," *Review of Scientific Instruments*, Vol. 8, Nov., 1937, pp. 444–447.

IBM (1986a): *IBM Journal of Research and Development*, Vol. 30, No. 4, pp. 353–440, Jul., 1986.

IBM (1986b): *IBM Journal of Research and Development*, Vol. 30, No. 5, pp. 441–572, Sept., 1986.

Jayawant, B.V., Hodkinson, R.L., Wheeler, A.R., and Whorlow, R.J. (1974): "Transducers and Their Influence in the Design of Magnetically Suspended Vehicles," I.E.E. Conf. on Control Aspects of New Forms of Guided Land Transport, I.E.E. Publication No. 117, Aug., 1974, pp. 200–206.

Jayawant, B.V., Sinha, P.K., Wheeler, A.R., and Whorlow, R.J. (1976a): "Development of 1-ton Magnetically Suspended Vehicle Using Controlled D.C. Electromagnets," *Proc. I.E.E.*, Vol. 123, No. 9, Sept., 1976.

Jayawant, B.V., Sinha, P.K., and Aylwin, D.G. (1976b): "Feedback Control Systems for D.C. Electromagnets in Passenger-Carrying Vehicles," *Int. J. Control*, Vol. 24, No. 5, pp. 627–639.

Jayawant, B.V., and Sinha, P.K. (1977): "Low-Speed Vehicle Dynamics and Ride Quality Using Controlled D.C. Electromagnets," *Automatica*, Vol. 13, pp. 605–610.

Jayawant, B.V. (1981a): "Electromagnetic Suspension and Levitation," *Rep. Prog. Phys.*, Vol. 44.

Jayawant, B.V. (1981b): *Electromagnetic Suspension and Levitation Techniques.* Edward Arnold Ltd., London, 1981.

Jenkins, A.W., and Parker, H.M. (1959): "Electromagnetic Support Arrangement with Three Dimensional Control—Part I, Theory," *Journal of Applied Physics*, Supplement to Vol. 30, No. 4, Apr., 1959, pp. 238S–239S.

Johnson, B. G. (1985): "Active Control of a Flexible Rotor," M.S. Thesis, M.I.T., Jan., 1985.

Johnson, B. G. (1986): "Active Control of a Two-Mass Rotor: The Use of Complex Notation," Ph.D. Thesis, M.I.T., Sept., 1986.

Kane, T.R., and Levinson, D.A. (1985): *Dynamics: Theory and Applications.* McGraw-Hill Book Co., New York, N.Y., 1985.

Kane, T.R., Likins, P.W., and Levinson, D.A. (1983): *Spacecraft Dynamics.* McGraw-Hill Book Co., New York, N.Y., 1983.

Keith, F.J., Williams, R.D., Allaire, P.E., and Schafer, R.M. (1988): "Digital control of magnetic bearings supporting a multimass flexible rotor," NASA Magnetic Suspension Technology Conference, Hampton, Va., Feb. 2–4, 1988.

Kemper, H. (1937): " Schewebebahn mit räderlosen Fahrzuegen, die mittels magnetischer Felder an eisernen Fahrschienen schwebend entlang gefürt werden," German Patent #644302 of 1937.

Kemper, H. (1938): " Schwebende Aufhängung Durch Electromagnetische Kräfte: eine Möglichkeit für eine Grundsätzlich neue Fortbewegungsart," *Electrotech. Zeits*, 59, 1938, pp. 391-395.

Kuo, B. C. (1987): *Automatic Control Systems.* 5th Edition, Prentice-Hall, Inc., Englewood Cliffs, N.J., 1987.

Laithewaite, E.R., ed. (1977): *Transport Without Wheels.* Paul Elek Ltd., London, 1977.

Lindsey, K., and Steuart, P. (1987): "NPL Nanosurf 2: A Sub-nanometer Accuracy Stylus-based Surface Texture and Profile Measuring System with a Wide Range and Low Environmental Susceptability," Fourth Int. Prec. Eng. Sem., Cransfield Inst. of Tech., England, May 11-14, 1987, pg. 15.

Matsuda, R., Nakagawa, M., and Yamada, I. (1984): "Output Control of Magnetically Suspended Linear Guide," *IEEE Transactions on Magnetics*, Sept., 1984.

Melcher, J.R. (1981): *Continuum Electromechanics* , MIT Press, Camb., Mass., 1981.

Milner, A. (1979): "Scaling Laws for Flywheel System Components," COO-4094-63, LIncoln Laboratory, Lexington, MA, Nov., 1979.

Morishita, M., Azukizawa, T., Kanda, S., Tamura, N., and Yokohama, T. (1986): "A New Maglev System for Magnetically Levitated Carrier System," IEEE Int'l Conf. on Maglev and Linear Drives, Vancouver, B.C., May 14-16, 1986, pp 199-204.

Murgatroyd, P.N., Carmichael, A.T., and Thomas, S.J.P. (1985): "Improved Differential Optical Position Detector for Magnetic Suspension Systems," *Review of Scientific Instruments*, Vol. 56, No. 8, Aug., 1985, pp. 1666–1668.

Nikolajsen, J.L., Holmes, R., and Gondhalekar, V. (1979): "Investigation of an Electromagnetic Damper for Vibration Control of a Transmission Shaft," *Proc. Instn. Mech. Engrs.*, Vol. 193, 1979, pp. 331–336.

Pham, V. (1989): "Control of a Five Degree of Freedom Magnetic Suspension System," Bachelor's Thesis, MIT, Camb., Mass., June, 1989.

Pratt, W.H. (1902): *Magnetic Suspension Device*, U.S. Patent #730,840, (Appl. Oct. 10, 1902; Pat. Jun. 9, 1903).

Roberge, J.K. (1975): *Operational Amplifiers: Theory and Practice.* John Wiley and Sons, New York, NY, 1975.

Scudiere, M.B., Willems, R.A., and Gillies, G.T. (1986): "Digital controller for a magnetic suspension system," *Review of Scientific Instruments*, Vol. 57, No. 8, Aug., 1986.

Schweitzer, G., and Ulbrich, H. (1980): "Magnetic Bearings — A Novel Type of Suspension," *Int'l Conference on Vibrations in Rotating Machinery*, 1980, pp. 151–156, Inst. Mech. Eng., Bury St., Edmunds, England.

Sinha, P.K., and Hulme, A.J. (1983): "Simulation and control of a nonlinear electromagnetic suspension system," Proc. International Symposium of Simulation in Engineering Sciences: Applications to the Control of Mechanical and Energy Systems, J. Burger and Y. Jarny (eds.), pp. 257–262, North-Holland, Amsterdam, 1983.

Sinha, P.K. (1987): *Electromagnetic Suspension — Dynamics and Control.* Peter Peregrinus Ltd., London, England, 1987.

Slocum, A.H., and Eisenhaure, D.B. (1988): "Design Considerations for Ultra-Precision Magnetic Bearing Supported Slides," NASA Magnetic Suspension Technology Conference, Hampton, Va. Feb. 2–4, 1988.

Spong, M., and Vidyasagar, M. (1989) *Robot Dynamics and Control*, Wiley, 1989, pp. 259-283

Stephens, T., Covert, E.E., Vlajinac, M., and Gilliam, G.D. (1972): "Recent Developments in a Wind Tunnel Magnetic Balance," AIAA 10th Aerospace Sciences Meeting, AIAA Paper No. 72-164, January 17-19, San Diego, CA.

Studer, P. (1977): " A Practical Magnetic Bearing," *IEEE Trans. on Magnetics,* Sept. 1977, p. 1155.

Su, R. (1982): "On the linear equivalents of nonlinear systems," Systems and Control Letters, vol. 2, No. 1, pp. 48-52, July, 1982.

Takagi, S., Kanda, S., Azukizawa, T., Yokohama, T. (1987): "Dust Free Wafer Transportation System for Semiconductor Plant— an Application of New Maglev Technology," IEEE Int'l Conf. on Maglev and Linear Drives, Las Vegas, May 19-21, 1987 pp 73-78.

Thornton, R. (1973): "Design Principles for Magnetic Levitation," *Proc. of the IEEE* , May, 1973, p. 586.

Traxler, A., Meyer, F., and Murbach, H. (1984): "Fast Digital Control of a Magnetic Bearing with a Microprocessor," International Kongress Mikroelektronik, Munich, Nov 13-15, 1984, pp 94-102.

Tuttle, M.H., Kilgore, R.A., and Boyden, R.P. (1983): Magnetic Suspension and Balance Systems—A Selected, Annotated Bibliography. NASA-TM-84661.

Wickramasinghe, H.K. (1989): "Scanned-Probe Microscopes," *Scientific American*, Oct., 1989.

Williams et al (1989): "Digital Control of Active Magnetic Bearings," *IEEE Transactions on Industrial Electronics*, Vol. 37, No. 1, Feb., 1989, pp. 19–27.

Woodson, H.H., and Melcher, J.R. (1968): *Electromechanical Dynamics - Part-I* , John Wiley and Sons, 1968.